2016

High Redshift Galaxies As Probes Of The Epoch Of Reionization

Jessie Frances Taylor
University of Pennsylvania, jessie.f.taylor@gmail.com

High Redshift Galaxies As Probes Of The Epoch Of Reionization

Abstract
Following the Big Bang, as the Universe cooled, hydrogen and helium recombined, forming neutral gas. Currently, this gas largely resides between galaxies in a highly diffuse state known as the intergalactic medium (IGM). Observations indicate that the IGM, fueled by early galaxies and/or accreting black holes, ``reionized" early in cosmic history--the entire volume of the Universe refilling with ionized gas. This thesis analyzes and develops several ways to use observations of high redshift galaxies to probe this period, the Epoch of Reionization (EoR).

We examine the redshift evolution of the Ly-alpha fraction, the percentage of Lyman-break selected galaxies (LBGs) that are Lyman-alpha emitting galaxies (LAEs). Observing a sharp drop in this fraction at z ~ 7, many early studies surmised the z ~ 7 IGM must be surprisingly neutral. We model the effect of patchy reionization on Ly-alpha fraction observations, concluding that sample variance reduces the neutral fraction required.

We quantify the prospects for measuring the enhanced spatial clustering of LAEs due to reionization with upcoming observations from the Hyper Suprime Cam. LBGs from that survey provide a useful comparison sample. We consider the effect of foreground ``interlopers" on the clustering signal. We conclude that if HSC observes back into the EoR, the abundance and spatial clustering of galaxies and the size distribution of void regions evolve more strongly with redshift for LAEs than LBGs. Moreover, measuring the cross-power spectrum between LAEs and LBGs reduces the interloper effect.

We examine line intensity mapping experiments which trace large scale structure by measuring spatial fluctuations in the combined emission, in some convenient spectral line, from individually unresolved galaxies. We develop a technique to separate ``interloper" emissions, which these surveys are vulnerable to, at the power spectrum level, based on distortions introduced when the interloper emissions are (incorrectly) assumed to originate from the target redshift. Applying this to a hypothetical [CII] emission survey at z ~ 7, we find the distinctive interloper anisotropy can be used to separate strong foreground CO emission fluctuations.

Degree Type
Dissertation

Degree Name
Doctor of Philosophy (PhD)

Graduate Group
Physics & Astronomy

First Advisor
Adam Lidz

Keywords
Cosmology: Theory, Dark Ages, Reionization, First Stars, Galaxies: High Redshift, Intergalactic Medium, Large Scale Structure of the Universe

HIGH REDSHIFT GALAXIES AS PROBES OF THE EPOCH OF REIONIZATION

Jessie Frances Taylor

A DISSERTATION

in

Physics and Astronomy

Presented to the Faculties of the University of Pennsylvania

in Partial Fulfillment of the Requirements for the Degree of Doctor of Philosophy

2016

Supervisor of Dissertation	Graduate Group Chairperson
Adam Lidz	Ravi Sheth
Associate Professor of Physics and Astronomy	Professor of Physics and Astronomy

Dissertation Committee:

James Aguirre, Associate Professor of Physics and Astronomy

Cullen Blake, Assistant Professor of Physics and Astronomy

Robert Hollebeek, Professor of Physics and Astronomy

Masao Sako, Associate Professor of Physics and Astronomy

for M. Bernell Graves

Acknowledgments

Coming to the end of my doctoral work, I am aware of how crucial the support and encouragement of so many people has to been this project.

I am grateful to my advisor, Adam Lidz, for his guidance as I have learned how to be a scientist. Adam's curiosity, breadth of knowledge and willingness to help me work through any point of confusion have been invaluable. I am incredibly grateful to have worked with him.

My time at Penn has been enriched by my fellow graduate students, who have been friends and officemates; who have wrestled with homework, with research, with life alongside me. I am particularly grateful to Madeleine Phillips, Mehmet Noyan, Rachel Wolf, and to my officemates: Alyssa Barlis, Dillion Brout, Johanna-Laina Fischer, John Fischer, Ravi Gupta, Saul Kohn, Christina Krawiec, and Jennifer Mosher.

I am also thankful for the rest of my community in Philadelphia: for roommates – Matt Allison, Joel Bassett, Brooke McDowell, and Jeremy Millington – who have been there for almost the whole degree; for community at City Church – and this list is too long to name – who have walked alongside me.

I do not think I would now be studying Physics without the grounding and foundation I received in the Physics and Astronomy Department at Calvin College. I am grateful for my friendships there with faculty and students alike, for the encouragement to ask questions, for the modeling of how to do science and for the introduction to the beauty of the cosmos.

Finally, I would like to thank my family for their support, for their encouragement, for their love, for proofreading this thesis, for letting me talk about cosmology even when they don't quite follow it, and just for being here.

ABSTRACT

HIGH REDSHIFT GALAXIES AS PROBES OF THE EPOCH OF REIONIZATION

Jessie Taylor

Adam Lidz

Following the Big Bang, as the Universe cooled, hydrogen and helium recombined, forming neutral gas. Currently, this gas largely resides between galaxies in a highly diffuse state known as the intergalactic medium (IGM). Observations indicate that the IGM, fueled by early galaxies and/or accreting black holes, "reionized" early in cosmic history– the entire volume of the Universe refilling with ionized gas. This thesis analyzes and develops several ways to use observations of high redshift galaxies to probe this period, the Epoch of Reionization (EoR).

We examine the redshift evolution of the Lyα fraction, the percentage of Lyman-break selected galaxies (LBGs) that are Lyman-α emitting galaxies (LAEs). Observing a sharp drop in this fraction at $z \sim 7$, many early studies surmised the $z \sim 7$ IGM must be surprisingly neutral. We model the effect of patchy reionization on Lyα fraction observations, concluding that sample variance reduces the neutral fraction required.

We quantify the prospects for measuring the enhanced spatial clustering of LAEs due to reionization with upcoming observations from the Hyper Suprime Cam. LBGs from that survey provide a useful comparison sample. We consider the effect of foreground "interlopers" on the clustering signal. We conclude that if HSC observes back into the EoR, the abundance and spatial clustering of galaxies and the size distribution of void regions evolve more strongly with redshift for LAEs than LBGs. Moreover, measuring the cross-power spectrum between LAEs and LBGs reduces the interloper effect.

We examine line intensity mapping experiments which trace large scale structure by measuring spatial fluctuations in the combined emission, in some convenient spectral line, from individually unresolved galaxies. We develop a technique to separate "interloper"

emissions, which these surveys are vulnerable to, at the power spectrum level, based on distortions introduced when the interloper emissions are (incorrectly) assumed to originate from the target redshift. Applying this to a hypothetical [CII] emission survey at $z \sim 7$, we find the distinctive interloper anisotropy can be used to separate strong foreground CO emission fluctuations.

Contents

List of Tables

List of Figures

Chapter 1

Introduction

This thesis focuses on the Epoch of Reionization (EoR). We begin in §1.1, by describing reionization and by placing it within the larger cosmic context, discussing how this period fits into the history of the Universe as a whole. We follow that in §1.2, with a brief discussion of some of the ways of observing the EoR, both current and planned. In §1.3, we summarize our current understanding of the EoR as informed by the observational probes of §1.2. This motivates the work carried out in the rest of this thesis, as described in the subsequent chapters. In §2 and §3, we consider current and future measurements of high redshift galaxies and the implications of these measurements for our understanding of the reionization history of the Universe. In these sections, we consider two prominent techniques for selecting high redshift galaxies: narrow band surveys for Lyα Emitting galaxies (LAEs) and dropout selected Lyman-Break Galaxies (LBGs). Specifically, in §2, we consider the effects of cosmic variance on measurements of the Lyα fraction, $f_{Ly\alpha}$, the fraction of LBGs that are LAEs. In §3, we make predictions for observations of galaxy clustering by the Hyper-Suprime Cam (HSC), a new instrument on the Subaru Telescope, and discuss how the clustering signal can be used to trace reionization. Then, in §4, we consider intensity mapping surveys, which provide another promising approach for mapping out large scale structure during the EoR. Here we develop a new method to circumvent contamination from interloper populations in these measurements. In §5, we

conclude.

1.1 A Very Good Place to Start

Looking at optical images of galaxies or the Hubble Ultra Deep field (Fig. 1.1) might convince you that the space between galaxies is empty and uninteresting. However, such an understanding could not be farther from the truth. In reality, the space between galaxies occupies most of the volume of the Universe, and contains most of its matter. Currently, roughly half of the dark matter exists in intergalactic structures, such as dark matter halos too small to host galaxies (McQuinn 2016). The situation is even starker as we peer further back into the Universe: by $z \sim 6$, 95% of the dark matter exists between galaxies (McQuinn 2016). Baryonic matter exhibits similar patterns. By $z \gtrsim 1.5$, 90% of the baryonic matter in the Universe resides in the space in between galaxies (Ferrara and Pandolfi 2014). This region is known as the intergalactic medium (IGM). And it is out of the IGM that the structure we observe around us formed. So the IGM is an intriguing area of study.

Interest in the EoR arises when one tries to harmonize observations of the early Universe with observations of the present day IGM. Observations of the Cosmic Microwave Background (CMB) (discussed in §1.2.2) tell us that by roughly 400,000 years after the Big Bang ($z \sim 1100$) the cosmic gas "recombined" forming neutral hydrogen and helium. However, when we examine the present day IGM, via, for example, the spectra of quasars (discussed in §1.2.3), we see that that hydrogen and helium are almost completely ionized. Clearly, at some point in the last 13 Gyrs the IGM was ionized. We believe that the IGM was gradually photoionized by star-forming galaxies and/or accreting black holes in a process termed "reionization". The time period over which this takes place is referred to as the "Epoch of Reionization" (EoR).

Technically, reionization was a multistep process. The threshold energy to ionize a hydrogen atom is 13.6 eV. Helium requires 24.6 eV to singly-ionize and 54.4 eV to

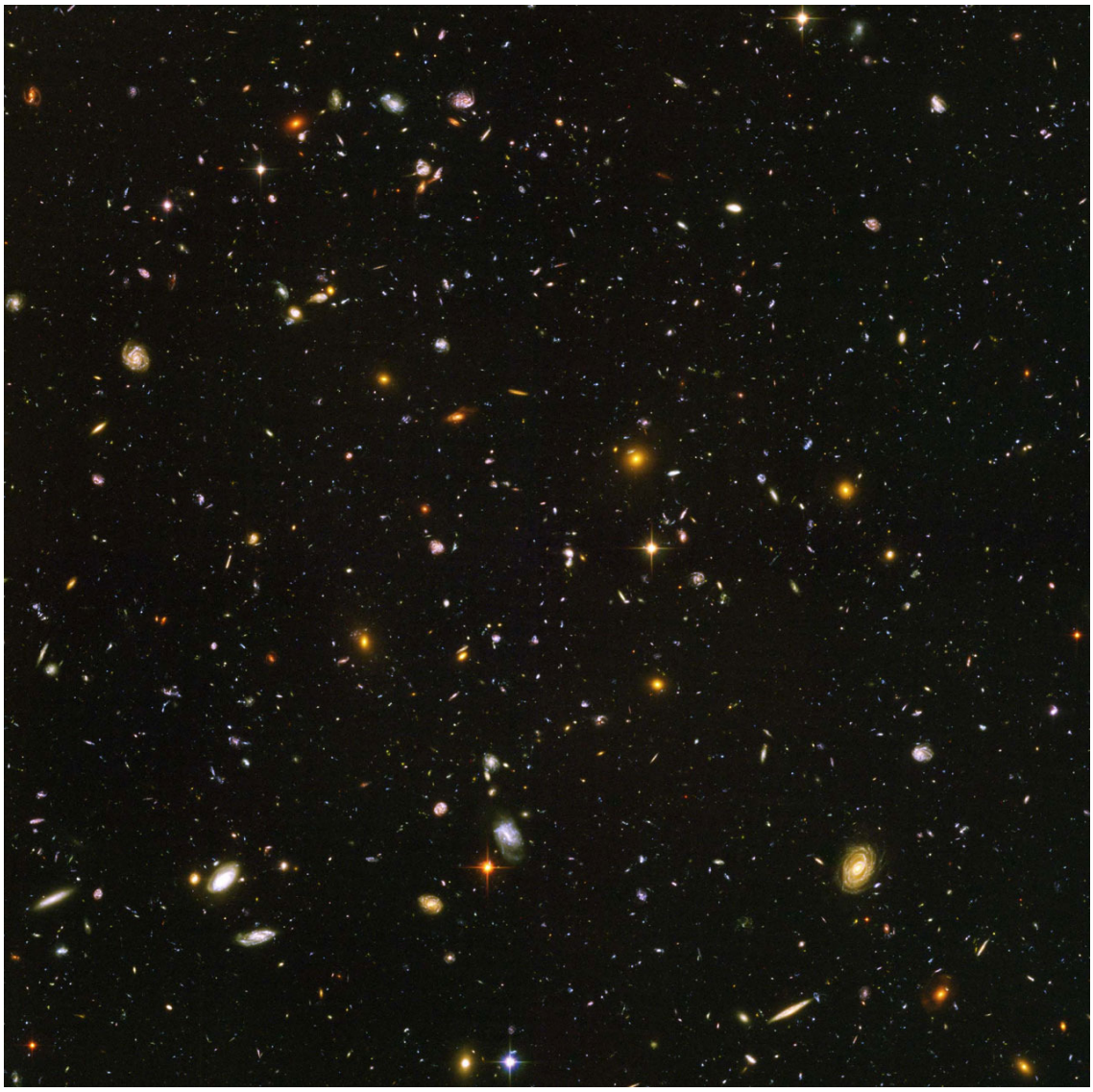

Figure 1.1: The Hubble Ultra Deep Field, spanning roughly $1/10$th the diameter of the full moon, appears largely empty in groundbased photos. However, a long exposure of the field, with the Hubble Space Telescope, shows $10,000$ galaxies, some from the end of the EoR. We are interested in the space between these galaxies. (Photo credit: NASA/ESA/S. Beckwith(STScI) and The HUDF Team)

doubly-ionize. Due to the similarities in energy required, it is believed that hydrogen ionization and helium single ionization happened at the same time, while helium double ionization was a much later process. Here we limit our focus to the former and refer to that period exclusively as “reionization" or the EoR.

In Fig. 1.2, we see a schematic of the history of the Universe with significant periods, particularly as they relate to reionization, delineated. Immediately following recombination we enter a period known as the cosmic dark ages: light-emitting objects, such as stars and accreting black holes, had not yet formed; the only light consisted of freely streaming CMB photons and 21-cm line photons from neutral hydrogen. At $z \sim 20-30$, the first stars form in dark matter halos of $\sim 10^6 M_\odot$. The halos are just big enough to host these stars but are too small for sustained star formation. The gas in the halo cools and condenses, ultimately forming stars, due to the presence of molecular hydrogen. However, molecular hydrogen is fragile and easily disassociated by the UV radiation from surrounding stars. Further, a single supernova would be energetic enough to unbind the cool and condensing gas out of which the stars were forming (Barkana and Loeb 2001). While these early stars provided some ionizing photons, the bulk of reionization required halos with total mass $\gtrsim 10^8 M_\odot$ to form. These halos were large enough to allow atomic line cooling and host the galaxies which in turn fueled reionization (McQuinn 2010). The first galaxies formed in abundance around $z \sim 10$ (Barkana and Loeb 2001; Bromm and Yoshida 2011). And reionization took place between roughly $z \sim 6$ and $z \sim 12$; so by $\gtrsim 1$ billion years after the Big Bang, the Universe was fully ionized.

1.1.1 Ionizing Sources

In the above, we have assumed that galaxies drove reionization. And, indeed, that is the general consensus (see, for example, Faucher-Giguère et al. (2008); Becker and Bolton (2013)). Historically, both galaxies and quasars were considered good candidates for fueling reionization. However, high redshift galaxy observations suggest that galaxies alone may reionize the Universe, provided that the escape fraction, $f_{\rm esc}$ is sufficiently

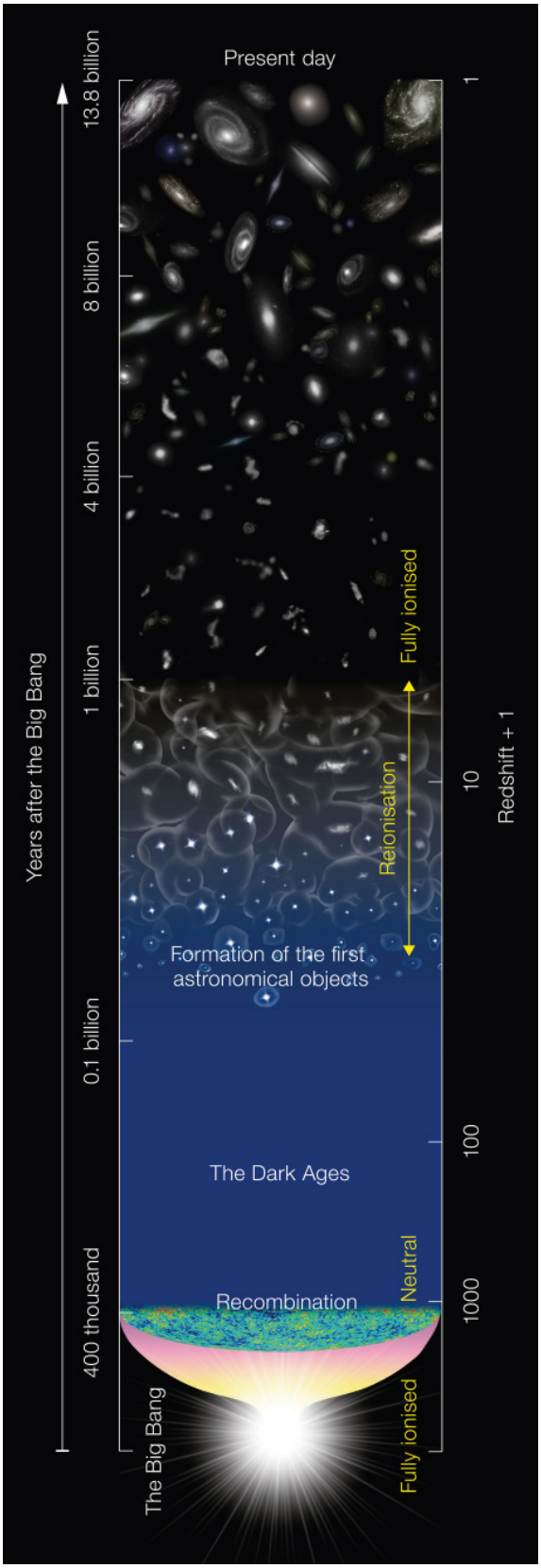

Figure 1.2: Schematic of the history of the Universe, from the Big Bang to the present day, including reionization and the end of the cosmic dark ages. (Image from NAOJ)

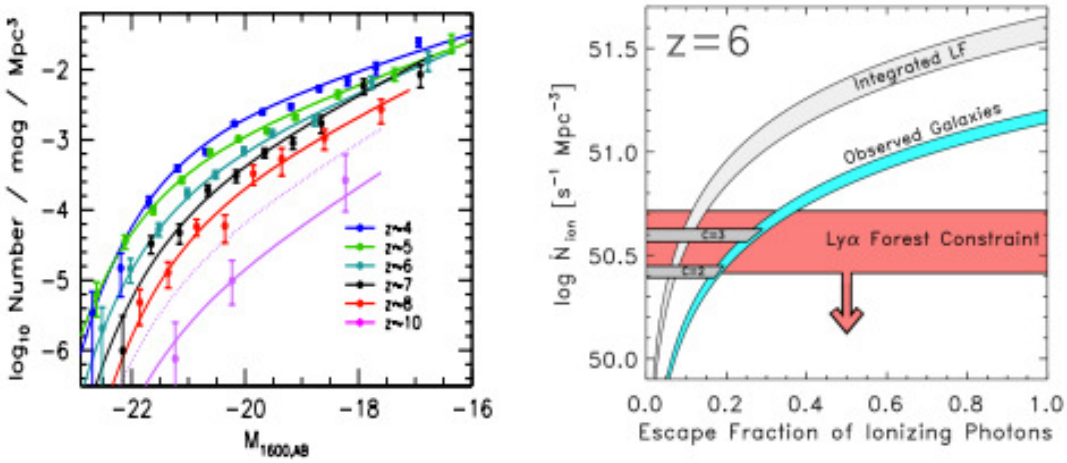

Figure 1.3: Figures from McQuinn (2016). *(Left)* Originally published in Bouwens et al. (2015). The luminosity functions of LBGs (for more information on this selection technique see §1.2.4.1) observed by the Hubble Space Telescope, for a range of redshifts covering much of reionization. *(Right)* Based off of luminosity functions, an estimate of whether galaxies can provide enough ionizing photons to maintain reionization. This figure shows an estimate of the emissivity of ionizing photons at $z \sim 6$, based both on the observed galaxy population and the integration of luminosity functions to include fainter galaxies, as a function of f_{esc}. These values are compared with the emissivities needed to maintain reionization using model values according to Kuhlen and Faucher-Giguère (2012). Becker and Bolton (2013) have concluded that emissivities several times those shown above are allowed.

large (Robertson et al. 2010; Finkelstein et al. 2012a). The escape fraction quantifies the average fraction of ionizing photons that escape each galaxy's host halo and are available to ionize atoms in the IGM. Further, we have a growing number of luminosity function measurements – the average abundance of galaxies as a function of their luminosity – for dropout-selected galaxies at $z > 6$ from the Hubble Space Telescope (HST) (Finkelstein et al. 2012b; Bouwens et al. 2012; Ellis et al. 2013; McLure et al. 2013) (for a more detailed discussion of luminosity functions, see §1.2.4.3). The left panel of Fig. 1.3 shows some current luminosity function measurements for a range of redshifts. As can be seen, the abundance of galaxies declines with increasing redshift. This behavior is expected since it parallels a drop in the halo mass function.

In order to estimate the ionizing flux provided by galaxies from the observed luminosity functions, one must make assumptions about the escape fraction, $f_{\rm esc}$. If $f_{esc} \gtrsim 0.2$, observed galaxies can maintain reionization at $z \sim 6$. However, if $f_{esc} \lesssim 0.2$, then fainter, and currently unobserved, galaxies are required to contribute to the ionizing budget. Indeed, measurements of the high redshift galaxy luminosity function indicate a steep faint end slope (Kuhlen and Faucher-Giguère 2012; McLure et al. 2013; Bouwens et al. 2015), implying that faint galaxies emit roughly twice as many ionizing photons as those emitted from currently observed galaxies. Of course, f_{esc} may scale with luminosity and there is a limit below which halos are not massive enough to host galaxies (McQuinn 2016). Better knowledge of f_{esc} will be necessary to more fully understand which galaxies drove reionization.

While we can estimate the number of ionizing photons based on the number of sources, we can also infer the total emissivity of ionizing photons – that is, the number of ionizing photons per volume per units time – based on quasar absorption lines. Miralda-Escude (2003) find that at $z = 4$, the ionizing emissivity is only slightly greater that that required to ionize hyrdrogen. To push this measurement to higher redshifts, we can turn to Bolton and Haehnelt (2007) who estimate that at $z \sim 6$, $1 - 3$ ionizing photons per hydrogen atom are emitted each Gyr. Since the age of the Universe at $z \sim 6$ is 0.94 Gyr, there

are just barely enough photons to ionize the Universe by this redshift. This model is called “photon-starved reionization." Of course, in this calculation, they have made assumptions about the evolution of the ionizing emissivity; a higher ionizing emissivity in the past would soften this conclusion. Becker and Bolton (2013) revisit their work with higher redshift data and more rigorous calculations and find that at $z \approx 5$, there can be up to 3-10 photons per hydrogen atom per Gyr. These higher limits would result in a less photon-starved reionization process. All of this is shown in the right panel of Fig. 1.3.

While galaxies are the generally assumed source of reionization, this still remains something of an open question. For example, Giallongo et al. (2015) claim to have detected enough quasars at $z \approx 6$ to reionize the Universe. Relying on quasars as the only source of reionization, however, is not without its own complications. Quasars provide a hard ionizing spectrum which would doubly-ionize helium by $z = 4$ (Madau and Haardt 2015). This conflicts with observations that support a later date for He II reionization; for instance, patchy absorption in the He II Lyα forest supports He II reionization completing only at $z \sim 2.7$ (Shull et al. 2010). Nonetheless, quasars certainly ionized their local environment. While galaxies are most likely the dominant source of reionization, a complete picture would have to include the effects of other ionizing sources, such as quasars.

In any case, once the Universe is ionized, a meta-galactic ionizing background maintains reionization. At high redshifts, this background is most likely maintained by those stars and galaxies which fueled reionization (McQuinn 2016). However, by $z \sim 2-3$, there are enough quasars to maintain it (Haardt and Madau 1996; Faucher-Giguère et al. 2008; Haardt and Madau 2012).

1.1.2 The Ionization State of the IGM

Interpreting almost all observations of reionization, such as those we will be discussing in §1.2, requires a model of the reionization process. Thus, accurate and precise models are crucial and have been the subjects of much work (see, for example, Furlanetto and Oh (2005); McQuinn et al. (2007b)). Here we focus on describing the broad contours

of the reionization process as it is currently understood. We follow Ferrara and Pandolfi (2014) in dividing the reionization process into three phases: "pre-overlap," "overlap" and "post-overlap."

Models for reionization generally assume a galaxy-fueled reionization. In the pre-overlap phase, galaxies ionize the gas surrounding them, creating an ionized bubble centered on the galaxy itself. Here, the IGM is essentially a two-phase medium; the gas is either ionized or neutral with a sharp transition between the two phases. Thus, reionization is extremely inhomogeneous. We can describe it as a "patchy" process. The ionization of a specific region is dependent only on its distance to the ionizing source and the efficiency of the ionization process. At these redshifts, the ionizing photons have a short mean free path so radiation can be treated locally, meaning that we can ignore the history of the ionizing emissivity and focus only on its instantaneous value when calculating the intensity of the ionization field (Lidz 2016).

Over time these bubbles grow and eventually begin to overlap and merge. This is the overlap phase. The stage should occur very rapidly as the bubble growth rate will accelerate as they merge. There is general agreement that the bubbles grow faster around groups of galaxies, due to the greater proximity of ionized regions. Thus, overdense regions ionized first and the ionized bubbles spread from there into the underdense regions. On large scales, reionization was an "inside out" process. This remains true even though dense regions are somewhat harder to ionize than less dense ones. In the dense regions, electrons and photons collide more often, recombining, and then need to be ionized again. Even so, the abundance of ionizing sources in the overdense regions is enough to overcome this (Barkana and Loeb 2004).

There will remain some small, dense clumps of neutral gas that do not contain an ionizing source. These clumps are self-shielding and ionize during the final phase. In this, the post-overlap phase, the ionized regions steadily push their way into the neutral gas ionizing them from the outside in (Barkana and Loeb 2007).

Fig. 1.4 shows this expected patchy reionization process in a map of 21-cm emission

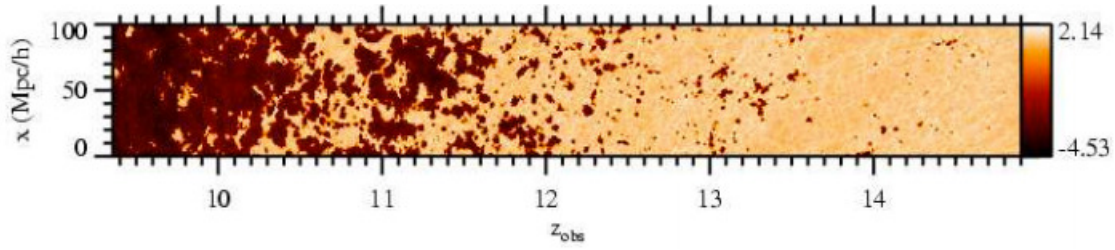

Figure 1.4: Figure from Mellema et al. (2006). A 21-cm map of the IGM based on numerical simulations showing the process of reionization. They plot here $\log_{10}(T_b)$, where T_b is the 21-cm temperature (in mK) relative to the CMB. This signal is discussed further in §1.2.1; for now, it is instructive to note the extended and patchy nature of the reionization process. The redshift range shown here is somewhat arbitrary and based on the details of their simulation. At early times, the Universe is smooth and neutral. However, as early ionizing sources turn on, bubbles of ionized gas appear. Those bubbles grow with time, eventually merging with other bubbles which accelerates their growth until the entire Universe is fully ionized.

from simulations. Ionized regions start as discrete patches and as we move to lower redshifts, the patches grow and merge, eventually ionizing the whole Universe.

In our discussion of the reionization process, we have only briefly mentioned why this field is significant and interesting. It is worthwhile to discuss this more explicitly here. First, as mentioned above, most of the matter in the Universe resides in the IGM. Thus, the IGM traces the underlying density field (Bond et al. 1996), and the structure we observe grew out of the IGM. The process of reionization impacts almost all of the baryonic matter in the Universe. Second, several important transitions occur during the EoR, and so it is a key period in the history of the Universe. During the EoR, the first galaxies formed. Prior to reionization, dark matter dominated structure formation. The EoR is the transition point where baryonic matter, in the form of gas in the IGM, became important in the formation and evolution of structure (Zaroubi 2013). Third, and this is related to the previous point, reionization heats the IGM to 10^4 K which has significant effects on latter galaxy formation. This may help in explaining the missing satellite problem, which can be described as follows: according to cold dark matter models of structure formation, the Milky Way halo should contain an abundance of small dark matter subhalos, yet relatively few satellite galaxies are actually observed (McQuinn 2016). Typically, for a cool IGM, galaxy formation is simply a matter of whether the gas in the halo had enough time to cool and condense. But after reionization, the heated IGM produces a pressure that opposes condensing and ultimately suppresses galaxy formation. This IGM pressure can force halos to be larger than they would otherwise be before accreting and forming stars (Quinn et al. 1996; Bullock et al. 2001; Bovill and Ricotti 2009). This results in fewer satellite galaxies than might be expected for the same underlying dark matter halo distribution.

Finally, observations are just beginning to reach into the midst of reionization. This is a period in the history of the Universe we are still working to understand. And that is exciting!

1.2 Observational Signatures of Reionization

As we have touched on above, observations of reionization are very important both in shaping our current understanding and in addressing the many open questions in this field. However, observing reionization is not a straightforward task. We are trying to study the gas in between galaxies roughly 13 billion years ago. Unlike galaxies or quasars, hydrogen gas is not highly luminous. Therefore, cosmologists have had to develop a variety of creative and clever ways to study the high redshift IGM. Broadly, these methods can be divided into two groups. The first group consists of direct observations of the neutral gas itself, primarily emission from neutral hydrogen due to hyperfine splitting of its ground state, which we discuss in §1.2.1. The second group relies on observations of objects formed either before or during reionization and the effect that neutral hydrogen (or free electrons, in the case of the CMB) along the line of sight to these objects has on our observations of them. Observations of CMB (§1.2.2), high redshift quasars (§1.2.3) and high redshift galaxies (§1.2.4) fall into this group.

1.2.1 21-cm Observations

As alluded to above, the most natural way of studying the EoR would be to observe the neutral hydrogen gas itself. Nature, fortunately, has provided a mechanism by which we might do so, thanks to the hyperfine splitting in the ground state of the hydrogen atom. When the spins of the proton and the electron in the hydrogen atom are aligned, the atom is in a higher energy state than when the spins are anti-aligned. Eventually the atom will transition into the lower energy, anti-aligned, state, emitting a photon with a wavelength of $\lambda = 21$ cm in the atom's frame. While this transition is forbidden, and thus has the extremely low transition rate of 2.9×10^{-15} s^{-1}, the amount of neutral hydrogen in in the Universe is significant enough to make this a promising observational probe (Zaroubi 2010). Because 21-cm emission undergoes cosmological redshift, observations of it will not just map the distribution of neutral hydrogen across the (2-dimensional) sky but in-

stead probe the full 3-dimensional distribution of the gas. In fact, 21-cm observations are an intriguing probe of not just the EoR, but also of the matter distribution during the cosmological dark ages. Furthermore, the redshifted 21-cm signal can be used to study the distribution of neutral gas left over after reionization completes, at which point neutral hydrogen remains only in galaxies and their circumgalactic media. Here, of course, we are interested in the 21-cm signal from hydrogen during the EoR. That signal will be redshifted to $\lambda = 21$ cm $(1+z)$, i.e., to a couple meters in wavelength at the redshifts of interest.

The key quantity in characterizing 21-cm emission is the spin temperature, T_S. The spin temperature is defined based on the ratio of the populations in the two hyperfine states:

$$\frac{n_1}{n_0} = 3\exp\left(\frac{-T_*}{T_S}\right), \tag{1.1}$$

where n_1 and n_0 are the number densities of hydrogen atoms in the excited triplet state and the ground singlet state, respectively; $T_* = 0.068$ K, the transition energy between the two states.

The spin temperature can be calculated as the weighted average of a number of different temperatures. This method is instructive as the interactions between these terms drive the emission that we are seeking to observe.

$$T_S = \frac{T_{CMB} + y_k T_k + y_\alpha T_k}{1 + y_k + y_\alpha}, \tag{1.2}$$

where T_{CMB} is the temperature of the CMB, T_k is the gas kinetic temperature, and y_k and y_α are the kinetic and Lyα coupling terms, respectively. Here, following Zaroubi (2010), we have assumed that the Lyα color temperature is equal to the gas kinetic temperature, $T_\alpha = T_k$. This is a reasonable assumption for the cases in which we are interested (Field 1958; Madau et al. 1997; Furlanetto et al. 2006). The three terms in this equation are the three competing processes that shape T_S: 1) absorption of CMB photons (T_{CMB}); 2) collisions with other particles (T_k); and 3) scattering of UV photons (T_α) (Loeb and Furlanetto 2013). This last term is also know as the Wouthuysen-Field effect (Field 1958,

1959; Wouthuysen 1952). T_S is influenced by different ionizing sources through these various processes; thus, observations of the spin temperature should help to clarify exactly which sources drove reionization (Thomas and Zaroubi 2008). As a general rule, since all observations must, by necessity, be of T_S against the background of the CMB, T_S is only visible when it differs from T_{CMB}.

Fig 1.5 shows how these temperatures change with redshift and which terms dominate T_S at various redshifts. T_{CMB} consistently decreases as $(1+z)$. At $z > 200$, T_k is coupled to the temperature of the CMB via Compton scattering off of free electrons left over from recombination. Here, due to the high density, T_S equilibrates with T_k. Thus, $T_S = T_{CMB}$ and there is no 21-cm signal. As the redshift drops, these temperatures begin to uncouple. From $z \sim 30$ to 200, T_k no longer follows T_{CMB}, since the density and ionized fraction are too low to couple them together. Instead, T_k cools as $(1+z)^2$, faster than the CMB is cooling. However, the density does remain high enough for T_S to continue to be coupled to T_k; thus, T_S is cooler than the CMB and the 21-cm signal may be observable in absorption (Carilli 2006). Somewhere in that range of redshifts, the density has dropped enough that collisions can no longer couple T_S to T_k and T_S again begins to follow T_{CMB}. From $z \sim 20$ to 30, the first ionizing sources begin to form, which again couples T_S and T_k. This is due to the Wouthuysen-Field effect. Continuum photons from these early sources excite the hydrogen atom from the $1s$ to the $2p$; the atom then spontaneously decays back to $1s$. In this process, the atom can change hyperfine states. Eventually T_k and T_S outstrip T_{CMB} and the 21-cm signal will be visible in emission (Zaroubi 2010). This transition happens before the Universe is significantly ionized and is due to X-ray heating which heats T_k above T_{CMB}, although the details here vary depending on the strength and efficiency of early X-ray sources. Once reionization is complete and the neutral hydrogen is ionized, the 21-cm signal will disappear.

The observable quantity is the brightness temperature contrast between a neutral hydrogen cloud and the CMB. Since the entire sky is glowing with CMB background radiation, we are specifically interested in the differential brightness temperature between the

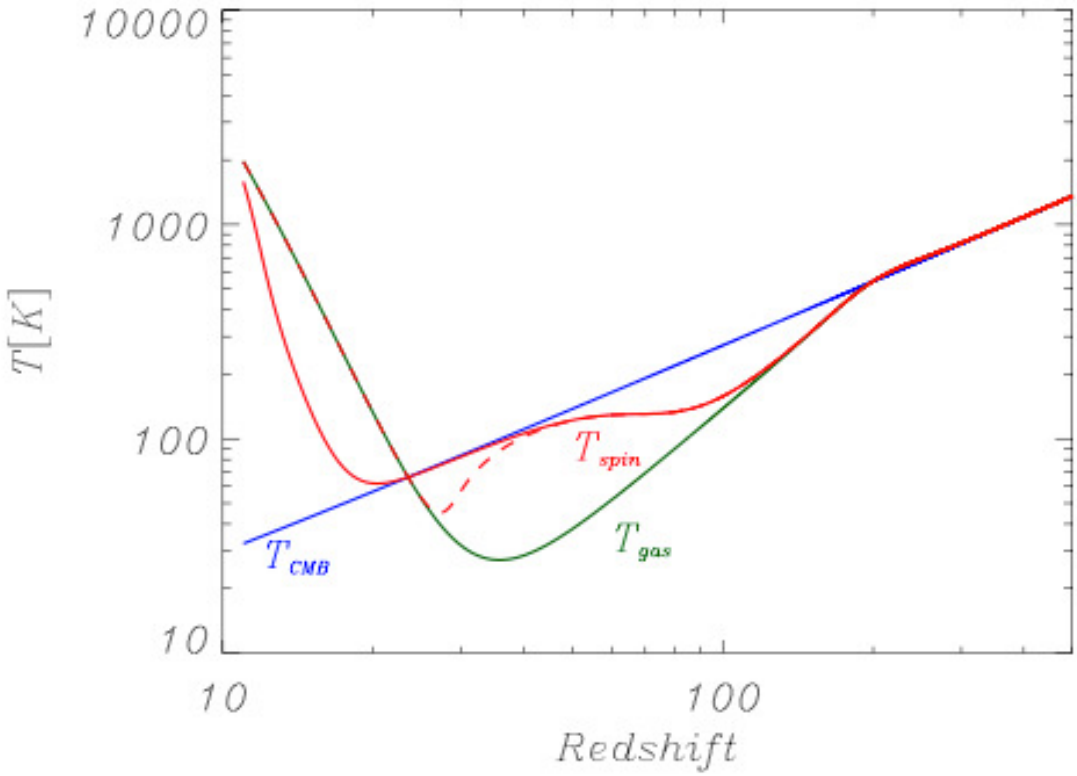

Figure 1.5: Figure from Zaroubi (2010). This figure illustrates the global evolution of the CMB temperature (blue), the gas temperature, T_k in the text, (green) and the spin temperature (red). The CMB temperature follows $(1+z)$. The dashed and solid red lines depict two different histories for T_S. The other temperatures have more complicated evolutions as discussed in the text.

21-cm emission and the CMB background. This brightness temperature can be calculated as follows:

$$\delta T_b = 28\,\mathrm{mK}\,(1+\delta)\,x_{HI}\left(1-\frac{T_{CMB}}{T_S}\right)\left(\frac{\Omega_b h^2}{0.0223}\right)\sqrt{\left(\frac{1+z}{10}\right)\left(\frac{0.24}{\Omega_m}\right)}, \tag{1.3}$$

where δ is the mass density contrast, x_{HI} is the neutral fraction, T_{CMB} and T_S are as we discussed them above, h is the Hubble constant in units of 100 km s^{-1} Mpc^{-1}, and Ω_b and Ω_m are the normalized baryonic matter and matter densities, respectively. Closer examination of this formula shows how the 21-cm signal can be used to study a diversity of topics. At $z \lesssim 15$, for plausible assumptions regarding the efficiency of X-ray heating and production, we can approximate $T_S \gg T_{CMB}$ and so $\left(1-\frac{T_{CMB}}{T_S}\right) \approx 1$. Thus, variations in δ and x_{HI} become much more significant. In the early stages of reionization, x_{HI} is close to 1, so variations in T_b should probe the underlying density field. However, variations in the spin temperature will also play a role in these early stages, at least after the first sources turn on. Of course, as reionization progresses, x_{HI} takes on a larger role and T_b should be able to tell us about the process of reionization (Zaroubi 2010). Fig 1.6 shows how T_b varies with redshift and how it corresponds to various stages in the Universe's history.

So far we have discussed the promise of 21-cm observations. The challenges, however, are many. While we want to observe the signal coming from the high redshift Universe, that signal must be untangled from foregrounds and noise. For studying the EoR, we are interested in frequencies of $\sim$ 100 MHz. In that regime, bright foregrounds dominate the sky; the neutral hydrogen emission is expected to be only 10^{-4} times as bright as the foreground emission (Carilli 2006). That is, the foregrounds are several orders of magnitude brighter than the signal of interest. Galactic synchrotron emission is by far the strongest foreground contaminant, contributing roughly 75%. The remaining 25% of foreground emission comes from a combination of other galactic sources (supernovae remnants and free-free emission) and extragalactic sources (radio galaxies and galaxy clusters). Extensive theoretical work has gone into studying the foregrounds of EoR measurements (Shaver et al. 1999; Di Matteo et al. 2002, 2004; Cooray 2004; Santos et al.

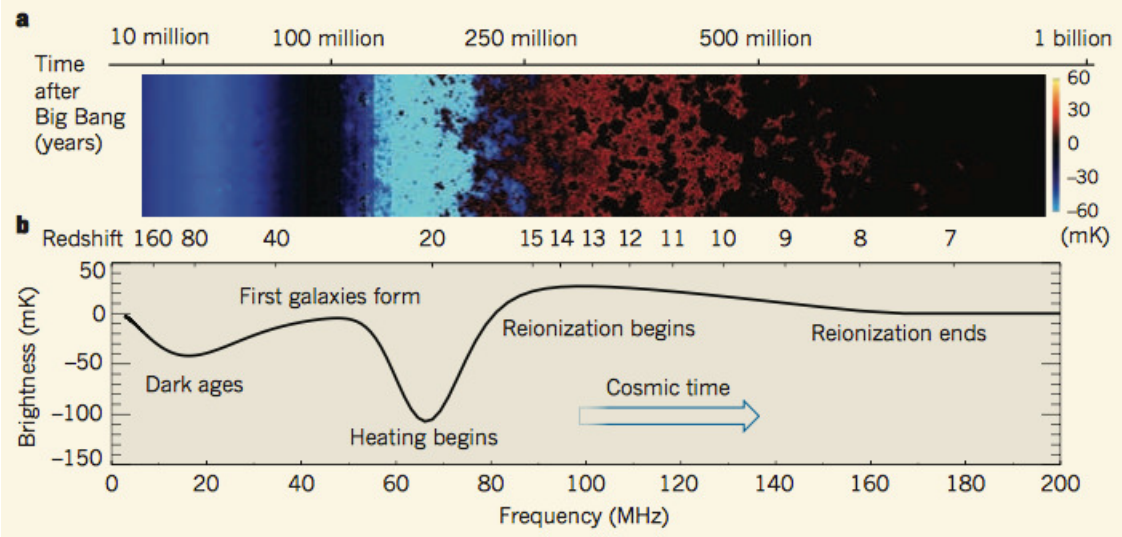

Figure 1.6: Figure from Pritchard and Loeb (2010). The upper panel (a) shows the evolution of fluctuations in the 21-cm signal. This timeline is pieced together from simulation slices. The cool colors (purple and blue) indicate absorption phases, black is no signal, and red is an emission phase, here due to reionization. The bottom panel (b) shows variation in T_b over roughly this same timescale.

2005; Jelić et al. 2008; Gleser et al. 2008; Wilman et al. 2008; de Oliveira-Costa et al. 2008; Sun et al. 2008; Waelkens et al. 2009; Sun and Reich 2009; Bowman et al. 2009). Shaver et al. (1999); Jelić et al. (2008, 2010); Bernardi et al. (2009) and Bernardi et al. (2010) have shown that these signals tend to be smooth along the frequency direction, in contrast to the high redshift signal which fluctuates along that direction. Thus, fitting these foregrounds and then subtracting them could allow us to recover the EoR signal (Zaroubi 2013).

Our ability to separate these signals has been enhanced by the development of the foreground wedge cleaning technique. 21-cm instruments measure the full power spectrum of spatial fluctuations across the sky. We can, however, when using interferometers, separate this signal into two components: $k_{\parallel}$, along the line of sight, and $k_{\perp}$, in the plane of the sky. It has been discovered that in $k_{\perp} - k_{\parallel}$ space, the foreground contaminates are confined to a specific wedge shaped region, while the EoR signal dominates the rest of the space. The precise dimension of the wedge and the sharpness of the boundary between the two regions is determined by a number of instrument parameters, such as antenna separation, signal reflection, angular response of the beam, and bandwidth. All this is based on a combination of theoretical and observational work (Datta et al. 2010; Morales et al. 2012; Parsons et al. 2012; Vedantham et al. 2012; Thyagarajan et al. 2013; Hazelton et al. 2013; Pober et al. 2013; Liu et al. 2014a,b). The promise of this technique is that observations in the right region of $k_{\perp} - k_{\parallel}$ space are essentially free from foreground contamination, leaving the EoR signal clearly, if faintly, visible (DeBoer et al. 2016). This technique has already been used to good effect by the Precision Array to Probe the Epoch of Reionization (PAPER), who, although they do not have the required sensitivity to actually detect the 21-cm signal due to reionization, were able to place a tight upper bound on it (Ali et al. 2015). Further, the Hydrogen Epoch of Reionization Array, which promises deeper observations than PAPER, is designed to use this technique to avoid many of the complications of foreground emission (DeBoer et al. 2016).

In addition to foregrounds several other effects can complicate observations. Iono-

spheric fluctuations, due to fluctuations in the index of refraction in the ionized plasma, are particularly insidious over large fields of view. Any calibration techniques are complicated by rapids variations in the ionosphere, due to storms or other disturbances. Thermal noise, either sky noise or receiver noise, is another complication. Finally, one of the more challenging problems in these observations, and in low-frequency radio astronomy in general, is man-made interference. The radio bands needed to observe the EoR are not protected ones, and, thus, are used for a variety of allocations. In an effort to avoid this problem, many of these instruments are built in remote areas (Carilli 2006).

Despite all this, multiple instruments are seeking to detect the 21-cm signal. Instruments such as the Giant Metrewave Telescope (GMRT) in India, the Low Frequency Array (LOFAR) in the Netherlands, the Murchinson Widefield Array (MWA) in western Australia, the Precision Array to Probe the Epoch of Reionization (PAPER) in South Africa are trying to detect 21-cm signals for $z \lesssim 12$. For these instruments, the signal-to-noise is too low for detailed images of the EoR; instead, they should be able to detect the signal statistically. The Hydrogen Epoch of Reionization Array (HERA), currently being built in South Africa, should provide still greater sensitivity. And, in the future, the Square Kilometer Array (SKA) will hopefully add to these efforts. We look forward to their observations in the coming years.

1.2.2 Cosmic Microwave Background

The CMB is our earliest view of the Universe; as such, the CMB photons stream through the EoR on the their way from the surface of last scattering to us. The reionization process imprints signals on these photons, allowing us to calculate constraints on both the timing of reionization, from the mean optical depth, and the duration of reionization, from the kinetic Sunyaev-Zel'dovich effect (kSZ). Both of these effects rely on scattering of the CMB photons off of free electrons. Thus, CMB observations will compliment well 21-cm observations; the former probes the distribution of ionized gas, the later the distribution of neutral gas.

1.2.2.1 Mean Optical Depth

By definition, ionization separates electrons from their atoms, resulting in an increase in the number of free electrons. This boost in the number density of free electrons causes an increase in Thomson scattering of the CMB photons, producing a detectable signal. This signal is parametrized by τ, the effective optical depth to reionization:

$$\tau_e = \int n_e(z)\,\sigma_T\,(cdt/dz)\,dz, \tag{1.4}$$

where n_e is the number density of free electrons, $\sigma_T = 6.65 \times 10^{-25}\,\mathrm{cm}^2$ is the Thomson cross section and c, of course, is the speed of light. The integral is over the line of sight distance the photons travel. Only periods in the history of the Universe when there are significant numbers of free electrons contribute to this integral. Thus, the period from recombination to reionization has little effect on τ_e. This calculation is dominated by the free electrons produced in the ionization of hydrogen and the single ionization of helium; the double ionization of helium contributes only a few percent of the total value of τ_e (Reichardt 2016)

Because of the integral nature of this calculation, τ_e is insensitive to the precise details of reionization. It is, however, sensitive to shifts in the number density of free electrons. If we assume reionization is an instantaneous process, there is only one such seismic shift. This is the simplest approximation, and following Loeb and Furlanetto (2013), equation 1.4 can be solved analytically for a flat universe:

$$\tau_e = 4.44 \times 10^{-3} \times \{[\Omega_\Lambda + \Omega_m\,(1+z_{reion})^3]^{1/2} - 1\}. \tag{1.5}$$

In this calculation, it has been assumed that helium singly-ionizes at the same time as hydrogen. z_{reion} is the redshift of instantaneous reionization which corresponds roughly to the midpoint of an extended reionization period. It is often reported alongside τ_e.

This Thomson scattering has two general effects on the CMB. First, it washes out small scale anisotropies in the CMB. After a moment's reflection on the scattering process, this is somewhat intuitive. Photons traveling along a line of sight to the observer

may be scattered out of that path; conversely, photons may be scattered into that line of sight from other directions. Together, these effects work to suppress the CMB anisotropy power. Unfortunately, this effect is highly degenerate with the amplitude of the primordial power spectrum of scalar perturbations as shown in Fig. 1.7 (Reichardt 2016).

Second, Thomson scattering can also produce polarization in the CMB. This process is slightly more complicated. Consider light scattering off of a free electron as shown in Fig. 1.8. While the incident light may have any polarization, only certain polarizations will be scattered. Specifically, the polarization of the scattered light must be perpendicular to its direction of travel. Thus, if we examine Fig. 1.8, for light incident from the left, only the vertically polarized photons will be scattered into the observer's line of sight, which points out of the page in the illustration. Similarly, for light incident from above, only the horizontally polarized light will be scattered into the line of sight. Since the electrons scatter light from all directions, the result is a mixture of horizontal and vertical polarizations. Now, if the incident light is not symmetric, specifically if the light is more intense coming from one direction than the other, the resulting scattered beam will be polarized. More precisely, if the incident field has a quadrupole anisotropy between the initial intensities along the horizontal and vertical axises, the resulting scattered light will have a net polarization (Loeb and Furlanetto 2013).

Since the CMB has such a quadrupole, Thomson scattering due to reionization leads to linear polarization. This signal peaks at large scales, leading to the reionization "bump" as shown in Fig. 1.7. This feature cannot be produced by any other parameter in standard cosmological models, making it a clear signal of τ_e. However, the "bump" only tells about optical depth; it is insensitive to changes in the duration of reionization. Current measurements from the Planck Collaboration et al. (2016) place τ_e at 0.058 ± 0.012, corresponding to $z_{reion} \simeq 8.8 \pm 0.9$.

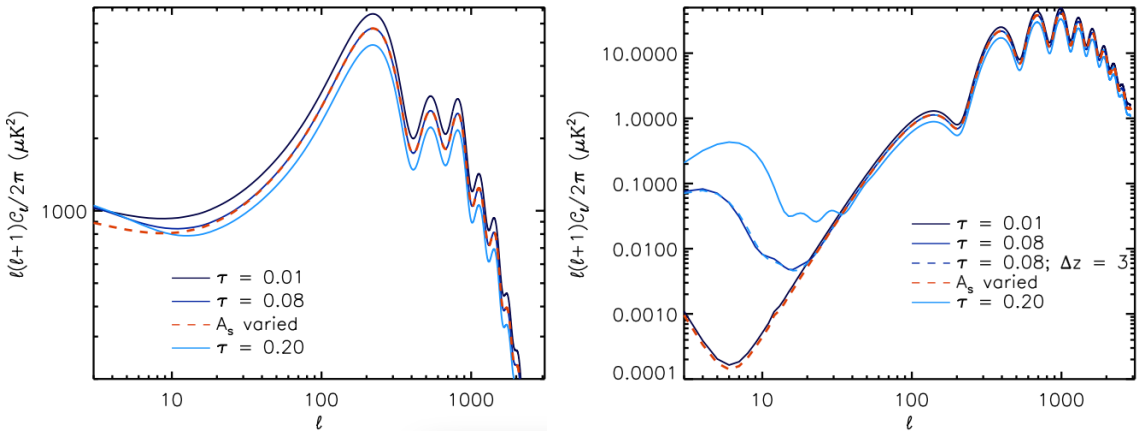

Figure 1.7: Figures from Reichardt (2016) showing the effect the Thomson optical depth has on observations of the CMB. *(Left)* The effects of varying optical depth, τ, and the amplitude of scalar perturbations, A_s, on the CMB temperature power spectrum. Increasing τ results in a decrease in the power spectrum. Specifically, the power is reduced by a factor of $e^{-2\tau}$ on scales $\ell \gtrsim 20$, smaller than the horizon at EoR. However, varying A_s can produce a signal that is degenerate with this decrease due to τ. Here, A_s, the dashed red line, has been tuned to match $\tau = 0.08$, the dark blue. *(Right)* The effects of varying optical depth on the CMB E-mode polarization power spectrum. Increasing τ produces a bump on large scales, $\ell \lesssim 20$, scales greater than the horizon size at the EoR. Unlike in the figure on the right, A_s, the red dashed line, cannot be tuned to mimic this bump at large scales. The dashed blue line and the solid dark blue line have the same optical depth, $\tau = 0.08$, but the duration of reionization is six times longer for the dashed versus the solid line. As is shown here, the duration of reionization has virtually no effect on E-mode power as long as the total optical depth is not changed.

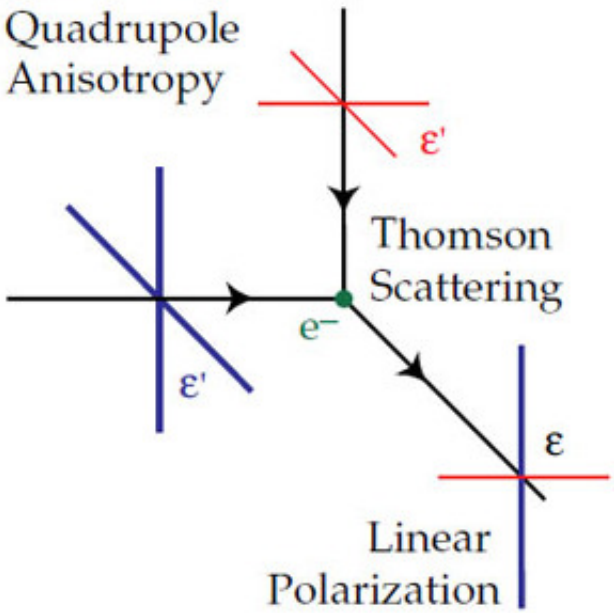

Figure 1.8: Figure from Hu and White (1997). This cartoon illustrates how CMB polarization is generated from Thomson scattering. The central electron scatters photons, here coming in from the left and above, into the line of sight to the observer, out of the page. Only polarizations that are perpendicular to both the line of sight and to a line connecting the incoming emission and the scattering electron are allowed. This means that for the light from the left, only the vertical polarization is allowed; similar, for the light from above, only the horizontal polarization is allowed. The resulting emission along the line of sight is a mix of those two states. However, if the incoming field is asymmetric, in particular, if it has quadrupole anisotropy between the initial intensities along the horizontal and vertical axises, the resulting field will be polarized.

1.2.2.2 Kinetic Sunyaev-Zel'dovich Effect

In our discussion so far, we have not yet considered the impact of the bulk velocity of the electrons. If the electrons have a bulk velocity relative to the CMB, photons scattering off of those electrons will experience a Doppler shift (Sunyaev and Zeldovich 1972; Phillips 1995; Birkinshaw 1999; Carlstrom et al. 2002). This shift is known as the kSZ effect: the observed CMB temperature is colder (hotter) if the scattering electrons move away (towards) the observer. Following Reichardt (2016), we can quantify the kSZ signal along the line of sight as:

$$\frac{\Delta T_{kSZ}}{T_{CMB}}(\hat{\mathbf{n}}) = \sigma_T \, \bar{n}_{e,0} \int d\eta \, a^{-2} \, e^{-\tau_e(\eta)} \, \bar{x}_i(\eta) \, (1+\delta_x) \, (1+\delta_b) \, (-\hat{\mathbf{n}} \cdot \mathbf{v}), \tag{1.6}$$

where σ_T is the Thomson scattering cross section; $\bar{n}_{e,0}$ is the current mean electron density; the integral is over conformal time, η; a is the scale factor at η; $\tau_e(\eta)$ is the optical depth from the observer along the line of sight to conformal time η; $\bar{x}_i(\eta)$ is the mean ionization fraction at η; δ_x and δ_b are perturbations in the ionization fraction and density field, respectively; $\hat{\mathbf{n}}$ is the line of sight unit vector; and $\mathbf{v}$ is the peculiar velocity of free electrons at η.

The kSZ effect, thus, has two physical components: the Ostriker-Vishniac effect (Ostriker and Vishniac 1986), based on density perturbations (δ_b) in the ionized Universe and the patchy reionization signal sourced by perturbations in the ionized faction (δ_x) due to the patchiness of reionization. The Ostriker-Vishniac effect is particularly significant at lower redshifts when the ionized IGM has the most significant fluctuations in velocity and density. Thus, this effect hardly depends on the properties of the EoR (Loeb and Furlanetto 2013). In contrast, the patchy reionization effect, as the name implies, does depend on the reionization process. The bubbles of ionized gas that make up the early stages of reionization have peculiar velocities relative to the background. It is these velocities that allow them to contribute to the kSZ. Qualitatively, their contribution to the kSZ depends both on the duration of reionization, and the distribution of bubble sizes. The longer the EoR was, and, thus, the longer the bubbles existed to contribute to the CMB fluctuations,

the greater the amplitude of the signal. Further, the patchy reionization signal peaks at the scale corresponding to the bubble sizes midway through reionization, at the point when reionization was maximally patchy (Loeb and Furlanetto 2013). The Ostriker-Vishniac effect and the patchy reionization signal are expected to have comparable power. Complicating the picture still further, it is difficult to differentiate between the two effects because they have the same spectral dependence and similar angular dependence (Reichardt 2016). Finally, there are still other contributions to the CMB anisotropies at the angular scales of interest, especially foreground fluctuations in the Cosmic Infrared Background (CIB), that must be separated from the kSZ signal. Thus, using the kSZ to study reionization is dependent on careful modeling and subtraction of the Ostriker-Vishniac effect and other foreground contributions (see, for example, Trac et al. (2011); Shaw et al. (2012)). Using the South Pole Telescope SZ survey data, George et al. (2015) are able to place an upper limit on the duration of reionization, concluding that $\Delta z < 5.4$.

1.2.3 Quasars and the Lyα Forest

Our most detailed probes of the IGM at high redshift, back into the EoR, currently come from quasars (Becker et al. 2015a). Quasars are the emission from accretion disks orbiting super massive black holes at the center of distant galaxies (Rees 1984). More relevant here, although quasars are rare, they can be found across the entire sky with similar spectra, such that absorption lines in their spectra are easy to identify. Most crucially, many quasars formed before the end of reionization; we have a growing population of quasars at $z > 6$ (Fan et al. 2006; Mortlock et al. 2011). Looking back at these quasars provides multiple lines of sight with which to study the IGM.

1.2.3.1 Lyα Forest

Absorption lines from the Lyα transition in the spectra of quasars are a signal of neutral gas along the line of sight to the quasar. As shown in Fig. 1.9, when the light emitted from the quasar encounters neutral hydrogen, that light is scattered. The quasar emission

arriving at $\lambda_\alpha = 1216$ Å in the frame of an intervening cloud of neutral hydrogen may be absorbed, exciting the hydrogen from the $1s$ to the $2p$ state. The atom eventually de-excites, reemitting the 1216 Å photon, but that process is isotropic – with a negligibly small chance of the photon being reemitted in the line of sight direction – and so the net result is an absorption line in the quasar's spectrum. Since the light from the quasar redshifts as it travels, multiple clouds of neutral hydrogen along the line of sight to the quasar produce multiple absorption lines. By the time the light reaches a new clump of neutral hydrogen, the absorption lines from other clouds of neutral hydrogen will have redshifted away from λ_α in the new cloud's frame. A new part of the quasar's spectrum will be at the right wavelength and ready to be scattered. All light at wavelength λ in the quasar's frame, where $\lambda < \lambda_\alpha$ is vulnerable to this, although, of course, the exact distribution of clouds of neutral hydrogen will determine whether a particular region of the spectrum is absorbed.

High redshift quasar spectra generally show a full "forest" of blended absorption lines, with each line constituting a "tree" in the Lyα forest. Fig. 1.10 shows the spectrum of a quasar at $z = 3.12$; the Lyα forest is clearly visible, tracing the distribution of neutral hydrogen along the line of sight to the quasar.

We can use the Lyα forest absorption lines to calculate the neutral fraction of hydrogen. In general, the optical depth τ is related to the fraction of light that passes freely through neutral hydrogen clouds, F, by:

$$F = e^{-\tau}. \tag{1.7}$$

$\tau_{Ly\alpha}$, the optical depth of a uniform medium of neutral fraction x_{HI}, can be calculated by:

$$\tau_{Ly\alpha} \approx 3.3 \times 10^5 \left(\frac{\Omega_m}{0.3}\right)^{-1/2} \frac{\Omega_b}{0.04} \left(\frac{1+z}{7}\right)^{3/2} x_{HI}, \tag{1.8}$$

where Ω_m, and Ω_b are the normalized matter and baryonic matter densities, respectively. Taking reasonable values for the matter densities, $\Omega_m = 0.27$, and $\Omega_b = 0.046$, we can calculate just how much of the hydrogen must be neutral in order to have a significant effect on the optical depth. For 90% of the light to be absorbed at $z \sim 6$, a neutral fraction

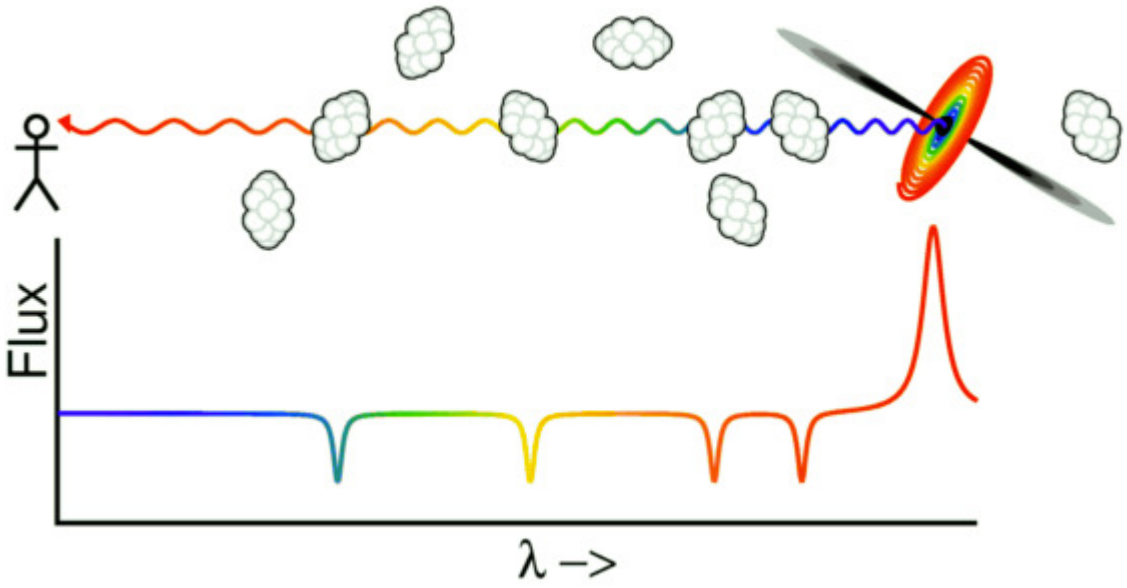

Figure 1.9: Image from Edward Wright (www.astro.ucla.edu). This cartoon shows how clouds of neutral hydrogen between the observer and the quasar produce the Lyα forest. Along the line of sight from the quasar to the observer are clouds of neutral hydrogen. As light from the quasar travels through those clouds, the light at 1216 Å in the cloud's frame is absorbed, resulting in an absorption line. By the time the light reaches the next cloud of neutral the light has redshifted and the previous absorption line is no longer at 1216 Å in the new cloud's frame. The light is again absorbed at 1216 Å, producing another absorption line. This process repeats with each cloud of neutral gas.

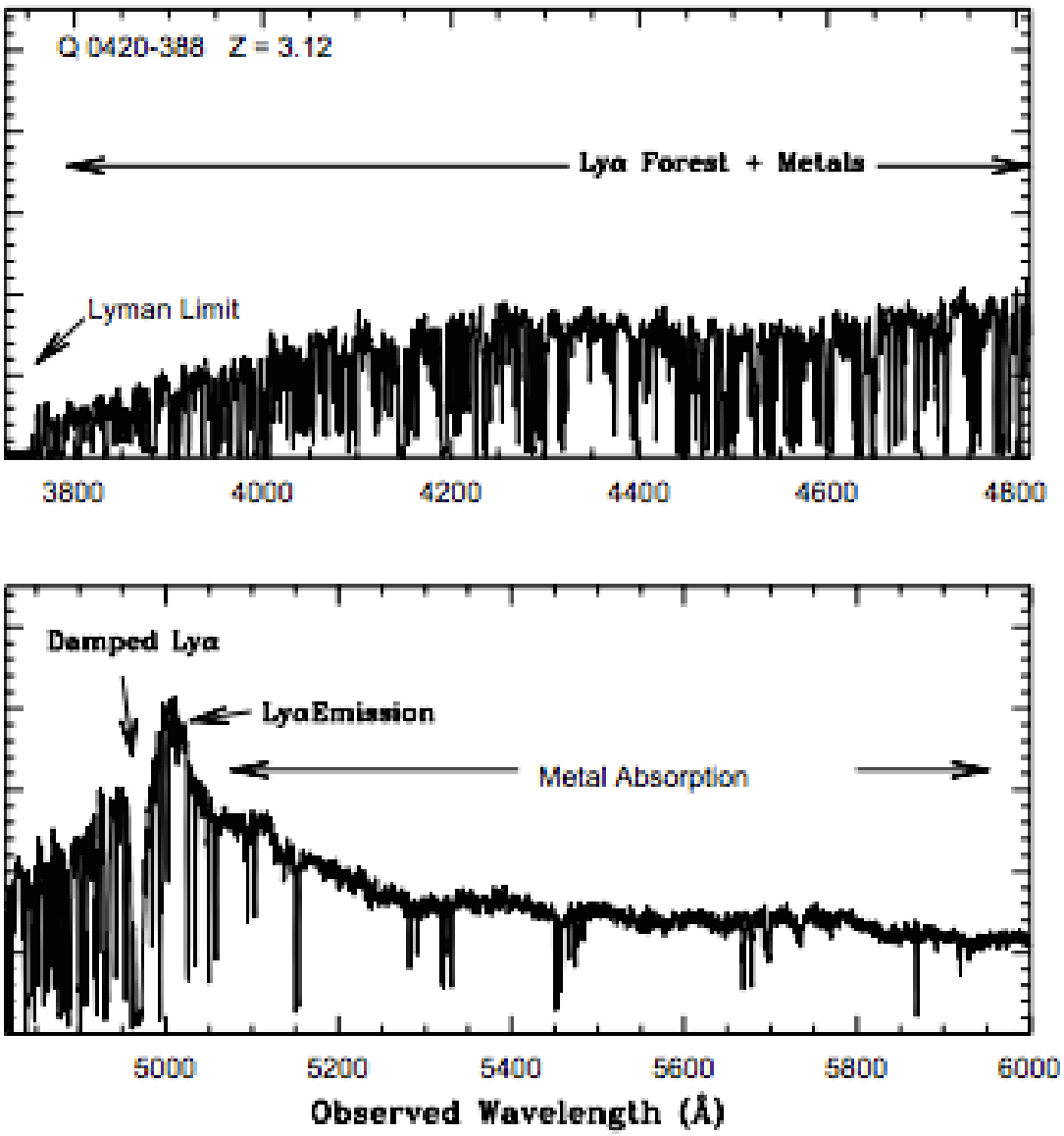

Figure 1.10: Spectra of $z = 3.12$ quasar (figure from Pérez-Fournon et al. (2010) as found in Zaroubi (2013)). Blueward of the Lyα emission feature (mostly the upper panel) is the Lyα forest. The numerous absorption lines, due to patches of neutral hydrogen along the line of sight to the quasar, create all of the "trees" in the Lyα forest.

of 6×10^{-6} would be sufficient, assuming the medium is uniform at the cosmic mean density. In fact, $\langle x_{HI} \rangle \gtrsim 10^{-4}$ results in effectively complete absorption, assuming a homogenous neutral fraction. The absence of strong absorption in low redshift quasars is one line of evidence that the IGM is fully ionized (Becker et al. 2015a).

From a large population of quasars at a range of redshifts, one can measure the evolution of the Lyα forest optical depth. A measurement of this quantity is shown in Fig. 1.11. The optical depth increases with increasing redshift, implying that the hydrogen neutral faction is increasing as one peers further back into the Universe. The rise in τ at $z \sim 6$ may be a signal of an extremely rapid end to reionization (Fan et al. 2006; Gnedin and Fan 2006). However, since low neutral fractions can result in complete absorption, the Lyα forest is only an effective probe for the outskirts of the EoR.

1.2.3.2 Gunn-Peterson Trough

As early as 1965, Gunn and Peterson (1965) showed that a sufficient quantity of neutral hydrogen distributed along the line of sight to a quasar can result in complete absorption of all photons with $\lambda < \lambda_\alpha$. While the quasar emission encountering distinct clumps of neutral hydrogen as it travels to the observer results in the discrete "trees" of the Lyα forest, a column of neutral gas will result in a completely absorbed trough. This trough is known as the Gunn-Peterson trough. The presence of a clear Gunn-Peterson trough in quasar spectra may be a signal of the end of reionization, though, of course, as shown in equation 1.8, the neutral fraction can be very low while still producing a Gunn-Peterson trough.

Fig. 1.12 shows the spectrum of quasars for a range of redshifts, starting at $z = 5.74$ and extending all the way out to $z = 6.42$. The low redshift quasars show the expected Lyα forest blueward of the quasar's own Lyα emission. However, as one looks to higher and higher redshift, the spectra of the quasars smooths out, eventually showing clear Gunn-Peterson troughs, suggesting that the end of reionization is approximately $z \sim 6$. Examination of individual spectra complicates this picture a bit. J1411+1217 at $z = 5.93$

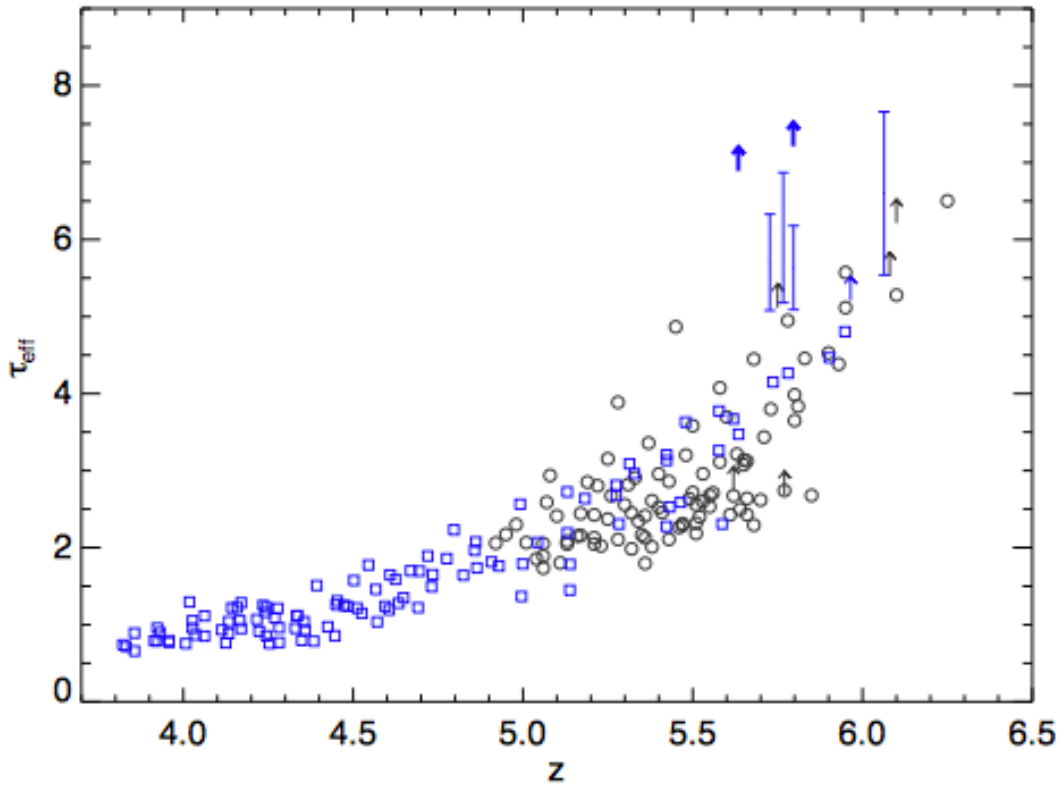

Figure 1.11: Evolution of the Lyα forest effective optical depth as a function of redshift (figure from Becker et al. (2015b) as found in Becker et al. (2015a)). The measurements in blue are from Fan et al. (2006) and in black, from Becker et al. (2015b). Increasing optical depth corresponds to increasing neutral fraction.

seems to have a Gunn-Peterson trough, while the quasars closest to it in redshift do not. Similarly, J1048+4637 at $z = 6.20$ has somewhat more features than one would expect in a true trough; its redshift neighbors, however, have complete absorption troughs. This variation should serve to remind us that reionization is a patchy process and that different lines of sight back to the same redshift will encounter different distributions of neutral and ionized hydrogen.

Together, the Gunn-Peterson trough and the Lyα forest suggest an end to reionization at $z \sim 6$. However, the idiosyncrasies of this measurement mean that this conclusion is somewhat open to interpretation. On the one hand, an earlier end to reionization could be consistent with this data. Since both signals saturate at a low neutral fraction, an almost completely ionized universe could, nevertheless, have enough neutral hydrogen at $z \sim 6$ to produce this data. On the other hand, significant troughs are observed at $z < 6$, perhaps indicating the presence of neutral hydrogen patches. This would argue for a later end to reionization.

1.2.3.3 Dark Gaps

Since the Gunn-Peterson trough saturates at low neutral fraction, one alternative is dark gap analysis, looking at the length of the troughs (Croft 1998; Barkana 2002; Songaila and Cowie 2002). For patchy reionization, even in a mostly neutral universe, there will be ionized regions. These comparatively small ionized regions will not produce Lyα absorptions lines, instead they will fully transmit the quasar emission. When looking at the quasar spectra, these regions will make their presence known in what appear to be spikes in the otherwise smooth Gunn-Peterson troughs. The troughs in between these spikes are the dark gaps. Analyzing their number and distribution intuitively seems like a good probe of the IGM. However, in practice it is difficult to convert the qualitative presence of the gaps into more quantative constraints. Indeed, statistics of the gap vary from observation to observation even of the same quasar (Mortlock 2016). As these statistics are not yet robust, it is difficult to use them to place actual constraints on the

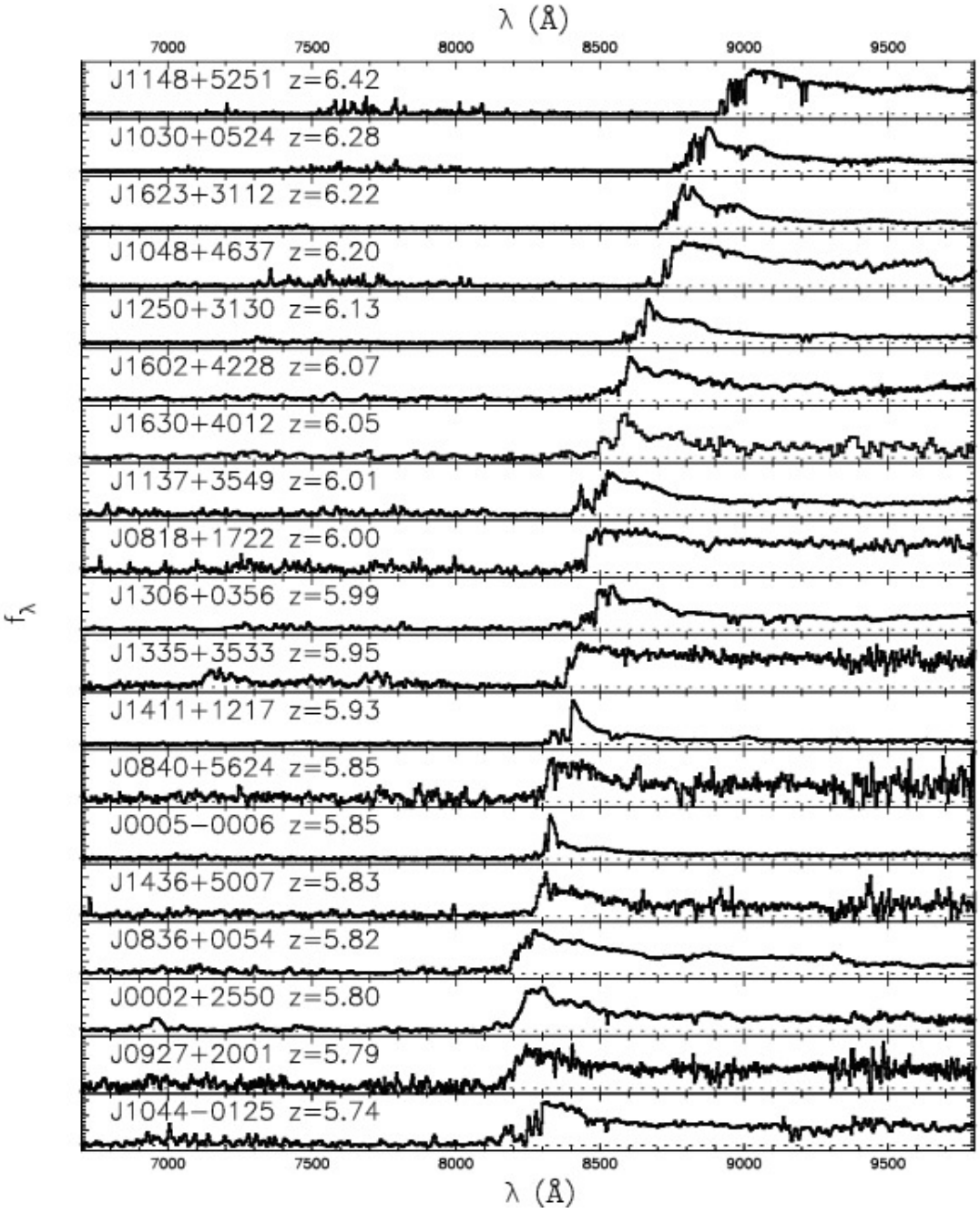

Figure 1.12: Quasar spectra from $z \sim 5.7$ to $z \sim 6.4$ (figure from Fan et al. (2006)). For the lower redshift quasars ($z \lesssim 6$), the Lyα forest is somewhat visible at the lower wavelengths. However, at higher redshifts, all emission in the equivalent regions in the spectra have been absorbed; this is the Gunn-Peterson trough.

ionized fraction.

1.2.4 Galaxies

In recent years, researchers have detected a growing number of galaxies out beyond $z \sim 6$. As we discussed in §1.1, this growing population of high redshift galaxy observations provides insight into which sources fueled reionization. Many of these galaxies, certainly the ones at $z \gtrsim 7$, formed during the EoR. Thus, the galaxies themselves are useful as observational probes for mapping the progress of reionization. As discussed below, galaxies, particularly LAEs, make possible several different measurements that may constrain reionization: in particular, LAE luminosity functions (in §1.2.4.3), the Lyα fraction (in §1.2.4.4), observed galaxy clustering (in §1.2.4.5), and intensity mapping (in §1.2.4.6).

The obvious way to select galaxies at a specific redshift is though spectroscopic surveys, using features in the galaxies' spectrum to select galaxies at the redshift of interest. While this has been useful at low redshift, for example the 2dF Galaxy Redshift Survey (Colless et al. 2001) and the the Sloan Digital Sky Survey (Gunn et al. 2006; Eisenstein et al. 2011; Dawson et al. 2013; Smee et al. 2013), such surveys require many hours of observations, and the time required only increases for more distant objects. Further, at high redshifts, the galaxies are too faint for wide-field, blind spectroscopic surveys (Finkelstein 2015). Instead, observers have turned to two main ways of detecting large populations of high redshift galaxies, both based on clever selections of filters with which to observe a given field: the Lyman-break selection technique, discussed in §1.2.4.1; and the narrowband Lyα selection technique, discussed in §1.2.4.2.

1.2.4.1 LBGs

We expect young, star-forming galaxies to have a strong ultraviolet continuum. Further, they, like all UV-bright astrophysical objects, should have a drop in their spectra at the Lyman limit, $\lambda_{rest} = 912$ Å in the rest frame. A photon of this wavelength can ionize a hydrogen atom in its ground state. In these young galaxies, we expect the drop to be

roughly an order of magnitude due to both the hydrogen edge in stellar photospheres, and absorption by interstellar neutral hydrogen, which is expected to be plenteous in young galaxies (Dunlop 2013). In addition, neutral hydrogen in the IGM will also contribute to the drop. The presence of this step, always at 912 Å in the galaxy's frame, gives us a way to quickly identify galaxies at a specific redshift. The step will redshift to $\lambda_{obs} = 912\ \text{Å}\,(1+z)$ in our frame and so, if we observe the field with broadband filters specifically chosen to fall on either side of the step, we should detect the galaxy in the red, but not the blue, band. Galaxies detected in this way are called Lyman Break Galaxies (LBGs) or dropout galaxies, often referred to as x-dropouts, where x is the name of the filter in which the galaxy is no longer visible or "dropped-out". Fig. 1.13 shows this technique in action for a $z \sim 7$ galaxy. This method was first used in the modern era by Guhathakurta et al. (1990) and Steidel and Hamilton (1992), who used U and B_j filters to look for galaxies at $z \sim 3$. The real power of this technique is in the use of filters to select galaxies at a specific redshift. Entire fields of view can be searched for galaxies at a target redshift at once, as opposed to spectroscopic observations which are limited to specific galaxies. Of course, as we will see below, this does come at some cost.

The Lyman limit, at an observed wavelength of $\lambda_{obs} = 912\ \text{Å}(1+z)$, sets the location of the observed step for low redshift galaxies. At higher redshifts, as the presence of neutral hydrogen surges, the ever-increasing Lyα forest shifts the step to 1216 Å in the rest frame. As we saw in §1.2.3.1, the neutral fraction does not have to be high for the Lyα forest to completely saturate. Thus, for all redshifts of interest to this thesis, we can consider the Lyman-break as occurring at 1216 Å. In fact, at $z \gtrsim 5$, the neutral hydrogen is expected to be dense enough for the break to be at least $\simeq 1.8$ mag (Madau 1995), making the Lyman-break more than twice as strong as any other intrinsic breaks in galaxy spectra (Dunlop 2013).

For most surveys, the two filters straddling the break are not considered enough. Instead several more red filters are considered necessary to truly identify the galaxy as an LBG. This can be seen in Fig 1.13 where in addition to the dropout filter, and the filter

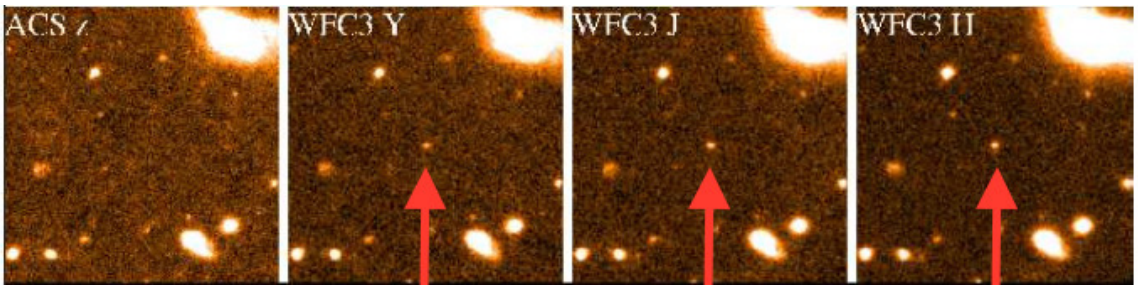

Figure 1.13: A $z \simeq 7$ galaxy found via the Lyman-break selection technique in the Hubble Ultra Deep Field (figure from Dunlop (2013)). Image taken with WTC3/IR on the HST in four filters, from left to right: z_{850}, Y, J_{110}, H_{160}. The galaxy is not visible in the first image, but in the longer wavelength, redder images, the galaxy can be seen in the center of the image. The galaxy is z-dropout galaxy, and these pictures together illustrate how the dropout selection technique works.

immediately redward of that, two more filters, in which the galaxy can be seen, are included. Indeed, the general requirement is for the galaxy to dropout in the band blueward of the break and for the galaxy to be visible in at least two bands redward of the break. This should confirm both the existence of the break and the galaxy's overall blue color longward of the break, as expected for young, UV-bright galaxies (Dunlop 2013).

So far, we have depicted the Lyman-break technique as able to select galaxies at specific redshifts. This is true up to a point. Finkelstein (2015) claims that this technique gives redshifts with a precision of $\Delta z \sim \pm 0.5$ for galaxies at $z > 6$. Throughout this thesis we have relied on Ouchi et al. (2009) who used Monte-Carlo simulations to calculate the redshift distribution of their z-dropout ($z \sim 6.9$) galaxies. Their distribution, shown in Fig. 1.14, peaks at $z \sim 6.9$ but has tails extending out half a redshift in each direction.

It is possible to increase the redshift accuracy of broad band measurements, though it still cannot match the accuracy of spectroscopic observations. This technique, known as photometric redshift fitting uses data from all the filters that the field has been imaged in. A prototypical galactic spectral energy distribution template is fit to the data from all the filters, and that fitting is used to determine a more accurate redshift. Of course, for this technique to be useful, images from more than 2 or 3 filters are necessary. In addition, the redshift is dependent on the templates used to fit the data (Finkelstein 2015).

While the Lyman-break technique is a widely used and highly successful method of detecting high redshift galaxies, its samples remain vulnerable to contamination by lower redshift objects. We grapple with some of these implications in §3.5.1. Spectroscopic followup has shown that Lyman Break surveys are vulnerable to three types of interlopers: 1) low redshift, dusty, red galaxies, 2) cool galactic stars and 3) post-starburst galaxies with a strong Balmer break (Dunlop 2013). Ouchi et al. (2009) argue that for z' dropouts, appropriate cuts – in their case, the drop-out selection and $z' - y > 1.5$ – can exclude all of the first category; thus, cool galactic stars will be the dominant source of interlopers. These interlopers may comprise up to 40% of the sample. At the moment, this contamination is one of the expected costs of Lyman-break surveys.

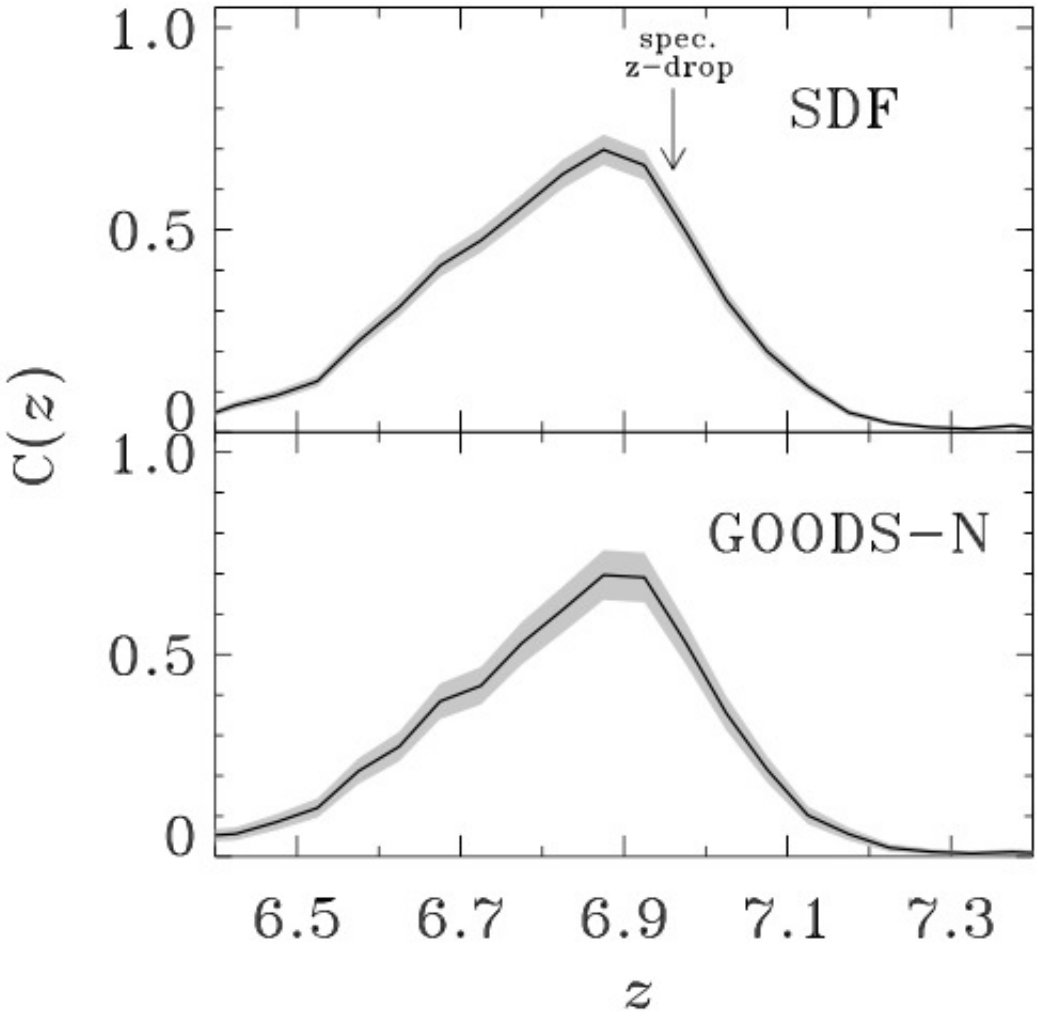

Figure 1.14: A plot of the redshift distribution of z-dropout galaxies detected in the Subaru Deep Field *(top)* and GOODS-N *(bottom)* based on observations performed by Ouchi et al. (2009), from whom the figure is taken. The distribution is derived from Monte Carlo simulations of their observations. The redshift of a galaxy whose redshift was confirmed spectroscopically is indicated by the arrow. While the redshifts of these z-dropout galaxies are ~ 7, they are distributed over a reasonable depth in redshift, making the precise redshift of any dropout galaxy difficult to quantify.

1.2.4.2 LAEs

So far, we have only talked about Lyα as an absorption line. One can also observe Lyα in emission, and use this to select high redshift galaxies. In galactic spectra, Lyα emission is mainly powered by two mechanisms. In the first, ionizing radiation from hot young O and B stars ionizes neutral hydrogen in the local interstellar medium. That gas will recombine, radiatively cascading to the ground state, and a significant fraction of the resulting radiation will be Lyα emission (see, for example, Johnson et al. (2009); Raiter et al. (2010); Pawlik et al. (2011)). In the second case, neutral hydrogen within the galaxy is collisionally excited. As the gas returns to the ground state, it may emit Lyα photons (Dijkstra 2014). In any case, a significant population of galaxies have strong emission lines at 1216 Å in their frame. Of course, this line is redshifted by the expansion of the Universe as it travels to us, with the wavelength of the line telling us the redshift of the emitting galaxy. This redshift forms the basis of the narrow band technique. The technique is as follows: observe a field in a broad continuum band and then again in a narrow band centered on 1216 Å$(1+z)$, for the redshift of interest. LAEs should be brighter in the narrow band than in the continuum band. Thus, by selecting the objects with those properties, one can develop a sample at the redshift of interest. Galaxies selected in such a way are called Lyα Emitters or LAEs.

LAEs are often characterized by their rest frame equivalent width, REW:

$$\text{REW} \equiv \int d\lambda \, (F(\lambda) - F_{cont})/F_{cont}, \tag{1.9}$$

integrated across the line, where the flux in the line is compared to the continuum flux F_{cont} redward of the line. The REW is often used to characterize the strength of the line; LAE surveys typically require REW $>$ 20 or 25 Å. For a typical star forming galaxy, a maximum physically allowed REW is 240 Å (Schaerer 2003; Laursen et al. 2013), although reducing the metallicity of the gas can allow slightly higher REWs (Laursen et al. 2013). Intuitively, it can be helpful to remember that REW $\sim$ FWHM $\times$ (relative peak flux density). Which is to say, for our 240 Å maximum REW, if we assume a

2 Å FWHM, which is reasonable, the flux is the line will be over 100 times that in the continuum (Dijkstra 2014).

There are several challenges with narrow band surveys. The first is specific to ground based surveys. Ground based narrow band surveys, particularly for high redshift objects, are vulnerable to the night sky emission lines; these sky lines become increasingly problematic at longer wavelengths. Fig. 1.15 shows these emission lines. Fortunately, gaps in the night sky emission lines, as indicated in the figure, allow us to search for LAEs at specific redshifts. Thus, the redshift distribution of LAEs is grouped in discrete narrow bands as opposed to the broader more continuous distribution of LBGs. And these samples are relatively narrower along the line of sight than the LBG samples. Because we are trying to detect galaxies that are bright only in a narrow emission band, the filters chosen are narrow, resulting in LAE samples with a narrow distribution in redshift, thus probing smaller cosmological volumes for the same field of view than the more broadly distributed drop-out samples. In yet another challenge, like LBG surveys, LAE surveys are also vulnerable to interlopers. In this case, lower redshift galaxies with emission lines redward of the Lyα line can be mistaken for LAEs. In particular, galaxies with strong OII, OIII or Hα lines can contaminate an LAE sample. We deal with some of these complications in §3.5.1.

Line Shape On a purely qualitative level, it is tempting to think about galactic Lyα emission as merely a featureless spike in the galactic spectra. However, in reality the shape of the line can vary based on transmission in the galaxy and interaction with the circumgalactic medium. Here we briefly explore these effects.

To start, we need an understanding of the Lyα absorption cross section. Following Dijkstra (2014), the frequency dependence of the cross-section, σ_α, can be modeled as a Voigt function:

$$\sigma_\alpha(x) = \sigma_0 \times \frac{a_v}{\pi} \int_{-\infty}^{+\infty} dy \frac{\exp(-y^2)}{(x-y)^2 + a_v^2} \equiv \sigma_0 \times \phi(x), \tag{1.10}$$

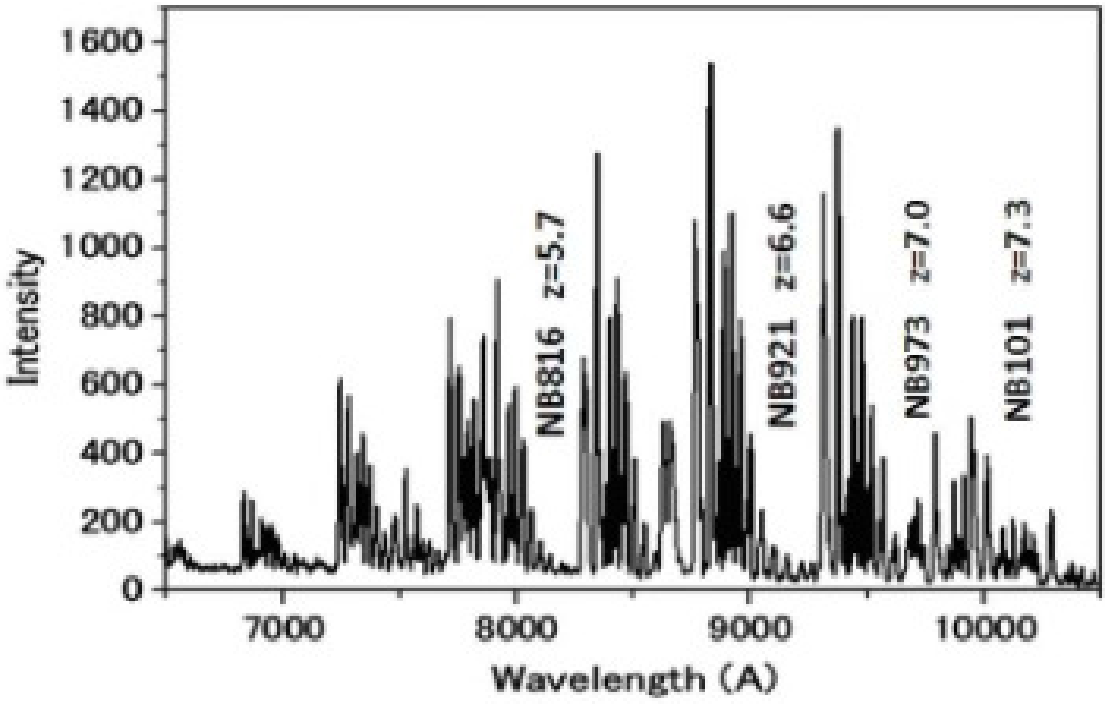

Figure 1.15: Figure, with some modifications, from Dunlop (2013) of OH night sky emission bands. Gaps in the bands, where we can observe the night sky with ground based instruments, are labeled with both the narrow band filters that are used by Suburu to observe in that gap and the redshift of the LAEs that would be selected by that filter. As can be seen here, ground based narrow band surveys only allow for detection of LAEs at specific redshifts.

where, σ_0, the cross-section at line center, is given by:

$$\sigma_0 = \frac{f_a}{\sqrt{\pi}\Delta\nu_D}\frac{\pi e^2}{m_e c} = 5.88 \times 10^{-14}(T/10^4\text{ K})^{-1/2}\text{ cm}^2. \tag{1.11}$$

Here, the frequency ν is expressed in terms of $x \equiv (\nu - \nu_\alpha)/\Delta\nu_D$, a dimensionless variable. $\nu_\alpha = 2.46 \times 10^{15}$ Hz, the frequency of Lyα emission and the Doppler broadening $\Delta\nu_D \equiv \nu_\alpha\sqrt{2k_BT/m_pc^2} \equiv \nu_\alpha v_{th}/c$. Here, k_B is Boltzmann's constant; T is the temperature of the gas that scatters the photons; m_p is the proton mass; m_e is the electron mass; e is the electron charge; c is the speed of light, v_{th} is the thermal speed; $f_\alpha = 0.416$ and is the Lyα oscillator strength; and $a_v = 4.7 \times 10^{-4}(T/10^4\text{K})^{-1/2}$ is the Voigt parameter. $\phi(x)$ is the Voigt function which can be approximated as:

$$\phi(x) \approx \begin{cases} e^{-x^2} & \text{'core', i.e. } |x| < x_{crit}; \\ \frac{a_v}{\sqrt{\pi}x^2} & \text{'wing', i.e. } |x| > x_{crit}. \end{cases} \tag{1.12}$$

If we assume a gas temperature of 10^4 K, $x_{crit} \sim 3.2$. All of this pays off when we consider the shape of the cross section. At the core, around ν_α, it is large and the photons are likely to be scattered; past x_{crit} the cross section falls off fairly quickly in the wings. Lyα emission can be scattered by material in the interstellar medium (ISM) and circumgalactic medium (CGM); these interaction influence the shape of the emission line as it leaves the galaxy. Having left the galaxy, the emission line then interacts with the IGM, where it may be scattered and attenuated by neutral hydrogen.

Scattering from the ISM and CGM First, let us consider the Lyα emission from a point source at the center of a uniform, static distribution of neutral hydrogen. This toy model approximates the effects of Lyα photons that are scattered by neutral hydrogen within their own galaxy. The photons may have their direction of travel changed, their frequency changed or both. Photons with frequencies that fall within the core of the scattering cross-section will be scattered more frequently than those in the wings, and, thus, will have a harder time escaping the galaxy. It is only once their frequencies have been shifted enough, via scattering, that the photons will escape. This results in a double

peaked line profile for Lyα emission, with peaks in the wings of the cross-section and almost no emission precisely at ν_α. If we increase the optical thickness of the interstellar medium, the photons will have to be scattered further into the wings of the cross-section before they can escape, increasing the separation between the two peaks. This effect can be seen in Fig. 1.16.

Now, let us consider Lyα emission from a point source inside a uniform distribution of expanding neutral hydrogen. This will allow us to gain some intuition about the expected emissions lines from young star-forming galaxies. These galaxies are expected to host Lyα emission and are believed to have strong galactic winds, resulting in outflows of neutral hydrogen. In that case, in the reference frame of the moving gas, the photons in the blue wing of the stationary cross-section are redshifted and appear near the core of the moving cross-section. These photons are then scattered and cannot escape unless their frequency shifts. The photons in the red wing are even more redshifted and are free to escape. In this case, the Lyα emission line consists only of the red peak and is no longer symmetric. By the same logic, galaxies with strong inflows, will produce Lyα emission with only a blue peak. The results of the these outflows on the emission lines are show in Fig. 1.17.

In addition to changing the shape of the emission, strong galactic winds can also enhance the Lyα signal. This can be understood by picturing the galactic winds as an expanding shell of material. The Lyα emission traveling away from the observer can backscatter off of the shell and into the line of sight. This Doppler boost shifts the Lyα photons to frequencies redward of ν_α. For a galaxy embedded within a larger region of neutral hydrogen, this Doppler boost can move the photons out of the Lyα absorption line and allow them to travel freely to the observer. In this case, for two galaxies that vary only in the strength of their outflow, the galaxy with the stronger galactic wind will have the brighter Lyα emission (Dijkstra 2011).

We can complicate this picture still further, and make it more realistic, by including the effects of dust. Let us add a uniform distribution of dust to our uniform distribution

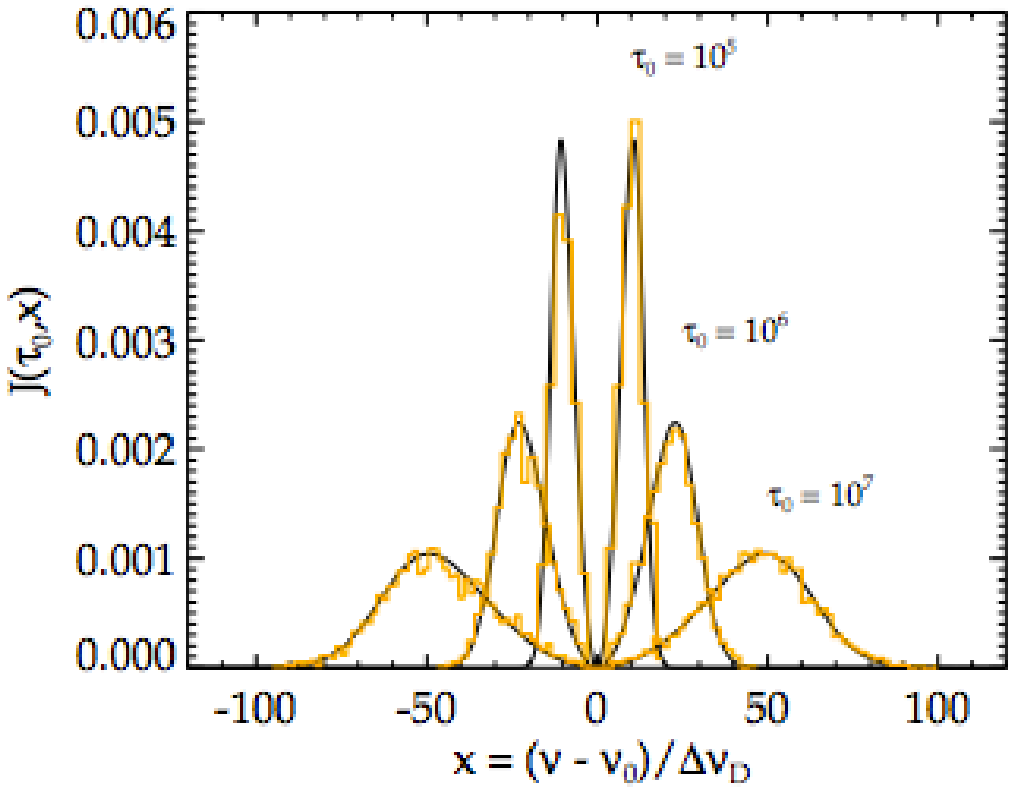

Figure 1.16: Lyα emission from a static sphere at $T = 10$K, for varying optical depths. Lyα emission only escapes the sphere when it has scattered from the core of the cross section out into the wings, producing the double peaked emission line. Increasing the optical depth broadens the core of the cross section, resulting in more widely separated emission peaks. The solid lines are the analytical solutions from Dijkstra et al. (2006) and the yellow histograms are the results from the Monte Carlo simulations of Orsi et al. (2012). Figure from Orsi et al. (2012)

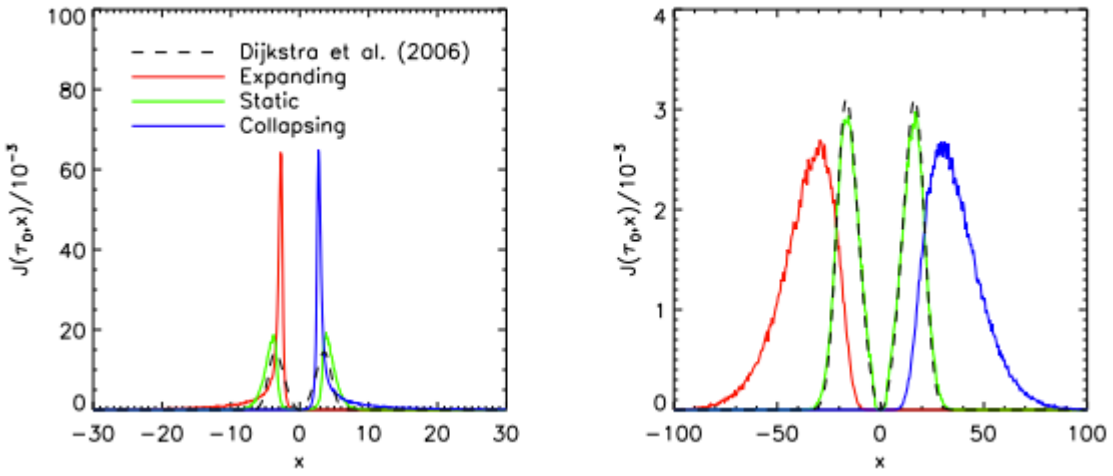

Figure 1.17: Figure, from Laursen et al. (2009), shows the effects of strong inflows or outflows of neutral hydrogen on Lyα emission. These spectra are from a simulation $T = 10^4$ K sphere of gas, that is either static (green), expanding (red) or collapsing (blue). The velocity at the edge of the sphere is $v_{max} = \pm 200$ km/s. The two panels show the results for two different column densities of neutral hydrogen: $N_{HI} = 2 \times 10^{18}$ cm^{-2} (left) and $N_{HI} = 2 \times 10^{20}$ cm^{-2} (right). Strong outflows, or inflows, result in an asymmetric line profile.

of neutral hydrogen. Neutral hydrogen scatters Lyα emission; dust partly absorbs and partly scatters it. If the dust is evenly distributed, its effect will be a net reduction in Lyα emission. As we discussed above, the Lyα photons scatter multiple times before they can make their way into the wings and escape. Each interaction increases the path length, making it more likely the photon will be absorbed, resulting in fainter emission.

Finally, let us consider a multiphase medium in which both the dust and neutral hydrogen are confined to thick, discrete clouds within a larger ionized and dust free medium. In this case, the Lyα emission will be enhanced (illustrated in Fig. 1.18). This is due to the difference in how line and continuum photons behave. The line photons will scatter off the surface of the clouds; the continuum photons will travel through the clouds. Thus, the continuum photons are more likely to be absorbed than the line photons, with the result that the continuum is depressed relative to the line, making the Lyα emission appear stronger (Loeb and Furlanetto 2013)

While we have obviously simplified the complicated realities of radiative transfer, these toy models have served to develop our understanding of the factors that go into shaping galactic Lyα emission.

Scattering from the IGM Once the Lyα emission has escaped from its galaxy, it is free to travel, interacting only with the IGM. Broadly speaking, we can divide the interaction with the IGM into two components: the resonant component and the red damping wing component. These two components correspond to different frequency regions of the Lyα emission spectra. If the Lyα photon leaves the galaxy at a frequency higher than ν_α, it will eventually redshift into resonance with the line. At that point, any neutral hydrogen will absorb it. During reionization, we can assume that the blue side of the line is completely absorbed.

Things become more complicated when we consider a photon with frequency lower than ν_α. These photons will not redshift into resonance; they only redshift farther away. Any absorption they experience will be due to the damping wings. The amount of ab-

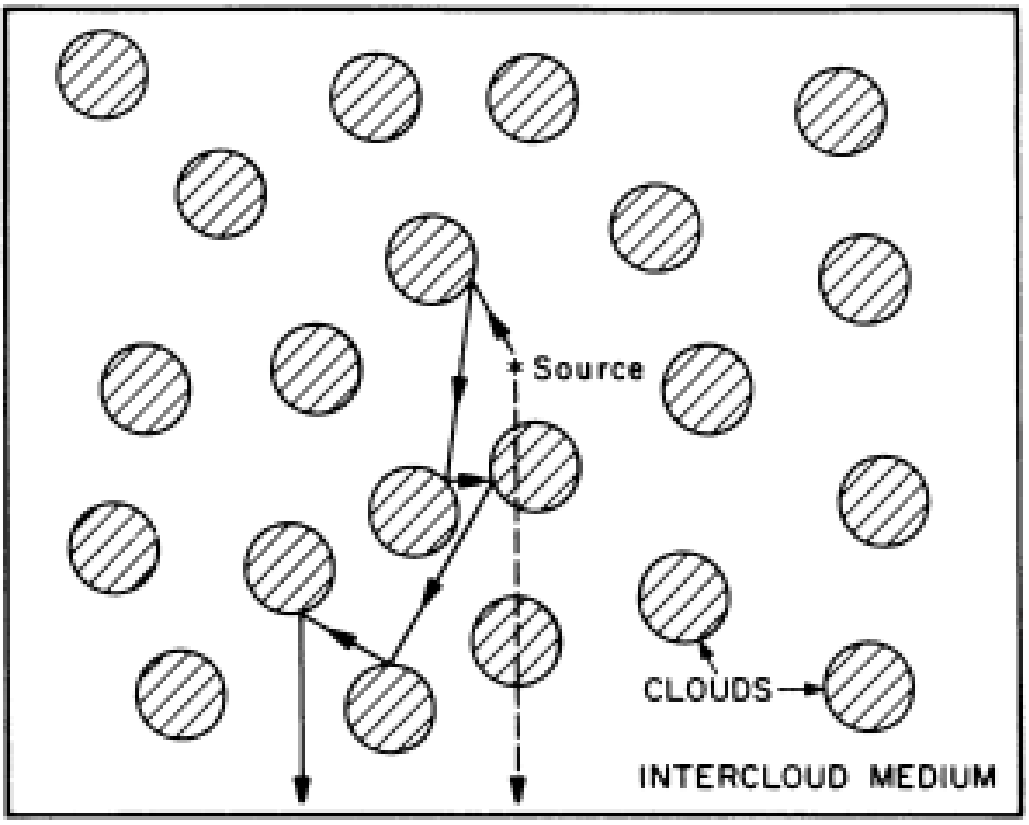

Figure 1.18: Figure from Neufeld (1991) illustrating how a multiphase medium can enhance Lyα emission relative to the the continuum emission. If a cloud of dust blocks the line of sight to the source, the source will be obscured and not visible in the continuum. However, the Lyα emission from that source will scatter multiple times as it interacts with the clouds of neutral hydrogen. Eventually, these interactions may scatter it back into the line of sight, even if it takes a long and convoluted path to do so. Thus, we may see the Lyα emission more strongly than the continuum emission from sources in a multiphase medium.

sorption they undergo, $\exp[-\tau_{DW}]$, is based on the damping wing optical depth:

$$\tau_{DW} = 6.43 \times 10^{-9} \left[\frac{\pi e^2 f_\alpha n_H(z_s)}{m_e c H(z_s)} \right] \left[I\left(\frac{1+z_{begin}}{1+z_s} \right) - I\left(\frac{1+z_{end}}{1+z_s} \right) \right], \tag{1.13}$$

where

$$I(x) \equiv \frac{x^{9/2}}{1-x} + \frac{9}{7}x^{7/2} + \frac{9}{5}x^{5/2} + 3x^{3/2} + 9x^{1/2} - \frac{9}{2}\ln\left[\frac{1+x^{1/2}}{1-x^{1/2}} \right] \tag{1.14}$$

and z_s is the redshift of the Lyα emitting source and $n_H(z_s)$ is the mean hydrogen number density of the IGM at that redshift. Here, we have summed up the contribution to the optical depth from each patch of neutral hydrogen extending from z_{begin} to z_{end} along the line of sight. In order to have appreciable optical depth in the damping wing, one needs a significant neutral column of hydrogen. Thus, the IGM's contributions to this term only become significant when sufficiently neutral regions exist (Mesinger and Furlanetto 2008).

Thus, the strength of any Lyα emission that we observe is dependent upon processes internal to the galaxy that determine the initial strength and shape of the line. That line is then modulated as it travels through the IGM. As we will discuss below, how the neutral IGM interacts with LAEs can be a strong signal of the progress of reionization.

1.2.4.3 LAE Luminosity Functions

One potential signature of reionization is a decrease in the number of LAEs, due to their Lyα emission being absorbed by neutral hydrogen in the IGM. The changing abundance of LAEs is commonly quantified by tabulating their luminosity functions versus redshift. These luminosity functions are frequently fit with a Schechter function (Schechter 1976):

$$\frac{dn}{dL} = \phi(L) = \phi^* \left(\frac{L}{L^*} \right)^\alpha e^{-(L/L^*)}, \tag{1.15}$$

where ϕ^* is the normalization density, L^* is the characteristic luminosity, and α is the power-law slope at low luminosity. A negative α, as is typically seen, implies an increasing number of galaxies at low luminosities (Dunlop 2013). While Schechter fits

are exceedingly useful, there can be degeneracies between ϕ^*, L^* and α, and so care is required when comparing these fits between research groups (Robertson 2010).

Interestingly, the Lyα luminosity function does not appear to evolve between $z \sim 3$ and $z \sim 5.7$ to within statistical errors (for example, Hu et al. (1998); Ouchi et al. (2008)). However, at $z > 6$, the Lyα luminosity function does evolve, as seen in Fig. 1.19 (Kashikawa et al. 2006a; Ouchi et al. 2010; Ota et al. 2010; Kashikawa et al. 2011). This decrease in the luminosity function may be due to an increasing neutral hydrogen fraction which absorbs the Lyα emission. Significantly, the UV luminosity function of LAEs shows no evolution between $z \sim 5.7$ and $z \sim 6.5$; the decrease is only seen in the Lyα luminosity function of LAEs. This strengthens the inference that the decrease is due to a reduction in Lyα, possibly due to an increasing hydrogen neutral fraction, as opposed to a reduction in the number density of LAEs (Kashikawa et al. 2006a; Kashikawa et al. 2011). The Lyα luminosity function decreases still further between $z \sim 6.6$ and $z \sim 7.3$, as is seen in Fig. 1.19. Note, though, that the $z \sim 7.3$ luminosity function has fairly large uncertainties, partly due to the small number of galaxies they were able to detect, complicating our interpretation of this decrease. This evolution seems to agree with the evidence from quasars: reionization ended around $z \sim 6$ and as we observe galaxies at higher redshifts we are looking back in the EoR.

1.2.4.4 Lyα Fraction

One of the challenges with interpreting the decrease in the Lyα luminosity function of LAEs is isolating the effects that caused the decrease. It is tempting to attribute the decrease to changes in the IGM, particularly given our interest in it. However, the decline may instead be due to intrinsic evolution in the galaxies themselves, whether an evolution in their overall number density or a shift in the escape fraction of Lyα photons, with any number of causes, or due to changes in the extrinsic properties of the galaxies, such as the ionized fraction of the IGM. The Lyα fraction measurement, proposed by Stark et al. (2010), works to sidestep some of these concerns about intrinsic evolution. In this

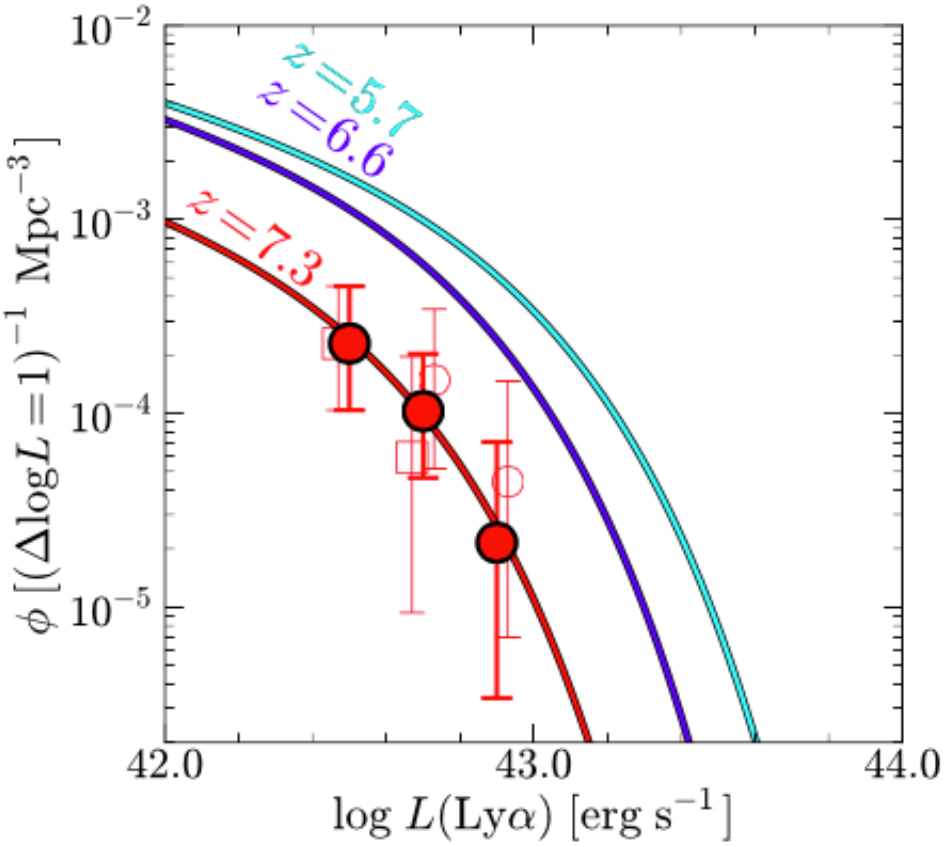

Figure 1.19: Evolution of the Lyα luminosity function of LAEs. Figure from Konno et al. (2014). The open red circles and squares are their luminosity function data from fields SXDS and COSMOS, respectively, surveyed for $z \sim 7.3$ LAEs. They combine those data sets in the solid red circles. The red curve is their best-fit Schechter function to the combined data. The blue curve is the best-fit Schechter function for $z \sim 6.6$ LAEs from Ouchi et al. (2008); the teal curve, the best-fit Schechter function for $z \sim 5.7$ LAEs from Ouchi et al. (2010). There is a decline in the luminosity functions, and, thus, in the number of LAEs detected from $z \sim 5.7$ to $z \sim 7.3$ and the rate of decline seems to be increasing with higher redshift. This may be evidence of an increasingly neutral Universe.

method, the Lyman-break technique is used to collect a large population of galaxies at a target redshift. Then, those galaxies are observed to see if they are LAEs; here previous studies generally require a Lyα REW > 25 Å for an LBG to be considered as an LAE. The Lyα fraction, $f_{Ly\alpha}$, is the fraction of LBGs that are also LAEs.

Since this method was proposed by Stark et al. (2010), a number of groups have set out to measure the Lyα fraction at a range of redshifts (Fontana et al. 2010; Vanzella et al. 2011; Pentericci et al. 2011; Schenker et al. 2012; Ono et al. 2012; Caruana et al. 2012; Furusawa et al. 2016). The results of Fontana et al. (2010); Vanzella et al. (2011); Pentericci et al. (2011); Schenker et al. (2012) and Ono et al. (2012) as combined by Ono et al. (2012) are shown in Fig. 1.20. Measurements of $f_{Ly\alpha}$ are historically divided into bins based on the strength of the Lyα emission and the UV continuum brightness. From $z \sim 4$ to $z \sim 6$, $f_{Ly\alpha}$ steadily increases. While all bins show this general trend, it is clearest for the faint galaxies with weak emission (bottom left panel). At these redshifts, quasar spectra suggest that the Universe is completely ionized. Stark et al. (2010, 2011) argue that decreasing dust levels in the galaxies, which likely happens with increasing redshift, leads to an increasing escape fraction for Lyα photons, and, thus, the observed increase in $f_{Ly\alpha}$. If that trend continues, we would expect a still higher value for $f_{Ly\alpha}$ at $z \sim 7$, as indicated by the grey band. However, when $f_{Ly\alpha}$ at $z \sim 7$ is measured, it is significantly lower than expected. And this decreasing trend continues out to $z \sim 8$ (Faisst et al. 2014; Schenker et al. 2014) One possible explanation for this decrease is an increasingly neutral IGM absorbing the Lyα emission. Based on early measurements of $f_{Ly\alpha}$, Pentericci et al. (2011); Schenker et al. (2012) argue for a neutral fraction of $x_{HI} \gtrsim 0.6$ at $z \sim 7$. Such a high neutral fraction would require a surprisingly rapid end to reionization, particularly in light of the other constraints on reionization we have discussed above.

The general consensus is that this downturn is in fact a signal that we are observing into the EoR. However, there remains some debate over how rapid an evolution of the IGM is required to accommodate such a measurement. Bolton and Haehnelt (2013) have argued that the decrease may be due to the increasing presence of dense self-shielding

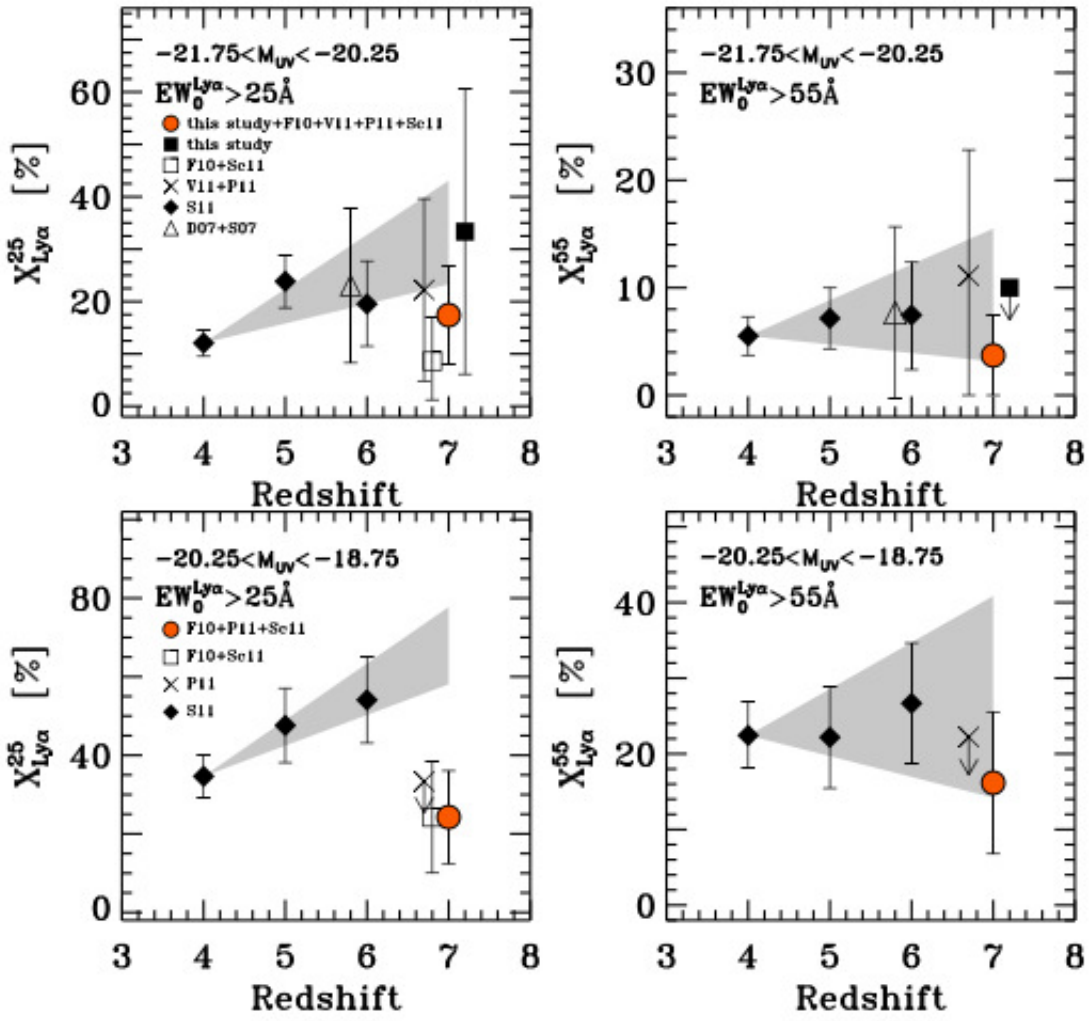

Figure 1.20: The Lyα fraction, the fraction of LBGs that are also LAEs, (here $\chi_{Ly\alpha}$, though we refer to it as $f_{Ly\alpha}$) from $z \sim 4$ to $z \sim 7$. The data is from observations of multiple fields with various instruments. This quantity is plotted for four bins of galaxies: the top row is for brighter galaxies with $-21.75 < M_{UV} < -20.25$; the bottom for fainter galaxies with $-20.25 < M_{UV} < -18.75$; the left column for galaxies with weaker Lyα emission (EW$>$ 25 Å); and the right column for galaxies with stronger Lyα emission (EW$>$ 55 Å). From $z \sim 4$ to $z \sim 6$, $f_{Ly\alpha}$ is clearly increasing; however, at $z \sim 7$ there is a sharp downturn. This trend is most clear in the bottom left panel, for the faint galaxies with weaker Lyα emission. This downturn may be a signal of an increasingly neutral Universe. Figure from Ono et al. (2012).

Lyman limit systems, increasing the optical depth of Lyα photons. This effect would be particularly pronounced in overdense regions where there are both more galaxies and more Lyman limit systems. When including such systems in their models, they argue that the decrease in $f_{Ly\alpha}$ only requires a neutral fraction of $10-20\%$ (see also Choudhury et al. (2015); Mesinger et al. (2015)). We also enter into this discussion, arguing, as is laid out more fully in §2, that the effects of sample variance due to patchy reionization on the small fields of view may be quite large. We conclude that the drop in $f_{Ly\alpha}$ is due to an increasing neutral fraction, but only require a neutral fraction of 5% (at the 95% confidence level) to explain the decrease. These lower neutral fractions are more easily harmonized with existing models and measurements of reionization.

1.2.4.5 Clustering

The patchy nature of reionization imprints an additional interesting signature on the LAEs. We have described reionization as starting with ionized bubbles centered on galaxies. As the ionization process continues, the bubbles grow, merging with other nearby bubbles to form still bigger bubbles. Eventually, all the bubbles have merged and the Universe is fully ionized. While the bubbles are still growing, LAEs may be preferentially observed if they exist in large ionized bubbles. In that case, the Lyα emission has time to redshift away from 1216 Å before it reaches the edge of the bubble; if it has redshifted far enough, the emission line can freely travel through the neutral Universe and we will be able to detect the LAE. For the bubbles to be large enough for this to be the case, they would have to be fueled by multiple galaxies. Thus, during reionization, an isolated LAE is unlikely to be observed, but a cluster of LAEs, that have jointly ionized their surrounding region, should be observable. In brief, patchy reionization should result in enhanced observed clustering of LAEs (Furlanetto et al. 2004a; McQuinn et al. 2007b; Mesinger and Furlanetto 2008; Ouchi et al. 2010; Jensen et al. 2013). Fig. 1.21, from McQuinn et al. (2007b), shows slices through a numerical reionization simulation that illustrates this effect. Observable LAEs should show enhanced clustering before reionization com-

pletes, with the enhancement growing as the IGM becomes more neutral. This suggests that a measurement of the clustering of LAEs could be a way to estimate the progress of reionization.

To observe this clustering enhancement, one needs a survey with a field of view that is much larger than the typical bubble size during reionization. The most likely candidate instrument to provide such a data set is Hyper Suprime Cam (HSC), a new instrument on the Subaru telescope. Their observations will reach out to $z \simeq 7.3$ and extend over several square degrees. In §3, we forecast observations of galaxy clustering from this HSC survey and predict how their measurements might place constraints on the process of reionization.

1.2.4.6 Intensity Mapping

As we discuss in §1.1, our current best understanding of reionization is that numerous faint galaxies fueled the reionization process. This implies that it is difficult to detect the sources that emit most of the ionizing photons individually. One method to estimate the collective impact of these faint sources is intensity mapping. Instead of trying to detect each galaxy individually, one measures the large scale spatial fluctuations in the collective emission from all luminous sources in a chosen spectral line (see, for example, Suginohara et al. (1999); Righi et al. (2008); Visbal and Loeb (2010); Gong et al. (2011); Carilli (2011); Lidz et al. (2011); Pullen et al. (2013); Breysse et al. (2014); Keating et al. (2015); Croft et al. (2016)). The "all" here is key; intensity mapping captures the contributions from all sources, even those too faint to be detected by traditional observations. Common emission lines used for these studies include Lyα, CO, and CII. The power of this technique, and how it differs from traditional galaxy surveys is depicted in Fig. 1.22. Using emission lines to map the galaxies allows this technique to be tuned to any desired redshift.

Intensity mapping surveys of EoR galaxies should result in a 3D map of the ionizing sources, which, naturally, will have ionized regions around them. This should comple-

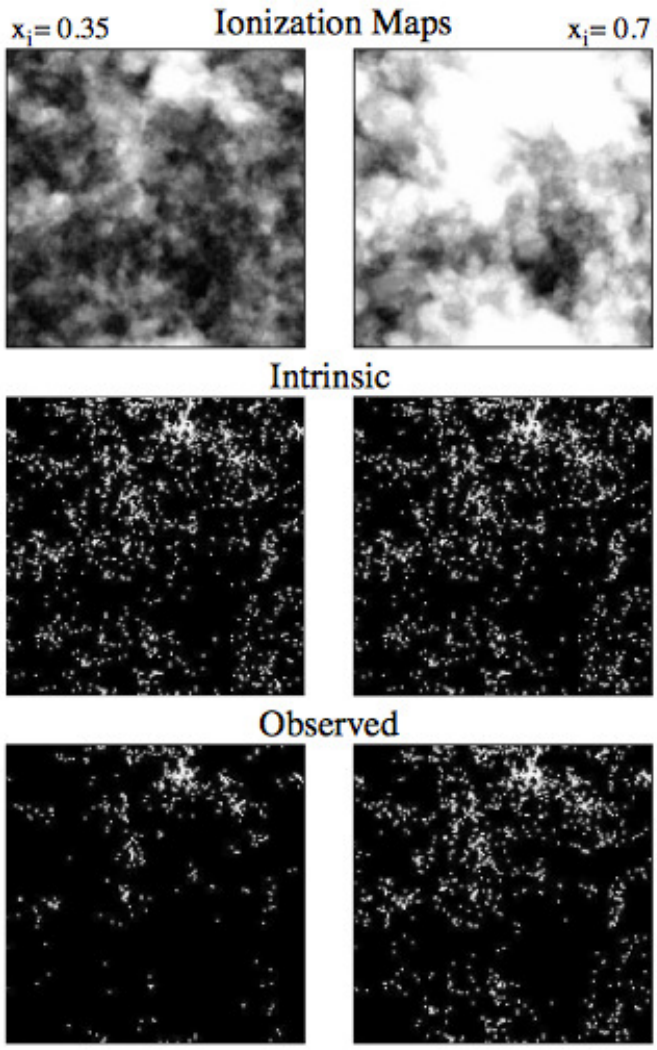

Figure 1.21: Figure from McQuinn et al. (2007b). Based on a mock survey at $z = 6.5$, the top panels show the projected ionization field of the simulation, for two different ionized fractions. The panels cover 0.36 deg^2 and correspond to survey depths along the line of sight of 31 Mpc. The middle panel shows the intrinsic distribution of the simulated galaxies, i.e. this shows the distribution the galaxies would have if they were not attenuated by surrounding neutral hydrogen. The bottom panel shows the distribution of observable LAEs, after accounting for the attenuation of their Lyα emission by neutral hydrogen along the line of sight. The clustering of the observed LAEs is enhanced relative to their intrinsic, unattenuated distribution, with the enhancement growing as the neutral fraction increases.

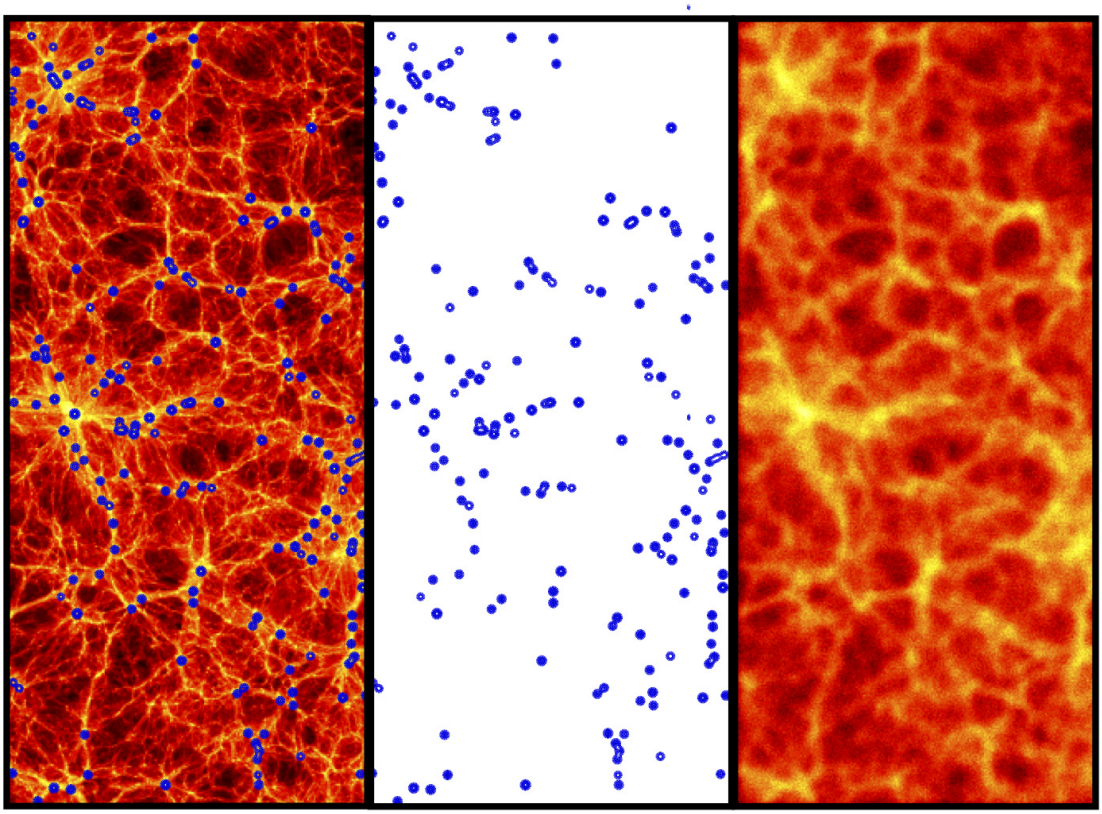

Figure 1.22: This figure illustrates the power of intensity mapping. The left panel depicts a numerical simulation of galaxies (bright galaxies indicated by the blue dots) and diffuse emission (redscale web), from sources such as dwarf galaxies and intra-halo light. The middle panel depicts what a typical galaxy survey would observe in that same field – i.e. all galaxies above some minimum luminosity threshold, but none of the faint galaxies or extended emission. Finally, in the right panel, we see the results of an intensity mapping survey. The diffuse emission and light from all the galaxies is recovered. (Figure from spherex.caltech.edu/science.)

ment well 21-cm observations which will trace the distribution of neutral gas. The one map should be the inverse of the other. Cross-correlating these two data sets should allow one to extract the 21-cm signal from reionization: foreground emission should not correlate with the intensity mapping signal; high redshift 21-cm emission should (Furlanetto and Lidz 2007; Lidz et al. 2009; Lidz et al. 2011). In addition, we should be able to extract information about the size of ionized regions forming around groups of galaxies using the scale-dependence of the cross-correlation (Lidz et al. 2009; Lidz et al. 2011; Gong et al. 2011).

While this appears to be a promising technique, one challenge is that, intensity mapping observations, like LAE surveys, suffers from contamination by interloper emission (Visbal and Loeb 2010). In §4, we lay out one approach for cleaning the intensity mapping signal of interloper contaminates.

1.3 Putting the Pieces Together

The preceding discussion has served to sketch out the many methods contributing to our current understanding of the EoR. In many ways, attempting to understand reionization is like working on a giant puzzle. Each type of observation, from 21-cm emission, to quasars, to the CMB to the whole host of galaxy observations, contributes or will contribute its piece, its constraint on reionization. Fitting those pieces together into one coherent picture is part of the challenge. Our best current understanding is that reionization was an extended and patchy process, ending sometime between $z \sim 6$ and $z \sim 7$. We expect it to have a duration, in redshift of $\Delta z < 5.4$. Thus, around $z \sim 12$ patches of ionized hydrogen became large enough to influence kSZ measurements. Studies of reionization are poised to acquire measurements of the processes of reionization, either through 21-cm observations or galaxy measurements.

In the following chapters, we detail our own contributions to this puzzle. Here we explore the implications of current measurements of high redshift galaxy populations for

our understanding the EoR, and develop strategies to learn more from upcoming high redshift galaxy surveys.

Chapter 2

What Do Observations of the Lyman-α Fraction Tell Us About Reionization?

2.1 Introduction

Recent studies have identified large samples of Lyα emitting galaxies (LAEs) back to $z \sim 7$ (e.g. Hu et al. 2010; Ouchi et al. 2010; Kashikawa et al. 2011). In addition to providing insight into the properties of early galaxy populations, these surveys can be used to probe the ionization state of the surrounding intergalactic medium (IGM) and the reionization history of the Universe. In particular, the Lyα optical depth in a significantly neutral IGM is so large that even the red side of a Lyα emission line should be attenuated by absorption in the damping wing of the line (Miralda-Escude 1998). This is, in turn, expected to lead to a decline in the abundance of observable LAEs as the Universe becomes significantly neutral. Indeed, Kashikawa et al. (2006) found evidence for a decline in the abundance of LAEs between $z = 5.7$ and 6.5 from observations in the Subaru Deep Field (SDF). Recent work has started to extend these measurements all the way out to $z = 7.7$ (e.g. Clément et al. 2012); this study finds no LAE candidates, possibly indicating a further drop in the abundance of LAEs from $z = 6.5$ to 7.7.

Published as Taylor and Lidz (2014)

The declining LAE abundance may result if these observations are, in fact, probing into the Epoch of Reionization (EoR) when the IGM is significantly neutral, but the existence of a decline (e.g. Hibon et al. 2010, 2011, 2012; Tilvi et al. 2010; Krug et al. 2012), its statistical significance (Ouchi et al. 2010) and the interpretation of the measurements (e.g. Dijkstra et al. 2006) are all still debated. One main challenge here is to isolate the *part of the evolution in the LAE abundance that arises from changes in the ionization state of the IGM*. The LAE abundance itself will, undoubtedly, grow with time as a result of the hierarchical growth of the underlying LAE host halo population. Furthermore, the *intrinsic properties* of the LAE populations should also evolve with time. Evolution in the dust content, the structure of the interstellar medium, and the strength and prevalence of large scale outflows can all impact the escape of Lyα photons from galaxies, and the observable abundance of the LAE populations.

In recent work, Stark et al. (2010) proposed an approach that partly circumvents concerns about intrinsic evolution in the underlying galaxy populations. The Stark et al. (2010) method uses the Lyman-break selection technique to find populations of galaxies at the redshift of interest, taking advantage of that technique's power in efficiently finding many galaxies within a given redshift range. Then, follow-up spectroscopy is done to determine which of those Lyman break galaxies (LBGs) have strong enough Lyα emission to be classified as LAEs. Since reionization should produce little to no effect on the observation of LBGs, but Lyα emission is attenuated by neutral hydrogen, the fraction of the LBGs that are also LAEs should decrease as the IGM becomes significantly neutral. With this technique, evolution in the abundance of the underlying population of star-forming galaxies 'divides out'. Evolution in the Lyα fraction induced by changes in the intrinsic LAE properties can be extrapolated from lower redshift measurements of this fraction at $z \leq 5$ or so, which clearly probe the post-reionization epoch. Moreover, the spectroscopic samples obtained in this approach allow one to search for spectroscopic signatures of intrinsic evolution in the LAEs' properties.

Several groups have recently applied this method for the first time; our focus here

will be on the theoretical interpretation of these new measurements. First, Stark et al. (2010, 2011) measured the Lyα fraction ($f_{Ly\alpha}$)[1] in several redshift bins, centered around $z = 4, 5$, and 6. The Universe should be completely ionized in this case, at least in the former two redshift bins, and so this measurement describes the redshift evolution in the intrinsic LAE properties towards high redshift. These authors find evidence that $f_{Ly\alpha}$ increases steadily from $z = 4 - 6$. They explain this trend by noting that dust levels in these galaxies tend to decrease with increasing redshift; this should likely facilitate the escape of Lyα photons and so $f_{Ly\alpha}$ should grow with increasing redshift. Having noted this trend, they make predictions for $f_{Ly\alpha}$ at $z \sim 7$, assuming there is no evolution in the ionized fraction. A lower measurement of $f_{Ly\alpha}$ than predicted would hence suggest that $z \sim 7$ observations are probing the significantly neutral era.

Very recently, several groups have extended these measurements out to $z \sim 7$, including Schenker et al. (2012), Pentericci et al. (2011), Ono et al. (2012) and Caruana et al. (2012). As we discuss in more detail subsequently, both Schenker et al. (2012) and Pentericci et al. (2011) see evidence for a decline in $f_{Ly\alpha}$ near $z \sim 7$. Both Ono et al.'s and Caruana et al.'s results are consistent with little evolution from Stark et al. (2011)'s lower redshift measurements to within their error bars. Although these measurements are still in their infancy, and come from ≤ 50 LBGs in total, the strong decline seems to suggest that the IGM is surprisingly neutral at $z \sim 7$. In particular, Pentericci et al. (2011) argue that the low $f_{Ly\alpha}$ indicated by their $z \sim 7$ measurement requires a volume-averaged neutral fraction of $\langle x_{\rm HI} \rangle \geq 0.6$. Schenker et al. (2012) quote a fairly similar constraint, although somewhat more tentatively.

Interestingly, the large neutral fractions suggested by this test are surprising given other constraints on reionization. In particular, the relatively large optical depth to Thomson scattering implied by *Wilkinson Microwave Anisotropy Probe* (*WMAP*) observations (Larson et al. 2011) and the low emissivity – only a few ionizing photons per atom per Hubble time at $z \sim 5$ – inferred from the mean transmission in the Lyα forest after reion-

[1]Throughout we denote the Lyα fraction by $f_{Ly\alpha}$, although some other works use $X_{Ly\alpha}$.

ization (Miralda-Escude 2003; Bolton and Haehnelt 2007) suggest that reionization is a fairly prolonged and extended process.[2] Furthermore, the absence of prominent Gunn–Peterson absorption troughs in $z \leq 6$ quasar spectra (Fan et al. 2006) is commonly taken to imply that the IGM is completely ionized by $z \leq 6$, a mere 175 Myr after the time period probed by the $z = 7$ Lyα fraction measurements. Hence the Lyα fraction test results, when combined with $z \leq 6$ quasar absorption spectra measurements, are hard to reconcile with other observational constraints – as well as theoretical models for the redshift evolution of the ionized fraction – which all prefer a more extended reionization epoch. One possibility is that reionization is sufficiently inhomogeneous to allow transmission through the Lyα forest before the process completes (Lidz et al. 2007; Mesinger 2010), potentially relaxing the requirement that reionization needs to complete by $z \geq 6$ (McGreer et al. 2011). Nevertheless, collectively current constraints on reionization prefer a significantly higher 'mid-point' redshift at which 50 percent of the volume of the IGM is neutral, z_{50}. For example, Kuhlen and Faucher-Giguère (2012) (see also Pritchard et al. 2010) combine measurements of the Thomson scattering optical depth, high redshift LBG luminosity functions, and measurements from the post-reionization Lyα forest, finding that the preferred redshift at which $\langle x_{\rm HI} \rangle = 0.5$ is $z_{50} = 10$ for a variety of models.

However, as we look back into the EoR we expect both the average abundance of LAEs to decrease and for there to *be increasingly large spatial fluctuations in the abundance of observable LAEs* (Furlanetto et al. 2006; McQuinn et al. 2007a; Mesinger and Furlanetto 2008; Jensen et al. 2013). This should result from the patchiness of the reionization process: LAEs that reside at the edge of ionized regions, or in small ionized bubbles, will have significant damping wing absorption from nearby neutral hydrogen, while those at the center of large ionized bubbles will be less attenuated. Ultimately, measuring these spatial variations is a very promising approach for isolating the impact

[2]However, a very recent analysis by Becker and Bolton (2013) favours a somewhat higher emissivity from the Lyα forest data. The higher inferred emissivity would help accommodate more rapid reionization models.

of the IGM and studying reionization, with existing data already providing some interesting constraints (McQuinn et al. 2007a; Ouchi et al. 2010). Presently, the important point is that these fluctuations imply that one must survey a rather large region on the sky to obtain a representative sample of the Lyα fraction. Perhaps existing $z \sim 7$ measurements in fact probe later stages in reionization than previously inferred, but are sampling regions on the sky with above average attenuation and correspondingly lower than average Lyα fractions. Here we set out to explore this sample variance effect, quantify its impact on existing measurements, and to understand the requirements for future surveys to mitigate its impact.

The significance of the observed drops in the Lyα fraction also depends on the relationship between LAE and LBGs; therefore, we examine a variety of models in an attempt to span some of the uncertainties in the properties of the galaxies themselves. We use simulations to explore the effects of small fields of view and various models for LBG luminosity and Lyα emission on $f_{Ly\alpha}$ and, thus, what can be confidently said about the ionized fraction of the Universe.

Throughout this chapter, we assume a Λ cold dark matter (ΛCDM) model with $n_{\rm s} = 1$, $\sigma_8 = 0.8$, $\Omega_{\rm m} = 0.27$, $\Omega_\Lambda = 0.73$, $\Omega_{\rm b} = 0.046$ and $h = 0.7$. These parameters are broadly consistent with recent results from the Planck collaboration (Planck Collaboration et al. 2014).

2.2 Observations

First, we describe all of the current $z \sim 7$ Lyα fraction measurements. We subsequently compare these measurements with theoretical models. The main properties of the current observations are summarized in Table 2.1.

Pentericci et al. (2011) describe observations they obtained over three fields of view: the Great Observatories Origins Deep Surey (GOODS)-South field (Giavalisco et al. 2004), the New Technology Telescope Deep Field (NTTDF; Arnouts et al. (1999); Fontana

et al. (2000)) and the BDF-4 field (Lehnert and Bremer 2003). Altogether, these fields span 200 arcmin^2 [roughly 700 (Mpc h^{-1})^2]. Within these fields, they did follow-up spectroscopy on galaxies that were selected as z-dropouts. As we will discuss, in practice their spectroscopic sample probes the Lyα attenuation across only a fraction of these full fields-of-view. Although these results are summarized and combined by Pentericci et al. (2011), they also published the initial measurements in stages. In Fontana et al. (2010), they report their observations on GOOD-S. In Vanzella et al. (2011), they do the same for galaxies in BDF-4. Finally, in Pentericci et al. (2011), they discuss their observations of NTTDF. In these fields combined, they found 20 LBGs, two of which had strong enough Lyα emission for them qualify at LAEs.

They bin these galaxies based both on ultraviolet (UV) magnitude and on the rest-frame equivalent widths of the Lyα lines, REWs. Since none of the faint galaxies ($-20.25 < M_{UV} < -18.75$) that they observe has strong Lyα emission, for the faint case they are only able to put upper limits on $f_{Ly\alpha}$. For the galaxies with stronger Lyα emission (REW > 55 Å), their results are consistent within error bars with the projections from lower redshifts by Stark et al. (2011). It is only for the weaker, but UV bright ($M_{\rm UV} < -20.25$), LAEs (REW > 25 Å) that they directly detect a significant drop.

Schenker et al. (2012) do spectroscopic follow-up on LBGs with z > 6.3 observed in the *Hubble Space Telescope (HST)* Early Release Science (ERS) field by Hathi et al. (2010) and McLure et al. (2011), 36.5 arcmin^2 [119 (Mpc h^{-1})^2]. In addition to the eight galaxies they observed in ERS, they also included 11 galaxies drawn from a variety of other surveys. From this sample of 19 galaxies, they found two that were LAEs. In order to boost their sample size, they also considered galaxies studied by Fontana et al. (2010) in their calculation of $f_{Ly\alpha}$. Note that since Fontana et al. (2010) is part of the sample sets from both Pentericci et al. (2011) and Schenker et al. (2012), these two sets of observations are not completely independent. Fontana et al. (2010) detected seven LBGs none of which was clearly LAEs. Thus, Schenker et al. (2012) worked from a total sample of 26 LBGs, two of which they identified as LAEs.

Combining these data sets and taking into account the various limits of the observations, they find that $f_{Ly\alpha}$ for the brighter galaxies ($-21.75 < M_{\rm UV} < -20.25$) is consistent with the lower redshift measurements. It is only for the faint galaxies ($-20.25 < M_{UV} < -18.75$) that they see a significant drop.

Ono et al. (2012) observed the SDF and GOODS-N, a total of 1568 arcmin^2 [roughly 5100 (Mpc h^{-1})^2]. However, their survey is much shallower than either Schenker et al. (2012) or Pentericci et al. (2011), only observing down to $y \simeq 26.0$ mag ($M_{UV} = -20.9$). Because of this shallowness, even though they are observing a relatively large area, they only identified 22 z-dropout candidates (Ouchi et al. 2009). From that sample, they took spectroscopic observations of 11 of them; three of those they identified as LAEs. Their study only goes as deep as the brightest of two M_{UV} bins ($-21.75 < M_{UV} < -20.25$). In that bin, their results are consistent with the projections of Stark et al. (2011) from lower redshifts.

Caruana et al. (2012) did spectroscopy for five z-band dropouts ($z \sim 7$) found in the *Hubble Ultra Deep Field*, 11 arcmin^2 [36 (Mpc h^{-1})^2], selected from earlier surveys. They observed no Lyα emission from the z-band dropouts, and, thus, only placed upper limits on the $f_{Ly\alpha}$ at $z \sim 7$; their upper limits are consistent with the projections from lower redshifts (Stark et al. 2011).

One might wonder, for all of these surveys, about the presence of low redshift interlopers. If the fraction of low redshift interlopers is larger near $z \sim 7$ than at lower redshifts, one might erroneously infer a drop-off in the Lyα fraction. For instance, in the simplest version of the Lyman break selection technique a lower redshift red galaxy may be mistaken for a higher redshift LBG. However, these groups have used a variety of techniques to ensure that the samples are truly from a redshift near $z \sim 7$, preferring to discard those galaxies that are likely, but not definitively, at the redshift of interest in order to obtain an uncontaminated sample. In particular, Pentericci et al. (2011), as discussed in Castellano et al. (2010), use multiple filters and a number of colour selection criteria, to ensure that low-redshift interlopers are excluded. Similarly, the sample used by Ono et al. (2012),

drawn from Ouchi et al. (2009), applies a variety of colour cuts to only select high redshift galaxies. Schenker et al. (2012) derive their main sample from McLure et al. (2011). McLure et al. (2011) fit the photometric redshifts of all potential candidates and required the ones that they retained to have both statistically acceptable solutions for $z > 6$ and to exclude lower redshift solutions at the 95 percent confidence level. Based on all of these techniques, interloper contamination appears not to be a significant worry.

Since only Pentericci et al. (2011) and Schenker et al. (2012) report significant decreases in $f_{Ly\alpha}$, the rest of the chapter will focus on their observations. As detailed in Table 2.1, it is notable that the typical comoving dimension of all but the shallower Ono et al. (2012) survey is ~ 10 Mpc h^{-1}. This scale is comparable to the size of the ionized regions during much of the EoR (see e.g. McQuinn et al. 2007b), suggesting that sample variance may be significant on these scales. Furthermore, as we detail subsequently, the LBGs identified for follow-up spectroscopy in these fields only *sparsely sample* sub regions of the full field, and so the surveys do not, in fact, sample Lyα attenuation across the entire field of view.

Table 2.1: Summary of published measurements of $f_{Ly\alpha}$

Field	Area	Shortest side	Limiting mag[a]	Faint[b]		Bright[c]		Source[d]
				LBGs	LAEs	LBGs	LAEs	
Pentericci et al. (2011)								
BDF-4	~ 50 arcmin^2	13.6 Mpc h^{-1}	26.5	1	0	5	2	Vanzella et al. (2011) Pentericci et al. (2011)
GOODS-S	~ 90 arcmin^2	13.6 Mpc h^{-1}	26.7	1	0	6	0	Fontana et al. (2010)
NTTDF	~ 50 arcmin^2	13.6 Mpc h^{-1}	26.5	0	0	7	0	Pentericci et al. (2011)
Schenker et al. (2012)								
GOODS-S	~ 90 arcmin^2	13.6 Mpc h^{-1}	26.7	1	0	6	0	Fontana et al. (2010)
ERS	36.5 arcmin^2	7.7 Mpc h^{-1}	27.26	8	0	0	0	Schenker et al. (2012)
Other fields[e]	–	–	–	7	2	4	0	Schenker et al. (2012)
Ono et al. (2012)								
GOODS-N	~ 150 arcmin^2	18.1 Mpc h^{-1}	26.0	0	0	1	1	Ono et al. (2012)
SDF	~ 1400 arcmin^2	48.9 Mpc h^{-1}	26.0	0	0	7	2	Ono et al. (2012)
Caruana et al. (2012)								
HUDF	~ 11 arcmin^2	6.0 Mpc h^{-1}	–[f]	3	0	2	0	Caruana et al. (2012)

[a] y band limiting magnitude [b] Faint galaxies are ones with $-20.25 < M_{UV} < -18.75$ [c] Bright galaxies are ones with $-21.75 < M_{UV} < -20.25$ [d] May not have originally observed these galaxies, but did the spectroscopic follow up and reported which ones had Lyα emission [e] Schenker et al. (2012) included several galaxies from a variety of other surveys and fields in their spectroscopic sample. These have been grouped together here. [d] Caruana et al. (2012) did spectroscopic follow up on galaxies drawn from several surveys. Thus, there is no consistent y-band limiting magnitude.

Summary of observations for the main papers we are discussing. The Fontana et al. (2010) sample is included in both the observations of Pentericci et al. (2011) and Schenker et al. (2012). This is because both groups used that data in their calculation of $f_{Ly\alpha}$. Galaxies were only counted as LAEs if their Lyα emission was greater than some minimum threshold (usually an equivalent width threshold of 25 Å). In compiling this table, summaries in Ono et al. (2012) were essential.

2.3 Method

Next we describe the various ingredients that enter into our simulated models of the Lyα fraction. Our calculations start from the reionization simulations of McQuinn et al. (2007a); these simulations provide realizations of the inhomogeneous ionization field and surrounding neutral gas, which in turn modulate the observable abundance of the simulated LAEs. In post-processing steps, we further populate simulated dark matter haloes with LBGs and LAEs, finally attenuating the LAEs based on the simulated neutral hydrogen distribution. A completely self-consistent approach would vary the reionization history jointly with variations in the properties of the LBGs and LAEs, but our post-processing approach offers far greater flexibility for exploring a wide range of models. In addition, most of the ionizing photons are likely generated by much fainter, yet more abundant, sources than the LBGs that are detected directly (thus far) and so the ionization history is somewhat decoupled from the LBG properties relevant here. Our philosophy for modeling the LAEs is to focus our attention on the impact of reionization and its spatial inhomogeneity. As a result, we presently ignore the complexities of the Lyα line transfer internal to the galaxies themselves; we will comment on their possible impact on our main conclusions.

2.3.1 Reionization Simulations

The reionization simulations used in our analysis are described in McQuinn et al. (2007b,a); here we mention only a few pertinent details. These simulations start from a 1024^3 particle, 130 comoving Mpc h^{-1} dark matter simulation run with GADGET-2 (Springel 2005) and treat the radiative transfer of ionizing photons in a post-processing step. The calculation resolves host haloes down to $\sim 10^{10} M\odot$, and so the simulation directly captures the likely host haloes of both LBGs and LAEs (smaller mass haloes host ionizing sources and are added into the simulation as described in McQuinn et al. (2007a)). We adopt the fiducial model of these authors in which each halo above the atomic cooling mass (on the

order of $M \sim 10^8 M\odot$, Barkana and Loeb 2001) hosts a source with an ionizing luminosity that is directly proportional to its halo mass. We consider simulation outputs with a range of ionized fractions, $\langle x_i \rangle$, in effort to explore how the Lyα fraction and its spatial variations evolve throughout reionization. In each case, we take the host haloes from a simulation output at $z = 6.9$, very close to the redshift of interest for the current Lyα fraction measurements. In the fiducial model of McQuinn et al. (2007a) studied here, the volume-averaged ionization fraction is $\langle x_i \rangle = 0.82$ at this redshift. In practice, when we explore smaller ionized fractions, we use slightly higher redshift outputs of the ionization field in the same model. This approximation was also adopted in McQuinn et al. (2007a) and should be adequate since – at fixed $\langle x_i \rangle$ – the properties of the ionization field depend little on the precise redshift at which the ionized fraction is reached (tests of this are given in McQuinn et al. 2007b).

2.3.2 LBG Model

The next step in our model is to populate the simulated dark matter haloes with LBGs. Here we follow the simple approach described in Stark et al. (2007). In this model, the star formation rate, $\dot{M}_\star$, is connected to the halo mass, $M_{\rm halo}$, by

$$\dot{M}_\star = \frac{f_\star (\Omega_{\rm b}/\Omega_{\rm m}) M_{\rm halo}}{t_{\rm LT}}, \tag{2.1}$$

where $f_\star$ is the efficiency at which baryons are converted into stars and $t_{\rm LT}$ is the time-scale for star formation, which is itself the product of the star formation duty cycle ($\varepsilon_{\rm DC}$) and the age of the Universe which – in the high-z approximation – is $t(z) = 2/(3H(z))$. We assume here that stars form at a constant rate in the haloes that are actively forming stars. We adopt Stark et al. (2007)'s best-fitting values of $f_* = 0.16$ and $\varepsilon_{\rm DC} = 0.25$, for LBGs at $z \simeq 6$. We further assume the conversion from star formation rate to UV luminosity (at a rest-frame wavelength of $\lambda = 1500$ Å) given in Madau et al. (1998):

$$L_{1500} = 8.0 \times 10^{27} \frac{\rm erg}{\rm Hz\ s} \left[\frac{\dot{M}_\star}{1 M\odot/{\rm yr}} \right]. \tag{2.2}$$

The conversion factor here assumes a Saltpeter initial mass function and solar metallicity, but we do not expect our results to be sensitive to the precise number here. In the simple model described here, $\epsilon_{\rm DC}$ also gives the fraction of host haloes that are UV luminous at any given time. However, we find that the observed number density of LBGs at $z \sim 7$ from Bouwens et al. (2011) is better reproduced if instead $1/6$th of simulated dark matter haloes host LBGs with the above luminosity. In practice we randomly select $1/6$th of our dark matter haloes as active LBG hosts and give them UV luminosities according to the above formulas (with $\epsilon_{\rm DC} = 0.25$). This also allows us to reproduce the bias factor found from large samples of LBGs (Overzier et al. 2006). The assumption here of a one-to-one relation between UV luminosity and host halo mass for the active hosts is undoubtedly a simplification, but we have experimented with adding a 20 percent scatter to the UV luminosity–halo mass relation above and found little difference in our results.

2.3.3 Properties of the LAEs

Next, we give each LBG a random amount of Lyα emission, as characterized by the REW of each emission line. Our main interest is to explore the impact of inhomogeneous damping-wing absorption on the Lyα fraction, and so we do not attempt a detailed modeling of each emission line. In addition to the complex impact of the Lyα line transfer internal to each galaxy, the resulting line will be modified by resonant absorption within the IGM (in addition to the damping wing absorption that we do explicitly model). It is sometimes assumed that each emission line is symmetric upon leaving the galaxy, and that the blue side of each line is removed by resonant absorption in the surrounding IGM while the red side is fully transmitted. The reality is of course more complicated, and even the resonant absorption in the IGM may have a wide range of effects depending on the strength of large-scale infall motions towards LAE host haloes (which can lead to resonant absorption on the red side of the line), the local photoionization state of the gas, outflows, and other factors (see e.g. Santos 2004; Dijkstra et al. 2007; Zheng et al. 2010; Verhamme et al. 2012; Yajima et al. 2012; Duval et al. 2014). We will assume that these

variations are captured by drawing the REW of each LBG from a random distribution. We will refer to this loosely as the *intrinsic* REW, and that the observed REW results from simply multiplying this intrinsic REW by a damping wing attenuation factor described below. In this sense, our intrinsic REW is intended to include resonant absorption from the IGM, and we implicitly assume that this distribution does not vary strongly from $z \sim 6$ to $z \sim 7$. We additionally neglect any spatial variations – induced by e.g., large scale infall motions – in the intrinsic REW distribution.

As in Dijkstra et al. (2011), we draw an REW for each simulated galaxy from an exponential distribution, $P(\mathrm{REW}) = \exp[-\mathrm{REW}/\mathrm{REW_c}]/\mathrm{REW_c}$. This exponential model provides a good fit to the distribution of REWs found in lower redshift galaxies (Gronwall et al. 2007; Blanc et al. 2011). We further allow the REW to be either uncorrelated, correlated, or anti-correlated with the UV luminosity of each simulated LBG. In our fiducial model, the REW and UV luminosity are anti-correlated since this trend appears to best reproduce existing observations. In order to produce REW distributions that are anti-correlated with UV luminosity, we draw REWs from the exponential distribution (with $\mathrm{REW_c} = 125$ Å in our fiducial model), and place them into various REW bins that are then populated with LBGs according to their UV luminosity. Specifically, we divide REWs into 10 bins based on width: the first bin is from 0 to 32 Å, the second from 32 to 110 Å and the remaining eight are 80 Å wide. The LBGs are then divided into 10 bins based on UV luminosity, and the most luminous galaxies are randomly assigned REWs from the first (smallest REW) REW bin, the next most luminous from the first and second bins, and so forth, until all the LBGs have REWs. Although the details of this procedure are somewhat arbitrary, it matches both the observed values of $f_{Ly\alpha}$ at $z \sim 6$ (for both UV bright and UV faint sources), as well as the correlation coefficient, ρ, between REW and UV luminosity. This is defined as

$$\rho = \frac{\sum_{i=1}^{n} (\mathrm{REW_i} - \overline{\mathrm{REW}})(\mathrm{L_i} - \overline{\mathrm{L}})}{\sqrt{\sum_{i=1}^{n} (\mathrm{REW_i} - \overline{\mathrm{REW}})^2} \sqrt{\sum_{i=1}^{n} (L_i - \overline{L})^2}}. \tag{2.3}$$

The sum here is over the LAEs in the observed or simulated sample, with n LAEs in total, $\mathrm{REW_i}$ denotes the rest frame equivalent width of the ith LAE in the sample, L_i is the UV luminosity of the ith LAE, while $\overline{\mathrm{REW}}$ and $\bar{L}$ denote the sample-averaged rest frame equivalent width and UV luminosity, respectively. The correlation coefficient in our fiducial model is $\rho = -0.23$, while from Fig. 12 of Stark et al. (2010), we infer $\rho = -0.41$; since the variance of the observational estimate is likely still sizeable, we consider this simple model to be broadly consistent with observations.

This negative correlation model is also physically plausible, as discussed in §2.4.2. Of course, our fiducial description of this correlation is only a toy model. Nevertheless, we believe that it captures the relevant features of the lower redshift observations, and, thus, should be a useful guide as we consider the $f_{Ly\alpha}$ measurements.

In addition to our fiducial model, we discuss three other models that seem both physically plausible and show a diversity of results: (1) the REWs are assigned randomly; (2) there is a weak positive correlation between the REW and continuum luminosity of the galaxy and (3) there is a weak negative correlation between the REW and the continuum luminosity of the galaxy – weaker than in our fiducial case. For the second and third cases, the REWs are assigned in a fashion similar to that in our fiducial case, except the galaxies, and REWs, are only divided into three bins, not 10. Thus, the correlation is weaker than in the fiducial case. For the weak positive correlation, the correlation coefficient is $\rho = 0.10$; for the weak negative correlation, $\rho = -0.11$. While these models are unlikely to perfectly capture the relationship between LAEs and LBGs, they suffice to explore how our results depend on the precise relationship between LBGs and LAEs.

2.3.4 Attenuated LAE Emission and Mock Surveys

The intrinsic emission from each LAE is then attenuated according to the simulated distribution of neutral hydrogen. We do this following McQuinn et al. (2007a) and Mesinger and Furlanetto (2008). Specifically, we shoot lines of sight through the simulation box towards each LAE and calculate the total damping wing contribution to the Lyα opti-

cal depth, summing over intervening neutral patches. As in this previous work, we calculate the damping wing optical depth $\tau_{\rm DW}$ (according to e.g., equation 1 of Mesinger and Furlanetto 2008, equation 1.13 of this thesis) only at the center of each emission line, i.e. at an observed wavelength of $\lambda_{\rm obs} = \lambda_\alpha(1+z_{\rm s})$ for a source at redshift $z_{\rm s}$, with $\lambda_\alpha = 1215.67$ Å denoting the rest-frame line center of the Lyα line. We ignore the impact of peculiar velocities and neglect any redshift evolution in the properties of the ionization field across our simulation box – we use snapshots of the simulated ionization field at fixed redshift. Calculating the optical depth at the center of each line, rather than the full profile, should be a good approximate indicator of which sources will be attenuated below observational REW cut-offs (see McQuinn et al. 2007a for a discussion and tests). The 'observed' REW of each simulated LBG is then an attenuated version of the initial intrinsic REW according to ${\rm REW}_{\rm obs} = {\rm e}^{-\tau_{\rm DW}}{\rm REW}$.

Armed with galaxy positions, UV luminosities and observed REWs, we produce mock realizations of the Schenker et al. (2012) and Pentericci et al. (2011) observations, and measure their statistical properties. We slice the simulation cube into strips with the perpendicular dimensions mimicking the geometry and field of view of the observations. In order to approximately mimic the survey window functions in the redshift direction, we assume each strip has a length of 100 comoving Mpc h^{-1}. We adopt this value based on the estimated redshift distribution of z'-band dropouts in Ouchi et al. (2009) (their Fig. 6, reproduce here as Fig. 1.14), which those authors determined from the SDF and GOODS-N fields. For simplicity, we assume a top-hat window function and find that a top-hat of width 100 Mpc h^{-1} reproduces the area under the redshift distribution curve of Ouchi et al. (2009) and so use this width throughout. While all three of these surveys (Ouchi et al. 2009; Pentericci et al. 2011; Schenker et al. 2012) use slightly different filters, they all peak at roughly the same wavelength and Ouchi et al. (2009)'s have the largest full width at half maximum (FWHM). Thus, this should be a reasonable approximation, although it may slightly overestimate the depth of the field.

Within these strips, we then select the galaxies that would be observable to the two

groups, based on the limiting magnitudes and REW limits they reported (see Table 2.1). One subtlety here is that the galaxies observed by both groups are not distributed across their entire fields. This likely occurs partly because the LBGs are clustered, and partly because their efficiency for detecting LBGs and performing spectroscopic follow-up is not uniform across each field. Because of the latter effect, we may underestimate the sample variance if we draw the simulated LBGs from the full field of view. To roughly mimic this, we draw our LBGs from randomly placed cylinders with diameters matching the largest separation between galaxies in each set of observations: 9.99 Mpc h^{-1} for Schenker et al. (2012) and 8.04 Mpc h^{-1} for Pentericci et al. (2011). We only consider observable galaxies that fall within each cylinder, effectively limiting the size of the observed fields and making them still closer to the size of the ionized bubbles in the simulation.

Furthermore, comparing to the $z \sim 7$ LBG luminosity function from (Bouwens et al. 2011), it is clear that the existing measurements perform spectroscopic follow-up on only a small fraction of the total number of LBGs expected in each survey field. This likely owes mostly to the expense of the spectroscopic follow-up observations. However, this implies that the Lyα fraction measurements only sparsely sample the Lyα attenuation across the entire field-of-view, and enhances the sample variance effect. To mimic this, in each mock survey we randomly select LBGs to match the precise number spectroscopically observed, and consider the Lyα emission and attenuation around only these galaxies. In the case of Schenker et al. (2012)'s ERS field, they actually do not observe any bright LBGs. To loosely consider this case – which will turn out to be less constraining – we randomly select four simulated LBGs, which matches their bright sample in the other fields and also corresponds to the number one would expect based on the size of their field of view and the follow-up capabilities in Pentericci et al. (2011).

One caveat here is that our simulation does not capture Fourier modes that are larger than our simulation box size (130 comoving Mpc h^{-1}), and so the sample variance we estimate is only a lower bound. We do not expect the 'missing variance' to be large, however. Although the full fields of view of some of the existing surveys correspond to

a decent fraction of our simulation volume (see Table 2.1), the effective volume probed by the observations is significantly smaller, as a result of the sparse sampling discussed previously. In addition, it is important to note that our simulation box size is large compared to the size of the ionized regions during most of the reionization epoch, and so it does suffice to capture a representative sample of the ionization field.

Since both teams did follow up spectroscopy on already identified LBGs, we look for Lyα emission in the selected LBGs that is strong enough to exceed the observed REW cuts. The field-to-field fluctuations in $f_{Ly\alpha}$ arise from both the sample variance we aim to study and from discreteness fluctuations. In our model, the latter arise because the REW of the Lyα emission from each LBG is drawn from a random distribution. This scatter is, of course, non-vanishing even in the absence of reionization-induced inhomogeneities, and moreover, it is already included in the error budget of the existing measurements (while the sample variance contribution has not been included). Hence we must separate the discreteness and sample variance contributions to the simulated variance in order to avoid double counting the discreteness component. To do this, we keep track of which LBGs fluctuate above and below the observational REW cuts as a result of an upward or downward fluctuation in the IGM attenuation. Some LBGs in the simulated sample are observable as LAEs only because of downward fluctuations in the IGM attenuation, while some are pulled out of the LAE sample because of upward fluctuations in the IGM attenuation. Finally, in some cases – depending on the LBG's intrinsic REW and IGM attenuation – the IGM attenuation does not impact the LBG's observability as an LAE. Monitoring which LBGs are pulled into or out of the sample owing to fluctuations in the IGM attenuation allows us to measure the scatter in $f_{Ly\alpha}$ arising from sample variance alone.

Schenker et al. (2012) combine observations from a variety of surveys. Their observations focus on galaxies selected from an LBG survey on the ERS field. To increase their sample size, Schenker et al. (2012) include observations from Fontana et al. (2010) and several other LBGs from a variety of fields in their analysis. Since Fontana et al.

(2010) is included in Pentericci et al. (2011)'s analysis and the other LBGs were not all detected in well defined drop-out surveys of the corresponding fields, we only model the observations of the ERS field of view when we analyse Schenker's results.

Pentericci et al. (2011) observed with four pointings of the High Acuity Wide Field K-Band Imager (HAWK-I; two in GOODS-S, one at BDF-4 and one at NTTDF). Although the two fields in GOOD-S are next to each other, for ease of calculation we treated each pointing as independent, and scaled the confidence regions accordingly. This may lead us to underestimate the sample variance from these observations slightly.

2.4 Discussion

2.4.1 Is a Large Neutral Fraction Required?

Before we present a detailed comparison between the Lyα fraction measurements and our simulated models and explore their implications for understanding reionization, a qualitative illustration of the main effect discussed here may be helpful. This is provided by Fig. 2.1, which shows a representative slice through the simulation volume, when the volume-averaged ionization fraction is $\langle x_{\rm i} \rangle = 0.82$. The dimension into and out of the page has been averaged over the size of an ERS field. The two red regions show example mock survey volumes that have the same size as an ERS field. Clearly the top field is fairly well covered by intervening neutral hydrogen, although it is still has patches of ionized hydrogen. On the other hand, the bottom cylinder is almost entirely clear of neutral hydrogen. Lyα emission of galaxies residing in the top cylinder will be much more attenuated than in the bottom panel.

Quantitatively, in the faint UV luminosity bin of Schenker et al. (2012), the simulated $f_{Ly\alpha}$ in the first simulated field is $f_{Ly\alpha} = 0.30$, while the Lyα fraction is almost twice as large in the second simulated field, $f_{Ly\alpha} = 0.58$. These numbers can be compared to the average across the entire simulation volume at this neutral fraction, which is $f_{Ly\alpha} = 0.51$. Using our fiducial model and supposing (incorrectly) that these fractions are represen-

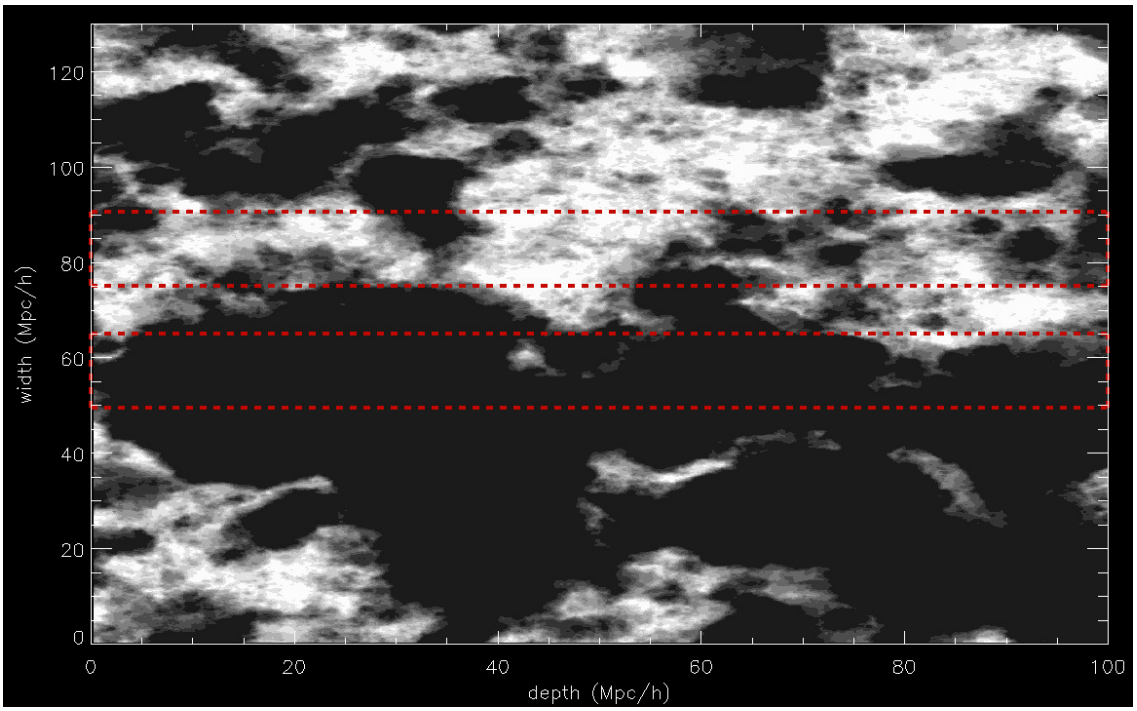

Figure 2.1: A slice through the simulation cube for an output with a volume-averaged ionization fraction of $\langle x_{\rm i} \rangle = 0.82$. The slice is averaged over one (perpendicular to the line of sight) dimension of the ERS field of view. Clouds of neutral gas are shown in grey-scale; the white areas being completely neutral. The dashed lines mark two potential mock ERS observations. The significant difference between these two fields illustrates that small regions on the sky may not provide representative samples of the overall average ionization state of the IGM.

tative, one would infer an ionized fraction of $\langle x_{\rm i} \rangle = 0.54$ for the first field, compared to $\langle x_{\rm i} \rangle = 1.0$ for the second field. Neither inference correctly returns the true ionized fraction of the field, $\langle x_{\rm i} \rangle = 0.82$. This suggests that a rather large area survey is indeed required to obtain representative measurements of the Lyα fraction. Perhaps the existing fields are more like the top cylinder, and the LBGs in these fields suffer above average attenuation. Assuming a survey like the top cylinder is representative of the volume averaged neutral fraction could clearly bias one's inferences of the neutral fraction. The chance of obtaining a biased estimate of the neutral fraction is enhanced if spectroscopic follow-up is done on only a few LBGs – effectively, a sparse sampling of each survey region – as is often the case for the existing measurements.

With this intuitive understanding, we turn to a more detailed comparison with the observations. Schenker et al. (2012) report a decline in $f_{Ly\alpha}$ at $z \sim 7$. This decline is particularly pronounced when compared to their observed $f_{Ly\alpha}$ values at lower redshifts. For $4 < z < 6$, they report an increase in the Lyα fraction with increasing redshift (Stark et al. 2011). At $z \sim 7$, $f_{Ly\alpha}$ is lower than the projected trend and lower than measured at $z \sim 6$. This decline suggests that that the observations may be probing into the EoR. Using Monte Carlo simulations of their full data sample, Schenker et al. (2012) conclude that in order to explain their results they require an ionized hydrogen fraction of at most $\langle x_{\rm i} \rangle \leq 0.51$.

Note that the low redshift measurements ($4 < z < 6$) come mainly from observations of the GOODS fields, both North and South. Some additional galaxies from other sources are also included. Altogether, Stark et al. (2011) observed 351 *B*-dropouts, 151 *V*-dropouts, and 67 *i'*-dropouts. Given the large sky coverage of these surveys, sample variance should not be a significant source of error for the low-redshift measurements. However, the same may not be true at higher redshift where the measurements come from smaller fields of view. In addition, if the high redshift measurements probe into the EoR, this should enhance the sample variance as we will describe.

In Fig. 2.2 we show simulated Lyα fractions for mock surveys mimicking the $z \sim 7$

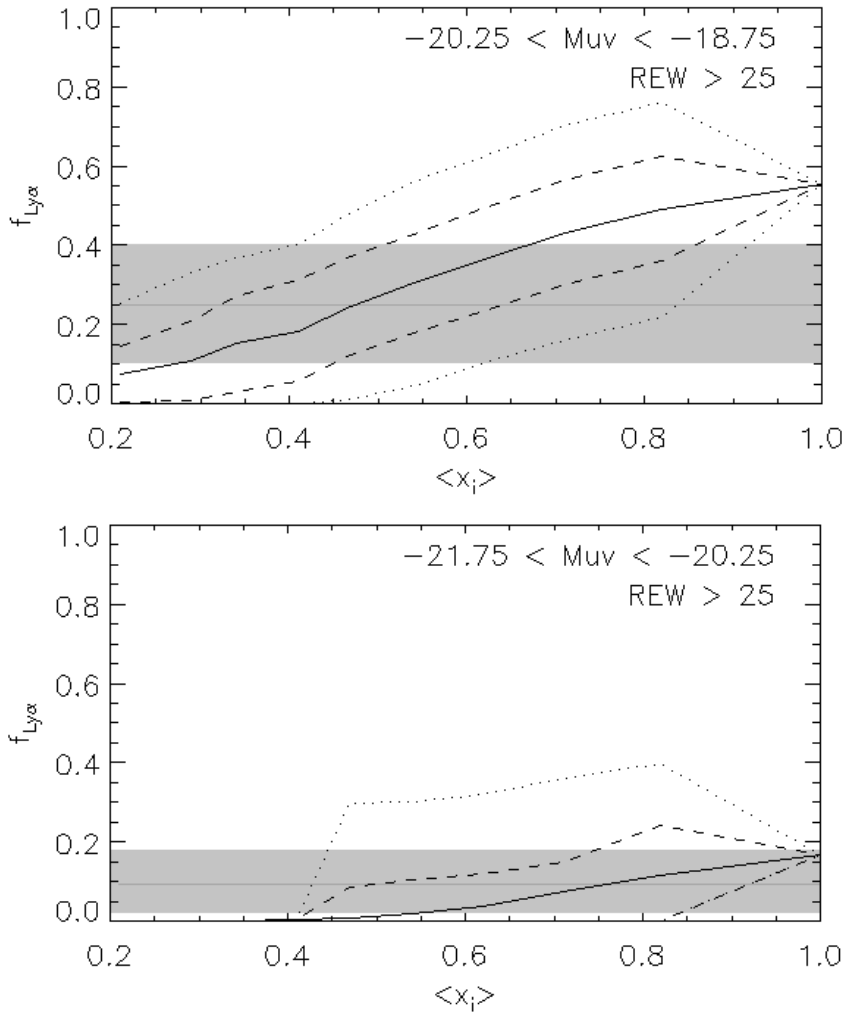

Figure 2.2: Comparison between mock Lyα fraction ($f_{Ly\alpha}$) measurements and the observations of Schenker et al. (2012), as a function of the volume-averaged ionization fraction, $\langle x_{\rm i} \rangle$. The solid lines show the average value of $f_{Ly\alpha}$ across the simulation volume in our fiducial model, while the dotted and dashed lines indicate the field-to-field spread in the simulated Lyα fraction, i.e. the sample variance. The dashed lines enclose the values of $f_{Ly\alpha}$ for 68 percent of the mock ERS fields, while the dotted lines enclose 95 percent of the simulated fields. The shaded regions show the 68 percent confidence interval reported by Schenker et al. (2012) (which neglect the sample variance contribution). The horizontal line near the center of the shaded bands gives their best-fitting value for the Lyα fraction. The top panel is for the UV faint bin of Schenker et al. (2012), while the bottom panel is for the UV bright bin.

measurements of Schenker et al. (2012) for the ERS field. In particular, we plot the average Lyα fraction across the entire simulation box (solid line), as well as 68 percent (dotted lines) and 95 percent (dashed lines) confidence intervals, as a function of the volume-averaged ionization fraction ($\langle x_{\rm i} \rangle$) in the models. The lines reflect the field-to-field variance (i.e. the sample variance) in the simulated $f_{Ly\alpha}$ values. The probability distribution of simulated $f_{Ly\alpha}$ values is somewhat non-Gaussian, and so we account for this in determining the confidence intervals. In order to compare with Schenker et al. (2012) we divide the simulated LBGs into UV bright ($-21.75 < M_{UV} < -20.25$) (bottom panel) and UV faint ($-20.25 < M_{UV} < -18.75$) (top panel) bins. The shaded region in each panel gives the allowed range in $f_{Ly\alpha}$ at 68 percent confidence reported by Schenker et al. (2012), while the horizontal line shows their best-fitting $f_{Ly\alpha}$ value. In calculating the 68 percent confidence range, Schenker et al. (2012) include LBGs from several fields. As discussed earlier, we only calculate the sample variance for the ERS field. The sample variance may thus be slightly overestimated when compared to the rest of the error budget. The shaded region neglects the sample variance contribution, and so a better estimate of the total error budget is the quadrature sum of the shaded regions and the dashed lines.

Focusing first on the UV faint bin (top panel), the first conclusion we draw from this comparison is that the *best-fitting* ionized fraction is indeed $\langle x_{\rm i} \rangle \approx 0.5$. This is consistent with the conclusions of Schenker et al. (2012). Note, however, that Schenker et al. (2012) infer the neutral fraction from the same McQuinn et al. (2007a) simulations used here, and so their constraint is not independent of the results here, although our present calculations adopt a different model for the LAE/LBG populations. The next conclusion to draw from the top panel is that the spread from sample variance is generally comparable to (although a little smaller than) the reported error budget, and so it is not in fact negligible, aside from the fully ionized case where it vanishes in this model. Here the sample variance describes spatial variations in the damping wing attenuation, which vanish in the fully ionized model. In reality, spatial variations in the resonant absorption likely lead to additional contributions, neglected here, which would make the sample variance non-

vanishing in the fully ionized case. Accounting for sample variance somewhat reduces the neutral fraction required by these observations; for instance an $\langle x_{\rm i} \rangle \approx 0.85$ model is just outside of the allowed 68 percent confidence range.

The bottom panel shows that the UV bright case is still easier to accommodate in a highly ionized IGM, at least in our fiducial LAE model. In this case, Schenker et al. (2012) found little evidence for redshift evolution. Since our fiducial model is constructed to give a lower $f_{Ly\alpha}$ fraction for UV bright LBGs after reionization, the Lyα fraction remains small at $z \sim 7$ in a highly ionized IGM. In fact, since the UV bright galaxies tend to have smaller intrinsic REWs in our fiducial model, these galaxies are particularly susceptible to attenuation: that Schenker et al. (2012) detect some Lyα emission from UV bright galaxies in this model then actually *slightly disfavours* more neutral models. At the 68 percent confidence level, $\langle x_{\rm i} \rangle \approx 0.42$ or smaller is disfavoured. The relatively small number of LBGs spectroscopically followed up in each field (only four) contributes to the size of the error bars. Recall that our sampling of four model galaxies here is somewhat arbitrary, as Schenker et al. (2012) did not in fact follow up any bright LBGs in the ERS field. Further, the trend of LAE fraction with ionization fraction depends somewhat on our particular model for the anti-correlation between intrinsic REW and UV luminosity, as we describe in §2.4.2.

Similarly, we can compare our mock Pentericci et al. (2011) observations with their actual measurements. This is shown in Fig. 2.3. Their survey is not as deep as Schenker et al. (2012), but covers a larger area on the sky. In the faint UV luminosity bin, they search for Lyα emission around two LBGs (see Table 2.1), and find no significant Lyα emission from either galaxy. This allows them to place only an upper limit on $f_{Ly\alpha}$ in this luminosity bin. Their quoted upper limit none the less implies a drop-off towards high redshift in $f_{Ly\alpha}$, when compared to the lower redshift measurements of Stark et al. (2011). However, the sample variance in our simulated samples is significant. In particular, the top panel shows that the upper limit on $f_{Ly\alpha}$ translates into a lower limit on the neutral fraction of 0.2 at the 68 percent confidence level. The spread in $f_{Ly\alpha}$ values is large

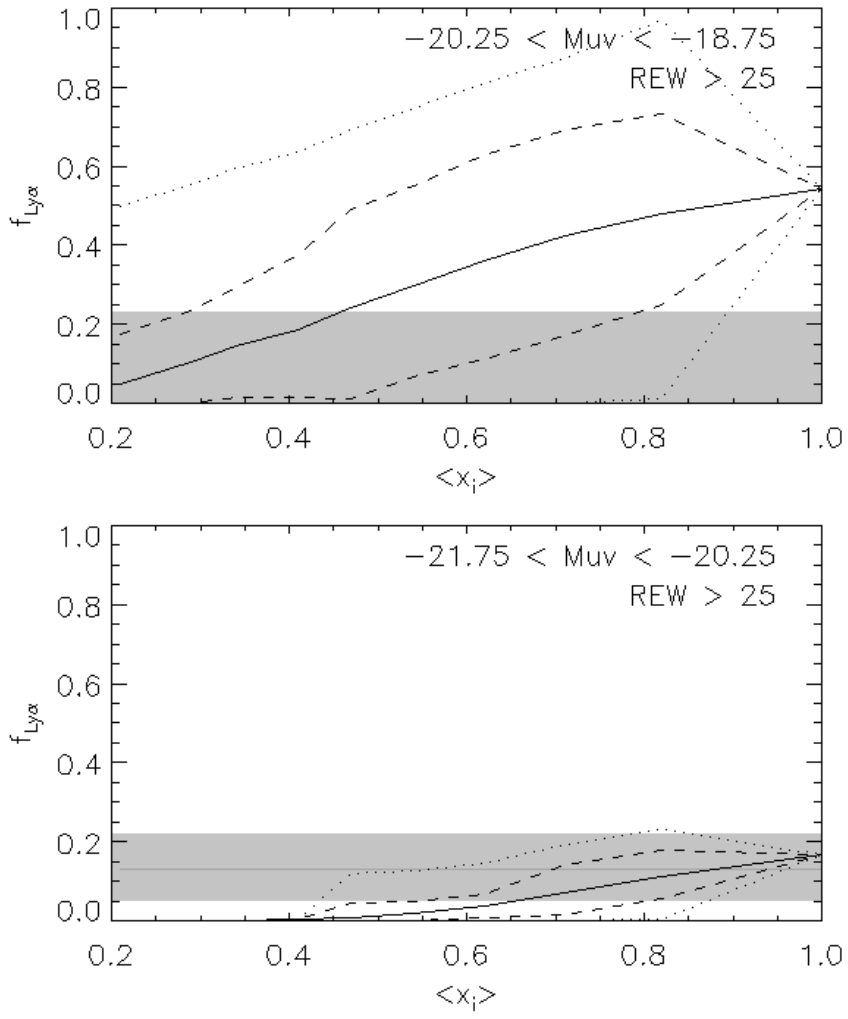

Figure 2.3: Comparison between mock Lyα fraction ($f_{Ly\alpha}$) measurements and the observations of Pentericci et al. (2011) as a function of the volume-averaged ionization fraction, $\langle x_{\rm i} \rangle$. This is similar to Fig. 2.2 expect here the shaded bands are the measurements from Pentericci et al. (2011), with UV faint measurements in the top panel, and UV bright ones in the bottom panel. Likewise, the simulated observations in this figure mimic those of Pentericci et al. (2011).

because only two LBGs are studied spectroscopically, and there are large variations in the amount of damping wing attenuation suffered by these two LBGs, depending on whether they reside towards the center of large ionized regions, at the edge of an ionized region, or in the center of a smaller ionized bubble.

For the UV bright galaxies, they do detect some Lyα emission; in this luminosity bin their Lyα fraction is lower for small REW (REW > 25 Å) lines than expected from extrapolating the lower redshift Stark et al. (2011) measurements out to $z \sim 7$. However, in our fiducial model the decline in the Lyα fraction for the UV bright sample is not especially constraining. As discussed previously, these sources tend to have smaller intrinsic REWs, and so even a small amount of attenuation from the IGM attenuates them out of the observable sample. Indeed the bottom panel of Fig. 2.3 shows that the Lyα fraction in the UV bright Pentericci et al. (2011) bin is compatible with a fully ionized universe in our fiducial model. As with the case of Schenker et al. (2012), this bin actually (slightly) disfavours too large a neutral fraction, $\langle x_{\rm HI} \rangle < 0.52$ at the 68 percent confidence level. Once the neutral fractions is less than 0.4, $f_{Ly\alpha}$ is consistent with zero; thus, that Pentericci et al. (2011) observe any Lyα disfavours a highly neutral universe.

Of course, that both Pentericci et al. (2011) and Schenker et al. (2012) observe evidence for a drop in $f_{Ly\alpha}$ near $z \sim 7$ strengthens the case that these observations probe back into the EoR. In order to quantify this, we combine the probability distributions for the separate observations shown in Figs 2.2 and 2.3. The results of this calculation are shown in Fig 2.4. Here the shaded regions show the 68 and 95 percent confidence intervals after combining the two measurements, assuming that the reported error distributions obey Gaussian statistics. For the combined UV faint case, we used directly the combined uncertainty calculated in Ono et al. (2012) which took into account that Fontana et al. (2010) was included in the calculations of both Pentericci et al. (2011) and Schenker et al. (2012). As before, the lines show the sample variance contributions calculated from our simulated models (and not included in the shaded error budgets).

We do not consider the observations of Ono et al. (2012) or Caruana et al. (2012)

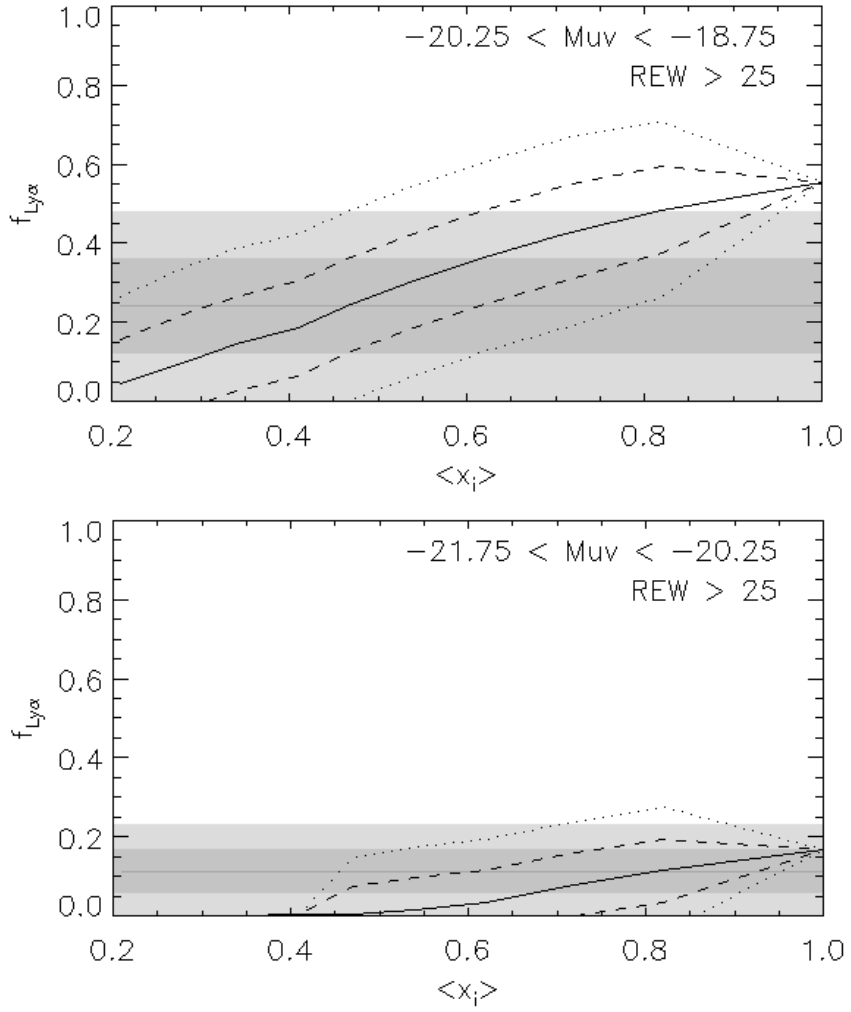

Figure 2.4: Confidence intervals on $f_{Ly\alpha}$ from combining the measurements of Schenker et al. (2012) and Pentericci et al. (2011). These constraints are compared to our fiducial model, as a function of $\langle x_{\rm i} \rangle$. Similar to Figs 2.2 and 2.3, except here the results reflect the constraints from combining the separate Lyα fraction measurements. The shaded regions reflect the combined reported errors, while the lines indicate the simulated average and sample variance contributions to the error budget. The top panel is for the UV faint luminosity bin, while the bottom panel is for the UV bright bin.

here since we do not expect them to have a significant effect on the combined constraints. While Ono et al. (2012) observed a large field, their survey was fairly shallow and focused on a small number of galaxies–only following up on 11 galaxies in the bright bin. Since the faint galaxies place the greatest constraints on the ionized fraction in our fiducial model, a shallow survey, focusing on the bright galaxies, is unlikely to increase the constraints. Further, Ono et al. (2012)'s observations are consistent with the increasing trend in $f_{Ly\alpha}$ seen in Stark et al. (2011); Ono et al. (2012) do not see a drop in $f_{Ly\alpha}$ at $z \sim 7$. Together, these characteristics of their observations, mean that not considering their observations does not significantly affect our results. Further, by only observing 11 galaxies, Ono et al. (2012) greatly reduce their survey's effective volume. Of course, a deeper survey, with more galaxies sampling the entire large field, would greatly reduce the effects of sample variance and could place significant constraints on the ionized fraction.

Caruana et al. (2012), on the other hand, focused on an extremely small field of view. The size of their field makes them particularly vulnerable to sample variance. Their observations are consistent with the trend from Stark et al. (2011). Thus, their observations would not place any further constraint on the sample variance.

The constraints in the combined case follow the trends found for each separate survey, but the overall significance is somewhat tightened. As before, the low Lyα fraction in the UV bright case is consistent with a fully ionized model. The UV faint case does, however, prefer a partly neutral IGM, but a very large neutral fraction is not required. For example, a model with $\langle x_i \rangle \sim 0.9$ lies within the 95 percent confidence range.

2.4.2 Model Dependance

It is also interesting to explore how the simulated Lyα fractions depend on the underlying model for the Lyα emission from LBGs. In particular, our fiducial model assumes that the intrinsic Lyα REW is anti-correlated with UV luminosity. A variety of studies seem to support this relationship. At $z \simeq 3$, Shapley et al. (2003) report an increase in the mean REW with fainter luminosity. Stark et al. (2010) extend this out to higher redshift;

for their sample of LBGs with Lyα emission at $3 \lesssim z \lesssim 6$, they find that the largest REWs tend to correlate with fainter UV continuum magnitudes. These observations are supported by a host of others (Ando et al. 2006; Ouchi et al. 2008; Vanzella et al. 2009; Balestra et al. 2010) that suggest that among the brightest sources, large REWs are scarce. Such a correlation has a plausible explanation; the fainter galaxies may be less dusty than their brighter counterparts, allowing more of the Lyα emission to be transmitted.

While this model does seem to match observations, there is still not widespread agreement on this point, see, for instance, Kornei et al. (2010). For LBGs at $z \sim 3$, Kornei et al. (2010) do not see a significant correlation between continuum luminosity and Lyα emission. Nilsson et al. (2009) argue that a flux or magnitude-limited survey, like the ones cited above, will generally observe both fewer instances of strong Lyα emission and fewer instances of bright LBGs since those are both rare. Thus, in order to conclude that continuum luminosity and Lyα REWs are anti-correlated one would need very large sample sizes, on the order of 1000 LBGs with measured REWs. In addition, note that our fiducial model was tuned to match the observations of Stark et al. (2011) in a fully ionized universe. However, there is still some uncertainty in the post-reionization Lyα fractions, even for UV bright sources. For example, Curtis-Lake et al. (2012) find a $z \sim 6$ Lyα fraction that is roughly two times as large as that of Stark et al. (2011) for UV bright sources, and comparable to that of the UV fainter sources from Stark et al. (2011).

Given the uncertainties in the relationship between LBGs and their intrinsic Lyα emission, we generate combined constraints along the lines of Fig. 2.4 for three additional LAE models. These additional models are described in §2.3.3 and correspond to cases with: a weaker negative correlation between intrinsic REW and UV luminosity than in our fiducial model (with $\rho = -0.11$ from Equation 2.3 compared to $\rho = -0.23$ in our fiducial model); a model where REW and UV luminosity are uncorrelated and a model with a weak positive correlation ($\rho = 0.10$).

The combined constraints in these additional models are shown in Fig. 2.5. It is reassuring that the results in the UV faint bin appear only weakly dependent on the underlying

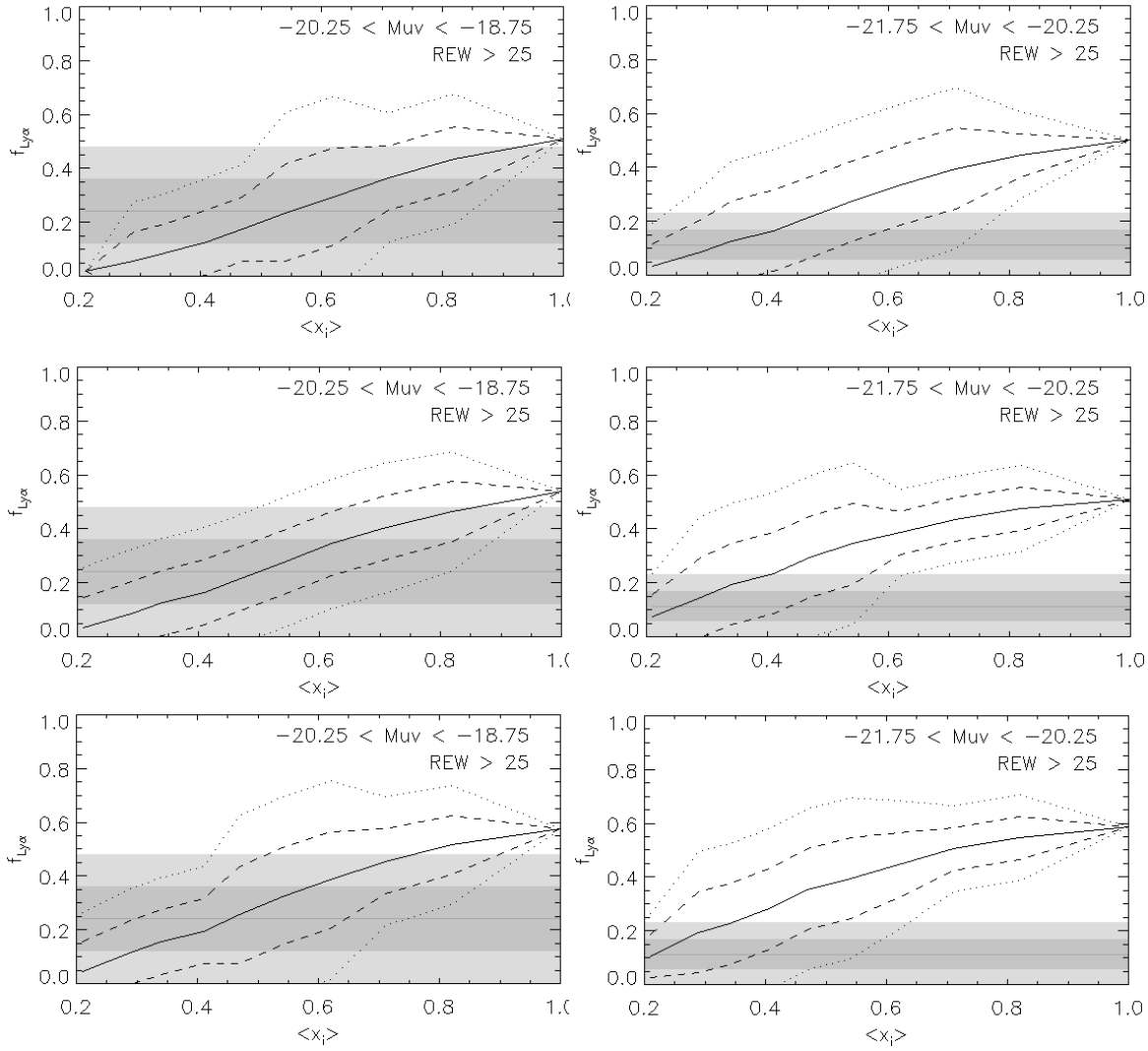

Figure 2.5: Dependence of $f_{Ly\alpha}$ on the LAE model. Similar to Fig. 2.4, but here we consider three different models for assigning Lyα REWs to LBGs. *(Top)* there is a weak negative correlation between the continuum luminosities and the Lyα REWs; the fainter galaxies have stronger Lyα emission, but the trend is less strong than in our fiducial model. *(Middle)* the Lyα REWs are assigned randomly to the LBGs, following the distribution in Dijkstra et al. (2011). *(Bottom)* there is a weak positive correlation between the continuum luminosities and the Lyα REWs; the brighter galaxies have stronger Lyα emission. The left panels are for UV faint bins, while the right panels show UV bright LBGs.

model for Lyα emission from LBGs. The UV bright case is, on the other hand, quite sensitive to the underlying LAE model. In particular, in these models the UV bright Lyα fractions are intrinsically larger than in our fiducial case, and so significant attenuation is required to explain the lower Lyα fractions measured in the high UV luminosity bin. However, the same qualitative behaviour is expected in the post-reionization Universe, and so each of these models is in conflict with the post-reionization ($z \sim 4-6$) measurements of Stark et al. (2011) which do show a significant drop in the Lyα fraction from UV faint to UV bright LBGs.

Our model does not consider the effects of galactic winds on Lyα emission. Backscattering of Lyα emission off of the far side of a galactic outflow can promote the escape of Lyα photons by shifting them redward of line center, and strong winds may therefore make Lyα emission more visible even in a highly neutral universe. Thus, explaining the drop in $f_{Ly\alpha}$ reported in these surveys would require a more neutral universe than we have argued (Dijkstra et al. 2011), strengthening the conclusions of Schenker et al. (2012) and Pentericci et al. (2011). However, while strong winds are observed from LBGs at $z \sim 3$ (e.g. Shapley et al. 2003), the outflow speed – and hence the redshift imparted to Lyα photons – may be substantially smaller around the smaller mass galaxies typical near $z \sim 7$. It is presently unclear how prevalent strong winds are from $z \sim 7$ LBGs.

Clearly, a better understanding of the relationship between LBGs and LAEs should help in interpreting current and future Lyα fraction measurements. Along these lines, Dayal and Ferrara (2012) have simulated LBGs and LAEs at $z \sim 6$, 7 and 8. They conclude that LAEs are a diverse subset of LBGs. While the faintest LBGs do not have Lyα emission, LAEs are found distributed throughout all other categories of LBGs. Similarly, Forero-Romero et al. (2012) model the relationship between LBGS and LAEs in the range $5 \leq z \leq 7$, concluding that, in order to match the observations of Stark et al. (2011), the Lyα escape fraction must be inversely correlated with galaxy luminosity. Further observational and theoretical work should help strengthen our understanding of the precise relationship between these two galaxy populations.

2.5 Conclusions

In order to summarize our findings and put them in the larger context of our current understanding of the EoR, we use the results of Fig. 2.4 to compute the likelihood function for $\langle x_{\rm i} \rangle (z \sim 7)$ given the results of both Schenker et al. (2012) and Pentericci et al. (2011). Fig. 2.6 shows the resulting 68 and 95 percent confidence regions for $\langle x_{\rm i} \rangle$, as compared to constraints from Kuhlen and Faucher-Giguère (2012), which combine recent *WMAP*-7 measurements of the Thomson scattering optical depth, along with observations of the $z \sim 2-5$ Lyα forest, and UV galaxy luminosity function measurements. Although the central value of $\langle x_{\rm i} \rangle (z \sim 7)$ we infer from the $f_{Ly\alpha}$ observations is outside of the range implied by the other measurements, accounting for sample variance and other sources of uncertainty in the $f_{Ly\alpha}$ measurements, we find that these various observations are in fact in broad agreement with each other. Interestingly, we conclude that a fully ionized IGM is disfavoured by the $f_{Ly\alpha}$ measurements, although a highly neutral IGM ($\langle x_{\rm i} \rangle \leq\sim 0.5$) is not required. Taken together with spectroscopic observations of a $z = 7.1$ quasar from Mortlock et al. (2011), the case that existing measurements probe into the EoR is strengthening.

It is also interesting to note that recent and improved measurements of the UV galaxy luminosity function from the Ultra Deep Field (UDF) survey and Cosmic Assembly Near-Infrared Deep Extragalactic Survey (CANDELS) favour somewhat later reionization than in the Kuhlen and Faucher-Giguère (2012) analysis (Oesch et al. 2013; Robertson et al. 2013). For instance, extrapolating the measured luminosity functions down to $M_{\rm UV} < -13$, Robertson et al. (2013) favours $z \sim 7.5$ for the redshift at which the Universe is 50 percent neutral by volume (see their Fig. 5). These results are more easily harmonized with the preferred (central) value of $\langle x_{\rm i} \rangle (z \sim 7)$ inferred from the $f_{Ly\alpha}$ observations.

We also find that the constraints from the Lyα fraction measurements depend somewhat on the model relating the properties of the LBGs and LAEs. In our fiducial model (shown here in Fig. 2.6), the intrinsic REW of Lyα emission from LBGs is anti-correlated with UV luminosity. In models without this anti-correlation, the lower Lyα fractions

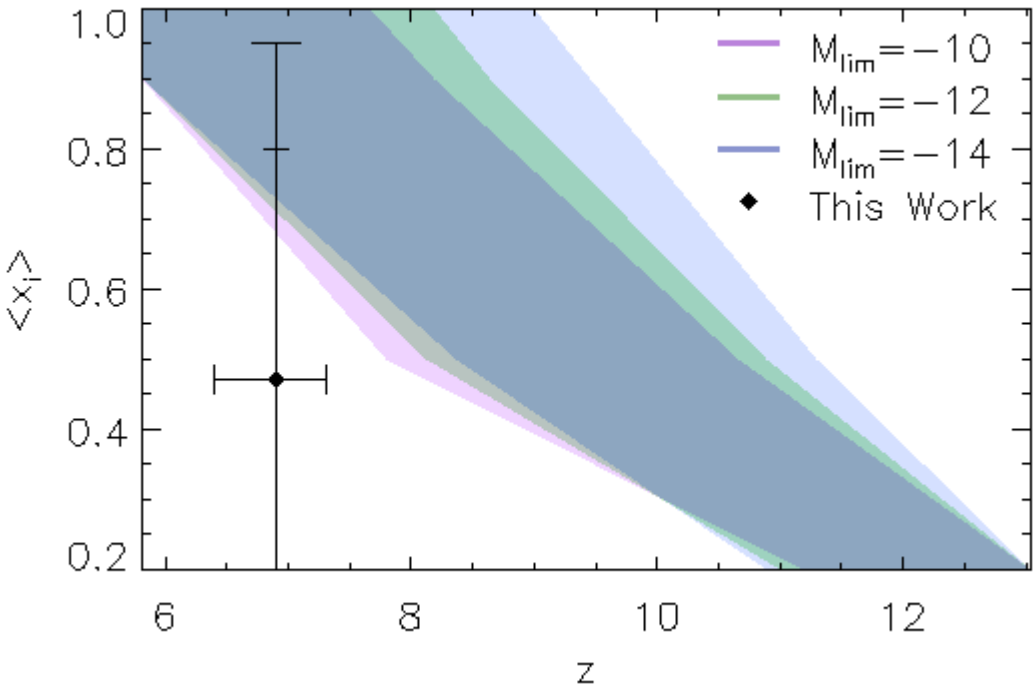

Figure 2.6: The reionization history inferred from a variety of observations. The shaded band shows constraints on the ionization fraction as a function of redshift from Kuhlen and Faucher-Giguère (2012), which come from combining *WMAP*-7 measurements of the optical depth to Thomson scattering, the intensity of the UV background inferred from the $z \sim$ 2-5 Lyα forest, and measurements of the UV galaxy luminosity function at high redshift. The luminosity functions are extrapolated down to faint luminosities; the different shaded bands show the dependence on the limiting UV magnitude ($M_{\rm lim}$) out to which this extrapolation is carried out. The point with error bars shows the constraint we infer from the Lyα fraction measurements of Schenker et al. (2012) and Pentericci et al. (2011). The lower vertical error bar shows the 68 percent confidence interval, while the upper vertical error bar shows the 95 percent confidence interval. The horizontal error bar gives the redshift uncertainty for the LBGs used in these measurements.

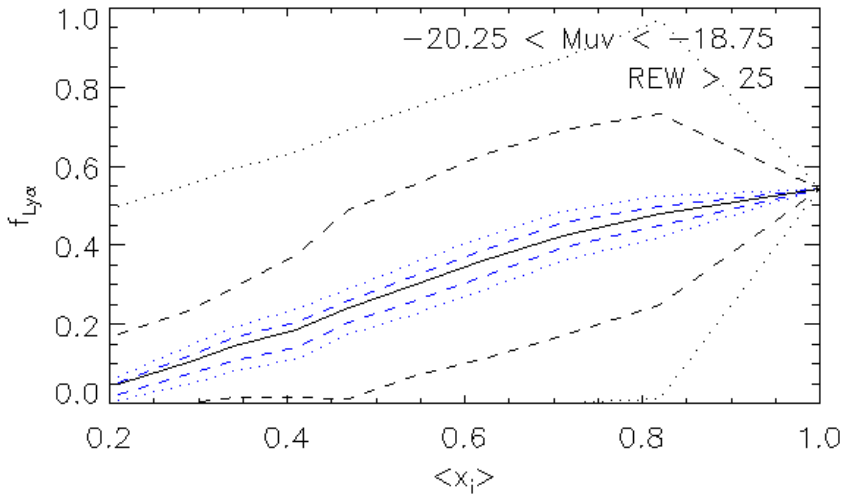

Figure 2.7: The impact of improved sampling of the Pentericci et al. (2011) fields on the sample variance error. Pentericci et al. (2011) looked for Lyα emission from two faint LBGs. This leads to the large sample variance, shown in the black dashed and dotted lines, at 68 and 95 percent, respectively (identical to the lines in the top panel of Fig. 2.3). The blue dashed and dotted lines show that the sample variance would dramatically shrink if a survey was done to search for Lyα emission from *all* of the LBGs in their fields.

among UV bright galaxies at both $z \sim 7$ and at lower redshifts ($z \sim 4-6$) are hard to understand.

Bolton and Haehnelt (2013) recently pointed out another effect that may also help reconcile the Lyα fraction measurements with other constraints on reionization. These authors suggest that the observed drops in the Lyα fraction towards high redshift may be driven mostly by strong evolution in the number of dense, optically thick absorbers in the vicinity of the observed LBGs, rather than reflecting prominent changes in the ionization state of the diffuse IGM. This effect would not be well captured in the simulations used in our analysis, since these dense absorbers are notoriously difficult to resolve in large volume reionization simulations. This effect would also, however, presumably show large field-to-field variations, similar to the spatial variations in the attenuation from the diffuse gas studied here. More detailed models will likely be necessary to disentangle the relative impact of optically thick, circumgalactic absorbers and the more diffuse IGM considered here.

More importantly, the prospects for improved observations are very good, and especially tantalizing given the current hints that $z \sim 7$ observations may probe into the EoR. Larger and deeper surveys for LBGs and LAEs should help clarify the interpretation of current observations. In particular, as shown in Fig. 2.7, observing down to $M_{UV} = -18.75$ over an area as large as that observed by Pentericci et al. (2011) would be enough to greatly reduce the effects of sample variance. Fully sampling such an area, however, would mean spectroscopically observing on the order of 100s of LBGs, looking for Lyα emission. However, even just sampling five galaxies per field (20 galaxies total) is enough to 'fill in' the sparse sampling and reduce the sample variance by a factor of 2. Alternatively, the use of narrow band filters to select the LBGs that are also LAEs should make observing 100s feasible.

The spatial fluctuations in the Lyα fraction studied here are presently a nuisance; however, they should *ultimately provide a very interesting and distinctive signature of reionization*, provided they can be mapped out over large volumes of the Universe. Map-

ping these fluctuations will require both larger fields of view and more fully sampled fields than currently available. This should, nonetheless, be possible using upcoming observations from the Hyper Suprime-Cam on the Subaru telescope, which will observe LAEs out to $z = 7.3$ over more than 5 deg^2.

Chapter 3

Probing Reionization with Upcoming Observations of Lyman-α Emitters and Lyman-break Galaxies from the Hyper-Suprime Camera

3.1 Introduction

The Epoch of Reionization (EoR) is the time period during which early generations of galaxies and accreting black holes form and gradually photoionize neutral hydrogen in the surrounding intergalactic medium (IGM). Since the EoR marks the birth of the first galaxies, it is important for our understanding of the history of structure formation, and has been the focus of much work over the past decade. This has led to significant progress in determining when reionization took place. Although a wide range of models are still viable, recent observations broadly suggest a later end to reionization than previously thought. For example, measurements of the polarization of the cosmic microwave background on large angular scales determine the probability that a CMB photon scatters off of free electrons during and after reionization. While measurements from nine years of

the Wilkinson Microwave Anisotropy Probe (WMAP) found an optical depth to electron scattering of $\tau_e = 0.088 \pm 0.014$ (Hinshaw et al. 2013), the most recent determination using data from the Planck High Frequency Instrument gives $\tau_e = 0.058 \pm 0.012$ (Planck Collaboration et al. 2016). In the unrealistic, but nevertheless illustrative case of instantaneous reionization, these measurements translate into reionization redshifts of $z_{reion} \simeq 10.5 \pm 1.1$ and $z_{reion} \simeq 8.8 \pm 0.9$, respectively. In the more physically plausible case that reionization is gradual, the process should complete at lower redshift than these instantaneous values. While the polarization data determine mostly just an integral over the entire ionization history, and systematic uncertainties in the Planck measurements are still large, the implied later end to reionization is supported by other observations. For example, spectra of the highest redshift quasar found to date, at $z = 7.1$, show evidence for damping wing absorption just redward of the Lyα line, possibly indicating significantly neutral gas in the IGM at this redshift (Mortlock et al. 2011; Simcoe et al. 2012). In addition, measurements of the Lyα fraction $f_{Ly\alpha}$, the fraction of Lyman Break Galaxies (LBGs) that are also Lyα emitters (LAEs), show a gradual rise from $z \sim 2$ to $z \sim 6$, followed by a pronounced drop from $z \sim 6$ to $z \sim 7$ (Pentericci et al. 2011; Schenker et al. 2012; Ono et al. 2012; Caruana et al. 2012), and a continued decline out to $z \sim 8$ (Schenker et al. 2014). The decreasing Lyα fraction may also indicate that much of the $z \sim 7$ IGM volume is filled with neutral hydrogen (e.g Mesinger et al. 2015). Furthemore, UV galaxy luminosity function measurements show declines toward high redshift (e.g. Bouwens et al. 2015). Although the precise implications depend on the escape fraction of ionizing photons, on extrapolations to fainter luminosities than observed, and on the spectrum of the ionizing galaxies, these results are more comfortable with a late end to reionization (Robertson et al. 2015). On the other hand, observations of transmission through the Lyα forest toward high redshift quasars and gamma ray bursts indicate that reionization completed by $z \leq 6$ (Fan et al. 2006; Bolton et al. 2011; Chornock et al. 2013; McGreer et al. 2015), although a small fraction of the IGM volume at $5.5 < z < 6$ may still contain remaining islands of significantly neutral hydrogen (Malloy and Lidz 2015).

Taken together, the observations suggest that reionization completed sometime between $5.5 < z < 7$.

This redshift range is nicely bracketed by observations of LAEs which target narrow redshift windows (in between bright night sky emission) at $z \sim 5.7$, 6.6, and $z \sim 7.3$, and significantly expanded LAE data sets are forthcoming. These new observations may allow more definitive determinations of the evolution of the volume-averaged ionization fraction over this interesting redshift range. Of particular interest are measurements of the spatial clustering of LAEs. Current theoretical models predict that reionization is a patchy process: ionized regions form first, and grow more quickly, around large-scale overdensities, while less dense regions contain smaller ionized regions and also remaining neutral gas (e.g. Furlanetto et al. 2004b; McQuinn et al. 2007b). The Lyα photons from an LAE at the center, or far edge, of a large ionized region redshift significantly before reaching neutral gas at the bubble wall, and thereby avoid scattering in the Lyα line. On the other hand, Lyα photons from LAEs in smaller ionized regions are unable to redshift out of the line before reaching neutral gas; they tend to be scattered out of the line of sight and rendered unobservable. In other words, observable LAEs should preferentially live in large ionized regions, and show strong clustering since these regions trace rare, overdense peaks in the density field. Consequently, as LAE observations probe back into the EoR, the observed clustering of LAEs should show a distinctive enhancement (Furlanetto et al. 2004a; McQuinn et al. 2007a; Mesinger and Furlanetto 2008; Ouchi et al. 2010; Jensen et al. 2013). The enhanced LAE clustering signature should be accompanied by a decline in the average abundance of LAEs, but the clustering enhancement can be dramatic and harder to mimic with evolution in the intrinsic properties of the galaxies themselves (e.g. McQuinn et al. 2007a).

The first precise measurements of LAE clustering at plausible EoR redshifts will soon be enabled by the Hyper Suprime Cam (HSC), a new instrument on the Subaru telescope. These observations will reach out to $z \simeq 7.3$ and, crucially, extend over several square degrees on the sky. The primary goal of the present chapter is to forecast the statistical

precision of these measurements, and to consider the resulting constraints on the ionization state of the IGM. The same survey will also detect many LBGs, and we demonstrate that this provides a useful comparison sample to contrast with the detected LAE populations. In particular, following the redshift evolution of both LAEs and LBGs should help isolate evolution caused by changes in the ionization state of the IGM from variations in the intrinsic properties of the galaxy populations. Furthermore, we explore a few different possible statistics; their combination may be used to most cleanly extract any signatures of incomplete reionization from the HSC observations. Specifically, we consider measurements of the abundance, power spectra, and void distribution of the LAEs and LBGs at different redshifts, as well as LAE-LBG cross spectra. Finally, we explore the impact of contamination from foreground interlopers and develop some strategies to mitigate this contamination. Our detailed statistical forecasts, comparisons between LAEs and LBGs, and consideration of foreground interlopers distinguish this work from previous theoretical studies that also considered the prospects for HSC's measurements (Jensen et al. 2014; Sobacchi and Mesinger 2015; Hutter et al. 2015).

This chapter is structured as follows. §3.2 lays out our method, while §3.3 describes the relevant HSC survey specifications. In §3.4 we construct mock HSC observations and measure the statistical properties of our simulated galaxy populations. §3.5 considers the impact of additional practical complications that may impact the HSC data sets. Finally, §3.6 summarizes our conclusions. Throughout this chapter, we assume a Λ cold dark matter (ΛCDM) model with $n_{\rm s} = 1$, $\sigma_8 = 0.8$, $\Omega_{\rm m} = 0.27$, $\Omega_\Lambda = 0.73$, $\Omega_{\rm b} = 0.046$ and $h = 0.7$. These parameters are broadly consistent with recent results from the Planck collaboration (Planck Collaboration et al. 2014). We report all magnitudes in the AB system (Oke 1974).

3.2 Method

In order to forecast the ability of HSC to make these measurements, we start with the reionization simulations of McQuinn et al. (2007a,b). These simulations provide models of the spatial distribution of neutral gas during the EoR, as well as the underlying matter distribution and dark matter halo populations. The reionization calculations are post-processed on top of a 1024^3 particle, 130 co-moving Mpc h^{-1} dark matter simulation run with GADGET-2 (Springel 2005). In a further post-processing step, we populate a fraction of the dark matter halos in the simulation with LBGs and LAEs. We attenuate the Lyα emission based on the surrounding neutral hydrogen. These post-processing steps are described in more detail below and in Taylor and Lidz (2014), §2 of this work.

In order to populate our simulated dark matter halos with LBGs, we start from a very simple model connecting host halo mass, $M_{\rm halo}$, and star formation rate, $\dot{M}_\star$, as in Stark et al. (2007):

$$\dot{M}_\star = \frac{f_\star(\Omega_{\rm b}/\Omega_{\rm m})M_{\rm halo}}{t_{\rm LT}}. \tag{3.1}$$

Here $f_\star$ is the efficiency with which baryons are converted into stars and $t_{\rm LT}$ is the time scale for star formation. We use Stark et al. (2007)'s best fit values of $f_\star = 0.16$ and $t_{\rm LT} = 0.25 * t(z)$, where $t(z)$ is the age of the Universe, for LBGs at $z \simeq 6$. Adopting a Salpeter Initial Mass Function, the star formation rate is connected to the UV luminosity by (Madau et al. 1998):

$$L_{1500} = 8.0 \times 10^{27} \frac{\rm erg}{\rm Hz\ s} \left[\frac{\dot{M}_\star}{1M\odot/{\rm yr}}\right], \tag{3.2}$$

at a rest frame wavelength of $\lambda = 1500$ Å. Provided star formation occurs mostly in short, constant bursts, only a fraction of the halos will host LBGs at any given cosmic time. It is common to fix the fraction of dark matter halos that are actively forming stars according to the duty cycle of star formation implied by Equation 3.1, $t_{LT}/t(z)$. However, we find a better match to the observed abundance and clustering of $z \sim 7$ LBGs (Bouwens et al. 2011), and the observed Lyα fraction (Schenker et al. 2012; Pentericci et al. 2011; Ono et al. 2012; Caruana et al. 2012), if we adopt a slightly different fraction of host

halos that are "active" as LBGs. We therefore fix this fraction to be $1/6$, which is in any case similar to the star formation duty cycle of $t_{LT}/t(z) = 0.25$ in the model of Equation 3.1. By varying which halos we (randomly) choose to host LBGs, we produce six non-overlapping samples, which can be used to reduce the modeling uncertainty introduced from the finite size of our simulated samples.

Each simulated galaxy is assigned Lyα emission, as characterized by the Rest-frame Equivalent Width (REW) of the emission line. Following Dijkstra et al. (2011), we draw the REWs from an exponential distribution: $\mathrm{P(REW)} = \exp[-\mathrm{REW}/\mathrm{REW_c}]/\mathrm{REW_c}$ with a central REW of $\mathrm{REW_c} = 50$ Å. This choice is motivated by measurements of REW distributions from lower redshift galaxy samples (Gronwall et al. 2007; Blanc et al. 2011), which are well fit by exponential distributions. In assigning REWs to simulated galaxies, we further assume that the REW and galaxy UV luminosity are anti-correlated. Specifically, the UV luminosities and REWs of the galaxies are divided into ten, rank-ordered bins, and the weakest Lyα lines are assigned to the UV-brightest galaxies. As detailed in §2, we choose an anti-correlation model because it is physically plausible–fainter galaxies may have less dust, allowing more Lyα emission to escape–and because it is supported by a host of observational studies (Shapley et al. 2003; Stark et al. 2010; Ando et al. 2006; Ouchi et al. 2008; Vanzella et al. 2009; Balestra et al. 2010).

In this work, we forego constructing detailed models for the Lyα emission line profiles emerging from each of our mock LAEs. In reality, the Lyα emission line profiles depend on a variety of factors including the distribution of neutral hydrogen and dust in the LAEs' interstellar and circumgalactic media, on large scale infall and outflows towards the LAEs, and on enhancements to the background photoionization rate near the host galaxy (see, for example, Santos 2004; Dijkstra et al. 2007; Zheng et al. 2010; Verhamme et al. 2012; Yajima et al. 2012; Duval et al. 2014). A number of recent works have developed multi-scale simulation techniques in effort to adequately model both the intrinsic Lyα line profile leaving the galaxy, as well as the subsequent scattering in the IGM (e.g. Zheng et al. 2010; Jensen et al. 2013; Choudhury et al. 2015; Mesinger et al.

2015; Kakiichi et al. 2015). Although refinements along these lines will be necessary to compare with the actual HSC data, the simplified approach considered here should be adequate in forecasting the precision of upcoming measurements, while including the main effects of patchy reionization. Here we assume that the complexities of Lyα transfer intrinsic to each source are captured by sampling from the REW distribution. We assume that resonant absorption in the IGM is also captured in this sampling. In the absence of outflows and infalling material, resonant absorption would absorb the blue half of each line, without impacting the photons initially redward of Lyα , but reality may be significantly more complex, as explored in the references above. The most significant limitations of our approach are that we assume the intrinsic REW distribution does not itself evolve with redshift and ionization state, and we ignore any large scale spatial variations in this distribution (see e.g. Zheng et al. 2010).

The intrinsic REWs and LAE luminosities are then attenuated based on the distribution of surrounding neutral hydrogen as modeled in the McQuinn et al. (2007a) reionization simulations. For simplicity, we calculate only the damping wing optical depth at the center of the Lyα line, $\tau_{\rm DW}$, and attenuate each mock LAE according to $e^{-\tau_{\rm DW}}$. Using the center of the line, rather than the full line profile, should allow us to model the impact of patchy reionization and determine which simulated LAEs are attenuated out of the sample; McQuinn et al. (2007a) discusses this approximation further. Note that, as in §2, we consider a range of ionization fraction models by drawing the ionization fields from different redshift outputs of the same reionization simulation, rather than running new calculations for each different reionization history we aim to study. As discussed in McQuinn et al. (2007b), this should be a good approximation for our present purposes.

3.3 HSC details

Now that we have a recipe for populating simulated data cubes with LBGs and LAEs, we can further tailor the mock data to match the specifications of upcoming HSC surveys.

HSC has a very large field of view, 1.5 degrees in diameter, and their survey plan is structured as a tiered or wedding cake approach. It is their deepest level, the Ultradeep layer, with which we concern ourselves. This tier, covering 3.5 deg^2 – which is just two fields of view across – is observed in 5 broadband filters (*grizy*) and 3 narrow band filters (NB816, NB921, NB101). The broad band filters will allow detection of LBGs out to $z \sim 7$ (z-dropouts) down to a limiting magnitude of 26.3. The narrow band filters are selected to detect LAEs at $z \sim 5.7, 6.6, 7.3$. The limiting magnitude for detecting LAEs at these redshifts are 26.5, 26.2, and 24.8, respectively (HSC Science Collaborations 2012). Since the HSC survey spans 3.5 deg^2 or 206 co-moving Mpc h^{-1} on a side at $z \sim 7$, it should be able to detect thousands of LAEs and LBGs across its wide survey area and is therefore well-suited for measuring the abundance and clustering of these galaxies. Provided the survey probes into the EoR, this survey area should be sufficient to span many different ionized and neutral regions, probing inhomogeneities in the reionization process.

3.3.1 Modeling HSC Observations

The total luminosity in the Lyα line for each galaxy may be determined from its REW and specific UV luminosity, according to (Dijkstra and Wyithe 2012):

$$L_\alpha = C \times \mathrm{REW} \times \mathrm{L_{UV,\nu}}, \tag{3.3}$$

where $L_{UV,\nu}$ is the continuum UV luminosity density, and $C \equiv \frac{\nu_\alpha}{\lambda_\alpha}(\frac{\lambda_{UV}}{\lambda_\alpha})^{-\beta-2}$, in which $\nu_\alpha = 2.47 * 10^{15}$ Hz, $\lambda_\alpha = 1216$ Å, and $\lambda_{UV} = 1700$ Å, the wavelength at which the UV continuum flux density is measured. For β, we use Dijkstra and Wyithe (2012)'s best fit value of -1.7, which is broadly consistent with Stark et al. (2010); Furusawa et al. (2016); Jiang et al. (2016).

In order to model the HSC observations, we implement the HSC limiting magnitude cuts specified above and further require that for a galaxy to be considered a bona-fide LAE, it must have a minimum rest frame equivalent width of REW ≥ 20 Å (as is common

practice, e.g. Stark et al. 2011). As we will discuss further in §3.5.1, this serves to screen out low redshift line-emitting galaxies that may be mistaken for higher redshift LAEs.

HSC's use of narrow and broad bands to detect galaxies means that LAEs and LBGs are detected over different depths. In order to best mimic their observations, we limit the depth of the simulation cube to match the depth of the observations. The LAE narrow band depth, calculated from the width of the filter, is roughly 20 Mpc h^{-1} at each of the redshifts of interest. The broad bands are more complicated. From other surveys (Ouchi et al. 2009) we expect z-dropouts to be distributed over a range of redshifts, from $z \sim 6.4$ to $z \sim 7.3$, peaking at $z \sim 6.9$ (see their Fig. 6, reproduced here as Fig. 1.14). We simplify this by assuming a top-hat window function, and find that a top-hat of width 100 Mpc h^{-1} at $z \sim 7$ reproduces the area under the observed redshift distribution. We use this width as the depth of the LBG survey field. Note that their dropout out filter, z', is different from the z band used by HSC; they are similar enough, however, for this to be a reasonable approximation.

3.4 Mock Observations

We now turn to analyze the statistical properties of the mock galaxy populations in our simulated samples. We discuss several different statistical measurements that may be performed by the HSC and consider their utility for constraining the ionization history.

3.4.1 Galaxy Abundance

The first observable to consider is the redshift evolution in the average abundance of both LAEs and LBGs. As the observations probe into the EoR, one expects the observed abundance of LAEs to drop: neutral hydrogen leftover in the surrounding IGM will scatter Lyα photons out of the line of sight and attenuate galaxies out of the observed sample. As the neutral fraction increases, progressively fewer LAEs should be observed. For example, if reionization is complete by $z \sim 5.7$, but incomplete at $z \sim 6.6$ and $z \sim 7.3$, then one ex-

pects a steady decline in the average abundance of LAEs across HSC's three narrow band filters. One would expect less redshift evolution in the detected LBG populations since these galaxies will be less influenced by the ionization state of the surrounding IGM (see §3.5 for further discussion). As these measurements are sharpened, one should compare the observed luminosity functions – i.e., abundance as a function of observed luminosity – with model predictions, but here we instead consider only the overall abundance of galaxies above the anticipated survey flux limits. A more refined star formation model than considered here is likely required to make robust predictions of the full LAE and LBG luminosity functions.

Fig. 3.1 shows our model predictions for the average abundance of LAEs and LBGs as a function of redshift as observed by HSC. The expected abundance of LAEs depends on the model volume-averaged ionization fraction. For illustration, the grey band in the figure indicates the model LAE abundance for a range of plausible values of the ionized fraction at different redshifts: the band assumes $\langle x_i \rangle = 1$ at $z \sim 5.7$, and spans $\langle x_i \rangle = 0.7$ to 1 at $z \sim 6.6$, and $\langle x_i \rangle = 0.3$ to 1 at $z \sim 7.3$. The red squares show the LAE abundance for a fiducial ionization history in which $\langle x_i \rangle = 1$ at $z \sim 5.7$, $\langle x_i \rangle = 0.82$ at $z \sim 6.6$ and $\langle x_i \rangle = 0.71$ at $z \sim 7.3$. The figure shows that our LBG and LAE models are broadly consistent with current measurements, although the LBG model somewhat underproduces the observed abundance from Bouwens et al. (2015). Although we adjusted the LBG duty cycle in part to match these observations, we also aim to match the observed LBG clustering and the observed Lyα fraction: the best overall match we found underproduces the abundance a little bit.

Considering the redshift evolution, first note that there is a small drop-off towards high redshift in both galaxy populations even in fully ionized models; this mostly arises because the surveys are shallower at high redshift. More interesting, however, is the expected decline in the LAE abundance that occurs in models in which the IGM is partly neutral at $z \sim 6.6$ and $z \sim 7.3$. This decline can be compared with the present measurements from Konno et al. (2014) and Matthee et al. (2015). These LAE abundance

measurements are consistent with the IGM being fully ionized at $z \sim 6.6$ and $z \sim 7.3$, but also with reionization being incomplete at these redshifts. In the context of our model, the Konno et al. (2014) measurements imply $1-\sigma$ lower limits on the ionized fraction of 0.84 at $z \sim 6.6$ and 0.46 at $z \sim 7.3$. Fortunately, the error bars should tighten considerably with HSC, due to expected higher number of galaxies detected. Of course, this number depends on the ionized fraction, but we should expect the error bars to tighten by an order of magnitude for LAEs at $z \sim 6.6$.

In terms of the overall total number of LBGs and LAEs that HSC should observe (over their Ultradeep 3.5 deg^2 field), we anticipate around 2,400 LBGs in the broad band around $z \sim 5.9$, and 1,100 LBGs near $z \sim 6.9$. For the range of ionized fractions spanned by the grey bands, we expect 3,000 LAEs at $z \sim 5.7$, between 1,500 and 2,500 at $z \sim 6.6$ and between 5 and 330 at $z \sim 7.3$.

Of course, evolution in the intrinsic properties of LAEs over the redshift range spanned by the HSC narrow bands may also lead to evolution in their average abundance. For example, the abundance of neutral hydrogen in the outskirts of the LAE host halos – that is, in the circumgalactic medium – may evolve and become more prominent at high redshift if the ionizing background is small just after reionization and increases towards lower redshift. This could lead to evolution in the average LAE abundance even if the diffuse gas in the low-density IGM remains highly ionized throughout the redshift range spanned by the HSC (e.g. Bolton and Haehnelt 2013). We consider this evolution to be "intrinsic" as it relates to changes in the properties of gas in the LAE host halos, rather than in the surrounding diffuse IGM. Our simple model for the LAEs does not capture the complex problem of Lyα scattering in the circumgalactic medium. Even if the interpretation of the abundance evolution may be somewhat subtle, it should nevertheless be part of the body of evidence regarding the ionization state of the $z \geq 6$ IGM, especially when paired with other clustering-based tests where evolution into the EoR should be less easily mimicked by intrinsic variations in a completely ionized IGM.

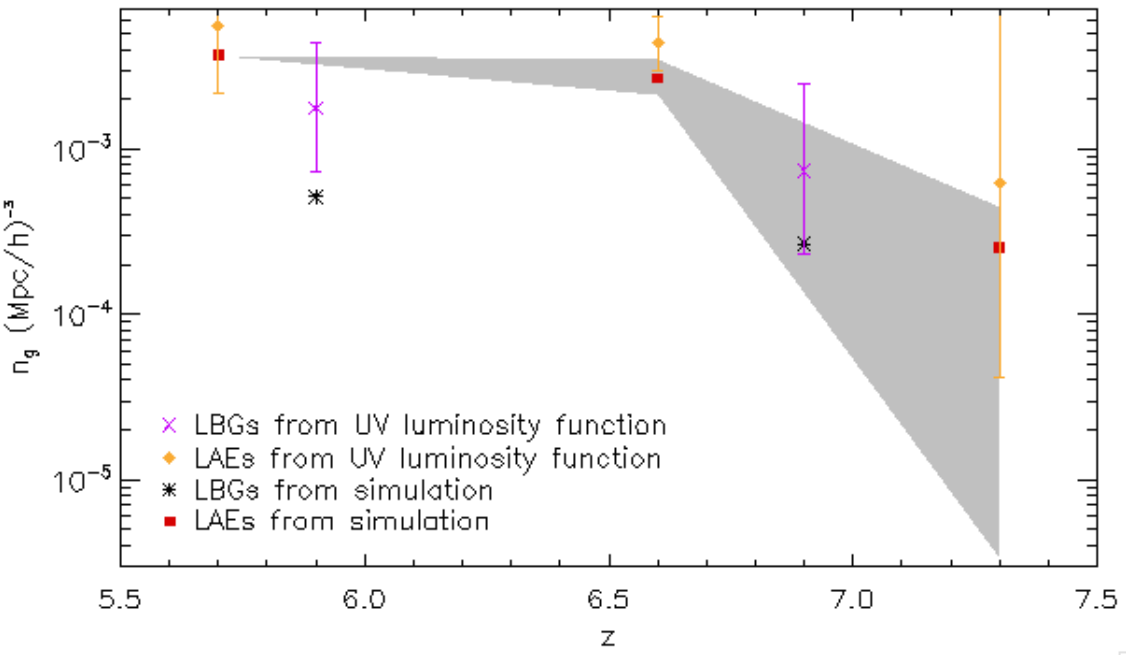

Figure 3.1: The number density of LAEs and LBGs that are observable by HSC. The black stars show the abundance of model LBGs above the limiting magnitudes in the HSC broad band filters, centered near $z \sim 5.9$ and $z \sim 6.9$, while the magenta stars and error bars show the expected abundance from recent UV luminosity function measurements (Bouwens et al. 2015). The grey band shows the abundance of LAEs above the HSC narrow band limiting magnitude cuts at $z \sim 5.7, 6.6$, and 7.3 for a range of different ionized fraction models. The band assumes $\langle x_i \rangle = 1$ at $z \sim 5.7$, $\langle x_i \rangle = 0.7$ to 1 at $z \sim 6.6$, and $\langle x_i \rangle = 0.3$ to 1 at $z \sim 7.3$. The red squares show the abundance for a fiducial ionization model in which $\langle x_i \rangle = 1$ at $z \sim 5.7$, $\langle x_i \rangle = 0.82$ at $z \sim 6.6$, and $\langle x_i \rangle = 0.71$ at $z \sim 7.3$. The orange points with error bars show current LAE abundance measurements from Konno et al. (2014). The figure illustrates both broad consistency of our model with current measurements, and it also quantifies how the average abundance of LAEs may evolve as the observations probe into the EoR.

3.4.2 Lyα Fraction

HSC can also perform a modified version of the Lyα fraction test discussed in the introduction (Pentericci et al. 2011; Schenker et al. 2012; Ono et al. 2012; Caruana et al. 2012; Schenker et al. 2014; Furusawa et al. 2016). This has the advantage of being less sensitive to intrinsic evolution in the underlying galaxy populations than the luminosity functions themselves; intrinsic evolution should in part divide out when taking the ratio of the abundance of the two populations. As mentioned in the introduction, current measurements show a gradual rise in the Lyα fraction from $z \sim 2-6$ – this is perhaps a consequence of a declining dust abundance across this redshift range – followed by a sharp drop above $z \geq 6$. An important virtue of HSC here is its large field of view, which is much larger than the size of the ionized regions during the EoR. This helps guard against sample variance, which may impact previous Lyα fraction measurements (Taylor and Lidz (2014), reproduced here as §2) since these surveys were conducted over relatively small fields.

Previous Lyα fraction test studies have performed follow-up spectroscopy on photometric LBG candidates. Here we consider a variant, which does not require follow-up spectroscopy. Specifically, we consider the projected distribution of LAEs and LBGs and their ratio across a mock HSC field of view ($\frac{N_{LAE}}{N_{LBG}}$), where the LAEs and LBGs are selected solely on the basis of the HSC narrow and broad band filters. We can consider this fraction both for LAEs selected from the $z \sim 5.7$ and $z \sim 6.6, 7.3$ narrow band filters, when combined with LBGs selected from the $z \sim 5.9$ and $z \sim 6.9$ broad band filters respectively. Since the broad and narrow band filters only partially coincide in wavelength, the selected LAE and LBG populations only partly overlap in redshift. That is, only a fraction of the galaxies selected by the two techniques are the same sources, and the two populations only partly trace the same large scale structure. Nevertheless, the ratio should show interesting redshift evolution as one probes back into the EoR. In addition, this fraction should be modulated by the patchiness of the reionization process. Essentially, the sample variance that was previously a nuisance for Lyα fraction measurements (Taylor and Lidz (2014), reproduced here as §2) in fact provides an interesting *signature*

of reionization, accessible to LAE/LBG surveys with large fields of view like the HSC. In principle, the scale-dependence of these variations provides information about the patchiness of reionization and the physical processes that drive it. Although the $\frac{N_{LAE}}{N_{LBG}}$ fraction considered here is less direct than the pure Lyα fraction test which considers only Lyα emission from previously detected LBGs, it can be measured from the upcoming data without expensive spectroscopic follow-up.

To illustrate, we use our mock projected $z \sim 6.6$ LAE and $z \sim 6.9$ LBG samples, and tabulate the number of LAEs and LBGs across each of 256^2 simulation cells. We estimate the fraction $\frac{N_{LAE}}{N_{LBG}}$ in each cell, and smooth this with a 2D Gaussian of width $\sigma = 6.09$ Mpc h^{-1}, corresponding to 24 simulation cells, and comparable to the size of the ionized regions in the simulation. In the event that there are no LBGs in a cell, the fraction is set to zero (before smoothing). The results of this calculation are shown in Fig. 3.2 for a model with an ionized fraction of $\langle x_i \rangle = 0.71$. In order to understand how this fraction is modulated by patchy reionization, we also estimate the fractional attenuation of the LAEs in each simulated cell, $\delta N/N$, where δN is the number of LAEs that fall below the HSC limiting magnitude cut after IGM attenuation. The attenuation fraction is shown by the grayscale in the left hand side of the figure, while the colored contours in the same panel show the abundance fraction, $\frac{N_{LAE}}{N_{LBG}}$. For further comparison, we show the projected ionization field from the same slice in the right hand panel of the figure. Visual comparison suggests that $\frac{N_{LAE}}{N_{LBG}}$ is a reasonable tracer of the relative LAE attenuation, with areas of high Lyα fraction having little attenuation, while low Lyα fraction regions trace heavily attenuated regions. The attenuation fraction is, in turn, a reasonable proxy for the projected ionization fraction.

The fraction shows interesting variations and is a good tracer of the underlying ionization field, but we caution that this is imperfect. First, note that the HSC LBG sample will have a significantly lower abundance than the LAE sample (at least for the ionized fraction assumed here). Since regions with no LBGs are assigned zero fraction, there will be some ionized regions that host LAEs but have zero fraction because no LBGs are detected

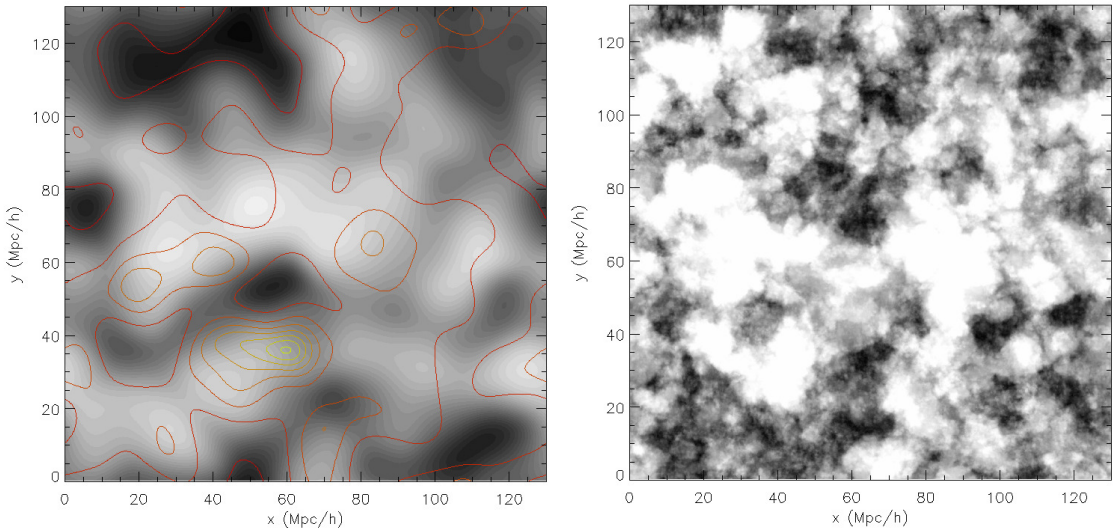

Figure 3.2: Spatial variations in the the ratio of the projected abundance of LAEs to LBGs. *(Left)* The grayscale shows variations in the fraction of LAEs in a region that are attenuated out of the mock LAE sample by scattering from neutral hydrogen in the surrounding IGM. The white regions correspond to zero attenuation, while the dark regions show attenuation fractions of 0.97 and so the LAEs are almost completely attenuated in these regions. The model is at $z \sim 6.6$ and $\langle x_i \rangle = 0.71$. The depth of the simulated slice corresponds to the width of the $z \sim 6.6$ HSC narrow band filter, while the other dimensions are 130 co-moving Mpc h^{-1} on a side, slightly smaller than the HSC Ultradeep field of view (206 Mpc h^{-1}). The colored contours show the smoothed fractional abundance of LAEs to LBGS, $\frac{N_{LAE}}{N_{LBG}}$, with the contours starting at 0.31 and increasing towards brighter colors with a step size of 1.25. This ratio can be larger than unity, because some of the LAEs are not also LBGs. This ratio traces fairly well, but imperfectly, the regions where LAEs are less attenuated. *(Right)* For comparison, this shows the projected ionization field in the same region and averaged over the depth of the LAE narrow band. The fraction $\frac{N_{LAE}}{N_{LBG}}$ is a reasonably good proxy for the ionized fraction, but there are some differences owing to our random draws from the REW distribution and clustering in the LBG populations.

in the region. Next, partly neutral patches can have high fractions: this is especially the case because of the empirically-motivated anti-correlation assumed in our model between REW and UV luminosity. Some low UV luminosity galaxies in partly neutral regions have sufficiently strong Lyα emission to escape complete attenuation, even though much of their Lyα emission is scattered by surrounding neutral gas. This effect is most prominent in more neutral models than considered in Fig. 3.2. In these alternate more neutral models, only very strong Lyα emission lines suffice to escape being attenuated out of the sample. In the more likely case that a significant, yet incomplete, fraction of the IGM volume is ionized at $z \sim 6.6$, this diagnostic appears quite interesting, and may allow an estimate of the typical size of the ionized regions.

3.4.3 Galaxy Clustering

We turn now to consider the clustering of the LAEs and LBGs in our mock HSC survey, as quantified by their 2D power spectra. The 2D power spectrum is the Fourier transform of the angular two-point correlation function which is sometimes considered. As mentioned previously, the clustering should be modulated on large scales by patchy reionization, and these fluctuations are hard to mimic with intrinsic variations which will mostly be coherent on smaller spatial scales.

Fig. 3.3 shows the 2D power spectrum, plotted as $\Delta^2_{2D}(k_\perp) = \frac{k_\perp^2}{2\pi} P_{2D}(k_\perp)$, where P_{2D} is the two dimensional power spectrum (with units of (Mpc h^{-1})^2), for LBGs and LAEs at $z \sim 6.6$ and for a range of ionization fraction models. Here $\Delta^2_{2D}(k_\perp)$ is the usual contribution to the variance per logarithmic interval in transverse wavenumber, $k_\perp$. The results are averaged over six independent sets of mock galaxies from our simulation cube, in an effort to reduce noise in the estimates. For the fully ionized scenario, the amplitude and shape of the LBG and LAE power spectra are fairly similar. This is partly a consequence, however, of the differing depth of the window functions of the two surveys. The broader window function of the LBGs dilutes their clustering more than in the case of the LAEs, which have a narrower window function. More interesting, however, is that the

LAE clustering amplitude increases strongly in the more neutral models. This is the LAE EoR clustering enhancement, mostly driven by the patchy ionization effects mentioned previously (e.g. McQuinn et al. 2007a). Here we consider the statistical precision at which HSC can measure these effects.

Towards this end, we calculate the power spectrum error bars assuming Gaussian statistics for simplicity:

$$\sigma_{PS,2D}(k_\perp) = \left[\frac{1}{\bar{n}_g} + P_{gg}(k_\perp)\right]\sqrt{\frac{2}{N_m(k_\perp)}}, \tag{3.4}$$

where $\bar{n}_g$ is the average number of galaxies per unit survey area (with units of (Mpc h^{-1})$^{-2}$), and $N_m(k_\perp)$ is the number of Fourier modes that fit into the survey. This may be calculated as $N_m(k_\perp) = \frac{k_\perp \Delta k_\perp A}{2\pi}$, where A is the survey area in units of (Mpc h^{-1})^2 and $\Delta k_\perp$ gives the width of a wavenumber bin centered on wavenumber $k_\perp$. Here $P_{gg}(k_\perp)$ is the two dimensional, shot-noise subtracted power spectrum $P_{gg}(k_\perp) = P_{2D}(k_\perp) - \frac{1}{\bar{n}_g}$. The first term, $\frac{1}{\bar{n}_g}\sqrt{\frac{2}{N_m(k_\perp)}}$, is the error due to shot-noise; the second term, $P_{gg}(k_\perp)\sqrt{\frac{2}{N_m(k_\perp)}}$, is due to sample or cosmic variance. In the case of the 3.5 degree^2 Ultradeep HSC survey, $N_m(k_\perp)$ is 30 on the largest scales spanned by our simulation for the binning shown, while it reaches 1,500 on the smallest simulated scales. In practice, most of the signal to noise comes from values of $k_\perp \lesssim 2.0\ h$ Mpc^{-1}. For LAEs and LBGs, the shot-noise term dominates on all except the largest spatial scales. For reference, Fig. 3.3 shows the anticipated statistical error bars on the LBG measurements: we anticipate HSC to return precise measurements of the power spectra (or equivalently the angular correlation function) for the LAEs at $z \sim 6.6$ and for the LBGs at $z \sim 6.9$.

As an alternate description of the clustering, we can divide out by the density power spectrum (after shot-noise subtraction) and calculate the (scale-dependent) bias factor:

$$b(k_\perp) = \sqrt{\frac{P_{gg}(k_\perp)}{P_{\delta\delta}(k_\perp)}}, \tag{3.5}$$

where $P_{gg}(k_\perp)$ is the shot-noise subtracted 2D galaxy power spectrum, $P_{gg}(k_\perp) = P_{2D}(k_\perp) - \frac{1}{\bar{n}_g}$ with $\bar{n}_g$ is the projected number density of galaxies, and $P_{\delta\delta}(k_\perp)$ is the windowed, 2D

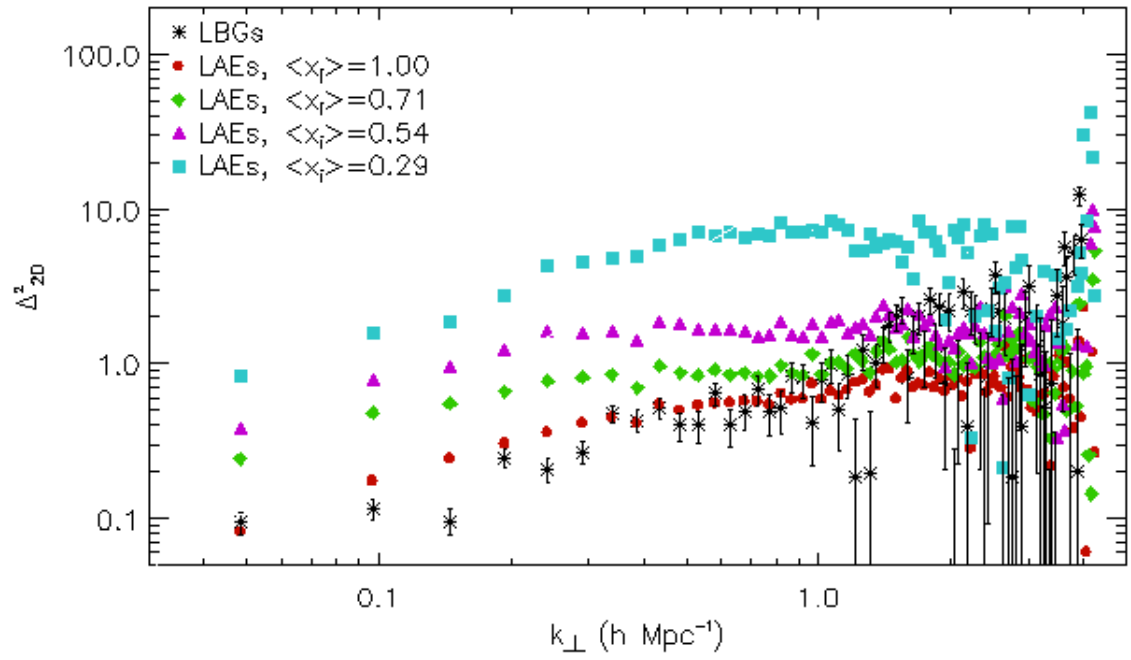

Figure 3.3: The 2D power spectra for LAEs and LBGs at $z \sim 6.6$ for a range of ionization fraction models. Here we plot $\Delta^2_{2D}(k_\perp)$ and show our forecast for the LBG error bars from the 3.5 degree^2 HSC survey. The LBG clustering is independent of the ionized fraction (see text), while the LAE clustering increases steeply as the ionized fraction drops. In comparing the LAE and LBG clustering it is important to keep in mind that the LBG window function is broader than the LAE one.

auto power spectrum of the density field, which we calculate directly from the simulations. This is calculated separately for each of the LAE and LBG windows: in order to keep our notation compact, we have not made this distinction explicit in Equation 3.5, but it is important to keep in mind that the windowed density power spectra for the LAE and LBG bias differ. In fact, an important advantage of $b(k_\perp)$ over the power spectrum itself is that the bias factor divides out the impact of the differing window functions, and so allows a more direct comparison between the LAEs and LBGs. In order to determine the bias factors from actual data, a model for the density power spectra will be required. As with our power spectrum measurements, we average over six independent mock realizations of the galaxy sample to reduce noise in the estimated bias factors. In order to account for scale-dependent biasing, we fit a quadratic function, $b_o + \alpha_1 \frac{k_\perp}{k_o} + \alpha_2 (\frac{k_\perp}{k_o})^2$ to $b(k_\perp)$ – which provides a good description of the scale dependence of the simulated bias factors – for each LBG and LAE model. Using the anticipated statistical error bars on the power spectrum from Equation 3.4, we can further calculate the expected error bars on each of the bias parameters, b_o, α_1, and α_2.

The results of these calculations are shown in Fig. 3.4. Here we have fixed the redshift to HSC's middle redshift bin at $z \sim 6.6$, perhaps the most promising bin for observing signatures of reionization, and varied the ionization fraction. The enhanced clustering with decreasing ionization fraction is clearly visible here, most prominently through the strong dependence of the constant biasing term, b_o, on the ionization fraction. In a fully ionized model, we expect the LAEs to be somewhat less clustered than the LBGs, with a smaller linear bias factor. This is the expected post-reionization behavior and reflects in part the observed anti-correlation between REW and UV luminosity. A number of studies have found that more luminous LBGs are more highly clustered than their lower luminosity counterparts (Kashikawa et al. 2006b; Lee et al. 2006; Overzier et al. 2006; Yoshida et al. 2008; Barone-Nugent et al. 2014), and that this holds true for a range of redshifts, from at least $z \sim 3$ to $z \sim 7$. Given the observed anti-correlation, the narrow band survey mostly selects LAEs that are faint LBGs, and are therefore less clustered

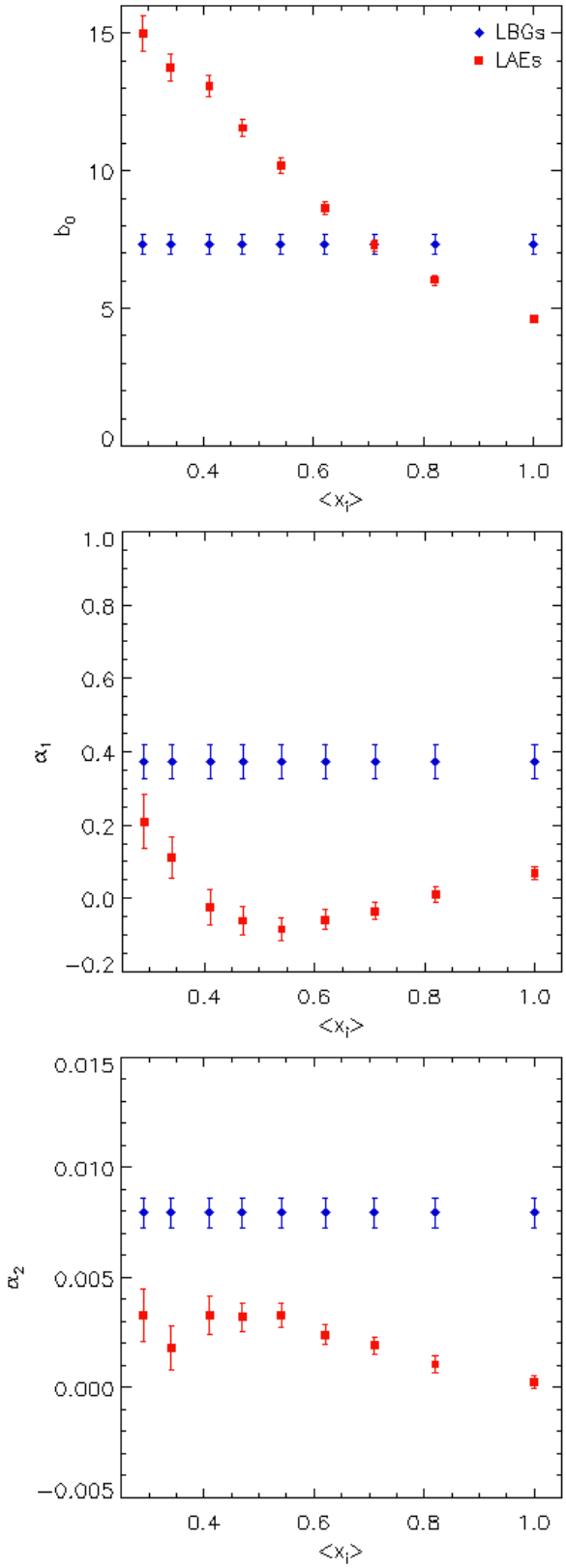

Figure 3.4: Model bias parameters with HSC statistical error bars, as a function of the volume-averaged ionization fraction at $z \sim 6.6$. The top, center, and bottom panels show constant, linear, and quadratic terms in our scale-dependent biasing model. The red points are for LAEs, while the blue points are for LBGs. The constant bias term shows strong evolution with decreasing ionized fraction. The linear and quadratic terms show gentler evolution with ionized fraction and are larger for the LBGs than the LAEs.

than the bright LBGs. However, the patchy reionization enhancement leads to the LAEs being more clustered than the HSC selected LBGs; in our model this occurs for ionization fractions $\langle x_i \rangle \leq 0.62$. In practice, this might be observed as a strong evolution in the linear bias factor, with b_o increasing sharply from $z \sim 5.7$ to $z \sim 6.6$, while the LBG bias may evolve only modestly between the redshift bins centered on $z \sim 5.9$ and $z \sim 6.9$. If the LAE bias even surpasses that LBG bias, this would indicate a significant neutral fraction ($\langle x_{\rm HI} \rangle \geq 0.38$ in our model). We also find that the LAE bias develops a slightly stronger scale dependence as the neutral fraction increases (center and right panels of Fig. 3.4), but the scale dependence is never as strong as in the simulated LBG populations.

While not shown here, we also calculate the bias for LAEs at $z \sim 7.3$. Since the survey is not as deep at this higher redshift, we anticipate a significantly smaller sample, ranging from a few (for $\langle x_i \rangle = 0.21$) to a couple hundred (for the fully ionized case). We see a similar increase in bias with decreasing ionized fraction. However, the error bars are at least four times larger. And due to the small sample size, the results become more and more uncertain as we examine more neutral models. Nevertheless, clustering measurements at $z \sim 7.3$ might help to cement trends observed between $z \sim 6.6$ and $z \sim 5.7$, although the utility of this will depend on the precise ionization history.

3.4.4 Void Probability Function

Another complementary measurement to the bias factor is the void probability function, as discussed in previous LAE work by Kashikawa et al. (2006) and McQuinn et al. (2007a). Here one considers the probability that a circle of radius R, placed randomly in the survey area, contains zero galaxies. This defines the void probability function, denoted here as VPF(R,0); McQuinn et al. (2007a) considers generalizations of this statistic where the circle of radius R encloses N galaxies (VPF(R,N) in our notation), but here we confine ourselves to pure voids with zero enclosed galaxies, As the IGM becomes more neutral, LAE voids should grow as progressively more emitters are attenuated out of the sample. In this case, observable LAEs are left only in the rare, high density peaks that are

surrounded by large ionized bubbles. As with the bias factors, HSC can measure the evolution in the VPF from $z \sim 5.7$ to $z \sim 6.6$ and then to $z \sim 7.3$, and contrast this with the LBG evolution across their two broad bands centered around $z \sim 5.9$ and $z \sim 6.9$. Note that the comparison between the VPFs of the LAEs and the LBGs is somewhat subtle in that the two populations are drawn from different depths. (This was also the case for the power spectrum, but not the bias factors.) The difference in the redshift evolution of the LAEs and LBGs should nevertheless show distinctive signatures if the LAE samples probe into the EoR, as we will see.

In order to measure this from our simulations, we randomly place 1,000 points across the area of our projected galaxy samples. We then calculate the probability that circles of various radii centered on these points do not contain any galaxies. We calculate error bars on the measurements by taking the standard deviation across six independent mock surveys drawn from the simulation cube, and scale these to the larger survey area of the HSC assuming Poisson statistics in performing this scaling. Our results are shown in Fig. 3.5. Here we have restricted ourselves to ionized fractions where $\bar{n_g}\pi R^2 \gg 1$. Large voids can be due to either observing only a small number of galaxies or an enhanced clustering of those galaxies. In order to study the later, we are careful only to examine ionized fractions where the number density of galaxies is sufficient. Also, note that it is somewhat complicated to compare these measurements across different filters; the different survey depths, both in luminosity and in width of the field, mean that the number density and perceived clustering vary from narrowband filter to narrowband filter. As expected, the probability of large voids grows as the IGM becomes more neutral, while the redshift evolution of the LBGs is generally weaker, reflecting only the relative shallowness of the higher redshift broad band sample. If the IGM is indeed partly neutral at $z \sim 6.6$ and $z \sim 7.3$, the trends should be observable at a high statistical significance. For example, the probability of having an $R = 15$ Mpc h^{-1} LAE void is almost an order of magnitude larger in a $\langle x \rangle = 0.71$ model than in the fully ionized case at $z \sim 7.3$. Likewise, such large voids should not be visible in the $z \sim 6.9$ LBG sample. The VPF appears to be a

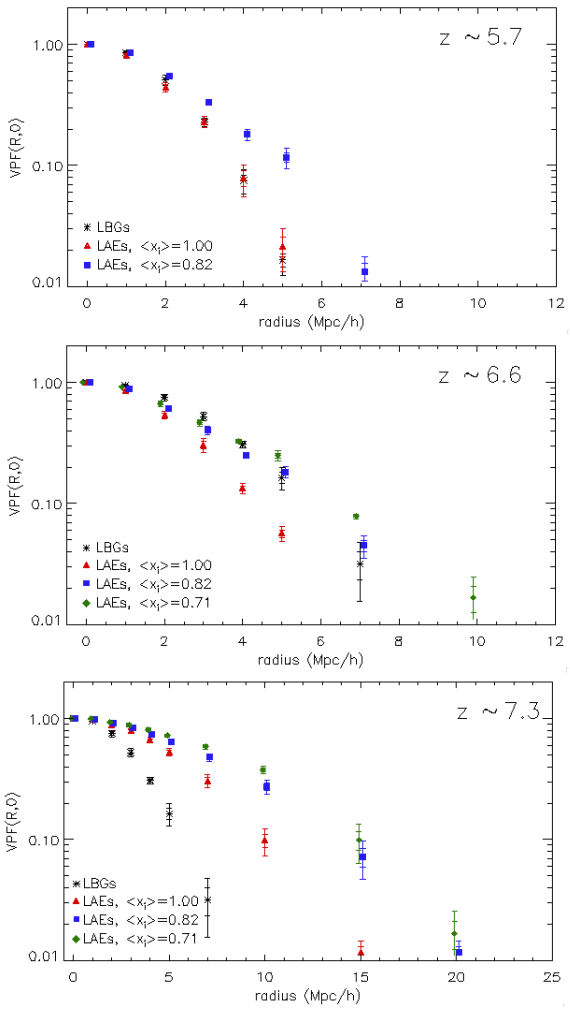

Figure 3.5: The void probability function (VPF) for LAEs and LBGs for a range of redshifts and ionization fractions. The top panel shows LAEs at $z \sim 5.7$ and LBGs in the broad band centered at $z \sim 5.9$, while the center panel shows LAEs at $z \sim 6.6$ and LBGs in the $z \sim 6.9$ broad band. The bottom panel shows LAEs at $z \sim 7.3$ and LBGs near $z \sim 6.9$. In each case, the error bars are forecast for HSC's 3.5 degree^2 Ultradeep field. The voids in the LAE distribution become more prominent as the IGM becomes more neutral. Note that the depths of the LAE and LBG samples are different, and so the comparison between LAE and LBG voids is not a perfect apples-to-apples comparison. Nevertheless, the stronger redshift evolution in the LAE VPF is a distinctive indicator of incomplete reionization. In order to ensure adequate sampling, we have restricted our plots to ionized fraction where $\bar{n_g}\pi R^2 \gg 1$. If, in reality, the Universe is significantly neutral at $z \sim 7.3$, HSC's survey may be too shallow in that band to make full use of this measurement.

promising statistic for studying reionization with the HSC.

3.5 Practical Complications

Thus far, we have considered highly idealized LAE and LBG surveys. Here we set out to explore some potential complications. First, we aim to quantify the impact of foreground interlopers on the LBG and LAE measurements. Next, we consider how Lyα emission may impact the LBGs detected by HSC; that is, we quantify the extent to which HSC's LBG selection may preferentially detect galaxies with strong Lyα emission lines.

3.5.1 Interlopers

The narrow band LAE selection will inevitably suffer at some level from line confusion: galaxies emitting in other lines may be confused for Lyα , especially lower redshift galaxies emitting in the OII, OIII, or Hα lines. One recent illustration is provided by the study of Pénin et al. (2015), who performed spectroscopic follow-up of three $z \sim 7.7$ (NB1060) narrow band selected LAE candidates, finding instead that they are most likely all low redshift OIII emitters. Similarly, the broad-band LBG selection may also potentially be contaminated by lower redshift galaxies or even red stars (Ouchi et al. 2009). The presence of these interlopers can bias measurements of the abundance, clustering, and void distributions. To explore this quantitatively, we have added interlopers into our simulated models.

3.5.1.1 Narrow Band Interlopers

First, we consider narrow band interloper contaminants. Since the narrow band interlopers arise from galaxies emitting in specific lines at common redshifts, the interlopers may themselves be spatially clustered. We focus on interlopers emitting in [OII], [OIII], and Hα emission lines, which are the most common Lyα interlopers (e.g. Dressler et al. 2011). We find, as detailed below, that the HSC can screen out many of these interlopers

through a judicious application of cuts. Some will nevertheless remain, and have some impact, so we consider this quantitatively in what follows.

We start with an expression to describe the apparent clustering of galaxies in our mock HSC sample, which consists of a mixture of high redshift LAEs, and low redshift interlopers. For brevity, our expression below assumes that the interlopers consist of a single dominant line-emitting population, although it is straightforward to generalize this to the case of several different interlopers. The total 2D power spectrum of the observed galaxies is then (e.g. Lidz and Taylor 2016, reproduced as §4 here):

$$P_{\rm combined}(k_\perp) = (1-f_{\rm int})^2 P_{{\rm Ly}\alpha}(k_\perp) + \frac{f_{\rm int}^2 b_{\rm int}^2}{\alpha_\perp^2} P_{\rm int}(\frac{k_\perp}{\alpha_\perp}), \tag{3.6}$$

where $f_{\rm int}$ describes the fraction of observed galaxies that are interlopers, and $P_{{\rm Ly}\alpha}(k_\perp)$ is the 2D LAE power spectrum. The second term involves the interloper clustering power spectrum, which we evaluate assuming linear biasing. Here $b_{\rm int}$ is the linear bias factor of the interlopers and $P_{\rm int}(k_\perp)$ is the 2D linear matter power spectrum at the redshift of the interlopers, while $\alpha_\perp \equiv D_{A,co}(z_{\rm int})/D_{A,co}(z_{{\rm Ly}\alpha})$ is a distortion factor that arises because the redshift of the Lyα emitters is assumed in mapping from observed angle on the sky to transverse co-moving distance (Lidz and Taylor (2016), or §4 of this thesis). Here $\alpha_\perp$ is defined by the ratio of the co-moving angular diameter distance to the redshift of the interloper divided by that to the LAEs.

In order to calculate the interloper term, we require the 2D linear matter power spectrum. To evaluate this, we start from the 3D linear power spectrum using the transfer function determined by CAMB (Lewis et al. 2000; Lewis and Bridle 2002; Howlett et al. 2012). We then calculate the 2D power spectrum according to:

$$P_{\rm int}(k_\perp) = \frac{1}{2\pi}\int |W(k_\parallel)|^2 P_{\rm 3D}(k_\perp, k_\parallel)\, dk_\parallel. \tag{3.7}$$

Here $W(k_\parallel)$ is the Fourier transform of the top-hat window function that describes the narrow band filter, and the filter width is converted to co-moving units according to the redshift of the interloper lines. In order to estimate the clustering of the interlopers, we use the linear bias factors measured from the near-infrared spectroscopic sample of de la

Torre et al. (2007) since their sample is drawn from similar redshifts to the $z \sim 6.6$ LAE interlopers. Here we assume that galaxies with strong OII emission, for example, have similar clustering to other galaxies at the same redshift. In making this assumption, we have chosen to focus on the redshift evolution of interloper clustering. To generalize to a few interloper lines, the second term in Equation 3.6 simply becomes a weighted sum over interloper lines, each with a separate interloper fraction, bias factor, distortion factor, and linear matter power spectrum. The first term maintains the form in Equation 3.6, except that $f_{\rm int}$ is now determined by the sum total fraction of the different interloper lines.

Next, we must estimate the interloper fraction itself. In order to determine the abundance of the Hα and OIII emitters, we use the luminosity function from Pirzkal et al. (2013), while we take the OII luminosity function from Comparat et al. (2015). In each case, we adopt the luminosity function at the redshift bin into which the desired interloper redshift falls. We then determine the limiting luminosity in each interloper line from HSC's narrow band flux limits, and the luminosity distance to the interloper. The minimum luminosities in the interloper lines are: 2.0×10^{39} erg s^{-1} for Hα; 4.8×10^{40} erg s^{-1} for OII; and 1.2×10^{40} erg s^{-1} for OIII. These are roughly one to two orders of magnitude fainter than L_* for Pirzkal et al. (2013) and Comparat et al. (2015) luminosity functions. Integrating over Schecter function fits to the observed luminosity functions, we determine the number density of emitters above the HSC flux limits in each line. The total number of interlopers across the HSC field then follows from multiplying the abundance by the co-moving volume of the HSC survey at the redshift of each interloper. The co-moving volume at the redshift of the interlopers is determined from the solid angle covered by the HSC, and the observed wavelength interval of the narrow band. These estimates are in rough agreement with the number of OII, OIII, and Hα interlopers reported in a survey of $z \sim 5.7$ LAEs by Dressler et al. (2011).

Thus far, we have determined the total number of foreground emitters in the HSC with flux above the survey limits, but additional steps can be made to distinguish interlopers and LAEs (using only the filter sets available to the HSC.) First, one can use the fact that

Lyα tends to be a stronger emission line than the interlopers, and apply an equivalent width cut to improve the purity of the sample. Specifically, we can use the traditional requirement that to be considered an LAE a galaxy need have an $REW \geq 20$ Å ($REW \geq 25$ Å is also frequently used, e.g. Schenker et al. 2012). Second, the LAE flux should be completely attenuated blueward of Lyα at the redshift of the galaxy (from the thick Lyα forest at the redshifts of interest, and further blueward from other Lyman line transitions and continuum opacity.) In contrast, the continuum spectra of the interlopers is relatively flat around the emission lines of interest. Consequently, one can use the HSC broad bands to help separate interlopers and LAEs. Specifically, an LAE should not be detected in *gr*, while many interlopers will be observable in *gr* if they are also visible in the *z* or *y* band.

To assess how effective these cuts may be, we use spectroscopic data from the Sloan Digital Sky Survey (SDSS) (Gunn et al. 2006; Eisenstein et al. 2011; Dawson et al. 2013; Smee et al. 2013), as detailed in their latest data release paper (Alam et al. 2015). The SDSS includes hundreds of thousands of galaxies emitting in the lines of interest, out to $z \lesssim 1.9$. All the interlopers fall within the redshift range probed by SDSS, although the OII interlopers, at $z = 1.408$ are at the far end. We assume that the properties of the SDSS line emitters over the entire redshift range are representative of the interlopers at the narrow redshift bands relevant for HSC. We also ignore any trend in the interloper properties with luminosity, which may be important since the SDSS emitters are more luminous than most of the HSC interlopers.

With these caveats in mind, we calculate the fraction of SDSS line emitters that exceed the minimum REW requirement mentioned previously and are also faint enough to avoid detection in *r*:

$$\begin{aligned} \text{REW} \ &\geq 20 \text{ Å and} \\ r &< 26.1 \text{ mag.} \end{aligned} \tag{3.8}$$

Note that this REW cut is in the *rest frame of the LAEs.* For our interlopers, who are at their own redshifts, this cut becomes $REW_i \geq 20$ Å λ_i/λ_α.

Indeed, the vast majority of the SDSS [OIII], [OII], and Hα line emitters have rela-

tively weak emission lines with low REWs. Thus, the REW cut is able, on its own, to screen out a significant number of interlopers. To take a representative case, the SDSS sample of OII emitters considered here contains 905,847 galaxies: only 2,690 (or 0.296%) of these have REW ≥ 20 Å. After both cuts, our estimate is that 94 OII interlopers, 10 OIII and 23 Hα interlopers will remain in the HSC Ultradeep 3.5 degree^2 survey for $z \sim 6.6$ LAEs. The interloper fraction, $f_{\rm int}$, depends, of course, on how many LAEs there are at this redshift: in our models, the interloper fraction ranges from 5% in a fully ionized universe to as much as 80% if the universe is only 21% ionized at this redshift. The results for a range of ionized fractions are shown in Fig. 3.6, and discussed further below.

3.5.1.2 Broad Band Interlopers

The HSC LBG sample will also include some foreground interloper contamination. Here the broad band selection is vulnerable to contamination from intermediate redshift red galaxies such as ellipticals and dusty starburst galaxies, and also to L/T dwarf stars. However, Ouchi et al. (2009) and HSC Science Collaborations (2012) show that with appropriate y and z band cuts and comparisons with lower redshift galaxy SEDs, one can effectively exclude the intermediate redshift red galaxies from the sample. Following Ouchi et al. (2009), we hence assume that most, if not all, interlopers in HSC's LBG survey are galactic late-type stars. Their estimate is that between $36-40$% of the HSC z-dropout sample will be dwarf stars rather than $z \sim 7$ LBGs. In order to incorporate these interlopers, we add L/T dwarf stars to our mock survey data (at an interloper fraction of 38%). We assume that these interlopers are randomly distributed.

3.5.2 Preferential Selection of LBGs with Strong Lyα Lines

For simplicity, we have thus far ignored any impact of Lyα emission on the observability of an LBG. However, an LBG's Lyα emission line will fall into the red-side broad band and a strong line may boost the detectability of the LBG. This effect may be enhanced by the observed anti-correlation between REW and UV luminosity: faint LBGs, most

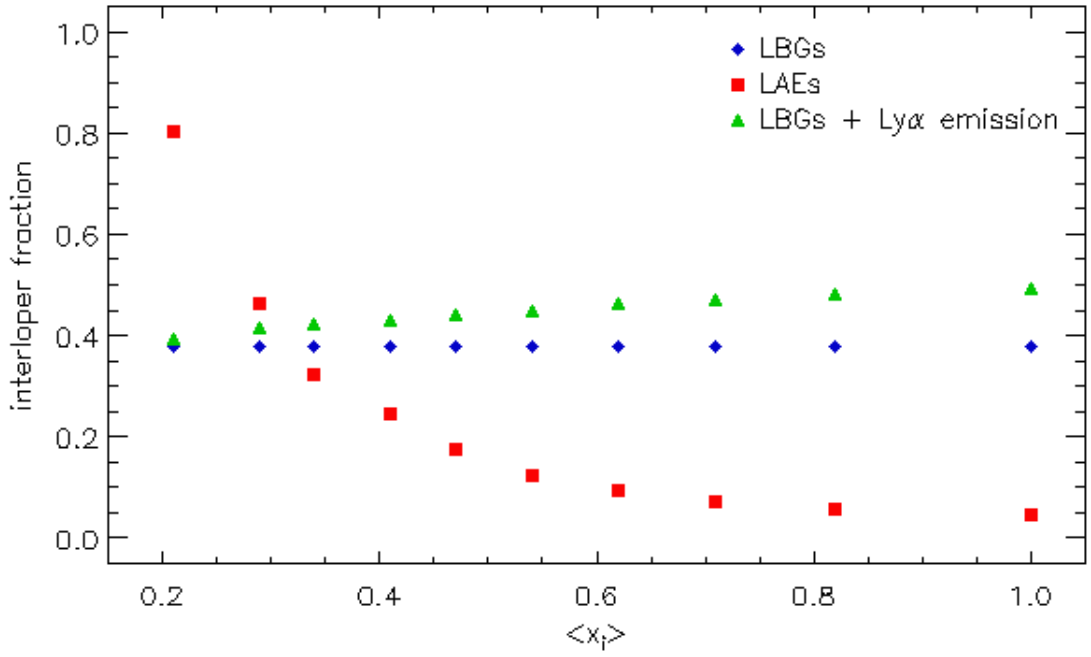

Figure 3.6: Estimates of the foreground interloper fraction for HSC surveys for $z \sim 6.6$ LAEs and $z \sim 6.9$ LBGs. The results are plotted as a function of ionization fraction (at fixed redshift). The red squares show the LAE interloper fraction, which is a strong function of $\langle x_i \rangle$: although the cross-correlation interloper abundance is independent of ionization, the abundance of observable LAEs drops off rapidly as the neutral fraction increases, and so the interloper fraction increases strongly towards low $\langle x_i \rangle$. The LBG interloper fraction (blue diamonds) is mostly set by the abundance of red L/T dwarf stars. The green triangles account for the additional effect that LBGs with strong Lyα emission are more likely to be observed, and so the LBG interloper fraction depends slightly on the ionization fraction.

in need of a boost in order to be detected, have the strongest Lyα emission. In principle, this selection bias could be reduced by having additional redward filters but this is probably impossible for ground based observations given the sensitivity required at long wavelengths. In any case, y is HSC's reddest band.

In order to consider this boost in our mock data, we enhance the luminosity of each mock LBG according to a simple prescription. By definition, the total luminosity in the Lyα line is related to the observed specific UV continuum luminosity (i.e., units of ergs sec^{-1} Å^{-1}) at the wavelength of the Lyα line by $L_\alpha = EW L_{UV,\lambda}$. Here all quantities are expressed in the observed frame, so EW is the observed equivalent width. The total UV luminosity in the broad band, including the Lyα line, is then: $L'_{UV} = L_{UV,\lambda} BBW + L_{UV,\lambda} EW$, where BBW is the wavelength extent of the broad band in the observed frame and we have approximated the continuum as flat over the extent of this band. We further assume that the Lyα line is completely contained within the broad band filter, so that the entire line luminosity is observed in that filter. The specific UV luminosity per rest frame frequency interval, which is the input for our LBG calculations (Equation 3.2) is therefore boosted by the Lyα emission line according to $L'_{UV,\nu} = L_{UV,\nu}(1 + \frac{EW}{BBW})$. Quantitatively, we find that 26% more LBGs are visible in the fully ionized case owing to the Lyα emission boost, while this boost is only 3% in a highly neutral model with $\langle x_i \rangle = 0.21$.

3.5.3 More Realistic Results

Fig. 3.6 summarizes our estimates of the HSC LAE and LBG interloper fractions. The figure also shows the impact of the preferential selection of LBGs that have strong Lyα emission lines. Since the number of observable LAEs drops with decreasing ionization fraction, while the number of narrow band interlopers is independent of ionization fraction, the LAE interloper fraction varies strongly with $\langle x_i \rangle$ and can be as large as 80% in the most neutral case shown (with $\langle x_i \rangle = 0.21$.) The LBG interloper fraction is a constant 38% in the absence of the Lyα boost, but becomes a weakly increasing function of ionization fraction when we account for this.

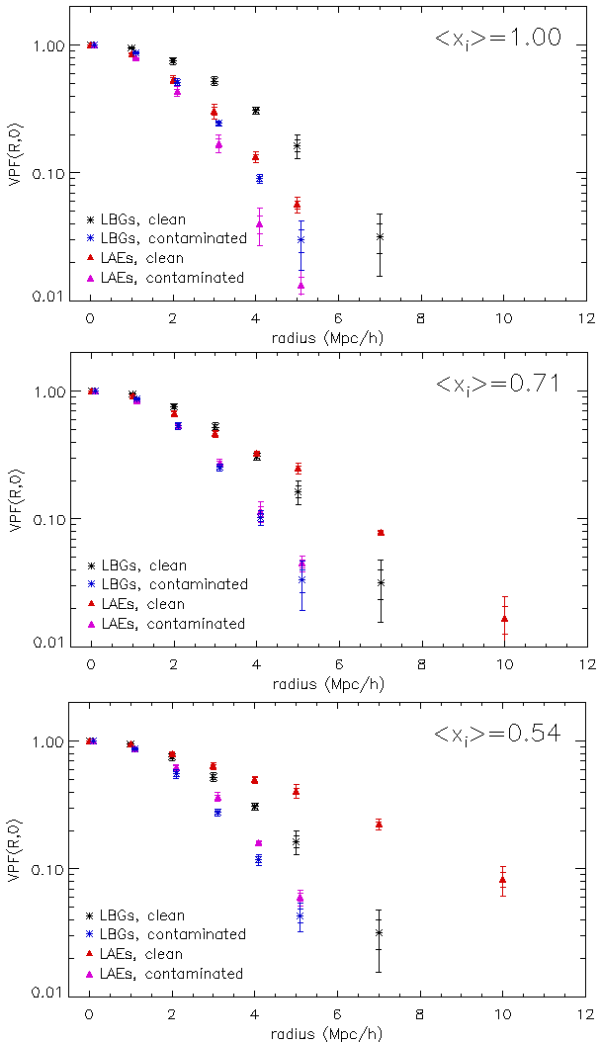

Figure 3.7: Void Probability Function for LAEs and LBGs, after accounting for foreground interlopers. This is similar to Fig. 3.5, except here we have accounted for the narrow band and broad band interlopers and the Lyα emission boost for the LBGs. Here we fix the narrow band redshift at $z \sim 6.6$ and the broad band redshift to $z \sim 6.9$, and consider three representative ionization fractions: $\langle x_i \rangle = 1$ (top) $\langle x_i \rangle = 0.71$ (center) and $\langle x_i \rangle = 0.54$ (bottom). Including these complications acts to shrink the size of the voids, but the LAE voids remain larger than the LBG ones and increasing the neutral fraction still enhances the differences.

We can now quantify the impact of interloper contamination, and the Lyα boost, on our mock HSC statistical measures, starting with the VPF. For assessing the impact on this quantity, we assume for simplicity that the interlopers are randomly distributed. The interlopers act to fill in the voids in the LAE and LBG distributions. In reality, at least the narrow band interlopers should be clustered, and contain larger voids than expected in a random distribution. These voids may by chance overlap with the LAE voids and reduce the contaminating effect on the VPF, which must then be more severe for the case of a random interloper distribution assumed here. The results of the more realistic VPF calculations are shown in Fig. 3.7. The interlopers lead to significant reductions in the probability of finding large voids, but there are nevertheless robust trends in the evolution of the VPF with neutral fraction. In addition, we still expect to see stronger redshift evolution in the LAE VPF than in the LBG VPF, provided the HSC LAE samples start to probe back into the EoR.

Fig. 3.8 shows the impact of the complications considered in this section on the LAE and LBG bias parameters and the expected HSC Ultradeep field error bars on these quantities. This plot fixes $z \sim 6.6$, and considers a range of ionization fractions at this redshift. It is identical to Fig. 3.8, except that here we have included our estimated interloper contamination and the Lyα boost. Unsurprisingly, the main effect is to dilute the clustering of the LAEs and LBGs. For the LAEs, this dilution is due to two processes, as detailed in Equation 3.6. First, the clustering signal from the LAEs is reduced by $(1 - f_{int})^2$; this reduction is due to merely the presence of interlopers and occurs without regard to the interloper clustering. Second, a clustering signal from the interlopers is included, which distorts the total clustering measurement. This term is only significant because the LAE interlopers are drawn from specific line-emitting populations. The impact is strongest in the more neutral models, where the interloper fraction is largest. Indeed, the distinctive and strong enhancement of the constant bias term with decreasing ionization fraction is modified: the apparent bias turns over at $\langle x_i \rangle = 0.40$ and decreases towards larger neutral fractions in the presence of interloper contamination. Interloper contamination may

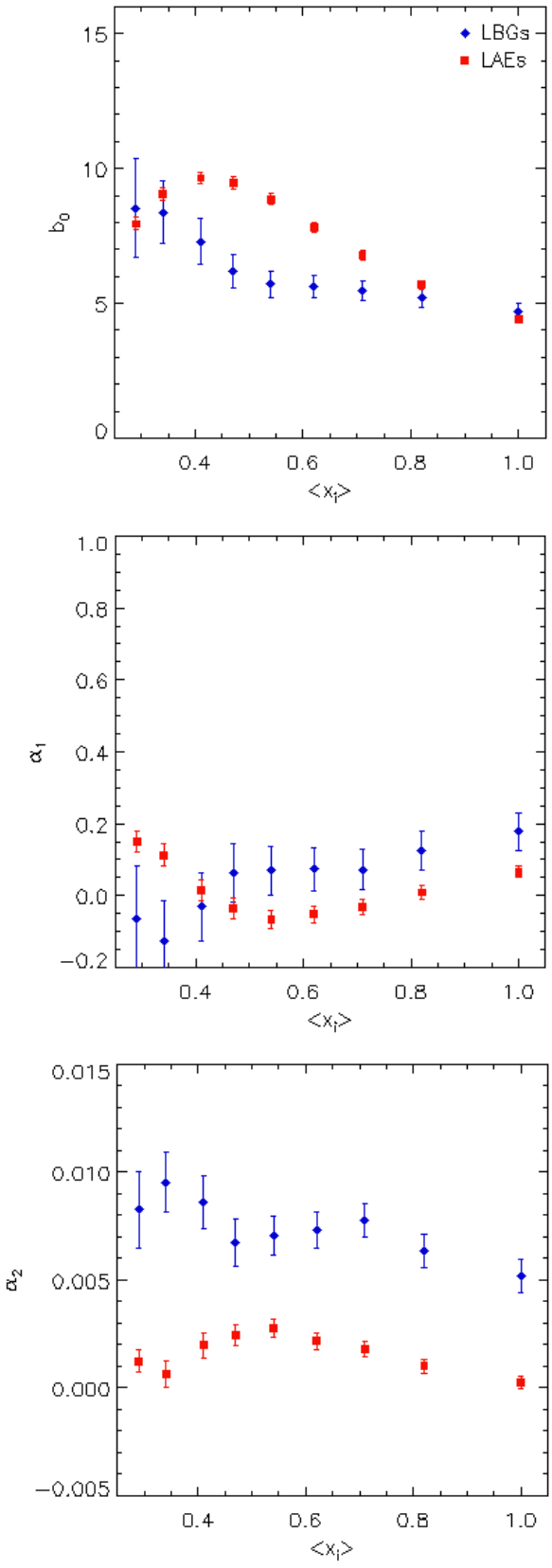

Figure 3.8: Model bias parameters for LAEs and LBGs at $z \sim 6.6$ for a range of ionized fractions, after accounting for practical complications. This is identical to Fig. 3.4, except here we have included the narrow and broad band interlopers and the impact of boosted Lyα emission. The interlopers make the Lyα clustering enhancement harder to discern, and boost the error bars. The effects are more prominent in highly neutral models.

therefore be an important systematic, especially if the $z \sim 6.6$ and/or $z \sim 7.3$ IGM are significantly neutral. One approach might be to fit jointly for the interloper contamination and the neutral fraction, using measurements of the abundance, VPF, and clustering, while anchoring the fits to post-reionization measurements.

3.5.4 Retrieving Clean Measurements

Another powerful approach, however, is to measure the cross power spectrum between the LBGs and LAEs. This has the important virtue that it should not be impacted by the clustering of the interlopers and can be carried out in conjunction with the other measurements to test consistency. In particular, note that the broad and narrow band interlopers are two completely different populations: the narrow band (LAE) interlopers are low redshift galaxies, while the broad band (LBG) interlopers are red galactic stars. Consequently, the clustering of the interlopers will not impact the ensemble-averaged cross-correlation between the LAEs and LBGs. Moreover, on large scales we expect the correlation coefficient between LAEs and LBGs to be unity to a very good approximation.

If we further assume linear biasing, we can estimate the Lyα emitter bias according to:

$$b_\alpha(1-f_{int,\alpha}) = \frac{P_{g\alpha}(k_\perp)}{b_{LBG}\,(1-f_{int,LBG})\,P^W_{\delta\delta}(k_\perp)}, \tag{3.9}$$

where b_α and b_{LBG} are the bias factors for LAEs and LBGs, respectively; and $f_{int,\alpha}$ and $f_{int,LBG}$ are the interloper fractions for the LAEs and LBGs, respectively. $b_{LBG}\,(1-f_{int,LBG})$ can be measured from the LBG auto spectrum. $f_{int,\alpha}$, however, is harder to estimate. $P_{g\alpha}(k_\perp)$ is the cross power spectrum of the LBGs and LAEs; and $P^W_{\delta\delta}(k_\perp)$ is a windowed auto power spectrum of the density field. Because the window functions for the LAEs and LBGs are different, the projected density power spectrum here is related to the 3D density power spectrum according to:

$$P^W_{\delta,\delta}(k_\perp) = \int \frac{dk_\parallel}{2\pi}\left[W_\alpha(k_\parallel)W^\star_g(k_\parallel) + c.c.\right] P_{3D}(k_\parallel,k_\perp), \tag{3.10}$$

where W_α denotes the Fourier space window function for the LAEs, and W_g is the same

for the LBGs, while $c.c.$ denotes complex conjugation, and P_{3D} is the 3D density power spectrum. In practice, the windowed density field will have to be modeled, and we extract it here directly from the simulations.

In summary, we can estimate the product of $b_\alpha b_{LBG}(1-f_{int,\alpha})(1-f_{int,LBG})$ from the measured LAE-LBG cross spectrum without concern for interloper clustering (on average), although there is some general attenuation of the signal. Since b_{LBG} is less sensitive to the ionization fraction, we can likely model it using post-reionization observations as input and the HSC-measured LBG auto spectrum (with a reasonable guess as to the broad band interloper fraction). We can then determine $b_\alpha(1-f_{int,\alpha})$ itself according to Equation 3.9, and use this to search for any clustering enhancement from reionization. For high ionized fractions, $f_{int,\alpha}$ is small and the cross spectrum allows us to measure b_α. For lower ionized fractions, $f_{int,\alpha}$ becomes significant; however, if HSC can estimate their LAE interloper fraction, they can divide out this term. Even if Equation 3.9 does not return b_α itself, due to a high interloper fraction, it still allows us to sidestep concerns about interloper clustering, making this a cleaner measurement than Equation 3.5.

We can calculate the error-bars for an HSC measurement of $P_{g\alpha}(k_\perp)$ according to:

$$\sigma^2_{g\alpha}(k_\perp) = \frac{1}{N_m(k_\perp)}\left[P^2_{g\alpha}(k_\perp) + \left(P_{gg}(k_\perp)+\frac{1}{\bar{n}_g}\right)\left(P_{\alpha\alpha}(k_\perp)+\frac{1}{\bar{n}_\alpha}\right)\right], \tag{3.11}$$

where $N_m(k_\perp) = \frac{k_\perp \Delta k_\perp A}{2\pi}$ is the number of modes enclosed in the survey area, $P_{g\alpha}(k_\perp)$ is as above, $P_{gg}(k_\perp)$ is the auto power spectrum of the LBGs, $P_{\alpha\alpha}(k)$ is the auto power of the LAEs, and $\bar{n}_g$ and $\bar{n}_\alpha$ are the the projected number density of the LBGs and LAEs, respectively. Here the auto spectra include the interloper contamination, along the lines of Equation 3.6. Here we neglect any Poisson contribution to the first term, which is appropriate if there is no overlap between the LBG and LAE samples.

If the LBG bias had no scale dependence, in other words, $b_{LBG}(1-f_{int,LBG})$ is a constant as a function of $\langle x_i \rangle$, we should be able to divide it out from Equation 3.9 and retrieve the values show in Fig. 3.4, modulated by $(1-f_{int,\alpha})$. As that figure shows that

is a reasonable first order approximation; we are only ignoring some small scale dependance. Nonetheless, if we divide $b_\alpha b_{LBG}(1-f_{int,\alpha})(1-f_{int,LBG})$ by a constant across all ionized fractions, we can recover $b_\alpha(1-f_{int,\alpha})$, at least to first order, as shown in the right panel of Fig. 3.9. There we have have held $z \sim 6.6$ and are varying the ionized fraction. For the more ionized universe, the cross-correlation points (green) match well the clean LAE measurement (red). However for more neutral cases ($\langle x_i \rangle \lesssim 0.5$, they diverge as $(1-f_{int,\alpha})$ begins to play a significant role. Nonetheless, for all ionized fractions, the cross-spectrum (Equation 3.9) better estimates the true LAE bias than Equation 3.5 once interlopers are included, since it is not effected by interloper clustering. If HSC can estimate their interloper fraction, even without knowing which galaxies are themselves interlopers, they will be still better able to calculate the LAE bias.

Although the LAE bias recovered from the cross spectrum has larger errors than that determined from the auto spectrum, we should keep in mind that we fixed the REW cut (REW $\geq$ 20 Å) in this comparison. However, this is in part motivated by a desire to limit interloper contamination; since the cross spectrum is immune (on average) to the interloper clustering, one could presumably get away with a lower REW cut. While such a cut would increase the interlopers numbers, as long as it similarly boosts the observed sample, it could still result in reduced error bars on the cross spectrum estimate.

Fig. 3.10 quantifies how well the HSC can constrain the ionization fraction, given the expected statistical precision of its LAE-LBG cross spectrum based determinations of the constant LAE bias term. We estimate the expected error on the volume-averaged ionization fraction according to:

$$\sigma_{\langle x_i \rangle} = \frac{\sigma_b}{\partial b / \partial \langle x_i \rangle}, \tag{3.12}$$

where σ_b is the error on the bias factor and $\partial b / \partial \langle x_i \rangle$ is the derivative of the bias factor with respect to ionization fraction, evaluated assuming some underlying "true" or "real" value of $\langle x_i \rangle$. In order to test the dependence on the true value of $\langle x_i \rangle$ we evaluate the derivative for several different values of $\langle x_i \rangle$. The results of Fig. 3.10 suggest that the HSC cross spectrum measurement should allow a determination of $\langle x_i \rangle$ to within about

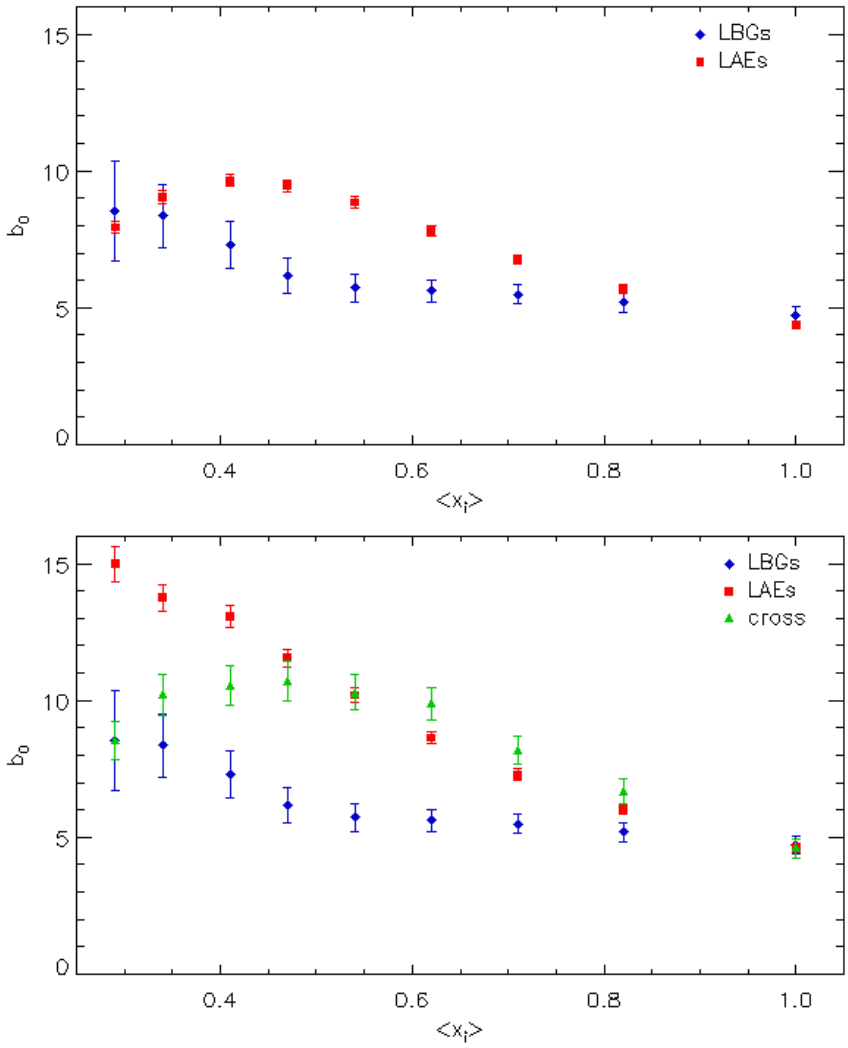

Figure 3.9: Estimates of the LAE bias from the LAE-LBG cross spectrum. *(Top)* This shows the first panel of Fig. 3.8, the constant bias term as a function of ionization fraction for LAEs and LBGs after accounting for interlopers and the Lyα emission boost. *(Bottom)* The green points and expected error bars show the constant bias term for the LAEs inferred from a measurement of the LAE-LBG cross spectrum. The error bars show our forecasts for an HSC Ultradeep 3.5 degree^2 survey measurement of the LAE-LBG cross spectrum. The red and blue points and error bars show, respectively, the LAE and LBG bias and errors estimated from their auto power spectra (ignoring foreground interlopers and the Lyα boost), as in Fig. 3.4. The cross spectrum allows a better recovery of the LAE bias.

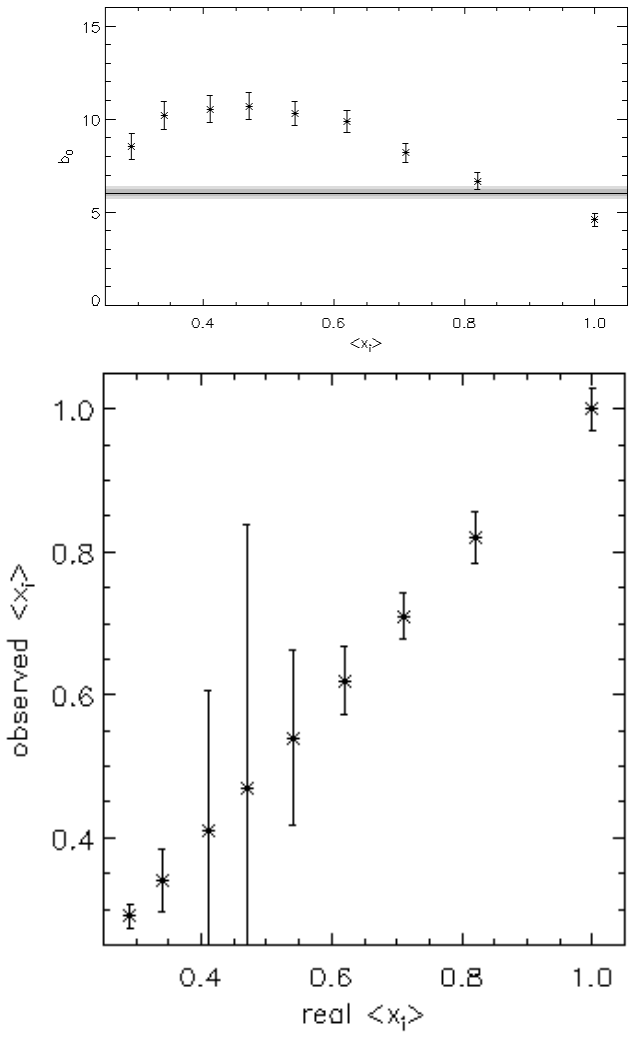

Figure 3.10: Forecasts for HSC constraints on the volume-averaged ionization fraction. *(Top)* The constant bias term and the expected error bars at $z \sim 6.6$ from an LAE-LBG cross spectrum measurement in the HSC 3.5 degree^2 Ultradeep field. To guide the eye, the grey band shows the bias and error bar for a fiducial model with $\langle x_i \rangle = 0.82$. *(Bottom)* The range of allowed $\langle x_i \rangle$s anticipated for a future cross spectrum measurement (y-axis) as a function of the true underlying value of $\langle x_i \rangle$ (x-axis). Note that unphysical values with $\langle x_i \rangle$ are allowed in these estimates. The forecasts fix our model for the intrinsic LAE parameters and vary only over the ionized fraction. The large error bars at $< x_i > \sim 0.5$ are due to the turnover in the bias at the same ionized fraction in the top plot. Simply put, an observed LAE bias ~ 11 corresponds to a range of ionized fractions.

0.1. Note that the estimate of Equation 3.12 allows unphysical values of $\langle x_i \rangle \geq 1$. The precision of the $\langle x_i \rangle$ constraint does not depend strongly on the assumed ionization fraction; this is because the error bar on the bias parameter increases towards high neutral fractions as the observed LAE abundance falls, but this is compensated by the stronger clustering enhancement at high neutral fractions. An important caveat here, however, is that these forecasts vary only $\langle x_i \rangle$, while fixing the parameters describing the intrinsic LAE and LBG emission. In future work, it will be important to marginalize over parameters describing the intrinsic properties of the LAEs and LBGs, although it is unclear how to be parameterize the problem. It would also be interesting to consider fitting the abundance, VPFs, auto and cross spectra jointly, but this is again beyond the scope of the present chapter.

3.6 Conclusions

We have forecast the ability of the HSC to detect LAEs and LBGs over their 3.5 degree^2 Ultradeep field, and considered a variety of different statistics to characterize these populations and extract information about the EoR. We found that the redshift evolution of the abundance, clustering, and void distributions for each of the LAEs and LBGs are interesting diagnostics for determining the ionization state of the surrounding IGM. In addition, spatial variations in the relative abundance of LAEs to LBGs may allow one to extract information regarding the typical sizes of ionized regions during the EoR. Furthermore, we proposed that the LAE-LBG cross spectrum as a useful quantity to measure since it is on average immune to interloper clustering contamination. The large HSC Ultradeep field should allow significant improvements beyond existing LAE and LBG clustering measurements. For example, the best current LAE clustering measurement at $z \sim 6.6$ comes from the Subaru analysis of Ouchi et al. (2010). We forecast that the error bars on the LAE bias will improve by a factor of three at this redshift with the HSC Ultradeep field observations. The LBG survey can also improve significantly on current state-of-the-art

clustering measurements from Barone-Nugent et al. (2014), which come from 743 $z \sim 7$ LBGs over a 300 arcmin^2 field. In our fiducial model, the improved HSC clustering statistics will allow one to determine the ionization fraction to within about 0.1 for $\langle x_i \rangle \gtrsim 0.5$ from the measured LAE-LBG cross spectrum alone.

In order to best interpret the upcoming measurements, more sophisticated models for LAEs and LBGs are required. One challenge is the vast range of spatial scales that are relevant for understanding the Lyα emission from high redshift galaxies during the EoR. However, multi-scale simulation approaches are underway to meet this challenge (e.g. Zheng et al. 2010; Jensen et al. 2013; Choudhury et al. 2015; Mesinger et al. 2015; Kakiichi et al. 2015). These models may partly be calibrated with post-reionization measurements. This can then be combined with the diverse range of statistical measurements considered here to determine the ionization state of the IGM over the interesting redshift range of $z \sim 5.7 - 7.3$ using the HSC.

Chapter 4

On Removing Interloper Contamination from Intensity Mapping Power Spectrum Measurements

4.1 Introduction

Intensity Mapping (IM) is an appealing approach for studying the large scale structure of the Universe and for characterizing the bulk properties of galaxy populations emitting in various spectral lines across cosmic time. IM observations forego detecting galaxies individually. Instead, one measures the large-scale spatial fluctuations in the collective emission from all of the luminous sources emitting in some convenient spectral line or lines (see e.g. Suginohara et al. 1999; Chang et al. 2008; Righi et al. 2008; Visbal and Loeb 2010; Gong et al. 2011; Carilli 2011; Lidz et al. 2011; Pullen et al. 2013; Uzgil et al. 2014; Breysse et al. 2014; Croft et al. 2016; Li et al. 2016; Mashian et al. 2015; Keating et al. 2015). This complements traditional galaxy surveys which target individual objects

Published as Lidz and Taylor (2016)

in that IM surveys are sensitive to the collective emission from *all* luminous sources, while traditional observations are limited to detecting only those sources that lie above survey flux limits. IM also probes line emission across a range of large-scale environments, and is sensitive to the emission from galaxies in underdense voids as well as sources in high density peaks. This is often impossible in a traditional survey, where spanning large-scale environmental variations requires capturing an enormous volume at high sensitivity.

One potentially powerful application is to the Epoch of Reionization (EoR). Current evidence suggests that the Universe is reionized largely by numerous low-luminosity sources (e.g. Robertson et al. 2015), and so it is extremely challenging to detect most of the ionizing sources individually. However, it may nevertheless be possible to study their collective impact using IM. In addition, by spanning a large field-of-view at coarse angular resolution while retaining redshift information, IM surveys would be well-matched to redshifted 21-cm observations of the EoR. The cross-correlation of IM measurements with redshifted 21-cm data sets could then be used to confirm the high redshift origin of a putative 21-cm signal from the EoR (Furlanetto and Lidz 2007; Lidz et al. 2009; Lidz et al. 2011). Only the high redshift portion of the redshifted 21-cm signal, and not residual foreground emission, should correlate with the IM data (asides for shared foregrounds). Furthermore, the scale-dependence of the cross-correlation between the two signals provides a powerful probe of the size of the ionized regions that form around groups of galaxies during reionization (Lidz et al. 2009; Lidz et al. 2011; Gong et al. 2011).

One systematic concern with IM measurements relates to foreground interloper emission (Visbal and Loeb 2010). This interloper emission arises from sources residing at lower (or possibly higher) redshifts – and emitting in different lines – than targeted by the IM survey, with the interlopers nevertheless contributing to the specific intensity at the observed wavelengths of interest. Explicitly, suppose the survey targets an emission line with a rest-frame wavelength of $\lambda_{r,t}$ and a target redshift around z_t. The observed wavelength of this emission is $\lambda_{\rm obs} = \lambda_{r,t}(1+z_t)$. Clearly an interloper source, emitting in a line with rest wavelength $\lambda_{r,i}$, can emit at the same observed wavelength provided its

redshift, z_i, satisfies $1+z_i = \lambda_{r,t}(1+z_t)/\lambda_{r,i}$. One approach to avoid bias from interloper emission is to probe two different emission lines from gas at the same redshift. The cross-correlation between the emission at the two corresponding observed wavelengths will, on average, only pick up contributions from gas at the target redshift (e.g. Visbal and Loeb 2010). Although each of the two observed wavelengths will contain interloper emission, the interlopers will be at widely separated redshifts and so uncorrelated. It will likely, however, be valuable to have additional handles to discriminate interloper emission. For one, it may not be feasible for the IM surveys to capture multiple bright lines from the same emitting gas, since this requires high sensitivity over a broad range of wavelengths. Moreover, it is necessary to clean interloper contamination to measure the *auto spectrum* of the emission fluctuations in a line of interest; this quantity contains information that is not available from the cross spectrum between two lines. Explicitly, as we will describe (see Equations 4.10 and 4.27), the large scale cross spectrum between two lines depends (mostly) on the product of the specific intensity and luminosity-weighted bias factor in *each line* while the auto spectrum depends on the product of the specific intensity and luminosity-weighted bias in the *single emission line of interest*. On small scales, the shot-noise term in the cross spectrum depends on the degree of overlap between the galaxy populations emitting in each line, while the shot-noise contribution to the auto spectrum is determined solely by the second moment of the luminosity function in the line. Put more generally, the auto spectrum depends only on the emission in a single line while the cross spectrum depends on the emission properties in two lines and therefore has a less direct interpretation.

Another possible approach is to mask out regions suspected of containing bright interloper emission, but this may require an additional survey to identify which regions to mask (e.g. Silva et al. 2015). The second survey must span the redshift range of all prominent interloper lines, and trace some quantity that is a good proxy for the interloper line emission. Furthermore, redshift information is required for all of the tracer galaxies. For some applications, it may be necessary to mask a significant fraction of the observed pix-

els. Finally, the resulting mask will reflect the clustering of the interloper sources; it must be deconvolved carefully to avoid introducing any bias in the inferred target emission fluctuations.

Here we develop an alternative approach for separating-out interloper contamination at the power spectrum level. Our starting point is to note that the mappings between observed wavelength/frequency and angle on the sky to co-moving length scales/wavenumbers are redshift dependent. If we assume the *target redshift* in converting between the observed frequencies and angles and co-moving coordinates, the interloper fluctuations will be mapped to the wrong wavenumbers. Since the remapping is different for the line of sight and transverse wavenumbers, the interloper contribution to the observed power spectrum will have a distinctive anisotropy. This is analogous to the Alcock-Paczynski (AP) effect (Alcock and Paczynski 1979; Ballinger et al. 1996), except in the case of the AP test a warping arises from assuming the wrong cosmology, while here the distortion results from adopting the incorrect redshift. We will show that this transfer of power and warping can be used to separate out the interloper contamination. This basic idea is mentioned in previous work by Visbal and Loeb (2010) and Gong et al. (2014), but we develop the technique further here and apply it to quantify the prospects for cleaning interloper lines from future $z \sim 7$ [CII] surveys. Although we focus on the illustrative example of IM with the [CII] line, our approach should be broadly applicable to IM surveys in other lines such as Lyα and CO transitions, and may also be of interest for traditional surveys detecting line-emitting galaxies.

The outline of this chapter is as follows. In §4.2, we describe and quantify the interloper distortion. This is then applied to the example case of a futuristic $z \sim 7$ [CII] emission survey (§4.3). §4.4 forecasts the constraints on [CII] and CO emission line properties that may be achieved by this survey. We further consider combining our technique with additional tracers of large-scale structure at the redshifts of prominent foreground interlopers (§4.5). We also discuss the prospects for cross-correlating with other emission lines at $z \sim 7$ (§4.6). We conclude in §4.7. Throughout we adopt a cosmological model

with $\Omega_m = 0.27$, $\Omega_\Lambda = 073$, $\Omega_b = 0.046$, $h = 0.7$, $\sigma_8(z=0) = 0.8$, and $n_s = 1$, broadly consistent with recent Planck measurements (Planck Collaboration et al. 2014).

4.2 Interloper Coordinate Mapping Distortions

In order to illustrate the technique, let us first suppose that our data cube contains only two sources of line emission: our target line of interest at redshift z_t, and a single dominant interloper line at redshift z_i. We will soon generalize to the case that several interloper lines contribute. We denote the observed frequency at the center of the data cube by $\nu_{\rm obs}$ and consider emission offset by a small frequency interval $\Delta\nu_{\rm obs}$ from the cube center. Further, let $\Delta\boldsymbol{\theta}$ be the angular separation from the center of the cube; the vector describes the two directions transverse to the line of sight and we work in the flat sky approximation. In order to convert from the observed $\Delta\nu_{\rm obs}$ and $\Delta\boldsymbol{\theta}$ to co-moving coordinates, we need to assume a cosmological model and a redshift for the emission.

Adopting the target redshift for this mapping will cause the interloper emission to *be mapped to the wrong co-moving coordinates*. Let us denote the apparent line of sight coordinate for the interloper emission by $\tilde{x}_\parallel$ and the apparent transverse coordinate by $\tilde{\boldsymbol{x}}_\perp$. Further suppose that the true line of sight and transverse coordinates at the interloper redshift are $x_\parallel$ and $\boldsymbol{x}_\perp$. The apparent coordinates are related to the observable frequency interval and angles by incorrectly assuming the emission is at the target redshift:

$$\tilde{x}_\parallel = \frac{c}{H(z_t)}(1+z_t)\frac{\Delta\nu_{\rm obs}}{\nu_{\rm obs}}, \tag{4.1}$$

and

$$\tilde{\boldsymbol{x}}_\perp = D_{\rm A,co}(z_t)\Delta\boldsymbol{\theta}, \tag{4.2}$$

where $H(z_t)$ is the Hubble parameter at the target redshift and $D_{\rm A,co}(z_t)$ is the co-moving angular diameter distance to the target redshift. (For a flat universe, $D_{\rm A,co}(z_t) = \chi(z_t)$ with $\chi(z_t)$ being the co-moving distance to redshift z_t.) The relations between the apparent

coordinates, $\tilde{x}_\parallel$ and $\tilde{\boldsymbol{x}}_\perp$, and the true coordinates, $x_\parallel$ and $\boldsymbol{x}_\perp$, are then:

$$\tilde{x}_\parallel = \frac{H(z_i)}{H(z_t)} \frac{1+z_t}{1+z_i} x_\parallel, \tag{4.3}$$

and

$$\tilde{\boldsymbol{x}}_\perp = \frac{D_{\rm A,co}(z_t)}{D_{\rm A,co}(z_i)} \boldsymbol{x}_\perp. \tag{4.4}$$

Since we are ultimately interested in the power spectrum, we also consider the line of sight and transverse components of the co-moving wavenumbers. The relevant factors here are just the inverse of the coordinate mappings:

$$\tilde{k}_\parallel = \frac{H(z_t)}{H(z_i)} \frac{1+z_i}{1+z_t} k_\parallel = \alpha_\parallel k_\parallel, \tag{4.5}$$

and

$$\tilde{\boldsymbol{k}}_\perp = \frac{D_{\rm A,co}(z_i)}{D_{\rm A,co}(z_t)} \boldsymbol{k}_\perp = \alpha_\perp \boldsymbol{k}_\perp. \tag{4.6}$$

Here we have defined "distortion" factors, $\alpha_\parallel$ and $\alpha_\perp$. These describe the remapping that occurs when the incorrect redshift is used to convert angles and observed frequencies to wavenumbers for the interloper population.

Turning now to power spectrum, we consider the fluctuations in the specific intensity field, $I_{\rm tot}(\boldsymbol{x})$. Note that throughout we will work with this quantity rather than with the power spectrum of $\delta_I(\boldsymbol{x}) = (I_{\rm tot}(\boldsymbol{x}) - \langle I_{\rm tot}\rangle)/\langle I_{\rm tot}\rangle$ – i.e., we don't divide out by $\langle I_{\rm tot}\rangle$. The apparent power spectrum of the interloper emission is then:

$$\tilde{P}_i(\tilde{k}_\parallel, \tilde{\boldsymbol{k}}_\perp) = \frac{1}{\alpha_\parallel \alpha_\perp^2} P_i\left(\frac{\tilde{k}_\parallel}{\alpha_\parallel}, \frac{\tilde{\boldsymbol{k}}_\perp}{\alpha_\perp}\right). \tag{4.7}$$

Here $\tilde{P}_i$ is the apparent interloper power spectrum, while P_i is the true interloper power spectrum. This equation reflects how the power spectrum transforms under a change of coordinates; the $1/(\alpha_\parallel \alpha_\perp^2)$ factor is the ratio of the apparent to actual volume surveyed at the interloper redshift (see Ballinger et al. 1996 for a related discussion in the context of the AP effect, and Visbal and Loeb 2010; Gong et al. 2014; Pullen et al. 2016 for earlier work on interloper contamination). With this transformation law in hand – to make our description more compact – we will generally drop the $(\tilde{k}_\parallel, \tilde{\boldsymbol{k}}_\perp)$ notation and

use $(k_\parallel, \boldsymbol{k}_\perp)$, nevertheless assuming the target redshift to map between wavelength/angle and co-moving units.

The total power spectrum of fluctuations in the specific intensity is then:

$$P_{\rm tot}(k_\parallel, \boldsymbol{k}_\perp) = P_t(k_\parallel, \boldsymbol{k}_\perp) + \frac{1}{\alpha_\parallel \alpha_\perp^2} P_i\left(\frac{k_\parallel}{\alpha_\parallel}, \frac{\boldsymbol{k}_\perp}{\alpha_\perp}\right). \tag{4.8}$$

The first term on the right hand side is the underlying "target" power spectrum that we seek to determine while the second term arises from the distorted interloper contamination. In the case that the target and interloper line redshifts are quite different – as will often be the case for high redshift intensity mapping observations – the distortion factors $\alpha_\parallel$ and $\alpha_\perp$ will differ significantly from unity and from each other. Interestingly, provided the target line is at higher redshift than the interloper lines, $\alpha_\parallel$ will be larger than unity, while $\alpha_\perp$ will be smaller than unity. In other words, the interloper fluctuations that appear at a given $k_\parallel, \boldsymbol{k}_\perp$ arise from modes that have *smaller* line of sight wavenumber and *larger* transverse wavenumber than supposed. Provided $P_i(k_\parallel/\alpha_\parallel, \boldsymbol{k}_\perp/\alpha_\perp)$ is a decreasing function of $k_\parallel$ and $\boldsymbol{k}_\perp$, the distortion then enhances the power for line of sight wavemodes relative to the transverse modes. As we will see, the shifting of power and the anisotropy induced from these coordinate re-mappings may potentially be used to separate out the target and interloper emission at the power spectrum level.

To provide quantatative information, Fig. 4.1 plots the distortion factors as a function of the interloper redshift for a few example target redshifts. Clearly the distortion factors are quite different from unity and from each other in the case that the target and interloper redshifts are widely separated.

Naturally, in the more general case that N important interlopers contribute to the power spectrum of fluctuations Equation 4.8 generalizes to:

$$\begin{aligned} P_{\rm tot}(k_\parallel, \boldsymbol{k}_\perp) =& P_t(k_\parallel, \boldsymbol{k}_\perp) \\ &+ \sum_{j=1}^{N} \frac{1}{\alpha_\parallel(z_j)\alpha_\perp^2(z_j)} P_j\left(\frac{k_\parallel}{\alpha_\parallel(z_j)}, \frac{\boldsymbol{k}_\perp}{\alpha_\perp(z_j)}\right). \end{aligned} \tag{4.9}$$

Here the index j denotes the jth of the N interloper lines, z_j is the redshift of the jth

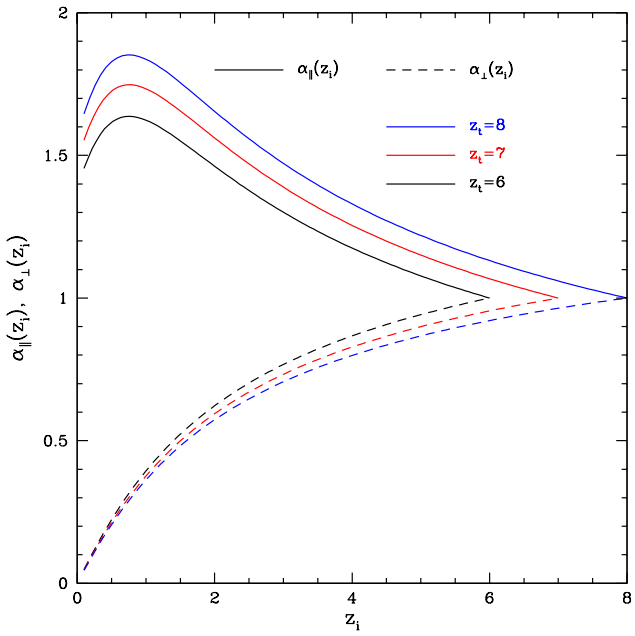

Figure 4.1: Interloper distortion mapping factors, as a function of the interloper redshift, z_i. The solid lines show the line-of-sight distortion factor, $\alpha_{\parallel}(z_i)$, while the dashed lines show the transverse factor, $\alpha_{\perp}(z_i)$. The black, red, and blue lines show target redshifts of $z_t = 6, 7$, and 8 respectively.

interloper emission line, P_j is the specific intensity power spectrum of this emission, and $\alpha_\parallel(z_j)$, $\alpha_\perp(z_j)$ are the distortion factors which depend on both the redshift of the interloper z_j and the target redshift z_t. (We suppress the dependence on the target redshift here to make the notation less cumbersome.) This equation assumes the interlopers and targets are all widely separated in redshift and so independent of each other (otherwise there would be cross-terms), which should be an extremely good approximation in the case considered below.

4.3 Example Application

Although this technique may have a range of applications, we illustrate it through the interesting example case of a hypothetical survey for [CII] emission at $z_t = 7$. Before proceeding further, we very briefly comment on the physics and phenomenology of the [CII] emission line. Recall that the ground state configuration of the five electrons in singly-ionized Carbon is $1s^2 2s^2 2p^1$, and so the ground state has total orbital angular momentum $L = 1$ and total spin angular momentum $S = 1/2$. The [CII] line is emitted in transitions from the higher energy fine structure level with total – orbital plus spin – angular momentum $J = 3/2$ to the lower energy state with $J = 1/2$, i.e. it is a ${}^2P_{3/2} \rightarrow 2P_{1/2}$ transition. The rest-frame wavelength of the transition is $\lambda_r = 157.7\mu$m, the excitation temperature of [CII] is 91 K, and the energy required to ionize CI to CII is 11.2 eV. Since the ionization potential is less than that of neutral hydrogen (13.6 eV) the [CII] emission traces – in part – neutral phases of the interstellar medium (ISM), while the low excitation temperature allows emission from warm/cool regions of the ISM. Consequently, [CII] emission may arise from diverse phases of a galaxy's ISM including photo-dissociation regions at the boundary between molecular clouds and HII regions; from the cold neutral medium; and from HII regions and diffuse ionized gas, provided the local UV radiation field is insufficiently hard to doubly-ionize carbon (see e.g. the recent review by Carilli and Walter 2013).

In low redshift galaxies, the [CII] line is a strong cooling line with a luminosity that is $0.1-1\%$ of the total far-infrared luminosity from the galaxy (Stacey et al. 1991). Despite the diverse set of conditions that can give rise to [CII] emission, the line luminosity is fairly well correlated with the star formation rate, at least at low redshift where there are currently good measurements. This is the case even for low-metallicity dwarf galaxies nearby, although the relation shows larger scatter towards low metallicity (De Looze et al. 2014). Recent observations have started to detect [CII] emission from Lyman-break selected galaxies and quasar host galaxies at $z \gtrsim 6$, although there are also a handful of upper limits tentatively suggesting that high redshift galaxies may mostly lie below local [CII] luminosity star-formation rate correlations (e.g. Knudsen et al. 2016 and references therein). It is hence unclear how luminous reionization-era galaxies will be in the [CII] line. Naturally, one of the main goals of IM is to provide a census of the total [CII] emission: while we have much to learn here, this also makes our forecasts uncertain. In this work we adopt a simplistic approach and assume that local correlations between [CII] luminosity and star-formation rate apply also at high redshift. Likewise, we adopt local correlations to assess the plausible level of interloper contamination. Future targeted observations of individual galaxies using ALMA will be important for refining estimates of the target and interloper line luminosities. It may also be instructive to construct models of the interstellar media of high redshift galaxies to try and *predict* the correlations between line luminosity and star formation rate directly (see e.g. Munoz and Furlanetto 2013).

The central observed wavelength and frequency for our $z_t = 7$ [CII] survey are $\lambda_{\rm obs} = 1.26 \times 10^3 \mu$m, and $\nu_{\rm obs} = 238$ GHz, respectively. The same observed frequencies will be polluted with emission from CO molecules at lower redshift undergoing rotational transitions. A CO molecule transitioning between rotational states J and $J-1$ emits a photon of rest-frame frequency $\nu_J = J \times 115$ GHz. As we will see, several different CO transitions may be significant interlopers for a $z_t = 7$ [CII] emission survey. In addition to the CO lines, additional atomic fine structure lines may also provide non-negligible

interloper emission but, as we detail below, these are subdominant to the CO interlopers in our models.

4.3.1 Target and Interloper Model Power Spectra

To proceed, let us first discuss the general form of the model intensity power spectra for both the target and interloper emission. Incorporating anisotropies from redshift space distortions, our model for the target power spectrum is (Lidz et al. 2011):

$$P_t(k_\parallel, \boldsymbol{k}_\perp) = \langle I_t \rangle^2 \langle b_t \rangle^2 \left(1 + \beta_t \mu^2\right)^2 D\left[\mu k \sigma_p(z_i)\right] P_\rho(k, z_t) + P_{\rm shot,t}. \tag{4.10}$$

Here $\mu = k_\parallel / k$ is the cosine of the angle between the wavevector $\boldsymbol{k}$ and the line of sight direction, $\langle I_t \rangle$ is the average specific intensity of the target emission, and $\langle b_t \rangle$ is the average luminosity-weighted bias of the emitting galaxies. The factor $\left(1 + \beta_t \mu^2\right)^2$ comes from the Kaiser effect (Kaiser 1987), while $D(\mu k \sigma_p)$ quantifies the small scale reduction of redshift-space power from the finger-of-god effect. The parameter $\beta_t = f_\Omega / \langle b_t \rangle$ with $f_\Omega = \frac{\rm dlnD}{\rm dlna}$ denoting the usual logarithmic derivative of the growth factor, which is well approximated by $f_\Omega \approx [\Omega_m(z)]^{0.55}$ (Linder 2005). For the finger-of-god suppression, we assume a Lorentzian form:

$$D(\mu k \sigma_p) = \frac{1}{1 + \sigma_p^2 \mu^2 k^2}, \tag{4.11}$$

and approximate the pairwise velocity dispersion by $\sigma_p(z) = \sigma_v(z)/\sqrt{2}$ with $\sigma_v^2(z)$ being the variance of the line-of-sight component of the velocity field according to linear theory. In our model, we assume pure linear biasing so that $P_\rho(k, z_t)$ denotes the matter power spectrum according to linear theory. Finally, $P_{\rm shot,t}$ is a shot-noise term that arises because the [CII] emitting galaxies are discrete objects. This term is assumed to be independent of scale. Note that we are taking a somewhat simplified model for the redshift-space emission power spectrum: for the most part we work on scales much larger than that of individual halos, but we nevertheless include a finger of god term (owing to virialized motions *within* halos). Although this is a bit inconsistent, the measurements we consider

are mostly confined to large scales where the finger-of god suppression and halo profile have negligible impact. In future work, it may be interesting to refine this model (see e.g. Cooray and Sheth 2002).

The above equation (Equation 4.10) also highlights another potential benefit of measuring the angular dependence of the power spectrum. Although the first term in this equation depends mostly on the product of $\langle I_t \rangle$ and $\langle b_t \rangle$, there is an additional separate dependence on $\langle b_t \rangle$ through the parameter β_t. If the angular dependence of the power spectrum may be measured well enough, this should help in breaking the otherwise perfect degeneracy between $\langle I_t \rangle$ and $\langle b_t \rangle$, and allow one to constrain each of these quantities separately (Lidz et al. 2011).

Similarly, the true interloper power spectrum for the jth interloper (see Equation 4.9) may be written as a function of the true underlying wavenumber components, $k_\parallel$ and $\boldsymbol{k}_\perp$, as:

$$P_j(k_\parallel, \boldsymbol{k}_\perp) = \langle I_j \rangle^2 \langle b_j \rangle^2 \left(1 + \beta_j \mu^2\right)^2 D\left[\mu k \sigma_p(z_j)\right] P_\rho(k, z_j) + P_{\rm shot,j} \tag{4.12}$$

The apparent interloper power is $1/(\alpha_\parallel \alpha_\perp^2) P_j(k_\parallel/\alpha_\parallel, \boldsymbol{k}_\perp/\alpha_\perp)$, where we momentarily suppress the j indices on the distortion factors. Note that under the coordinate transformation of Equations 4.1–4.6 μ maps to $\mu \rightarrow (k_\parallel/\alpha_\parallel)/\sqrt{(k_\parallel/\alpha_\parallel)^2 + (k_\perp/\alpha_\perp)^2}$.

Our model for the total power is then specified by the average specific intensity of the target and interloper emission, $\langle I_t \rangle$ and $\langle I_j \rangle$, the luminosity-weighted average bias factors, $\langle b_t \rangle$ and $\langle b_j \rangle$, and the shot-noise terms, $P_{\rm shot,t}$ and $P_{\rm shot,j}$. For simplicity, we generally fix $\langle b_t \rangle = 3$ and $\langle b_j \rangle = 2$ (for each interloper j) in what follows. In the case explored here, the important interlopers are at lower redshift than the target line galaxies and so one expects the interlopers to be less clustered. This should be the case unless the interloper galaxies live in especially massive halos. In some other applications of our method, the interlopers may instead be mostly at higher redshift than the target line emitters. In this case, the interlopers would likely have a higher bias factor than the target line emitters. This would go in the direction of making the interloper emission harder to clean, but this should be

offset in part by the smaller linear growth factor at high redshift. In any case, the impact of the interlopers will depend also on their average specific intensities relative to that in the target line.

In order to determine plausible values for the average specific intensity and shot-noise terms, we seek guidance from empirical correlations between the luminosity in the emission lines of interest and galactic star formation rates. These correlations can be combined with Schechter function fits to the abundance of galaxies as a function of their star formation rate to estimate the remaining quantities of interest, as in Pullen et al. (2013). The Schechter form for the star formation rate function is (Schechter 1976):

$$\phi(\mathrm{SFR})d\mathrm{SFR} = \phi_\star \left(\frac{\mathrm{SFR}}{\mathrm{SFR}_\star}\right)^\alpha \exp\left[-\frac{\mathrm{SFR}}{\mathrm{SFR}_\star}\right]\frac{d\mathrm{SFR}}{\mathrm{SFR}_\star}, \tag{4.13}$$

with α denoting the faint-end slope, and $\mathrm{SFR}_\star$ and $\phi_\star$ giving, respectively, the characteristic star-formation rate and number density.

The average specific intensity in each line can be estimated from the co-moving emissivity in the line according to (Lidz et al. 2011; Pullen et al. 2013):

$$\langle I_L \rangle = \frac{\varepsilon_L}{4\pi\nu_{\mathrm{rest,L}}}\frac{c}{H(z)}, \tag{4.14}$$

where $\nu_{\mathrm{rest,L}}$ is the restframe emission frequency, ε_L is the co-moving emissivity of the line emission, and the line profile has been approximated as a delta function in frequency. We further approximate the luminosity as a linear function of the star formation rate:

$$L = L_0 \frac{\mathrm{SFR}}{1M_\odot \mathrm{yr}^{-1}}. \tag{4.15}$$

Using the Schechter form for the star-formation rate function, it follows that the co-moving emissivity in each line L is (Pullen et al. 2013):

$$\varepsilon_L = \phi_\star L_0 \frac{\mathrm{SFR}_\star}{1M_\odot \mathrm{yr}^{-1}}\Gamma(2+\alpha). \tag{4.16}$$

We adopt the values of $L_0^{\mathrm{CII}} = 6\times10^6 L_\odot$ and the luminosity of the CO transitions given in Visbal and Loeb (2010) (see also Righi et al. 2008). For reference, $L_0^{\mathrm{CO(3-2)}} =$

$7.0 \times 10^4 L_\odot$, while nearby higher order rotational transitions have slightly higher luminosities until the luminosity declines again above CO(7-6). The CO luminosities are based on correlations between the strength of these emission lines and galactic star formation rates, as measured at low redshift, while the [CII] luminosity-SFR relation is normalized to M82. Using the SFR functions from Smit et al. (2012) (adopting their nearest redshift bin for each interloper redshift), we can then estimate the emissivity and average specific intensity according to Equations 4.13–4.16. This gives $\langle I_t \rangle = 5.7 \times 10^2$ Jy str^{-1} for [CII] emission at $z_t = 7$. Likewise, summing over interloper transitions, we find a combined average interloper intensity of $\langle I_{\rm j,combined} \rangle = 7.0 \times 10^2$ Jy str^{-1}, after including all non-negligible CO lines. Interestingly, the interloper and target contributions are comparable and so it will indeed be important to disentangle these two contributions. The top panel of Fig. 4.2 gives further information, quantifying which interloper lines contribute most prominently to the total average intensity. According to our estimate, several distinct lines contribute significantly with the CO(4-3) at $z = 0.88$, CO(5-4) at $z = 1.4$, CO(6-5) at $z = 1.8$, and CO(7-6) at $z = 2.3$ transitions each contributing more than 10^2 Jy str^{-1}. While these simple estimates provide a useful guide, we caution that they adopt simplistic assumptions about the relationship between star-formation and luminosity, and extrapolate empirical correlations beyond the redshifts at which they have been determined. (See also the discussion in the beginning of this section.) Our results are nevertheless broadly consistent with previous estimates in Silva et al. (2015), but differ in the details of the modeling and the empirical constraints adopted. Given the uncertainties in the signal and interloper strengths, we aim to devise a flexible approach for separating the interloper and target emission signals.

We also checked the impact of interloper emission from additional fine structure lines: [CI] 610μm at $z = 1.1$, [CI] 371μm at $z = 2.4$, [NII] 205μm at $z = 5.2$, and [OI] 145μm at $z = 7.7$[1]. In our model, the strongest of these lines is [CI] 371μm which has an average

[1]The latter line is at slightly higher redshift than the target line, and so might instead be referred to as an "extraloper" line.

specific intensity of $\langle I_{\mathrm{CI},371\mu\mathrm{m}}\rangle = 54$ Jy str^{-1}, and so it contributes less than 10% of the target emission. As justified further in the next paragraph, we neglect these potential interlopers in this work.

In order to quantify the relative importance of the interloper transitions to the power spectrum of intensity fluctuations, which is ultimately the signal we are after, we need to consider more than just the average specific intensity. Equations 4.12 and 4.10 imply that the relative strengths of the fluctuations depend mostly – asides for the shifting of power in wavenumber – on $P_j \propto \langle b_j\rangle^2\langle I_j\rangle^2 D^2(z_j)/\left[\alpha_\parallel(z_j)\alpha_\perp^2(z_j)\right]$, with $D(z_j)$ being the linear growth factor at redshift z_j. This applies on large scales where shot-noise contributions are negligible. We plot the relative strength of fluctuations, as characterized by this one number, in the bottom panel of Fig. 4.2. In comparison to the average specific intensity, this number is enhanced for the lower J transitions because the distortion factor $1/\left(\alpha_\parallel(z_j)\alpha_\perp^2(z_j)\right)$ and the growth factor $D(z_j)$ increase towards lower redshift. For the power spectrum of fluctuations, the dominant emission comes from the CO(4-3) line in this model, and the fluctuations in this line are more than a factor of two larger than in the target [CII] line. Fluctuations from CO(3-2), CO(5-4), and CO(6-5) each contribute between $5-20\%$ of the total interloper fluctuations. Higher order transitions contribute less than several percent to the interloper fluctuations, and we will assume they contribute negligibly in what follows. The same is true of the [CI], [NII], and [OI] interloper/extraloper lines discussed above, and so we neglect them as well. We will discuss relaxing this assumption where appropriate; it is straightforward to include additional interloper lines in our calculations, but this adds additional parameters to the modeling.

In addition to the clustering term, we should also consider the shot-noise contribution to the power spectrum from the target and interloper lines. This contribution may also be estimated from the $L-SFR$ correlation, and the observed SFR Schechter function fits. Specifically, we expect the shot-noise from galaxies emitting in line L to be (e.g. Uzgil et al. 2014):

$$P_{\mathrm{shot,L}} = \frac{\langle I_L\rangle^2}{\phi_\star}\frac{2+\alpha}{\Gamma(2+\alpha)}. \tag{4.17}$$

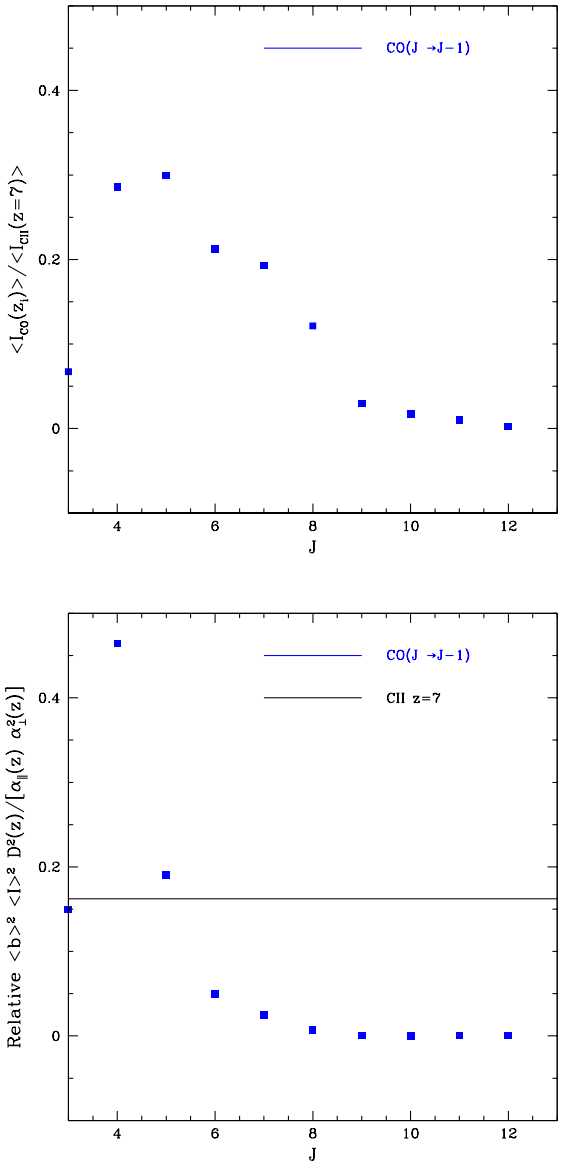

Figure 4.2: Relative importance of interloper lines to the average specific intensity and to the power spectrum of intensity fluctuations. (*Top*) The estimated intensity of different interloper transitions, CO$(J \to J-1)$ as a function of J, relative to the model [CII] target emission intensity. (*Bottom*) The y-axis shows a factor that determines the relative contribution of different interloper lines to the total power spectrum of intensity fluctuations (see text). The normalization has been set here so that the factor sums (over all lines) to unity. The black horizontal line shows the same factor for the target line, [CII] at $z = 7$.

Using the numbers from Smit et al. (2012) for $\phi_\star$ and α, we find $P_{\rm shot,t} = 2.9 \times 10^5$ Jy^2 str^{-2} $\left(\mathrm{Mpc}\, h^{-1}\right)^3$ for the target emission line. Summing over all of the interlopers, up to and including the CO(6-5) transition gives $P_{\rm shot,j,combined} = 1.2 \times 10^7$ Jy^2 str^{-2} $\left(\mathrm{Mpc}\, h^{-1}\right)^3$, after including the distortion factors. The shot-noise from the interlopers is hence almost 50 times that in the target emission. In this work we will consider the combined target plus interloper shot-noise as a single "nuisance" term that we aim to subtract out.

4.3.2 Apparent Interloper and Signal Power Spectra

We now turn to examine the model signal and interloper power spectra. As a first convenient way of characterizing the target and interloper power spectra, we expand the spectra in terms of Legendre polynomials and calculate the monopole and quadropole moments. The quadropole-to-monopole ratio may be written as

$$Q(k) = \frac{\frac{5}{2}\int_{-1}^{1} d\mu \left[3\mu^2/2 - 1/2\right] P(k,\mu)}{\frac{1}{2}\int_{-1}^{1} d\mu P(k,\mu)}. \tag{4.18}$$

We can calculate the intrinsic target quadropole to monopole ratio, as well as that for the apparent interloper power spectra, incorporating the distortions as described by Equations 4.8–4.12.

The spherically averaged (monopole) power spectra are shown in the left panel of Fig. 4.3. The solid black line shows the target [CII] emission power spectrum at $z_t = 7$, $k^3 P_t(k)/(2\pi^2)$. In this model, the [CII] power spectrum has a strength of about $\Delta^2 \approx 10^2$ Jy^2 str^{-2} at $k \sim 0.01\ h$ Mpc^{-1}, $\Delta^2 \approx 3 \times 10^5$ Jy^2 str^{-2} at $k \sim 1\ h$ Mpc^{-1}, and reaches $\Delta^2 \approx 1.5 \times 10^7$ Jy^2 str^{-2} at $k \sim 10\, h$ Mpc^{-1}. The clustering term dominates on large scales at $k \lesssim 3\ h$ Mpc^{-1} or so, while the shot-noise term is more important on smaller scales. The blue-dashed and red-dotted lines show the interloper contamination power, with and without coordinate distortions, respectively. For each interloper line, the coordinate distortions shift power from $k_\parallel \to k_\parallel/\alpha_\parallel(z_j)$ and from $\boldsymbol{k}_\perp \to \boldsymbol{k}_\perp/\alpha_\perp(z_j)$, while boosting the fluctuation power by the overall $1/(\alpha_\parallel(z_j)\alpha_\perp^2(z_j))$ factor. After spherical averaging, this

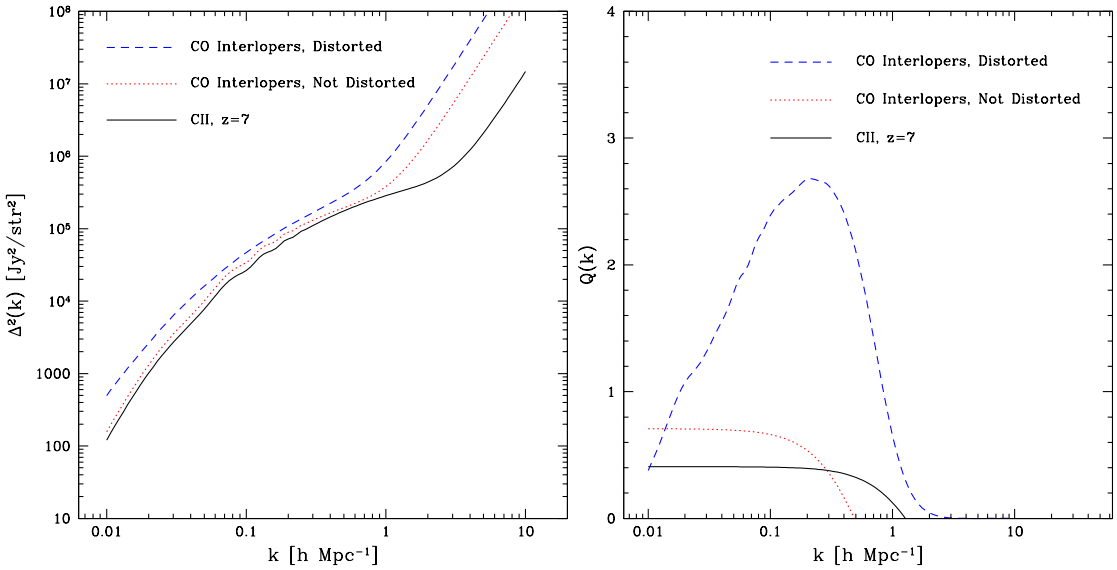

Figure 4.3: Monople and quadropole to monopole ratios for the interloper and signal power spectra. (*Left*) The power spectrum monopole, multiplied by $k^3/(2\pi^2)$ so that each line shows the usual spherically-averaged contribution to the variance per $\ln(k)$. The lower black solid line shows our model for the target [CII] intensity fluctuation power at $z_t = 7$. The blue dashed line shows our model for the total CO$(J \to J-1)$ contamination including the impact of the coordinate distortions. The red dotted line shows the true total interloper power spectrum monopole, neglecting the remapping effects. (*Right*) The quadropole to monopole ratio of the power spectra in each case. The true power spectra are anisotropic only because of the Kaiser and finger-of-god effects, while incorporating the remapping distortions boosts the interloper quadropole to monopole ratio on large scales. These ratios turn over on small scales (high k) due to the finger-of-god effect and shot-noise contamination.

leads to a shift and boost in the apparent interloper power, as may be discerned by comparing the blue dashed and red dotted lines in Fig. 4.3. As anticipated in the previous section, the combined CO interloper power exceeds the target [CII] emission power by a factor of several on large scales – the precise excess depends on scale because of the coordinate distortions – and so it is crucial to remove this contamination. On smaller scales the target and interloper power differ because of the larger Poisson noise from the interloper populations: we expect the interloper shot-noise to swamp that in the [CII] target emission. The larger interloper shot-noise mostly results because star-formation occurs in lower mass, yet more abundant systems at high redshift and so the Poisson noise in the high redshift target line is relatively low. As mentioned previously, in this work we will be content to extract only the [CII] clustering term and forego trying to separate out the [CII] shot-noise term in the presence of this large interloper contamination.

Although the shape of the target and interloper monopole power differ only subtly, the angular dependence of the target and interloper power is quite different. For example, the right panel of Fig. 4.3 shows the quadropole to monopole ratio for both the target and interloper emission power spectra. For illustration, we show the CO interloper quadropole to monopole ratio both with and without coordinate mapping distortions. The quadropole to monopole ratio for the target emission, and the interloper emission without coordinate mapping distortions, have the usual form expected from redshift space distortions. On sufficiently large scales, $Q \rightarrow (4\beta/3 + 4\beta^2/7)/(1 + 2\beta/3 + \beta^2/5)$ – the Kaiser effect result (Kaiser 1987) – while the quadropole anisotropy diminishes on smaller scales owing to the finger-of-god effect and the isotropic shot-noise term. The intrinsic interloper $Q(k)$ turns over on larger scales (smaller k) than the target $Q(k)$ because the interloper shot-noise term is bigger and because the finger-of-god suppression is stronger at the (lower) redshifts of the interloper lines. The blue dashed line shows the quadropole to monopole ratio after incorporating the coordinate mapping distortion. This *reaches much larger values* than expected from the Kaiser effect, with the model Q peaking near $Q = 2.6$ at $k = 0.2\,h$ Mpc^{-1} before gradually turning over on smaller scales owing to the finger-of-

god effect and shot-noise. This is a direct consequence of the difference between the mapping factors, $\alpha_{\parallel}(z_j)$ and $\alpha_{\perp}(z_j)$, and the shape of the linear power spectrum of density fluctuations. The increasing $Q(k)$ from $k \sim 0.01 - 1\ h\ \mathrm{Mpc}^{-1}$ reflects the steepening of the power spectrum spectral index towards small scales. This can be verified by calculating the quadropole to monopole ratio for a pure power law power spectrum (of varying spectral index) under the coordinate warping transformation. The steeper k dependence at small scales enhances the difference between the line of sight and transverse power after applying the warping. Note that on scales larger than the co-moving horizon size at matter radiation equality, $k \leq k_{\mathrm{eq}} \sim 0.015\ h\ \mathrm{Mpc}^{-1}$, the net interloper distortion is sub-Kaiser because the linear matter power spectrum is an increasing function of k on these scales.

In order to further characterize and visualize the target and interloper power spectrum anisotropies, we plot contours of constant power in the $k_{\perp} - k_{\parallel}$ plane (Fig. 4.4, see also Gong et al. 2014). The left panel illustrates the redshift space distortion in the target emission. As mentioned earlier, if the large scale anisotropy shown here can be measured accurately, we can determine the luminosity-weighted bias of the emitters in the target line (from the dependence on β_t), as well as the average specific intensity of the target emission (from the overall amplitude of fluctuations). The contours in the right panel show a strong elongation in the $k_{\parallel}$ direction from the coordinate mapping distortion, which sources the strong quadrupole moment shown in Fig. 4.3 as discussed previously. Note that the total interloper power spectrum in our model is the sum of four separate interloper lines from different redshifts, CO(3-2) at $z = 0.407$, CO(4-3) at $z = 0.877$, CO(5-4) at $z = 1.35$, CO(6-5) at $z = 1.82$. The total anisotropy of the interloper emission, illustrated in Fig. 4.3 and Fig. 4.4 hence reflects a weighted average of these four interloper lines, with the CO(4-3) line having the strongest weight in our model (see the bottom panel of Fig. 4.2).

It is also worth noting that while the Kaiser effect produces vanishing multipole moments beyond the octupole, this is not the case for the interloper mapping distortion. In principle, then, it may be possible to separate the interloper emission by measuring

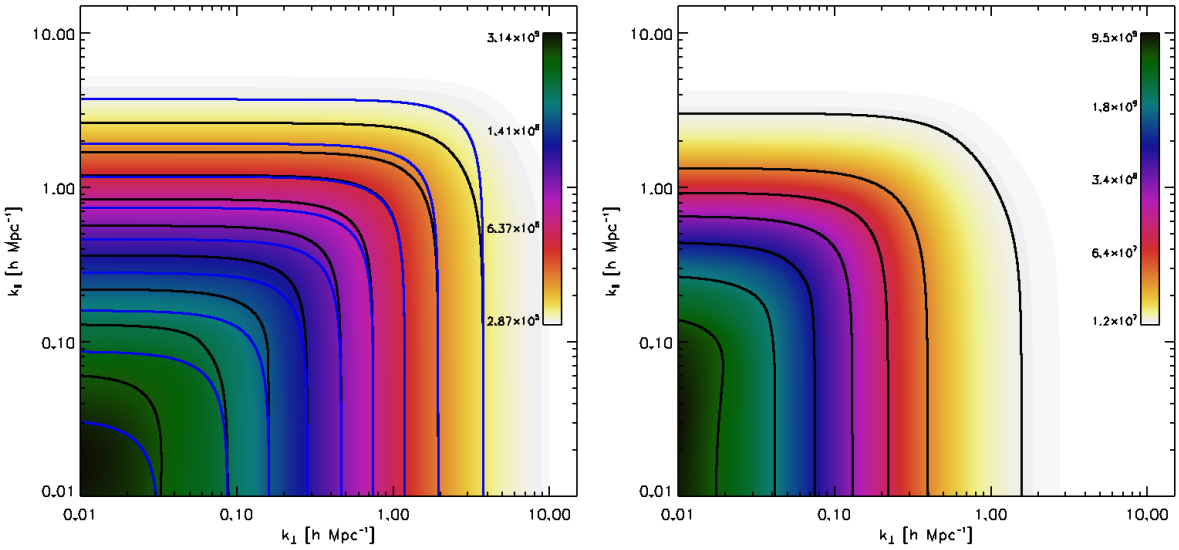

Figure 4.4: Anisotropy of the target and interloper power spectra from redshift space and coordinate mapping distortions. (*Left*) Contours of constant power in the $k_\perp - k_\parallel$ plane for the target [CII] power spectrum at $z_t = 7$. The blue contours neglect redshift space distortions, while the black contours and color-scale incorporate them. On large scales, the power spectra show the Kaiser enhancement for wave numbers in the line of sight direction. This effect turns around and the contour just past $k \sim 1\ h\ \mathrm{Mpc}^{-1}$ is nearly isotropic, with the finger-of-god effect dominating at slightly higher k until isotropic shot-noise dominates. The colorbar is in units of $(\mathrm{Jy\ str}^{-1})^2(\mathrm{Mpc}\ h^{-1})^3$. The lowest contour is at $P(k) = 5 \times 10^5 (\mathrm{Jy\ str}^{-1})^2\ (\mathrm{Mpc}\ h^{-1})^3$ and the contours increase inwards as $d\ln P = 1$. (*Right*) The black contours and color-scale show the anisotropy of the total interloper emission power spectrum including the coordinate mapping distortion. The lowest contour is at $P(k) = 1.3 \times 10^7 (\mathrm{Jy\ str}^{-1})^2 (\mathrm{Mpc}\ h^{-1})^3$ and the contours increase inwards as $d\ln P = 1$. The interloper anisotropy is much stronger than that in the target line; this can be used to separate-out the interloper contamination.

higher multipole moments which should reflect only the interloper contamination. Here we instead consider fitting the full angular dependent power spectrum using parameterized models.

4.4 Forecasts

Having quantified the power spectrum anisotropy, we now forecast the prospects for using this to separate out the interloper and target contributions to the power spectrum. Here we assume that Equtations 4.9–4.12 provide a perfect description of the measured power spectra. We then investigate how well the parameters of the model may be determined by hypothetical [CII] surveys. The shortcoming of this approach is that it relies on simple models for the power spectra of intensity fluctuations, which may be imperfect. In future work, it will be important to develop consistency checks of this model, and/or to develop a more sophisticated description. We discuss some possible observational tests in §4.5 and §4.6.

In general, we consider a seven-dimensional parameter space described by a vector, $\boldsymbol{q}$, with seven components: $\{q_1, q_2, ..., q_7\} = \{\langle I_t \rangle, \langle b_t \rangle, \langle I_{32} \rangle, \langle I_{43} \rangle, \langle I_{54} \rangle, \langle I_{65} \rangle, P_{\rm shot,tot}\}$. The parameters describe the specific intensity of the target emission, the average bias of this emission, the specific intensity of each of the four important interloper lines (indexed by the rotational states of the CO transitions with $J, J-1$ as subscripts: e.g., $\langle I_{32} \rangle$ is the average specific intensity in the $J = 3 \rightarrow 2$ transition), and the total (target plus all interlopers) shot-noise. Here we implicitly fix the bias of the fluctuations in each interloper line to $\langle b_j \rangle = 2$. Since the interloper power is determined mostly by the overall product of specific intensity and bias (asides for the additional dependence on β through the Kaiser effect which is small relative to the anisotropy induced by assuming an incorrect redshift), one can think of the specific intensity constraints derived as confidence intervals on the product $\langle b_j \rangle \langle I_j \rangle$.

Our main goal then is to determine whether the target emission fluctuations, charac-

terized by the parameters $\langle I_t \rangle$ and $\langle b_t \rangle$, may be determined accurately in the presence of the interloper fluctuations. We investigate this by calculating Fisher matrices for futuristic [CII] surveys. The components of the Fisher matrix for parameters q_i and q_j are given by:

$$F_{ij} = \int_{\mu_{\rm min}}^{\mu_{\rm max}} d\mu \times \int_{k_{\rm min}}^{k_{\rm max}} \frac{dk k^2 V_s}{4\pi^2} \frac{\partial P(k,\mu)}{\partial q_i} \frac{\partial P(k,\mu)}{\partial q_j} \frac{1}{{\rm var}[P(k,\mu)]}, \tag{4.19}$$

where we have approximated the discrete sum over modes in the survey by a continuous integral. Here the integral over angle runs over the upper half-plane, between some (k-dependent) limits $\mu_{\rm min}$ and $\mu_{\rm max}$ that we will describe below, and the integral over wavenumber ranges between the limits $k_{\rm min}$ and $k_{\rm max}$. The quantity V_s is the co-moving volume of the survey. This expression depends on that variance of the total power spectrum of fluctuations for each k-mode, var$[P(k,\mu)]$. We compute this, neglecting non-Gaussian contributions to the variance, as:

$${\rm var}[P(k,\mu)] = [P_{\rm tot}(k,\mu) + P_N(k,\mu)]^2 . \tag{4.20}$$

Here $P_{\rm tot}(k,\mu)$ is the total signal plus interloper emission power spectrum, including the shot-noise contribution, and $P_N(k,\mu)$ is the detector noise power spectrum.

It is also instructive to consider the number of Fourier modes in the upper-half plane in a bin of k and μ, $N_m(k)$. For a survey of co-moving volume V_s, the number of modes contained within the survey volume in a wavenumber bin of thickness $\Delta\ln(k)\Delta\mu$ is:

$$N_m(k) = \frac{k^3 V_s}{4\pi^2} \Delta\ln(k) \Delta\mu . \tag{4.21}$$

Note that this is just included for illustration, since the mode-counting is already handled implicitly in the Fisher matrix calculation (Equation 4.19).

4.4.1 Survey Parameters

It will be challenging to measure the power spectrum and its angular dependence precisely enough to separate the faint interloper and target signals using this methodology.

Nevertheless, experiments are already underway to detect the reionization-era [CII] signal (e.g. the TIME-Pilot experiment, Crites et al. 2014); we anticipate that the sensitivity of these measurements will increase rapidly, fueled by advances in detector technology. As a convenient baseline, we consider the "CII-Stage II" survey described in Silva et al. (2015). Unfortunately, we find that even this is less sensitive than we require and so we generally consider a still more sensitive experiment, as specified subsequently.

Our baseline survey is described in Silva et al. (2015) and consists of a single 10 meter dish, with 16,000 bolometers and an $N_{\rm sp} = 64$-beam spectrometer with a frequency resolution of $\Delta\nu = 0.4$ GHz. The hypothetical survey spans 100 deg^2 on the sky for a total observing time of $t_{\rm survey}$ =2,000 hours. We consider a $B = 20$ GHz bandwidth of observations near $z = 7$, which is small enough for us to neglect evolution in the signal across the survey bandwidth. The angular resolution of the survey is $\Delta\theta = 0.43$ arcminutes. In co-moving coordinates, the pixels span $x_{\perp,res} = 0.790$ Mpc h^{-1} in the transverse direction and $x_{\parallel,res} = 3.42$ Mpc h^{-1} in the line of sight direction. In the line of sight direction, the survey length is $L_\parallel = 171$ Mpc h^{-1}, while the transverse dimension is $L_\perp = 1.09 \times 10^3$ Mpc h^{-1}. The total survey volume is $V_s = 2 \times 10^8 ({\rm Mpc}\, h^{-1})^3$. For reference, the number of modes surveyed is $N_m(k) = 5.2 \times 10^3 (k/0.1\, h\, {\rm Mpc}^{-1})^3 \Delta\ln(k) \Delta\mu$ in a bin around $k = 0.1\, h\, {\rm Mpc}^{-1}$.

The survey noise power spectrum may be written as (e.g. Uzgil et al. 2014):

$$P_N(k_\parallel, k_\perp) = \frac{\sigma_N^2}{t_{\rm obs}} V_{\rm pix} e^{(k_\parallel x_{\parallel,res})^2 + (k_\perp x_{\perp,res})^2}, \tag{4.22}$$

where $\sigma_N^2/t_{\rm obs}$ is the noise per pixel in specific intensity units (squared), $V_{\rm pix}$ is the pixel volume, and the exponential factor accounts for the finite angular and spectral resolution of the instrument. We can extract plausible numbers for the noise power spectrum from Table 8 of Silva et al. (2015), converting from the Noise Equivalent Flux Density (NEFD) to the specific intensity noise($\times$ square-root of time in seconds), using $\sigma_N = {\rm NEFD}/(\Delta\Omega_{\rm pix})$. Note also that the observing time per pixel is $t_{\rm obs} = t_{\rm survey}\, N_{\rm sp}\, \Delta\Omega_{\rm pix}/\Delta\Omega_{\rm survey}$, where $N_{\rm sp}$ is the number of spatial pixels and $t_{\rm survey}$ is the total survey observing time.

This resulting noise power spectrum is:

$$\frac{\sigma_N^2}{t_{\rm obs}} V_{\rm pix} = 8.7 \times 10^8 \frac{\rm Jy^2}{\rm str^2} \left(\frac{\rm Mpc}{h}\right)^3 \left[\frac{\sigma_N}{3.1 \times 10^5 {\rm Jy/str}\sqrt{\rm sec}}\right]^2 \times \left[\frac{V_{\rm pix}}{2.13({\rm Mpc}/h)^3}\right] \left[\frac{64}{N_{\rm sp}}\right] \left[\frac{2{,}000 \text{ hrs}}{t_{\rm survey}}\right]. \quad (4.23)$$

Since we find that even this sensitivity is insufficient for our purposes, we consider a still more sensitive experiment with $(\sigma_N^2 V_{\rm pix})/t_{\rm obs} = 4.3 \times 10^7 {\rm Jy}^2\ {\rm str}^{-2} ({\rm Mpc}\ h^{-1})^3$. This value represents our fiducial noise level in what follows. We caution that the noise power here is approximately twenty times smaller than in the Stage-II experiment considered by Silva et al. (2015), and so the rms noise in our fiducial case is $4-5$ times smaller than in this previous work. Naturally, it will be important to see if this sensitivity is in fact achievable. Improvements may be possible by going to space, in which case the CMB would set the photon background noise rather than emission from the Earth's atmosphere. Rapid progress in detector development may also help to increase sensitivity beyond what is assumed here, e.g. it may be possible to increase the number of spatial pixels, $N_{\rm sp}$. We will describe how the results depend on this somewhat arbitrary choice of noise power.

It may also be possible to make progress with noisier survey data by masking bright pixels suspected of containing CO interloper emission, while using the anisotropy of the residual fluctuation power spectrum to further clean interloper contamination. In other words, the masking approach advocated in previous work may be combined with the technique developed here. Further work is required to explore whether the two techniques may indeed be combined fruitfully. If one masks pixels suspected of interloper contamination, this should reduce the interloper fluctuation power and make it harder to fit-out interloper contributions. Nevertheless, applying our approach after masking might provide a valuable cross-check: if distinctive anisotropic emission remains, this suggests residual interloper contamination. We expect this combination of techniques to be most valuable in the case that the interloper contamination is stronger than assumed here. Finally, there may be some benefit to a spare-sampling survey strategy to build up a large field-of-view quickly – rather than mapping contiguous regions on the sky – although this

will lead to aliasing from high-k modes (Kaiser 1998; Chiang et al. 2013).

We are almost ready to calculate the Fisher matrix elements using Equation 4.19, but we need to comment first on one additional complication. The issue relates to the continuum foreground, which is significantly larger than the line interloper emission. The continuum emission at the frequencies of interest is dominated by the Cosmic Infrared Background (CIB), produced by dust grains in galaxies at a range of redshifts, and has an average specific intensity of a $\sim$ a few $\times 10^5$ Jy str^{-1} (Silva et al. 2015). Although this is two to three orders of magnitude larger than the expected [CII] emission, the continuum foreground should nevertheless be separable using the fact that it is spectrally smooth, i.e., one can use exactly the same strategy as advocated for cleaning foregrounds from redshifted 21-cm fluctuation measurements (e.g Zaldarriaga et al. 2004). In order to separate the spectrally smooth foreground, however, one inevitably sacrifices measuring long wavelength modes along the line of sight. Additional modes will likely be lost as well, since the frequency dependence of the beam, calibration errors, and instrument imperfections can also produce spurious spectral structure in the foregrounds, *as observed by the instrument*. Here we will ignore this "mode-mixing" problem (e.g. Liu and Tegmark 2011; Ali et al. 2015), and take a simplistic approach: we simply remove line-of-sight modes with wavelength smaller than the bandwidth of the measurement, i.e. modes with line-of-sight wavenumber smaller than $k_{\parallel,\mathrm{min}} = 2\pi/L_\parallel = 0.037\,h\,\mathrm{Mpc}^{-1}$. Further work is required to determine whether measuring the angular dependence of the power spectrum is feasible in the presence of realistic levels of mode-mixing. Mode-mixing should be significantly less bad here than in the case of 21-cm; in part this is because the continuum to line emission ratio is smaller, and also because the instrumental beam is simpler for this single dish experiment.

Before exploring forecasts for marginalized constraints on the parameters $\boldsymbol{q}$, it is instructive to explicitly examine some of the derivatives that enter the Fisher matrix calculation of Equation 4.19. Fig. 4.5 compares the derivatives of the total power spectrum with respect to each of the specific intensity parameters as a function of angle, μ, for

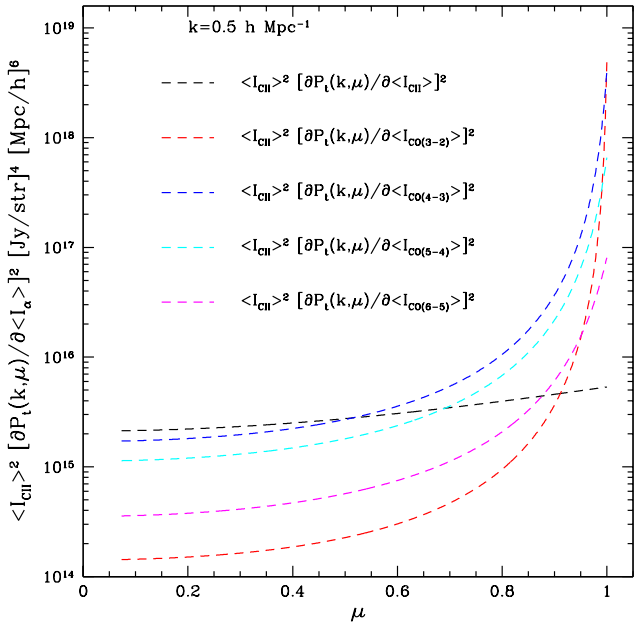

Figure 4.5: Derivatives with respect to average specific intensity in different lines as a function of angle. Here the power spectrum derivatives are computed for $k = 0.5\ h$ Mpc^{-1}. The derivatives are much stronger functions of angle for the interloper line – owing to the coordinate distortions – than for the target [CII] emission, which depends on angle only through the Kaiser effect. The low order CO transitions show a stronger dependence on angle because their coordinate distortions are larger.

fixed $k = 0.5\ h$ Mpc^{-1}. The range of μ accessible is limited slightly by removing the spectrally smooth modes with $k_\parallel \leq 2\pi/L_\parallel$ to $\mu \geq \mu_{\rm min} = k_{\parallel,{\rm min}}/k = 0.074$ for $k = 0.5\ h$ Mpc^{-1}. The derivatives with respect to the interloper line intensities show a steeper angular dependence than the target emission, as expected. This is because the interlopers are subject to the coordinate distortion, while the target line depends on angle primarily through the Kaiser effect (at the wavenumber considered, the finger of god effect is subdominant). A simple way to understand the angular dependence of the interloper power is to note that, approximating the power spectrum at the wavenumber of interest by a power-law of spectral index $k^{-n_{\rm eff}}$, the ratio of the power at $\mu = 1$ to that at $\mu = 0$ is simply $(\alpha_\parallel(z_j)/\alpha_\perp(z_j))^{n_{\rm eff}}$. This rough estimate ignores the Kaiser effect, which will further enhance this ratio. For $k = 0.5$ h Mpc^{-1}, $n_{\rm eff} = -d{\rm ln}P/d{\rm ln}k = 2.1$[2] , and this ratio is 110 for the strongest case of the CO(3-2) interloper distortion. The derivative shown is proportional to the square of this number and so the ratio reaches four orders of magnitude, and the result in Fig. 4.5 is still slightly larger because it includes the Kaiser distortion.

In any case, Fig. 4.5 further motivates that the angular dependence can be used to separate the target and interloper contributions to the power spectrum if it can be measured with small enough error bars. In addition, comparing the angular dependence of the derivatives with respect to the intensity in the various lines gives some sense for which lines will be most degenerate with each other. For example, the weaker angular dependence of the target line derivative suggests that $\langle I_{\rm CII}\rangle$ should not be strongly degenerate with the intensities in the interloper lines, provided the full angular range shown is well-measured. This should be especially so in comparison to the low-order transitions that show the strongest angular variation. On the other hand, we expect the intensity in the CO(4-3) and CO(5-4) lines to be more degenerate given their relatively similar redshifts and distortion factors.

We now turn to calculate the Fisher matrix of Equation 4.19, and invert this matrix

[2] A more detailed estimate would also take into account that the local spectral index should really be evaluated separately at each of $k/\alpha_\parallel$ and $k/\alpha_\perp$.

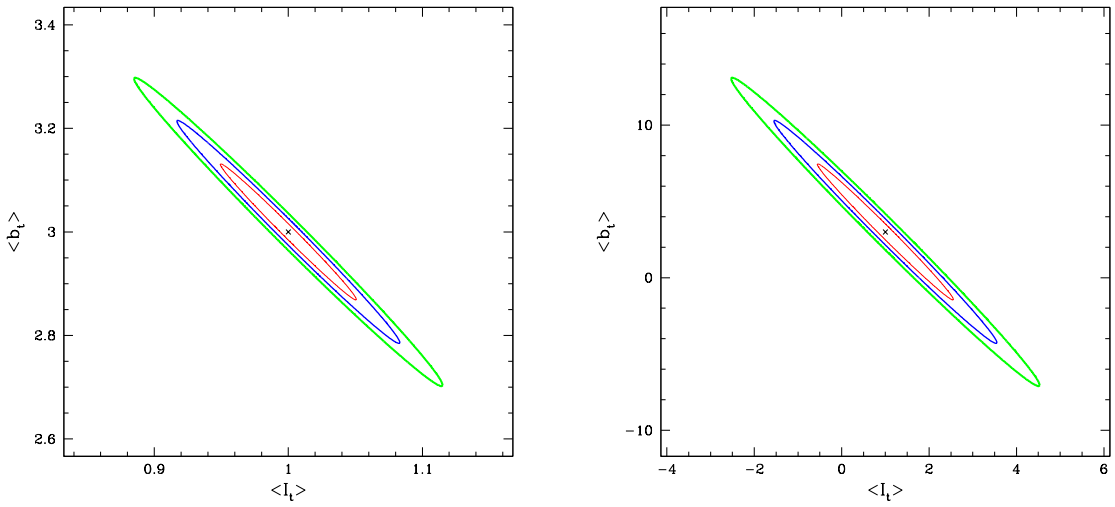

Figure 4.6: Forecast of constraints in the $\langle I_t \rangle - \langle b_t \rangle$ plane, marginalized over the interloper contamination and shot-noise parameters for two noise levels. *Note that the range of values shown along the x and y-axes differ significantly between the two panels.* The red, blue, and green contours show $1, 2$, and $3-\sigma$ confidence intervals, while the "x" marks the assumed central value. (The contours and "x"s have the same meaning in subsequent plots.) The specific intensity, $\langle I_t \rangle$, has been expressed in units of the our fiducial model value, $\langle I_t \rangle = 5.7 \times 10^2$ Jy str^{-1}. (*Left*) In this case, a sample-variance limited experiment is shown, i.e., the noise power spectrum is taken to be negligibly small. (*Right*) Here the noise power spectrum instead follows Equation 4.23, as expected for the "stage-II" [CII] survey. Evidently, the target fluctuations can be extracted using the angular dependence of the emission power spectrum but greater sensitivity is required than in the hypothetical stage-II survey. Note that we allow regions in parameter space where the parameters are negative. In practice, one might invoke a prior to exclude such regions as unphysical.

to find the constraints on the various parameters. We first consider the constraints on the target signal, contrasting the results for the stage-II survey with noise power at the level of Equation 4.23 and a sample-variance (also known as "cosmic-variance") limited survey, with negligibly small noise power, over the same volume. The left panel of Fig. 4.6 shows the projected errors in the $\langle I_t \rangle - \langle b_t \rangle$ plane, marginalized over the interloper parameters. The contours show that the hypothetical sample-variance limited survey is capable of constraining $\langle I_t \rangle$ and $\langle b_t \rangle$, even in the presence of strong interloper contamination. Quantitatively, we forecast $\sim 3\%$ level $1-\sigma$ marginalized constraints on these parameters in the sample variance limit. The ellipse shows the expected strong degeneracy between increasing $\langle I_t \rangle$ and decreasing $\langle b_t \rangle$; nevertheless, the Kaiser effect allows separate constraints on the two parameters although they are highly correlated. However, it is hard to achieve the requisite sensitivity given the bright night sky at these frequencies. If we instead incorporate noise at the level of Equation 4.23, the marginalized errors blow up considerably, as illustrated by the right panel of Fig. 4.6. In this case the marginalized constraints on the average specific intensity and the bias only give $1-\sigma$ detections – i.e., without attempting to mask interloper emission, a significant detection is not possible for this survey.

For now, we simply consider a more sensitive experiment with $(\sigma_N^2 V_{\rm pix})/t_{\rm obs} = 4.3 \times 10^7 {\rm Jy}^2\ {\rm str}^{-2} ({\rm Mpc}\ h^{-1})^3$. The $\langle I_t \rangle - \langle b_t \rangle$ results, marginalized over the interloper parameters, are shown for this level of noise in Fig. 4.7. Unless otherwise noted, we adopt this value for the noise power spectrum in what follows. In this case, 20% level constraints on the target emission parameters are achievable (at $1-\sigma$) and the target and interloper emission fluctuations can indeed be separated.

The [CII] emission signal at $z \sim 7$ may also be stronger than in the model considered here, which could relax the stringent requirements on the noise power spectrum found here. Indeed, as we were finalizing this manuscript we learned of similar work by Cheng & Chang (2016, in prep).[3] These authors' model gives a $z = 6$ [CII] emission signal

[3]Thanks to the "Opportunities and Challenges in Intensity Mapping Workshop" held at Stanford.

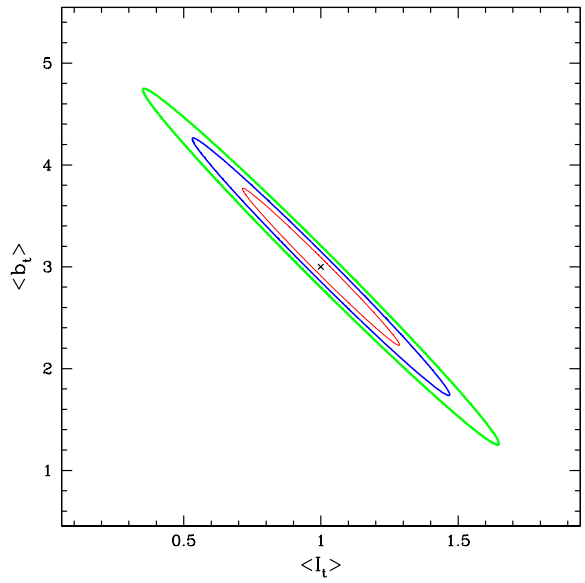

Figure 4.7: Forecast of constraints in the $\langle I_t \rangle - \langle b_t \rangle$ plane, marginalized over the interloper contamination and shot-noise parameters for our fiducial noise power spectrum. Identical to Fig. 4.6, except for our fiducial noise level (see text).

that is more than an order of magnitude larger than our $z = 7$ predictions, and so they are more optimistic about the prospects of applying this method using upcoming datasets. For the most part, the difference stems from the larger bias factor in their model, with $\langle b_t \rangle^2$ almost six times as large as in our calculations. Their bias factor comes from relating the line luminosity to the CIB and from empirically-calibrated models connecting CIB luminosity and halo mass. Since most of the CIB emission comes from lower redshift, the $z = 6-7$ predictions are still, however, uncertain. In any case, this further illustrates the uncertainties in forecasting the expected signal. Improved constraints on the relationships between line-luminosity, star formation rate, and halo mass, will be needed to refine our predictions for the target and interloper emission fluctuations.

It is also helpful to examine the constraints on the interloper emission parameters. Some example confidence intervals are shown in Fig. 4.8. The left hand panel shows the joint forecasted constraints in the $\langle I_{CII} \rangle - \langle I_{CO(4-3)} \rangle$ plane. This plane is of special interest because our model predicts that emission in the CO(4-3) line actually provides the largest contribution to the total power spectrum (Fig. 4.2). Interestingly, the constraints on the CO(4-3) intensity and the [CII] intensity show little degeneracy. This is actually unsurprising given the differing angular dependence of the Fisher matrix derivatives illustrated in Fig. 4.5, and the sensitive hypothetical survey we consider. However, the different interloper lines themselves *are* rather degenerate with each other. This higher level of degeneracy results because the pairs of interloper lines are much closer together in redshift than the interloper-target pairs. As a result, the interloper pairs have similar distortion factors, $\alpha_\parallel$ and $\alpha_\perp$, and their power spectra hence show almost the same angular dependence. For example, the right hand panel of Fig. 4.8 gives confidence intervals in the $\langle I_{CO(4-3)} \rangle - \langle I_{CO(5-4)} \rangle$ plane, and this reveals the expected strong anti-correlation between the emission in these two lines. Quantitatively, the correlation coefficient in this plane is $\rho = -0.81$. After marginalizing over all of the interloper parameters, the error bars on the average intensity of each interloper line are large: in our fiducial case, we only expect a greater than $2-3-\sigma$ detection of $\langle I_{CO(4-3)} \rangle$, even though we obtain a sig-

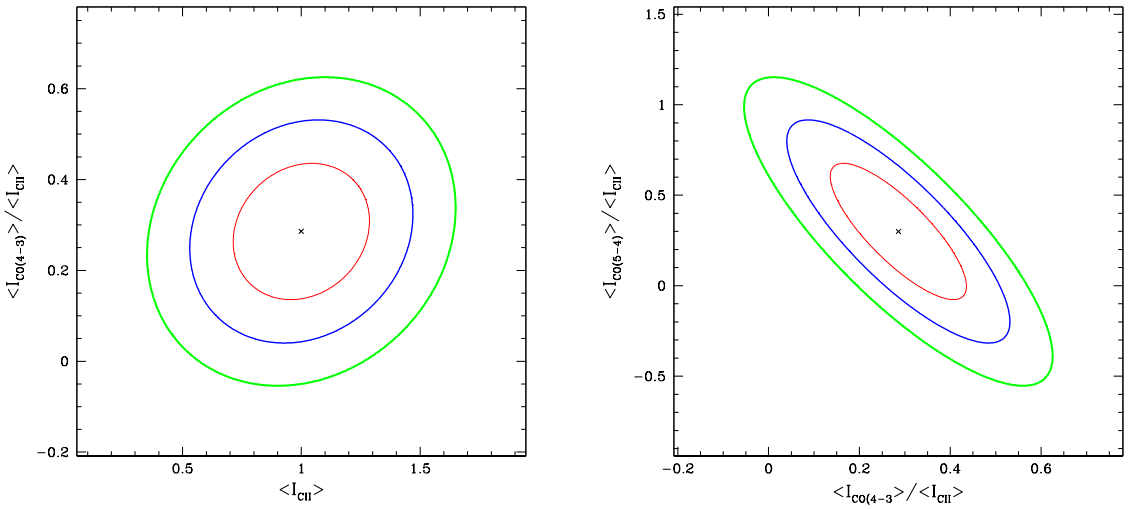

Figure 4.8: Forecasted constraints on the average specific intensity of two of the interloper emission lines. (*Left*) Constraints in the $\langle I_{CII}\rangle - \langle I_{CO(4-3)}\rangle$ plane. The fractional error is larger for the interloper emission than for the target emission. This is because the average specific intensity of the target line is larger, and because the intensity of this interloper line is highly degenerate with that of other interloper lines. (*Right*) Constraints in the $\langle I_{CO(4-3}\rangle - \langle I_{CO(5-4)}\rangle$ plane. The constraint ellipses show a strong degeneracy, since increasing the strength of one interloper line may be mostly compensated by reducing the strength of another line. As in Fig. 4.6, we allow unphysical regions where the parameters are negative.

nificant detection ($\geq 5-\sigma$) of the [CII] target emission line. For reference, our fiducial survey numbers forecast detections of the specific intensity in the CO(3-2) and CO(5-4) lines at only slightly better than $1-\sigma$, while the CO(6-5) specific intensity is still less detectable.

In summary, the angular dependence of the emission fluctuations can be used to separate the target and interloper emission fluctuations if the noise power spectrum is sufficiently small. Since the main goal is to extract information about the target [CII] emission, perhaps it is not a big concern that the individual CO interlopers are themselves somewhat degenerate, and the constraints on these parameters are weaker. However, further checks seem valuable given that our approach relies on having a good model for each source of emission fluctuations.

4.5 Cross-Correlating with LSS Tracers

Fortunately, there are other approaches we can pursue as further cross checks on the analysis of the previous section, some of which should enable separate constraints on each interloper line. First, we can correlate the intensity mapping data cubes with spectroscopic galaxy and/or quasar catalogues at the interloper redshift (Silva et al. 2015). We expect that by the time [CII] intensity mapping experiments are underway, there will be other extensive large-scale structure surveys, spanning large fields of view and overlapping in redshift with the prominent CO interloper transitions. We can use cross-correlations with LSS tracers at different redshifts to separately constrain the parameters of each of the various CO interloper lines.

For instance, consider the cross power spectrum between interloper line j and the abundance of spectroscopic galaxies at the same redshift, z_j. Suppose the average bias of these tracer galaxies is $\langle b_{\rm gal} \rangle$. In order to extract the cross spectrum of interest, it is convenient to convert from angles and wavelengths to co-moving units assuming the interloper redshift z_j, rather than the target [CII] redshift, z_t. The target line and the other

interloper lines will not contribute on average to the cross spectrum with the LSS tracer at z_j since these lines originate at significantly different redshifts, but they will contribute to the *variance* of the cross spectrum, as we will describe. For this purpose, the total power spectrum of intensity fluctuations from line emission is computed along the lines of Equation 4.9, except that the warping is now relative to the coordinates of an interloper at redshift z_j. The cross power spectrum with the galaxy tracer field is then:

$$\begin{aligned} P_x(k,\mu) =& \langle I_j \rangle \langle b_j \rangle \langle b_{\rm gal} \rangle \left(1+\beta_j \mu^2\right) \left(1+\beta_{\rm gal} \mu^2\right) \\ & \times D\left[\mu k \sigma_p(z_j)\right] P_\rho(k, z_j), \end{aligned} \tag{4.24}$$

where $\beta_j = f_\Omega(z_j)/\langle b_j \rangle$ and $\beta_{\rm gal} = f_\Omega(z_j)/\langle b_{\rm gal} \rangle$ are the Kaiser parameters for the interloper line and the galaxy density field, respectively. We have assumed here that the finger-of-god suppression has an identical form for the IM galaxies and for the LSS tracer population at the same redshift; although this is unlikely true in detail, we expect this simplification to have little impact on our results. Here for simplicity we have also assumed that the CO emitting populations and the tracer galaxies are largely disparate populations; otherwise, there should be an additional shot-noise term in Equation 4.24. In any case, if the cross spectrum can be measured accurately enough we can infer constraints on $\langle I_j \rangle$, $\langle b_j \rangle$, and $\langle b_{\rm gal} \rangle$, or at least their overall product. One final caveat here, however, is that we have not included a stochasticity parameter "r" in the above equation and so we are implicitly assuming that the galaxies and interloper populations are perfect tracers of large scale structure on the scales of interest for this measurement. In addition, the auto spectrum of the tracer galaxies may be used to measure $\langle b_{\rm gal} \rangle$. Ideally, future LSS surveys will provide tracer galaxy or quasar samples at the redshifts of each of the prominent CO interlopers. These measurements can then be combined with the angular dependence of the intensity auto spectrum, to further separate the interloper contaminants from the target emission fluctuations.

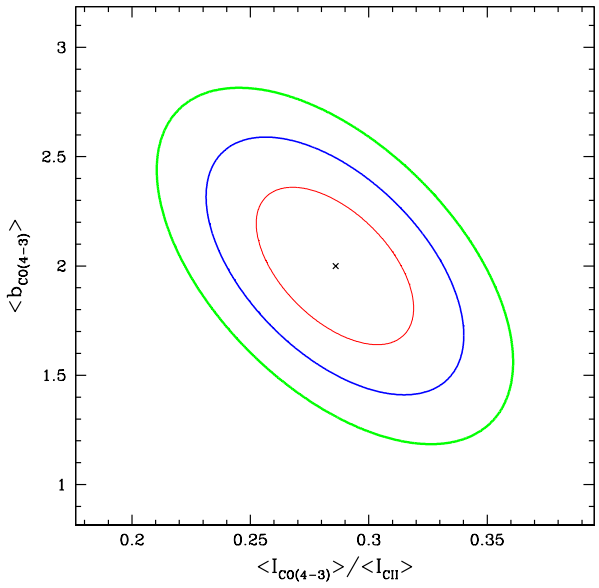

Figure 4.9: Constraints on the parameters of an interloper line (CO(4-3)) from cross-correlating with a large-scale structure tracer at the relevant redshift ($z_j = 0.88$). A 10% prior on $\langle b_{\rm gal} \rangle$ has been incorporated since this parameter will be constrained from measuring the *auto spectrum* of the tracer galaxies. Here $\langle I_{\rm CO(4-3)} \rangle$ is in units of $\langle I_{\rm CII}(z=7) \rangle$, and our fiducial IM noise power spectrum has been assumed.

The variance (per mode) of the cross-spectrum is given by:

$$\mathrm{var}\left[P_x(k,\mu)\right] = \Bigg[P_x^2 + \left(P_{\rm tot}(k,\mu) + P_N(k,\mu)\right) \times \left(P_{\rm gal}(k,\mu) + \frac{1}{n_{\rm gal}}\right)\Bigg], \tag{4.25}$$

where $P_{\rm tot}(k,\mu)$ is the total line intensity power spectrum, except computed here with the distortion factors considered relative to the coordinates at the interloper redshift z_j, $P_N(k,\mu)$ is the noise power spectrum for the intensity mapping survey (Equation 4.22), while $P_{\rm gal}$ and $1/n_{\rm gal}$ are the clustering and shot-noise terms for the tracer galaxies. After specifying the properties of our tracer galaxies and the survey parameters, the cross spectrum Fisher matrix, F_{ij}^x, may be computed along the lines of Equation 4.19:

$$F_{ij}^x = \int_{\mu_{\rm min}}^{\mu_{\rm max}} d\mu \times \int_{k_{\rm min}}^{k_{\rm max}} \frac{dk k^2 V_s}{4\pi^2} \frac{\partial P_x(k,\mu)}{\partial q_i} \frac{\partial P_x(k,\mu)}{\partial q_j} \frac{1}{\mathrm{var}[P_x(k,\mu)]}. \tag{4.26}$$

Here the parameter vector is specified by just three components: $q_\alpha = \{\langle I_j\rangle, \langle b_j\rangle, \langle b_{\rm gal}\rangle\}$.

As an example of the cleaning that may be feasible with future data sets, we consider surveys for narrow emission-line galaxies using the Dark Energy Spectroscopic Instrument (DESI) (Levi et al. 2013). We suppose that the entire volume of the intensity mapping survey is contained within the DESI narrow emission line galaxy survey, which is plausible given that DESI will cover a large-fraction of the full sky. In this case, the number of modes surveyed and the spatial and spectral resolution of the cross spectrum measurement are entirely limited by the intensity mapping survey specifications and the only additional relevant parameters for our Fisher matrix forecasts are the tracer galaxy bias parameters (this fixes $P_{\rm gal}(k,\mu)$ in our linear biasing model), and the abundance $n_{\rm gal}$ which determines the shot-noise contribution to the variance for the DESI galaxies. We adopt the abundance of narrow emission-line galaxies that may be observed by DESI as reported in Levi et al. (2013). In this case, near the redshift of the CO(4-3) interloper emission, we expect a number density of $n_{\rm gal} = 5.2 \times 10^{-4}\ h^3\ \mathrm{Mpc}^{-3}$. The expected

abundance of DESI tracer galaxies at the redshifts of the other prominent interlopers are comparable. Finally, we would like to account for the constraint that will be possible on $\langle b_{\rm gal} \rangle$ from a measurement of the auto-spectrum of the tracer galaxy survey. Note that the DESI emission line galaxies will themselves suffer from interloper contamination (e.g. Pullen et al. 2016) and this will need to cleaned in order to measure the auto-spectrum and $b_{\rm gal}$. Rather than investigate this in detail here, for simplicity we suppose that $b_{\rm gal}$ is measured to 10% fractional accuracy. We believe this is conservative. This is then incorporated as a prior in the cross-spectrum Fisher matrix calculation (Equation 4.26). For the bias of the tracer galaxies, we adopt a central value of $b_{\rm gal} = 2.5$.

Fig. 4.9 shows an example of the constraints that may be obtained for the case of CO(4-3) interloper line emission. Evidently, the cross spectrum with the DESI narrow emission line galaxy sample should allow significantly tighter constraints on $\langle I_{\rm CO(4-3)} \rangle$ than from the total intensity mapping auto spectrum. For our fiducial assumptions, the $1-\sigma$ fractional error bar on $\langle I_{\rm CO(4-3)} \rangle$ improves by a factor of more than four. Similar measurements should be possible for each of the other CO interloper transitions. These cross spectrum measurements should be useful both as a consistency check on the interloper modeling, and can be used in combination with the total intensity mapping auto spectrum to reduce error bars on the target emission parameters. Quantitatively, we can incorporate the DESI-like cross spectrum constraints on the specific intensity of the interloper lines as $(1-\sigma)$ priors in our auto-spectrum Fisher matrix calculations. Doing this, we find that the error bars on the [CII] specific intensity and bias shrink by a factor of 1.5 and 1.4 respectively. Although these numbers are indicative, the precise gain will depend on the noise power spectrum in the IM experiment and on how accurately the auto-spectra of the DESI galaxies are measured.

4.6 Cross Spectrum with Other Lines

Finally, an additional approach to help confirm the presence of target [CII] emission fluctuations is to cross-correlate with a data cube centered on a different frequency that contains emission from another line at the same redshift (e.g. Visbal and Loeb 2010). Indeed, this measurement may potentially be done with the same data set. For example, the hypothetical [CII] survey discussed in Silva et al. (2015) spans 200-300 GHz. In addition to the [CII] 158μ m line at $z = 7$, the same survey should include [OI] emission at $z = 7$ with a rest frame wavelength of 146μ m, at an observed frequency of $\nu_{\rm obs} = 259$ GHz. Further, just outside the fiducial range spanned by this hypothetical survey is an [NII] 122μ m emission line at $z = 7$, $\nu_{\rm obs} = 308$ GHz. The cross spectrum between the [CII] and [OI] data cubes, for example, should follow

$$P_{x,\mathrm{CII-OI}}(k,\mu) = \langle I_t\rangle\langle I_{\rm OI}\rangle\langle b_t\rangle\langle b_{\rm OI}\rangle\left(1+\beta_t\mu^2\right)\left(1+\beta_{\rm OI}\mu^2\right) \times D\left[\mu k\sigma_p(z_t)\right]P_\rho(k,z_t) + P_{\rm shot,CII-OI} \tag{4.27}$$

where $\langle I_{\rm OI}\rangle$ and $\langle b_{\rm OI}\rangle$ denote the specific intensity and linear bias factor of the [OI] emitters that lie at the same redshift as the [CII] emission, and the other symbols have their usual meanings. Similar to Equation 4.24, we assume that the finger-of-god suppression has an identical form for each set of emitters. In what follows, we neglect the shot-noise term, $P_{\rm shot,CII-OI}$. Strictly speaking, this is only correct in the limit that disparate populations of sources produce the [CII] and [OI] emission. However our sensitivity here is coming from large scales where the shot-noise contribution should be small, so we don't expect neglecting it to impact our estimates.

Here we consider using the cross-spectrum between [CII] and [OI] as a test of the high redshift origin of a potential [CII] contribution to the intensity mapping data cube. For this purpose, we define $A = \langle I_t\rangle\langle I_{\rm OI}\rangle\langle b_t\rangle\langle b_{\rm OI}\rangle$ and consider the significance at which

A can be shown to be non-zero. Here the relevant variance is:

$$\begin{aligned}\mathrm{var}\left[P_{x,\mathrm{CII-OI}}(k,\mu)\right] = \Bigg[& P^2_{x,\mathrm{CII-OI}} \\ & + \Big(P_{\mathrm{tot,CII}}(k,\mu) + P_{N,\mathrm{CII}}(k,\mu)\Big) \\ & \times \Big(P_{\mathrm{tot,OI}}(k,\mu) + P_{N,\mathrm{OI}}(k,\mu)\Big)\Bigg], \end{aligned} \tag{4.28}$$

where $P_{\mathrm{tot,OI}}(k,\mu)$ is the total [OI] signal auto spectrum, including the interlopers for this line. For simplicity, we approximate the interloper power contamination to the [OI] line as identical to that of the [CII] line. This should be a good but imperfect approximation, since the two lines lie at fairly similar observed frequencies. Likewise, we approximate the noise power spectrum as identical at the observing frequencies centered around each of the [CII] and [OI] lines. Based on the local relation between line luminosity and star-formation rate in Visbal and Loeb (2010) and using Equation 4.14, we infer that $\langle I_{\mathrm{OI}}\rangle(z=7) = 0.05\langle I_{\mathrm{CII}}\rangle(z=7)$. We can then estimate the total signal to noise at which the single parameter, A, may be detected using Equations 4.27 and 4.28. For our fiducial numbers we find that the cross spectrum may be detected at $8.6-\sigma$ significance, and so considering the cross spectrum between the two lines seems promising. If the frequency range can be extended somewhat, the cross spectrum between [CII] and [NII] might be detectable. In fact, based on the local line-luminosity star formation rate correlation tabulated in Visbal and Loeb (2010) we expect this correlation to be more detectable than that between [CII] and [OI]: using the numbers in Visbal and Loeb (2010) gives a $17-\sigma$ detection forecast. However, assuming the local relation is especially suspect for [NII]: there is unlikely to be enough prior star formation to build up a significant nitrogen abundance at the high redshifts of interest here (Suginohara et al. 1999).

Unfortunately – for our fiducial survey numbers – we don't expect significant detections of the auto spectra in [OI] or [NII] given the large interloper "noise" and the lower expected specific intensity in these lines. Consequently, a measurement of the cross-spectrum between [CII] and [OI] and/or [NII] can help establish the high redshift origin

of a possible [CII] signal, but it won't provide a full check on the values of $\langle I_t \rangle$, $\langle b_t \rangle$ inferred from the [CII] auto spectrum, since the bias and intensity of the [OI] and/or [NII] emission will remain uncertain.

4.7 Conclusions

Line confusion provides an important systematic concern for many intensity mapping surveys and for some traditional surveys targeting emission-line galaxies. Interloper line emission will likely be especially strong in future intensity mapping surveys aimed at detecting reionization-era signals in the [CII] and Ly-α lines. Here we developed an approach to fit-out interloper contamination at the power spectrum level, using the fact that the interloper contribution to the emission power spectrum will have a distinctive anisotropy that results when the target redshift is assumed in mapping from frequency and angle to co-moving units.

We applied this to the case of a $z = 7$ [CII] intensity mapping experiment, in which the $z \sim 7$ signal fluctuations are expected to be smaller than the combined emission fluctuations from several CO interloper lines. In the limit of low noise power, the interloper fluctuations can be separated from the [CII] power spectrum signal. A more sensitive instrument than currently planned is however required. In the near term, it would be interesting to investigate whether the power spectrum anisotropy technique advocated here may be fruitfully combined with a masking approach. Additional careful work is required to study this; in this context, it is crucial to examine optical and infrared tracers to quantify whether they may serve as faithful proxies for the CO interloper emission. We therefore defer this to future work.

We also explored how the intensity mapping data cube may be cross-correlated with large scale structure tracers to extract the properties of likely interloper lines. We showed that emission-line galaxy samples from DESI will be a good data set for cross-correlations, allowing one to extract CO interloper properties for $z \sim 7$ [CII] emission surveys. Finally,

we briefly considered the cross-correlation between two different fine structure lines at the same redshift; this can help verify the high redshift origin if a possible signal is seen in the $z \sim 7$ [CII] auto spectrum. For all of these studies, it will be important to further consider foreground contamination systematics. Specifically, additional work is needed to quantify the impact of mode-mixing on efforts to measure the angular dependence of the [CII] power spectrum. It will also be important to quantify how correlated the foregrounds for different tracer lines – such as [CII] and [OI] – are.

In any case, intensity mapping is a potentially powerful approach for tracing large-scale structure at early times and may capture the collective impact of sources that are undetectable using traditional means. Although interloper contamination is a concern for many of these measurements, it may be circumvented using a combination of techniques, including the power spectrum anisotropy approach considered here.

Chapter 5

Conclusion

We began this thesis by discussing our best understanding of the reionization process and some of the observational methods and theories by which we developed that understanding. We saw that reionization is expected to be an extended, patchy process fueled by galaxies. Our best current constraints on the EoR come from quasars and the CMB. Quasar spectra suggests that reionization is over by $z \sim 6$. The CMB, via constraints on the Thomson optical depth, puts $z_{reion} \simeq 8.8 \pm 0.9$. It also places an upper bound on the duration of reionization though the kSZ: $\Delta z < 5.4$. Together, these observations paint an extremely broad-stroked picture of reionization as a process that took place between $z \sim 6$ and $z \sim 12$. However, these observations do not tell us much about how reionization proceeded. For example, we have very limited observational constraints on how the ionization fraction evolves with redshift. In addition, we have yet to determine the size distribution of the ionized regions at different stages of the reionization process. Observations that will be able to provide that, such as those using high redshift galaxies, are still coming into their own. In the other chapters of this thesis, we have focused on exactly that, the use of high redshift galaxies as tools with which to understand the EoR.

We began in §2 by reconsidering measurements of $f_{Ly\alpha}$, the fraction of LBGs that are also LAEs. Measurements of this quantity (Pentericci et al. 2011; Schenker et al. 2012; Ono et al. 2012; Caruana et al. 2012), showed a significant decrease at $z \sim 7$ compared

to the increasing trend in $f_{Ly\alpha}$ from $z \sim 4$ to $z \sim 6$. $f_{Ly\alpha}$ is designed to highlight extrinsic evolution of galaxy properties, i.e. changes in the IGM; thus, this sudden decrease is a strong signal of an increasing neutral fraction, indicating that they were observing back into the EoR. However, when they attempted to estimate the ionized fraction at $z \sim 7$, they concluded that $x_i \lesssim 0.4$. Harmonizing this with the other constraints on the EoR requires a very rapid end to reionization. This end is more rapid than other models suggest. Motivated by this discordance, we set out to consider the effect of sample variance on the measurements of $f_{Ly\alpha}$.

The measurements of the Lyα fraction were performed over small fields of view, with typical dimensions on the order of 10 Mpc h^{-1} at $z \sim 7$, comparable to the expected size of ionized bubbles. These fields are too small to provide a representative sample of the Universe at that redshift. Further, we found that the selected galaxies do not sample the entire field. While they selected LBGs via broad band surveys, they chose only a fraction of those galaxies to follow-up on with spectroscopic observations, thus, further reducing their fields of view. Therefore, even though multiple fields of view were observed, the total area covered remained small enough that sample variance made a significant contribution to their the error budget. This was unaccounted for by the error budgets given in previous work.

We used simulations to model the observations of $f_{Ly\alpha}$. We calculated the mock Lyα fraction for a range of ionization histories and several models describing the relationship between LAEs and LBGs. We found that the drop in $f_{Ly\alpha}$, while most likely due to an increasingly neutral Universe, only required a neutral fraction $x_{HI} \sim 0.05$ at the 95% confidence level.

In §3, we considered how the spatial fluctuations that obscured the Lyα fraction measurements could actually be used as a signal of reionization. We did this by examining how the patchy nature of reionization will enhance the clustering of LAEs, due to their preferential selection in large ionized bubbles. We focused here on HSC's prospects for measuring this signal. HSC, a new instrument on Subaru, will, via a combination of

broad band and narrow band observations, detect thousands of LBGs and LAEs at $z \sim 7$. Working from simulations, we modeled potential HSC observations. We considered the effects of reionization on galaxy abundance, a modified version of the Lyα fraction, and on galaxy clustering. In all these cases, we compared LAEs to LBGs and concluded that, provided HSC observations are reaching back into the EoR, the signal from LAEs should evolve more strongly with redshift than that from LBGs.

We used several methods to quantify the enhanced LAE clustering, specifically void probability functions, the probability that a random circle of radius R contains zero galaxies in the survey, and measurements of the bias factor. In both cases, we found that the LAE clustering was enhanced, either via larger voids or a larger bias factor, as the neutral fraction grew. LBG clustering, on the other hand, remained constant, making it a good comparison sample.

We also set out to quantify the effect of foreground interlopers on these calculations. LBG interlopers, likely red galactic stars, are not clustered in these observations, so their effect on the LBG clustering signal is to reduce it slightly. LAE interlopers, on the other hand, are drawn from specific emission lines and may themselves be clustered. If the ionization fraction is sufficiently high, the LAE interlopers will not be a problem. However, in more neutral cases, the observed LAE abundance declines, and so the interloper fraction increases. These interlopers can obscure the very signal in which we are interested. We find, however, that the cross spectrum of LAEs and LBGs is not effected by the interloper clustering and, thus, provides a better estimate of the bias factor of the LAEs. In our fiducial model, in which the universe is $\sim 20\%$ neutral at $z = 6.6$, we forecast that the HSC can measure the linear bias of the LAEs at 11% accuracy and that this determines the volume-weighted neutral fraction to within about 0.1.

In §4, we turned our attention to intensity mapping, a technique that is sensitive to the emission from all sources in a given emission line, even ones too faint to be detected by other methods. Intensity mapping targeting the EoR should allow the spatial fluctuations of ionizing sources to be mapped and the collective impact of faint sources on the ionizing

process to be quantified. One significant concern for intensity mapping is the presence of foreground interloper emission which can dilute or obscure the signal.

We developed an approach for separating out the interloper contamination from the intensity mapping power spectrum. Since intensity mapping is based on emission lines, the interlopers are foreground galaxies with emission lines redward of the target emission line. Thus, the interlopers all come from the same redshift or redshifts, depending on the number of lines that can be contaminants for the target line. Projecting the interloper onto the target redshift will cause the interlopers to be mapped to the wrong co-moving coordinates. Specifically, in Fourier space, along the line of sight, the interlopers will be mapped to larger wavenumbers; in the transverse direction, the interlopers will be mapped to smaller wavenumbers. This results in a distinctive anisotropy, which can be used to cleanly fit out the interloper contribution.

We applied this technique to a hypothetical $z = 7$ [CII] intensity mapping experiment and showed that, provided the noise power is small enough, the interloper fluctuations can be separated out from the [CII] signal; this is true even though the interloper fluctuations are larger than the target signal. However, the low noise power requirement necessitates instruments more sensitive than currently planned.

We also considered two cross-correlation measurements. First, we considered cross-correlating the intensity mapping with a three dimensional map of large scale structure at the redshift of the interlopers. This cross-correlation selects the interloper contribution and should allow properties of the interloper lines to be calculated. Second, we considered the cross-correlation between intensity maps of two different lines at the same (high) redshift. While both lines are vulnerable to interlopers, they would draw their interlopers from different redshifts. The cross-correlation should select only the signals from the same redshift, allowing the high redshift signals to be isolated.

The future observations considered here, from the HSC and intensity mapping surveys, will access new information about reionization. Both observations should tell us about the distribution of ionized bubbles. LAEs are preferentially observed in ionized

bubbles so clusters of LAE should trace the distribution of large bubbles. Intensity mapping will map the spatial distribution of the ionizing sources, allowing the bubble distribution to be inferred. These observations, particularly if combined with 21-cm observations which will trace the neutral gas, should allow us to understand on an observational level the spatial fluctuations of reionization and, hopefully, the evolution of the neutral faction as a function of redshift. The next years, as these future observations become reality, should be an exciting time to be studying the EoR.

Bibliography

Alam, S., Albareti, F. D., Allende Prieto, C., et al.: 2015, *ApJS* **219**, 12

Alcock, C. and Paczynski, B.: 1979, *Nature* **281**, 358

Ali, Z. S., Parsons, A. R., Zheng, H., et al.: 2015, *ApJ* **809**, 61

Ando, M., Ohta, K., Iwata, I., et al.: 2006, *ApJ* **645**, L9

Arnouts, S., D'Odorico, S. Cristiani, S., Zaggia, S., Fontana, A., and Giallongo, E.: 1999, *A&A* **341**, 641

Balestra, I., Mainieri, V., Popesso, P., et al.: 2010, *A&A* **512**, A12

Ballinger, W. E., Peacock, J. A., and Heavens, A. F.: 1996, *MNRAS* **282**, 877

Barkana, R.: 2002, *NAR* **7**, 85

Barkana, R. and Loeb, A.: 2001, *Phys. Rep.* **349**, 125

Barkana, R. and Loeb, A.: 2004, *ApJ* **609**, 474

Barkana, R. and Loeb, A.: 2007, *Reports on Progress in Physics* **70**, 627

Barone-Nugent, R. L., Trenti, M., Wyithe, J. S. B., et al.: 2014, *ApJ* **793**, 17

Becker, G. D. and Bolton, J. S.: 2013, *MNRAS* **436**, 1023

Becker, G. D., Bolton, J. S., and Lidz, A.: 2015a, *PASA* **32**, e045

Becker, G. D., Bolton, J. S., Madau, P., et al.: 2015b, *MNRAS* **447**, 3402

Bernardi, G., de Bruyn, A. G., Brentjens, M. A., et al.: 2009, *A&A* **500**, 965

Bernardi, G., de Bruyn, A. G., Harker, G., et al.: 2010, *A&A* **522**, A67

Birkinshaw, M.: 1999, *Physics Reports* **310**, 97

Blanc, G. A., Adams, J. J., Gebhardt, K., et al.: 2011, *ApJ* **736**, 31

Bolton, J. S. and Haehnelt, M.: 2013, *MNRAS* **429**, 1695

Bolton, J. S. and Haehnelt, M. G.: 2007, *MNRAS* **382**, 325

Bolton, J. S., Haehnelt, M. G., Warren, S. J., et al.: 2011, *MNRAS* **416**, L70

Bond, J. R., Kofman, L., and Pogosyan, D.: 1996, *Nature* **380**, 603

Bouwens, R. J., Illingworth, G. D., Oesch, P. A., et al.: 2012, *ApJ* **754**, 83

Bouwens, R. J., Illingworth, G. D., Oesch, P. A., et al.: 2011, *ApJ* **737**, 90

Bouwens, R. J., Illingworth, G. D., Oesch, P. A., et al.: 2015, *ApJ* **803**, 34

Bovill, M. S. and Ricotti, M.: 2009, *ApJ* **693**, 1859

Bowman, J. D., Morales, M. F., and Hewitt, J. N.: 2009, *ApJ* **695**, 183

Breysse, P. C., Kovetz, E. D., and Kamionkowski, M.: 2014, *MNRAS.* **443(4)**, 3506

Bromm, V. and Yoshida, N.: 2011, *ARA&A* **49**, 373

Bullock, J. S., Kravtsov, A. V., and Weinberg, D. H.: 2001, *ApJ* **548**, 33

Carilli, C. and Walter, F.: 2013, *ARA%A* **51**, 105

Carilli, C. L.: 2006, *NAR* **50**, 162

Carilli, C. L.: 2011, *ApJ* **730**, L30

Carlstrom, J. E., Holder, G. P., and Reese, E. D.: 2002, *ARA&A* **40**, 643

Caruana, J., Bunker, A. J., Wilkins, S. M., et al.: 2012, *MNRAS* **427**, 3055

Castellano, M., Fontana, A., Paris, D., et al.: 2010, *A&A* **524**, A28

Chang, T.-C., Pen, U.-L., Peterson, J. B., and McDonald, P.: 2008, *Phys. Rev. Lett.* **100**, 091303

Chiang, C.-T. et al.: 2013, *JCAP* **1312**, 030

Chornock, R., Berger, E., Fox, D. B., et al.: 2013, *ApJ* **774**, 26

Choudhury, T. R., Puchwein, E., Haehnelt, M. G., and Bolton, J. S.: 2015, *MNRAS* **452**, 261

Clément, B., Cuby, J.-G., Courbin, F., et al.: 2012, *A&A* **538**, A66

Colless, M., Dalton, G., Maddox, S., et al.: 2001, *MNRAS* **328**, 1039

Comparat, J., Richard, J., Kneib, J.-P., et al.: 2015, *AAp* **575**, A40

Cooray, A.: 2004, *Phys. Rev. D.* **70(6)**, 063509

Cooray, A. and Sheth, R.: 2002, *Phys. Rep.* **372**, 1

Crites, A. T., Bock, J. J., Bradford, C. M., et al.: 2014, in *Millimeter, Submillimeter, and Far-Infrared Detectors and Instrumentation for Astronomy VII*, Vol. 9153 of *Proc. SPIE*, p. 91531W

Croft, R. A. C.: 1998, in A. V. Olinto, J. A. Frieman, and D. N. Schramm (eds.), *Eighteenth Texas Symposium on Relativistic Astrophysics*, p. 664

Croft, R. A. C., Miralda-Escudé, J., Zheng, Z., et al.: 2016, *MNRAS* **457**, 3541

Curtis-Lake, E., McLure, R. J., Pearce, H. J., et al.: 2012, *MNRAS* **422**, 1425

Datta, A., Bowman, J. D., and Carilli, C. L.: 2010, *ApJ* **724**, 526

Dawson, K. S., Schlegel, D. J., Ahn, C. P., et al.: 2013, *AJ* **145**, 10

Dayal, P. and Ferrara, A.: 2012, *MNRAS* **421**, 2568

de la Torre, S., Le Fèvre, O., Arnouts, S., et al.: 2007, *A&A* **475**, 443

De Looze, I. et al.: 2014, *A&A* **568**, A62

de Oliveira-Costa, A., Tegmark, M., Gaensler, B. M., et al.: 2008, *MNRAS* **388**, 247

DeBoer, D. R., Parsons, A. R., Aguirre, J. E., et al.: 2016, *ArXiv e-prints*

Di Matteo, T., Ciardi, B., and Miniati, F.: 2004, *MNRAS* **355**, 1053

Di Matteo, T., Perna, R., Abel, T., and Rees, M. J.: 2002, *ApJ* **564**, 576

Dijkstra, M.: 2011, *ArXiv e-prints*

Dijkstra, M.: 2014, *PASA* **31**, e040

Dijkstra, M., Haiman, Z., and Spaans, M.: 2006, *ApJ* **649**, 14

Dijkstra, M., Lidz, A., and Wyithe, S.: 2007, *MNRAS* **377**, 1175

Dijkstra, M., Mesinger, A., and Wyithe, J. S. B.: 2011, *MNRAS* **414**, 2139

Dijkstra, M. and Wyithe, J. S. B.: 2012, *MNRAS* **419**, 3181

Dijkstra, M., Wyithe, S., and Haiman, Z.: 2006, *MNRAS* **379**, 253

Dressler, A., Martin, C. L., Henry, A., Sawicki, M., and McCarthy, P.: 2011, *APJ* **740**, 71

Dunlop, J. S.: 2013, in T. Wiklind, B. Mobasher, and V. Bromm (eds.), *The First Galaxies*, Vol. 396 of *Astrophysics and Space Science Library*, p. 223

Duval, F., Schaerer, D., Östlin, G., and Laursen, P.: 2014, *A&A* **562**, A52

Eisenstein, D. J., Weinberg, D. H., Agol, E., et al.: 2011, *AJ* **142**, 72

Ellis, R. S., McLure, R. J., Dunlop, J. S., et al.: 2013, *ApJL* **763**, L7

Faisst, A. L., Capak, P., Carollo, C. M., Scarlata, C., and Scoville, N.: 2014, *ApJ* **788**, 87

Fan, X., Strauss, M. A., Becker, R. H., et al.: 2006, *AJ* **132**, 117

Fan, X.-H., Strauss, M. A., Becker, R. H., et al.: 2006, *AJ* **132**, 117

Faucher-Giguère, C.-A., Lidz, A., Hernquist, L., and Zaldarriaga, M.: 2008, *ApJ* **688**, 85

Ferrara, A. and Pandolfi, S.: 2014, *ArXiv e-prints*

Field, G. B.: 1958, *Proceedings of the IRE* **46**, 240

Field, G. B.: 1959, *ApJ* **129**, 551

Finkelstein, S. L.: 2015, *ArXiv e-prints*

Finkelstein, S. L., Papovich, C., Ryan, R. E., et al.: 2012a, *ApJj* **758**, 93

Finkelstein, S. L., Papovich, C., Salmon, B., et al.: 2012b, *ApJ* **756**, 164

Fontana, A., D'Odorico, S., Poli, F., et al.: 2000, *AJ* **120**, 2206

Fontana, A., Vanzella, E. Pentericci, L., Castellano, M., et al.: 2010, *ApJ* **725**, L205

Forero-Romero, J. E., Yepes, G., Gottlöber, S., and Prada, F.: 2012, *MNRAS* **419**, 952

Furlanetto, S. and Lidz, A.: 2007, *ApJ* **660**, 1030

Furlanetto, S. R., Hernquist, L., and Zaldarriaga, M.: 2004a, *MNRAS* **354**, 695

Furlanetto, S. R. and Oh, S. P.: 2005, *MNRAS* **363**, 1031

Furlanetto, S. R., Oh, S. P., and Briggs, F. H.: 2006, *Physics Reports* **433**, 181

Furlanetto, S. R., Zaldarriaga, M., and Hernquist, L.: 2004b, *ApJ* **613**, 1

Furlanetto, S. R., Zaldarriaga, M., and Hernquist, L.: 2006, *MNRAS* **365**, 1012

Furusawa, H., Kashikawa, N., Kobayashi, M. A. R., et al.: 2016, *ApJ* **822**, 46

George, E. M., Reichardt, C. L., Aird, K. A., et al.: 2015, *ApJ* **799**, 177

Giallongo, E., Grazian, A., Fiore, F., et al.: 2015, *A&A* **578**, A83

Giavalisco, M., Ferguson, H. C., Koekemoer, A. M., et al.: 2004, *ApJ* **600**, L93

Gleser, L., Nusser, A., and Benson, A. J.: 2008, *MNRAS* **391**, 383

Gnedin, N. Y. and Fan, X.: 2006, *ApJ* **648**, 1

Gong, Y., Cooray, A., Silva, M. B., Santos, M. G., and Lubin, P.: 2011, *ApJ* **728**, L46

Gong, Y., Silva, M., Cooray, A., and Santos, M. G.: 2014, *ApJ* **785**, 72

Gronwall, C., Ciardullo, R., Hickey, T., et al.: 2007, *ApJ* **667**, 79

Guhathakurta, P., Tyson, J. A., and Majewski, S. R.: 1990, *ApJ* **357**, L9

Gunn, J. E. and Peterson, B. A.: 1965, *ApJ* **142**, 1633

Gunn, J. E., Siegmund, W. A., Mannery, E. J., et al.: 2006, *AJ* **131**, 2332

Haardt, F. and Madau, P.: 1996, *ApJ* **461**, 20

Haardt, F. and Madau, P.: 2012, *ApJ* **746**, 125

Hathi, N. P., Ryan, R. E., Cohen, S. H., et al.: 2010, *ApJ* **720**, 1708

Hazelton, B. J., Morales, M. F., and Sullivan, I. S.: 2013, *ApJ* **770**, 156

Hibon, P., Cuby, J.-G., Willis, J., et al.: 2010, *A&A* **515**, A97

Hibon, P., Kashikawa, N., Willott, C., Iye, M., and Shibuya, T.: 2012, *ApJ* **744**, 89

Hibon, P., Malhotra, S., Rhoads, J., and Willott, C.: 2011, *ApJ* **741**, 101

Hinshaw, G., Larson, D., Komatsu, E., et al.: 2013, *ApJS* **208**, 19

Howlett, C., Lewis, A., Hall, A., and Challinor, A.: 2012, *JCAP* **1204**, 027

HSC Science Collaborations: 2012

Hu, E., Cowie, L., Barger, A., et al.: 2010, *ApJ* **725**, 394

Hu, E. M., Cowie, L. L., and McMahon, R. G.: 1998, *ApJL* **502**, L99

Hu, W. and White, M.: 1997, *NA* **2**, 323

Hutter, A., Dayal, P., and Müller, V.: 2015, *MNRAS* **450**, 4025

Jelić, V., Zaroubi, S., Labropoulos, P., et al.: 2010, *MNRAS* **409**, 1647

Jelić, V., Zaroubi, S., Labropoulos, P., et al.: 2008, *MNRAS* **389**, 1319

Jensen, H., Hayes, M., Iliev, I. T., et al.: 2014, *MNRAS* **444**, 2114

Jensen, H., Laursen, P., Mellema, G., et al.: 2013, *MNRAS* **428**, 1366

Jiang, L., Finlator, K., Cohen, S. H., et al.: 2016, *ApJ* **816**, 16

Johnson, J. L., Greif, T. H., Bromm, V., Klessen, R. S., and Ippolito, J.: 2009, *MNRAS* **399**, 37

Kaiser, N.: 1987, *MNRAS* **227**, 1

Kaiser, N.: 1998, *ApJ* **498**, 26

Kakiichi, K., Dijkstra, M., Ciardi, B., and Graziani, L.: 2015, *ArXiv e-prints*

Kashikawa, N., Shimasaku, K., Malkan, M. A., et al.: 2006, *ApJ* **648**, 7

Kashikawa, N., Shimasaku, K., Malkan, M. A., et al.: 2006a, *ApJ* **648**, 7

Kashikawa, N., Shimasaku, K., Matsuda, Y., et al.: 2011, *ApJ* **734**, 119

Kashikawa, N., Yoshida, M., Shimasaku, K., et al.: 2006b, *ApJ* **637**, 631

Keating, G. K. et al.: 2015, *ApJ* **814(2)**, 140

Knudsen, K. K., Richard, J., Kneib, J.-P., et al.: 2016, *MNRAS* **462**, L6

Konno, A., Ouchi, M., Ono, Y., et al.: 2014, *ApJ* **797**, 16

Kornei, K. A., Shapley, A. E., Erb, D. K., et al.: 2010, *ApJ* **711**, 693

Krug, H. B., Veilleux, S., Tilvi, V., et al.: 2012, *ApJ* **745**, 122

Kuhlen, M. and Faucher-Giguère, C.-A.: 2012, *MNRAS* **423**, 862

Larson, D., Dunkley, J., Hinshaw, G., et al.: 2011, *ApJS* **192**, 16

Laursen, P., Duval, F., and Östlin, G.: 2013, *ApJ* **766**, 124

Laursen, P., Razoumov, A. O., and Sommer-Larsen, J.: 2009, *ApJ* **696**, 853

Lee, K.-S., Giavalisco, M., Gnedin, O. Y., et al.: 2006, *ApJ* **642**, 63

Lehnert, M. D. and Bremer, M.: 2003, *ApJ* **593**, 630

Levi, M., Bebek, C., Beers, T., et al.: 2013, *ArXiv e-prints*

Lewis, A. and Bridle, S.: 2002, *Phys. Rev.* **D66**, 103511

Lewis, A., Challinor, A., and Lasenby, A.: 2000, *ApJ* **538**, 473

Li, T. Y., Wechsler, R. H., Devaraj, K., and Church, S. E.: 2016, *ApJ* **817(2)**, 169

Lidz, A.: 2016, in A. Mesinger (ed.), *Understanding the Epoch of Cosmic Reionization: Challenges and Progress*, Vol. 423 of *Astrophysics and Space Science Library*, p. 23

Lidz, A., Furlanetto, S. R., Oh, S. P., et al.: 2011, *ApJ* **741**, 70

Lidz, A., McQuinn, M., and Zaldarriaga, M.: 2007, *ApJ* **670**, 39

Lidz, A. and Taylor, J.: 2016, *ApJ* **825**, 143

Lidz, A., Zahn, O., Furlanetto, S., et al.: 2009, *ApJ* **690**, 252

Linder, E. V.: 2005, *Phys. Rev.* **D72**, 043529

Liu, A., Parsons, A. R., and Trott, C. M.: 2014a, *Phys. Rev. D* **90(2)**, 023018

Liu, A., Parsons, A. R., and Trott, C. M.: 2014b, *Phys. Rev. D* **90(2)**, 023019

Liu, A. and Tegmark, M.: 2011, *Phys. Rev. D* **83(10)**, 103006

Loeb, A. and Furlanetto, S. R.: 2013, *The First Galaxies in the Universe*, Princeton Series in Astrophysics, Princeton University Press, Princeton, NJ

Madau, P.: 1995, *ApJ* **441**, 18

Madau, P. and Haardt, F.: 2015, *ApJL* **813**, L8

Madau, P., Meiksin, A., and Rees, M. J.: 1997, *ApJ* **475**, 429

Madau, P., Pozzetti, L., and Dickinson, M.: 1998, *ApJ* **498**, 106

Malloy, M. and Lidz, A.: 2015, *ApJ* **799**, 179

Mashian, N., Sternberg, A., and Loeb, A.: 2015, *JCAP* **11**, 028

Matthee, J., Sobral, D., Santos, S., et al.: 2015, *MNRAS* **451**, 400

McGreer, I. D., Mesinger, A., and D'Odorico, V.: 2015, *MNRAS* **447**, 499

McGreer, I. D., Mesinger, A., and Fan, X.: 2011, *MNRAS* **415**, 3237

McLure, R. J., Dunlop, J. S., Bowler, R. A. A., et al.: 2013, *MNRAS* **432**, 2696

McLure, R. J., Dunlop, J. S., de Ravel, L., et al.: 2011, *MNRAS* **418**, 2074

McQuinn, M.: 2010, in L. M. Stanford, J. D. Green, L. Hao, and Y. Mao (eds.), *New Horizons in Astronomy: Frank N. Bash Symposium 2009*, Vol. 432 of *Astronomical Society of the Pacific Conference Series*, p. 65

McQuinn, M.: 2016, *ARA&A* **54**, 313

McQuinn, M., Hernquist, L., Zaldarriaga, M., and Dutta, S.: 2007a, *MNRAS* **381**, 75

McQuinn, M., Lidz, A., Zahn, O., et al.: 2007b, *MNRAS* **377**, 1043

Mellema, G., Iliev, I. T., Pen, U.-L., and Shapiro, P. R.: 2006, *MNRAS* **372**, 679

Mesinger, A.: 2010, *MNRAS* **407**, 1328

Mesinger, A., Aykutalp, A., Vanzella, E., et al.: 2015, *MNRAS* **446**, 566

Mesinger, A. and Furlanetto, S. R.: 2008, *MNRAS* **386**, 1990

Miralda-Escude, J.: 1998, *ApJ* **501**, 15

Miralda-Escude, J.: 2003, *ApJ* **597**, 66

Morales, M. F., Hazelton, B., Sullivan, I., and Beardsley, A.: 2012, *ApJ* **752**, 137

Mortlock, D. J.: 2016, in A. Mesinger (ed.), *Understanding the Epoch of Cosmic Reionization: Challenges and Progress*, Vol. 423 of *Astrophysics and Space Science Library*, p. 23

Mortlock, D. J., Warren, S. J., Venemans, B. P., et al.: 2011, *Nature* **474**, 616

Munoz, J. A. and Furlanetto, S. R.: 2013, *MNRAS* **435**, 2676

Neufeld, D. A.: 1991, *ApJL* **370**, L85

Nilsson, K. K., Möller-Nilsson, O., Møller, P., Fynbo, J. P. U., and Shapley, A. E.: 2009, *MNRAS* **400**, 232

Oesch, P. A., Bouwens, R. J., Illingworth, G. D., et al.: 2013, *ApJ* **773**, 75

Oke, J. B.: 1974, *ApJS* **27**, 21

Ono, Y., Ouchi, M., Mobasher, B., et al.: 2012, *ApJ* **744**, 83

Orsi, A., Lacey, C. G., and Baugh, C. M.: 2012, *MNRAS* **425**, 87

Ostriker, J. P. and Vishniac, E. T.: 1986, *ApJ* **306**, L51

Ota, K., Iye, M., Kashikawa, N., et al.: 2010, *ApJ* **722**, 803

Ouchi, M., Mobasher, B., Shimasaku, K., et al.: 2009, *ApJ* **706**, 1136

Ouchi, M., Shimasaku, K., Akiyama, M., et al.: 2008, *ApJS* **176**, 301

Ouchi, M., Shimasaku, K., Furusawa, H., et al.: 2010, *ApJ* **723**, 869

Overzier, R. A., Bouwens, R. J., Illingworth, G. D., and Franx, M.: 2006, *ApJ* **648**, L5

Parsons, A. R., Pober, J. C., Aguirre, J. E., et al.: 2012, *ApJ* **756**, 165

Pawlik, A. H., Milosavljević, M., and Bromm, V.: 2011, *ApJ* **731**, 54

Pénin, A., Cuby, J.-G., Clément, B., et al.: 2015, *A&A* **577**, A74

Pentericci, L., Fontana, A., Vanzella, E., et al.: 2011, *ApJ* **743**, 132

Pérez-Fournon, I., Balcells, M., Moreno-Insertis, F., and Sánchez, F.: 2010, *Galaxies at High Redshift*

Phillips, P. R.: 1995, *ApJ* **455**, 419

Pirzkal, N., Rothberg, B., Ly, C., et al.: 2013, *ApJ* **772**, 48

Planck Collaboration, Adam, R., Aghanim, N., et al.: 2016, *ArXiv e-prints*

Planck Collaboration, Ade, P. A. R., Aghanim, N., et al.: 2014, *A & A* **571**, A16

Pober, J. C., Parsons, A. R., Aguirre, J. E., et al.: 2013, *ApJL* **768**, L36

Pritchard, J. and Loeb, A.: 2010, *Nature* **468**, 772

Pritchard, J. R., Loeb, A., and Wyithe, J. S. B.: 2010, *MNRAS* **408**, 57

Pullen, A. R., Chang, T.-C., Doré, O., and Lidz, A.: 2013, *ApJ* **768**, 15

Pullen, A. R., Hirata, C. M., Dore, O., and Raccanelli, A.: 2016, *Publ. Astron. Soc. Jap.* **68**, 12

Quinn, T., Katz, N., and Efstathiou, G.: 1996, *MNRAS* **278**, L49

Raiter, A., Schaerer, D., and Fosbury, R. A. E.: 2010, *A&A* **523**, A64

Rees, M. J.: 1984, *ARA& A* **22**, 471

Reichardt, C. L.: 2016, in A. Mesinger (ed.), *Astrophysics and Space Science Library*, Vol. 423 of *Astrophysics and Space Science Library*, p. 227

Righi, M., Hernandez-Monteagudo, C., and Sunyaev, R.: 2008, *A&A* **489**, 489

Robertson, B. E.: 2010, *ApJ* **713**, 1266

Robertson, B. E., Ellis, R. S., Dunlop, J. S., McLure, R. J., and Stark, D. P.: 2010, *Nature* **468**, 49

Robertson, B. E., Ellis, R. S., Furlanetto, S. R., and Dunlop, J. S.: 2015, *ApJ* **802**, L19

Robertson, B. E., Ellis, R. S., Furlanetto, S. R., and Dunlop, J. S.: 2015, *ApJ* **802(2)**, L19

Robertson, B. E., Furlanetto, S. R., Schneider, E., et al.: 2013, *ApJ* **768**, 71

Santos, M. G., Cooray, A., and Knox, L.: 2005, *ApJ* **625**, 575

Santos, M. R.: 2004, *MNRAS* **349**, 1137

Schaerer, D.: 2003, *A&A* **397**, 527

Schechter, P.: 1976, *ApJ* **203**, 297

Schenker, M. A., Ellis, R. S., Konidaris, N. P., and Stark, D. P.: 2014, *ApJ* **795**, 20

Schenker, M. A., Stark, D. P., Ellis, R. S., et al.: 2012, *ApJ* **744**, 179

Shapley, A. E., C., S. C., Pettini, M., and Adelberger, K. L.: 2003, *ApJ* **588**, 65

Shaver, P. A., Windhorst, R. A., Madau, P., and de Bruyn, A. G.: 1999, *A&A* **345**, 380

Shaw, L. D., Rudd, D. H., and Nagai, D.: 2012, *ApJ* **756**, 15

Shull, J. M., France, K., Danforth, C. W., Smith, B., and Tumlinson, J.: 2010, *ApJ* **722**, 1312

Silva, M. B., Santos, M. G., Cooray, A., and Gong, Y.: 2015, *ApJ* **806(2)**, 209

Simcoe, R. A., Sullivan, P. W., Cooksey, K. L., et al.: 2012, *Nature* **492**, 79

Smee, S. A., Gunn, J. E., Uomoto, A., et al.: 2013, *AJ* **146**, 32

Smit, R., Bouwens, R. J., Franx, M., et al.: 2012, *ApJ* **756**, 14

Sobacchi, E. and Mesinger, A.: 2015, *MNRAS* **453**, 1843

Songaila, A. and Cowie, L. L.: 2002, *AJ* **123**, 2183

Springel, V.: 2005, *MNRAS* **364**, 1105

Stacey, G. J., Geis, N., Genzel, R., et al.: 1991, *ApJ* **373**, 423

Stark, D. P., Ellis, R. S., Chiu, K., Ouchi, M., and Bunker, A.: 2010, *MNRAS* **408**, 1628

Stark, D. P., Ellis, R. S., and Ouchi, M.: 2011, *ApJ* **728**, L2

Stark, D. P., Loeb, A., and Ellis, R. S.: 2007, *ApJ* **668**, 627

Steidel, C. C. and Hamilton, D.: 1992, *AJ* **104**, 941

Suginohara, M., Suginohara, T., and Spergel, D. N.: 1999, *ApJ* **512**, 547

Sun, X. H. and Reich, W.: 2009, *A&A* **507**, 1087

Sun, X. H., Reich, W., Waelkens, A., and Enßlin, T. A.: 2008, *A&A* **477**, 573

Sunyaev, R. A. and Zeldovich, Y. B.: 1972, *Comments on Astrophysics and Space Physics* **4**, 173

Taylor, J. and Lidz, A.: 2014, *MNRAS* **437**, 2542

Thomas, R. M. and Zaroubi, S.: 2008, *MNRAS* **384**, 1080

Thyagarajan, N., Udaya Shankar, N., Subrahmanyan, R., et al.: 2013, *ApJ* **776**, 6

Tilvi, V., Rhoads, J. E., Hibon, P., et al.: 2010, *ApJ* **721**, 1853

Trac, H., Bode, P., and Ostriker, J. P.: 2011, *ApJ* **727**, 94

Uzgil, B. D., Aguirre, J. E., Bradford, C. M., and Lidz, A.: 2014, *ApJ* **793(2)**, 116

Vanzella, E., Giavalisco, M., Dickinson, M., et al.: 2009, *ApJ* **695**, 1163

Vanzella, E., Pentericci, L., Fontana, A., et al.: 2011, *ApJ* **730**, L35

Vedantham, H., Udaya Shankar, N., and Subrahmanyan, R.: 2012, *ApJ* **745**, 176

Verhamme, A., Dubois, Y., Blaizot, J., et al.: 2012, *A&A* **546**, A111

Visbal, E. and Loeb, A.: 2010, *JCAP* **11**, 016

Waelkens, A., Jaffe, T., Reinecke, M., Kitaura, F. S., and Enßlin, T. A.: 2009, *A&A* **495**, 697

Wilman, R. J., Miller, L., Jarvis, M. J., et al.: 2008, *MNRAS* **388**, 1335

Wouthuysen, S. A.: 1952, *AJ* **57**, 31

Yajima, H., Li, Y., Zhu, Q., and Abel, T.: 2012, *MNRAS* **424**, 884

Yoshida, M., Shimasaku, K., Ouchi, M., et al.: 2008, *ApJ* **679**, 269

Zaldarriaga, M., Furlanetto, S. R., and Hernquist, L.: 2004, *ApJ* **608**, 622

Zaroubi, S.: 2010, *ArXiv e-prints*

Zaroubi, S.: 2013, in T. Wiklind, B. Mobasher, and V. Bromm (eds.), *The First Galaxies*, Vol. 396 of *Astrophysics and Space Science Library*, p. 45

Zheng, Z., Cen, R., Trac, H., and Miralda-Escude, J.: 2010, *ApJ* **716**, 574